THE PHYSICS AND CHEMISTRY OF HIGH CAPACITY CARBONACEOUS MATERIALS FOR LITHIUM-ION BATTERIES

by

Tao Zheng
B.Sc., Nanjing University (P.R. China), 1988
M.Sc., University of Toronto, 1993

THESIS SUBMITTED IN PARTIAL FULFILLMENT OF THE REQUIREMENTS FOR THE DEGREE OF DOCTOR OF PHILOSOPHY

in the Department
of
Physics

SIMON FRASER UNIVERSITY
May 1996

APPROVAL

Name: Tao Zheng
Degree: Doctor of Philosophy
Title of Thesis: The Physics and Chemistry of High Capacity Carbonaceous Materials for Lithium-Ion Batteries

Examining Committee:

Chairperson: Dr. Konrad Colbow

Dr. Jeff R. Dahn
Senior Supervisor

Dr. Robert F. Frindt

Dr. George Kiricenow

Dr. Steven Holdcroft
Internal Examiner

Dr. Stuart A. Solin
External Examiner
NEC Research Institute
Princeton, NJ, USA

Date Approval: 31 May 1996

PARTIAL COPYRIGHT LICENSE

I hereby grant to Simon Fraser University the right to lend my thesis, project or extended essay (the title of which is shown below) to users of the Simon Fraser University Library, and to make partial or single copies only for such users or in response to a request from the library of any other university, or other educational institution, on its own behalf or for one of its users. I further agree that permission for multiple copying of this work for scholarly purposes may be granted by me or the Dean of Graduate Studies. It is understood that copying or publication of this work for financial gain shall not be allowed without my written permission.

Title of Thesis/Project/Extended Essay

The Physics and Chemistry of High Capacity Carbonaceous Materials for Lithium-Ion Batteries.

Author: _____
(signature)

Tao Zheng
(name)

4 June 1996
(date)

ABSTRACT

The mechanism of lithium insertion depends on the carbon type. The carbonaceous materials of commercial relevance as lithium-ion anodes are divided into three groups: (1) graphitic carbons, (2) hydrogen containing carbons heated to between 500°C and 800°C, and (3) some hard carbons heated to about 1000°C.

The probability P of turbostratic disorder (random shifts or rotations between adjacent carbon layers) in graphitic carbons determines the capacity Q for lithium intercalation, i.e., $Q = 372(1 - P)$ mAh/g. This suggests that no lithium can be inserted between adjacent parallel layers which are turbostratically misaligned. The effect of turbostratic disorder on staging phase transitions which occur during the intercalation of lithium in graphitic carbons was carefully studied by in-situ X-ray diffraction and electrochemical methods. A staging phase diagram was then developed in the P-x plane, where x is the lithium concentration in intercalated graphitic carbons.

Many organic precursors heated between 500 and 800°C contain substantial amounts of hydrogen. They all have similar voltage profiles for lithium insertion, with very large capacity, approaching 900 mAh/g, but also have large hysteresis between charge and discharge. We demonstrated for the first time that this high capacity exhibiting large hysteresis is proportional to the hydrogen content of the carbons. We have carefully studied the electrochemical insertion of lithium in these hydrogen-containing carbons using a variety of charge-discharge rates and cycling temperatures. These measurements allow the hysteresis to be quantified. It is believed that the lithium atoms may bind on hydrogen-terminated edges of hexagonal carbon fragments causing a change in the bond from sp^2 to sp^3. A simple model has been developed to understand the hysteresis. Achieving high capacity carbons needs a coupling of fundamental research (understanding) and applied research (to apply concepts in synthesis). Good understanding will lead to high quality samples.

A number of disordered hard carbons were prepared from phenolic resins. These materials have reversible capacities which exceed 500 mAh/g, a low voltage plateau near zero volts, and little hysteresis in their voltage profiles. These hard carbons with high capacity were found to be made up with a large fraction of single layers, stacked like a "house of cards". We believe that lithium can be adsorbed onto both sides of the carbon sheets, leading to a large capacity. Using small-angle scattering techniques, we showed that the micropore sizes in these carbons are on the order of 10 to 15 Å in diameter. The understanding of high capacity of hard carbons makes it possible to prepare high capacity carbons with low cost and good performance.

More recently, we have been studying ways to make such hard carbons with high capacity from coal. Coal has a large carbon content and can have a highly aromatic condensed structure, leading high product yields after heat treatment. We thought this might be a cheap way to make carbon electrode material for lithium-ion batteries. The physical properties of the pyrolyzed coals varies from sample to sample because of the varied chemistries of the initial coals. Nevertheless, the amount of lithium that the pyrolyzed coals can accommodate is largest for coals with large fraction of single layers and many nanoscopic pores. This gives us further confidence that our model for the reversible capacity of coals is correct.

ACKNOWLEDGMENTS

First of all, I would like to express my deepest gratitude to my senior supervisor Dr. Jeff Dahn for his guidance and many many help during my Ph.D. program at Simon Fraser University. I am very lucky and very happy to have been a student working in his active lab.

When I just began to work in this lab, Dr. Brian Way (at Moli Energy Ltd. (1990)), a formal Ph.D. student in this lab, helped me through a lot of technical problems. I appreciate his help very much.

I wish to thank many fellow students and postdoctoral fellows who were or are in Jeff's lab for their kindly supports during my study. Particular thanks goes to Dr. Wu Li, Dr. Yuan Gao, Dr. Meijie Zhang, Dr. Weibing Xing, Alf Wilson, Oliver Schilling, Monique Richard, and Edward Buiel.

I would like to thank Dr. Robert F. Frindt, and Dr. George Kirczenow for being members of my supervisory committee. I would like to thank Dr. Stuart A. Solin for being my External Examiner, and Dr. Steven Holdcroft for being my Internal Examiner.

Financial support from Simon Fraser University, the British Columbia Science Council and Moli Energy Ltd. (1990) are acknowledged.

Finally, I wish to thank my wife, Qian Guan, for her constant understanding and support.

TABLE OF CONTENTS

List of Tables

List of Figures

Chapter 1

INTRODUCTION

1.1 Lithium-Ion Battery

Interest in batteries covers a wide range of applications from very small batteries for portable consumer electronics to powerful batteries for electric vehicles (Linden, 1995). In many of these applications, the battery limits the performance, size and weight of the equipment. The development of super batteries is critical. In the last ten years, physicists and chemists have greatly improved the performance of most conventional battery types and have developed many new battery systems.

The rechargeable lithium-ion battery is one of a number of new battery technologies which have been developed in the last ten years. This battery system, operating at room temperature, offers several advantages compared to conventional aqueous battery technologies, for example,

1. Higher energy density (up to 120 Wh/kg, 240 Wh/L);
2. Higher cell voltage (from 3.5 to 3.9 V);
3. Longer shelf life (up to 5-10 years) and cycle life (1000 to 3000 cycles).

Lithium-ion batteries are presently the state-of-the-art rechargeable power sources for consumer electronics (Nagaura, 1990). They are now produced by several Japanese and Canadian manufacturers, and many other firms worldwide are engaged in their development. This technology is based on the "rocking chair" concept, that is using two suitable lithium intercalation compounds as cell electrodes. Thus lithium ions are shuttled back and forth between the two intercalation hosts as the cell is charged and discharged. The cell voltage is then determined by the difference in the chemical potential of lithium in the two hosts, *i.e.*,

$$V = -\frac{(\mu_{cathode} - \mu_{anode})}{e}, \qquad (1\text{-}1)$$

where $\mu_{cathode}$ is the chemical potential of lithium in the cathode material, μ_{anode} is the chemical potential of lithium in the anode material, and e is the magnitude of the electron charge. Obviously, a large chemical potential difference will lead to a high cell voltage. Figure 1-1 gives a diagram of the "binding energies" of lithium in lithium compounds. The binding energy (as defined here) is the negative of the chemical potential. Presently, the lithium transition metal oxides $LiNiO_2$, $LiCoO_2$, or $LiMn_2O_4$ are chosen as the cathode and carbonaceous materials as the anode. These transition metal oxides have high binding energies (3.7 — 4.3 Volts), while carbons have a binding energy close to that of lithium metal, resulting in a large cell voltage. LiF and $LiNiVO_4$ are not acceptable candidates for the cathode material. The former is an ionic solid which does not intercalate at all and the later can only reversibly intercalate a small amount of lithium.

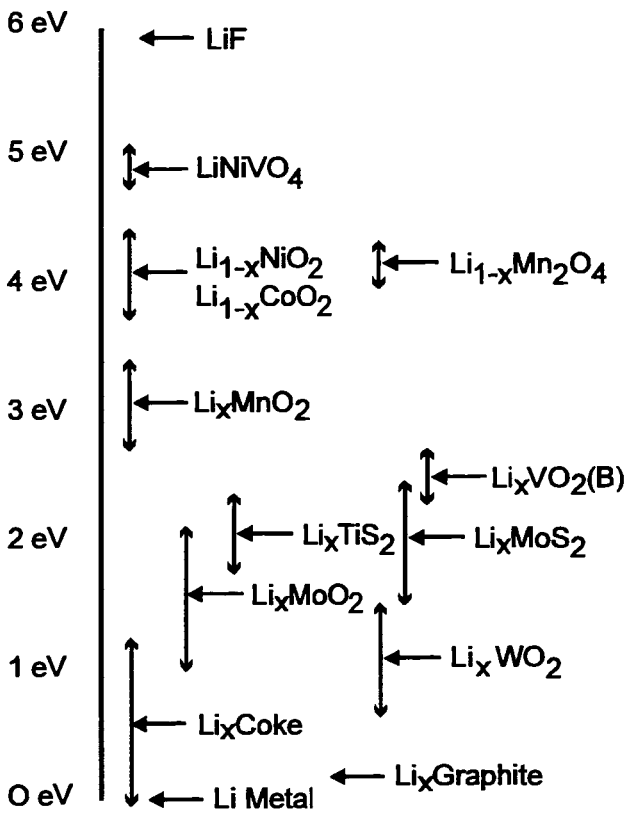

Figure 1-1 Binding energy of lithium in various lithium compounds.

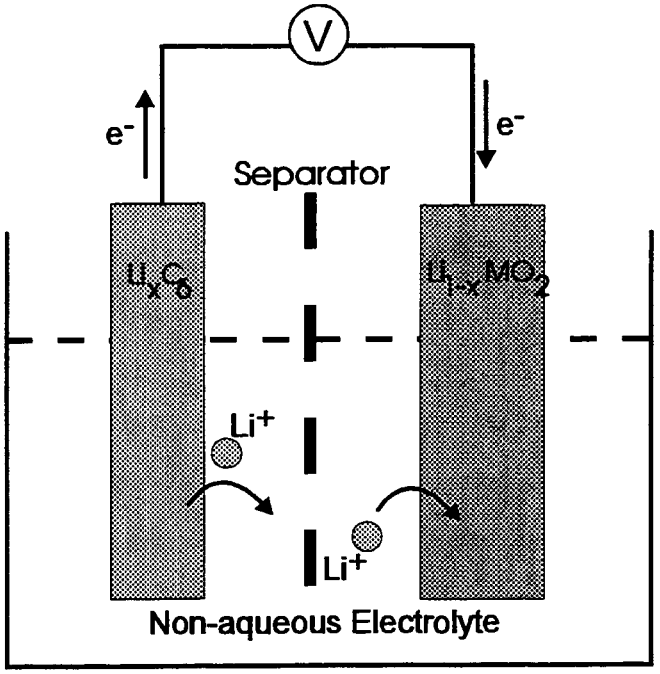

(a)

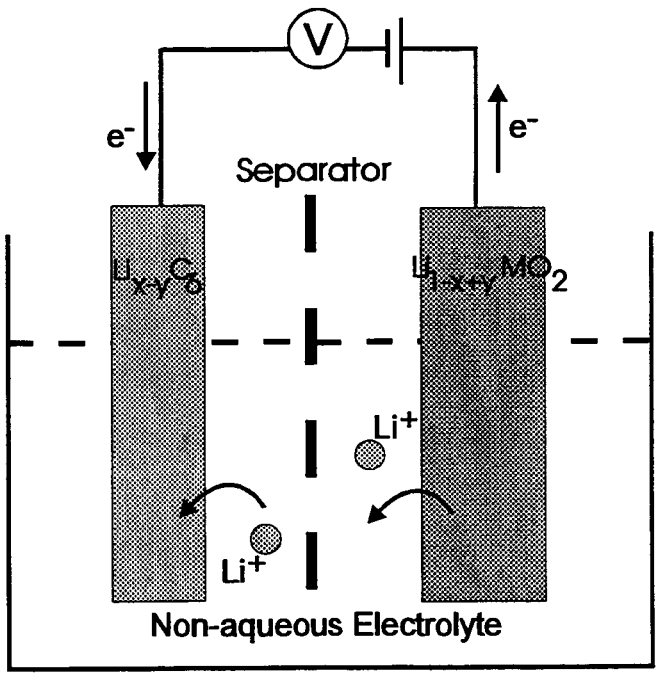

(b)

Figure 1-2 Schematic drawing of a lithium-ion cell. (a) during discharge, (b) during charge.

The choice of electrolyte for lithium-ion batteries is also critical (Hossain, 1995). The electrolyte should have: a) good ionic conductivity to minimize internal resistance; b) lithium ion transference number approaching unity; c) a wide electrochemical voltage window; d) good thermal stability; and e) compatibility with the other cell components. Based on these conditions, electrochemists have identified electrolytes which can be used in the lithium-ion battery (Hossain, 1995). Among them, liquid organic electrolytes are the most common electrolytes.

A suitable porous polymer material is used for the separator. The function of the separator is to prevent physical contact between the electrodes and to provide a conducting path between them. Microporous polypropylene or polyethylene films are commonly used.

Figure 1-2 schematically shows a lithium-ion cell during both the discharge and charge processes. The electrode reactions which occur in the cell are:

$$Li_xC_6 \Leftrightarrow Li_{x-y}C_6 + yLi^+ + ye^- \qquad (1\text{-}2)$$

at the carbon anode, and

$$Li_{1-x}MO_2 + yLi^+ + ye^- \Leftrightarrow Li_{1-x+y}MO_2 \qquad (1\text{-}3)$$

at the transition metal oxide cathode. Both equations lead to an overall cell reaction

$$Li_xC_6 + Li_{1-x}MO_2 \Leftrightarrow Li_{x-y}C_6 + Li_{1-x+y}MO_2 \qquad (1\text{-}4)$$

where $Li_{1-x}MO_2$ represents the lithiated metal oxide intercalation compound. The forward direction of the reactions corresponds to the discharge of the cell. The recharge of the cell is accomplished by placing a power supply in the external circuit of the cell and forcing the electrons and ions to move in the opposite directions to those during discharge.

1.2 Why is Carbon a Suitable Candidate for the Anode of a Lithium-Ion Battery?

During the 1970's and 1980's, the search for high-energy-density batteries led to the use of lithium metal as the anode material for rechargeable lithium cells which had a reasonable cycle life. Lithium metal was later proven very difficult to make safe in a large scale cell, such as an *AA* size cell. The formation of dendrites on the surface of the lithium

electrode and changes in the shape of the lithium electrode, can lead to potential safety problems. When lithium is electroplated onto a metallic lithium anode during recharge, it forms a more porous deposit with a larger surface area than the original metal. Therefore, cell cycling causes the area of contact between the lithium metal and the electrolyte to get larger and larger. The thermal stability of the original lithium metal is good in many non-aqueous electrolytes. However, after a large number of cycles, the significant increase of the surface area of the metallic lithium leads to conditions which are very sensitive to thermal, mechanical and electrical abuse (Dahn, 1993).

A possible solution to this problem is to use an electrolyte, such as a solid polymer electrolyte, which is less reactive with lithium metal (Hossain, 1995). Another simple solution is the lithium-ion cell.

In the lithium-ion approach, the metallic lithium anode is replaced by a lithium intercalation material. Then, two intercalation compounds hosts, with high reversibility, are used as electrodes. The structures of the two electrode hosts are not significantly altered as the cell is cycled. Therefore the surface area of both electrodes can be kept small and constant. In a practical cell, the surface area of the powders used to make up the electrodes is normally in the 1 m^2/g range and does not increase with cycle number (Dahn, 1991b). This means the safety problem of AA size cells can be solved.

One criterion for the anode material is that the chemical potential of lithium in the anode host should be close to that of lithium metal. Carbonaceous materials are therefore good candidates for replacing metallic lithium because of their low cost, low potential versus lithium, and wonderful cycling performance. Practical cells with $LiCoO_2$ and carbon electrodes are now commercially available. Finding the best carbon for the anode material in the lithium-ion battery is still a work in progress.

1.3 Introduction to This Thesis

The work presented in this thesis involves the study of high capacity carbonaceous materials as anodes for lithium-ion battery applications. There are hundreds and thousands of carbonaceous materials commercially available. Lithium can be inserted

reversibly within most of these carbons. In order to prepare high capacity carbons for lithium-ion batteries, one has to understand the physics and chemistry of this insertion. Good understanding will ultimately lead to carbonaceous materials with higher capacity and better performance.

The mechanism of lithium insertion in carbonaceous materials depends on the carbon type. At the beginning of the thesis, we describe the basic structural unit of carbonaceous materials. Then we show that the structure of carbons depends strongly on the type of organic precursors used to make them. Carbonaceous materials have historically been divided into two groups: soft and hard carbons. The soft carbons graphitize nearly completely upon heating to above ~3000°C. The hard carbons never become graphite unless a high pressure is applied. The reversible capacities of many carbons for lithium depend on both pyrolysis temperature and precursor type. There are three important groups of carbons showing high capacity for lithium insertion or intercalation. The three classes are: graphitic carbons made from soft carbon precursors at temperatures above 2400°C, hydrogen-containing carbons made from all carbonaceous materials at temperatures near 700°C, and hard carbons with large amounts of monolayers and associated nanopores. The later materials are made from hard carbon precursors near 1000°C. We carefully describe the structure of these three classes of carbonaceous materials.

Chapter 3 describes the characterization of carbonaceous materials by the CHN test, powder X-ray diffraction, small-angle-X-ray scattering, and by measurements of surface area and tap density. The CHN test determines the content of carbon, hydrogen, and nitrogen in the samples. Powder x-ray diffraction can be used to determine the structure of graphitic carbons heated at high temperature (typically, > 2000°C) (Shi, 1993a; Shi, 1993b). Powder X-ray diffraction and small angle X-ray scattering measurements on poorly crystalline carbonaceous materials can be used to estimate their structure. Finally, the surface area measurement is used to investigate the open porosity in the carbon samples.

Electrochemical studies of carbonaceous materials are based on lithium/carbon coin cells. These techniques are introduced in chapter 4. These cells use metallic lithium

foil as the anode and a carbonaceous material as the cathode. The purpose of using these cells rather than lithium-ion cells for the study of carbonaceous materials is that lithium atoms have a constant chemical potential in metallic lithium. Therefore the chemical potential of lithium in carbons is easily obtained from the cell voltage. However, in lithium-ion cells, the chemical potentials of lithium in both electrode hosts change simultaneously. This makes the chemical potential of lithium in carbon electrodes hard to measure. Chapter 4 describes the experimental tests we use to measure the electrochemical properties of the carbonaceous materials. In-situ X-ray diffraction using lithium/carbon cells with beryllium X-ray windows is also introduced as a basic experimental method to explore the phase transitions and structural changes during the insertion of lithium in carbonaceous materials.

From chapter 5, through chapters 6 and 7, lithium insertion in the three most interesting carbon types is discussed theoretically and experimentally.

Chapter 5 begins with synthesis, followed by structural models for graphitic carbons. The structural parameters for graphitic carbons are obtained from the structure refinement program for disordered carbons developed in this laboratory by Hang Shi. We describe the general features of lithium intercalation in graphite. Turbostratic disorder in graphitic carbons determines the capacity for lithium intercalation and affects the staging phase transitions which occur during the intercalation of lithium. A simple theoretical model is developed to explain some of the staging features in turbostratically misaligned graphitic carbons.

In chapter 6, lithium insertion in hydrogen-containing carbons is carefully studied. In all carbonaceous materials heated to ~700°C, hydrogen becomes the largest constituent left except carbon, leading to hydrogen-containing carbons. Powder X-ray diffraction, SAXS, and Brunauer-Emmett-Teller (BET) surface area measurements show these hydrogen-containing carbons include both soft and hard carbons, with different amounts of nanopores in the samples. Carbonaceous materials with high hydrogen content have high capacity for lithium insertion which shows large hysteresis. It is believed that the lithium atoms may bind to hydrogen terminated edges of hexagonal carbon fragments causing a change in the carbon bond from trigonal sp^2 to tetrahedral sp^3. We use a simple

model which treats the bonding change as an activated process to understand the hysteresis of lithium insertion.

Lithium insertion in hard carbons is described in chapter 7. High capacity hard carbons can be made from many hard carbon precursors, such as coal, wood, sugar, and different types of resins. Hard carbons made from resole and novolac resins at temperatures near 1000°C have a reversible capacity of about 550 mAh/g, show little hyteresis and have a large low voltage plateau on charge. The analysis of powder X-ray diffraction, SAXS, and BET measurements show that the high capacity hard carbons are made up of graphene monolayers stacked at arbitrary angles. Such a structure implicitly requires small pores between the oddly stacked sheets. The structure resembles a "house of cards", and the mechanism of lithium insertion in such hard carbons is discussed next. We believe that the lithium can be adsorbed on the internal surfaces of the graphene monolayers. The monolayers can adsorb lithium on both sides, leading to a large reversible capacity which may ultimately approach twice that of graphite for materials with the ideal disordered structure. However, these hard carbons have a lower density compared to graphite. This will limit the advantages of using these carbons in practical cells.

Finally, we conclude this thesis in chapter 8.

TYPES OF CARBONACEOUS MATERIALS

Carbon has a number of different forms, with different structures, and different types of carbon-carbon bonds. Diamond and graphite are two well-known crystalline forms of carbon. C_{60}, named "Buckminster Fullerence" or "Bucky Balls", is the third crystalline form of carbon, discovered only recently. The structure of diamond is a face-centered cubic (fcc) lattice with a two atom basis. The three dimensional linking of tetrahedral carbon-carbon bonds (sp^3) makes diamond the hardest material found in nature. Graphite is a layered crystal. The trigonal and σ bonding (sp^2) between each atom and its three neighbors results in the formation of a honeycomb layer in-plane, while weaker van der Waals forces hold the planes together. The face-centered cubic structure was also found in Bucky Balls. In this structure 60 carbon atoms form a soccerball-like closed structure. Carbon also can take other forms with varying levels of disorder, i.e., any number of quasi-crystalline forms ranging from the near amorphous to the highly crystalline graphitic state. Evaporated carbon films are more disordered than any other forms of carbon. Their structure includes both sp^2 and sp^3 bonding, resulting in a network of tetrahedral graphite-like bonding and tetrahedral diamond-like bonding (Kakinoki, 1960).

2.1 Basic Structural Unit of Carbon

In fact, all carbonaceous materials are initially made of similar elemental units arranged differently relative to each other (Oberlin, 1989). These elemental units, or so-called "Basic Structural Units (BSUs)", are made up of planar aromatic structures (called graphene layers) consisting of less than 10 to 20 rings (Oberlin, 1989). The BSU can be two to several graphene layers piled up more or less in a parallel way, or it can even be a single graphene layer. Oberlin classified the possible symmetries in the three dimensional

arrangement of BSUs into two groups: spherical symmetry and cylindrical symmetry, either true or statistical.

For most immature natural, or low temperature heated, carbonaceous materials, the graphene layers of aromatic structures can be highly distorted. Small BSUs are associated edge to edge with tilted and twisted boundaries (Oberlin, 1989). In these boundary regions, a small amount of tetrahedral bonds (sp^3) can be found. When the heat-treatment temperature increases, such BSUs do not grow obviously in thickness up to 1000°C and in diameter up to 1500°C in most cases.

2.2 Soft Carbons and Hard Carbons

The final structure of a carbonaceous material depends strongly on the organic precursor from which it was made. During the early stages of pyrolyzing organic precursors in inert gas (400°C—700°C), organic compounds decompose and different gases (depending on precursor composition) are released. The remaining carbon atoms condense into graphene layers. If the organic precursors form a semi-liquid phase during pyrolysis, these planar graphene sheets can easily align in a more or less parallel fashion that finally leads to graphitization at very high heat treatment temperature (*e.g.*, 3000°C). Such precursors give "soft" or "graphitizable" carbons (Franklin, 1950; Franklin, 1951a). However, if the organic precursor cross-links, a liquid-like phase is not realized during pyrolysis and the planar graphene sheets can not align parallel to each other. These materials are hard to graphitize even at high heat treatment temperatures and are called "hard" or "nongraphitizable" carbons.

2.3 High Capacity Carbonaceous Materials — the Three Important Regions

Carbon structure greatly influences the mechanism of lithium insertion. Figure 2-1 shows the reversible capacities of many carbons prepared by the pyrolysis of organic precursors as a function of the heat-treatment temperature (Dahn, 1995). (Much of the work of this thesis was used to prepare figure 2-1.)

Carbons in the three highlighted regions of figure 2-1 are currently used or have been proposed for use in commercial lithium-ion batteries. Region 1 contains graphitic carbons prepared by heating soft carbon precursors to temperatures above 2400°C (Zheng, 1995a, Zheng, 1995b, Zheng, 1996b). Region 2 contains both soft and hard carbons, heated to between 500 and 700°C, which have substantial hydrogen content (Zheng, 1995c; Zheng, 1996a; Zheng, 1996c). Region 3 contains hard carbons made up predominantly of single graphene layers that include appreciable nanoporosity and are stacked more or less like a "house of cards" (Zheng, 1995c; Zheng, 1995d; Liu, 1996; Zheng, 1996d).

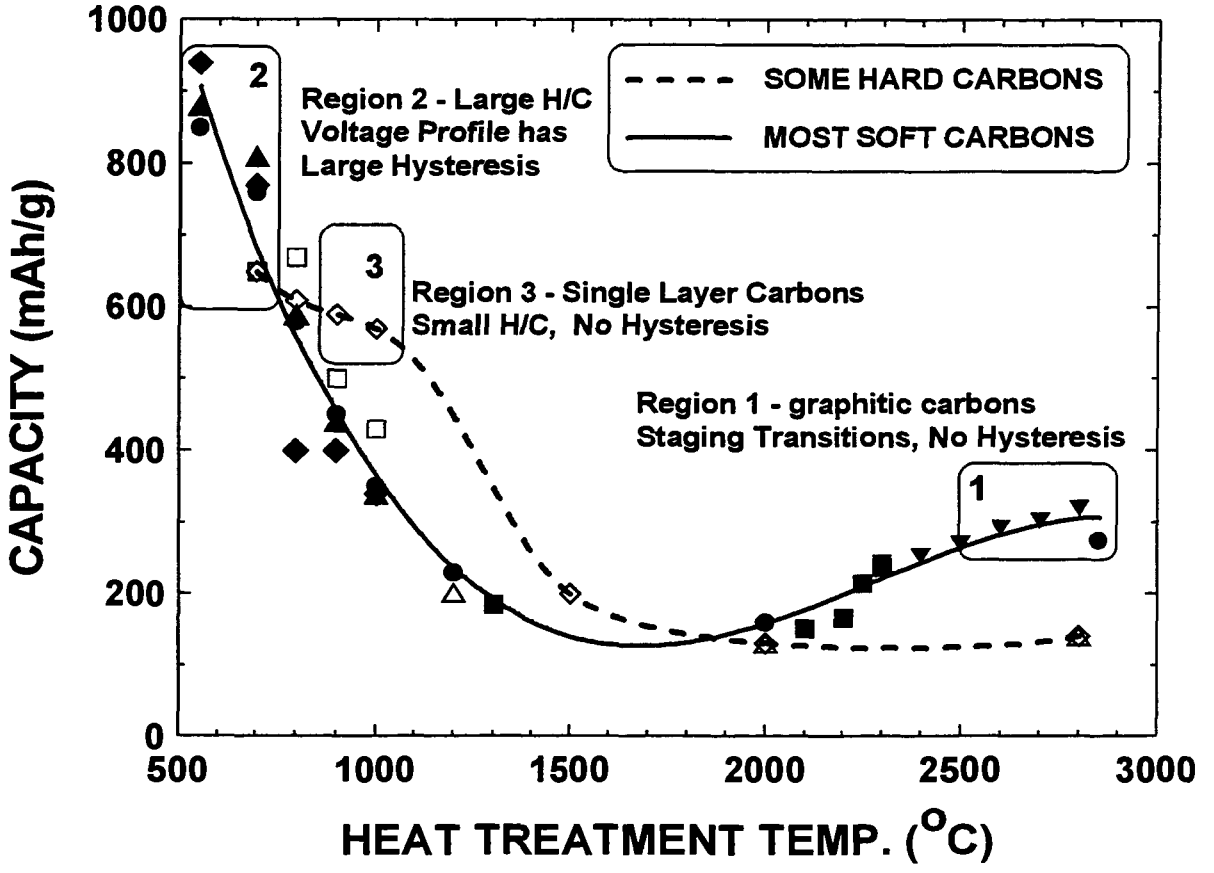

Figure 2-1. The "master graph" of reversible capacity for lithium plotted versus heat treatment temperature for a variety of carbon samples. The three regions of commercial relevance are marked. Solid symbols are data for soft carbons, open symbols are data for hard carbons.

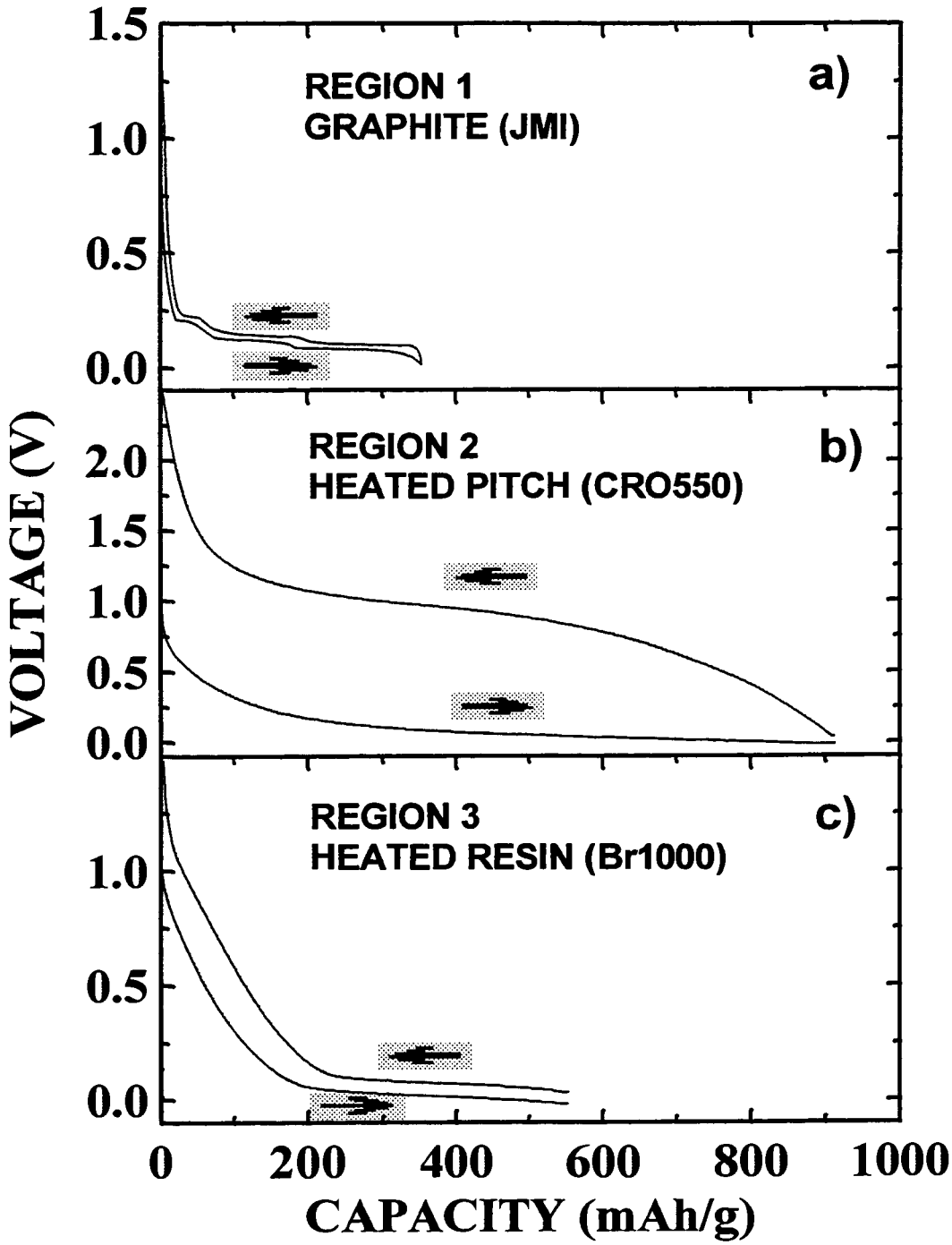

Figure 2-2. Second cycle voltage profiles of carbons representative of regions (1), (2), and (3). a) JMI synthetic graphite, b) Crowley petroleum pitch heated to 550℃, and c) a resole resin heated to 1000℃.

Figure 2-2 shows the voltage-capacity relation for lithium/carbon electrochemical cells made from representative materials from each of the three regions of figure 2-1. The synthetic graphite (Johnson-Matthey Inc.) sample gives a reversible capacity of about 355 mAh/g (Zheng, 1995a). Petroleum pitch heated to 550°C to get $H_{0.4}C$ gives a reversible capacity of near 900 mAh/g (Zheng, 1995c). The voltage profiles for all materials in region 2 show appreciable hysteresis; that is, the lithium is inserted near zero volts (versus lithium metal) and removed near one volt. Resole resin heated to 1000°C contains less hydrogen and gives a reversible capacity of about 550 mAh/g (Zheng, 1995d). The voltage profiles for each material in figure 2-2 are markedly different, which suggests that different reaction mechanisms are important in each of the three regions in figure 2-1.

To understand the mechanisms of the reaction of lithium with different carbons is the goal of the thesis. However, before we can do this, we need clear structural pictures of carbonaceous materials in each of the three regions. Before moving on further, we will review some previous structural work in the rest of this chapter.

2.4 Graphitic Carbons — Region 1

The graphitic carbons are the most crystalline of the carbonaceous materials of the three regions in figure 2-1. During the last 40 years, the structure of graphitic carbons has been carefully studied by many scientists (Franklin, 1950; Walker, 1965 & 1966; Dahn, 1993).

2.4.1 Turbostratic Disorder

Graphitic carbons can be readily converted from soft carbons, such as petroleum coke, by heating. When the heat treatment temperature is limited to about 1000°C, coke-type materials are formed. These carbonaceous materials have graphene layers of relatively small extent (about 10 to 40 Å) which are stacked in a roughly parallel fashion, but with random rotations and translations between every pair of layers. This type of disorder has been given the name "turbostratic disorder" (Warren, 1941). As the carbons

are then heated from 1000 to 2000°C, the lateral extent of the layers grows and the stacking becomes quite parallel as evidenced by a sharpening of the (002) Bragg peak. However, at 2000°C there is still complete turbostratic disorder. Upon heating above 2000°C, the turbostratic disorder is relieved in a more or less continuous way, the amount of remaining turbostratic disorder decreasing to zero monotonically by 3000°C.

Turbostratic disorder in graphitic carbons plays an important role in lithium intercalation as discussed in chapter 5.

2.4.2 Structure of Graphite

The structure of graphite consists of a succession of graphene layers parallel to each other. In each graphene layer, carbon atoms are linked in a honeycomb fashion. The in-plane distance between carbon atoms is 1.42 Å, resulting in an in-plane lattice constant of 2.45Å, whereas the distance between adjacent layers (d_{002}) is 3.35Å. Figure 2-3a shows a part of one graphene layer where **a** and **b** are in-plane crystal axes.

In the normal graphite structure, the graphene layers are stacked in a "hexagonal" fashion, leading to a crystal with hexagonal symmetry. This structure (2H) is shown in figure 2-3b where the dashed lines label a unit cell. It is clear that this stacking sequence along the c-axis (which is normal to the in-plane graphene layer) can be represented by a registry of ...ABABAB..., where adjacent layers A and B are shifted by 1/3 of a unit cell along the (110) crystal direction with respect to each other. It is also found, less commonly, that some graphites have the rhombohedral stacking (3R) that can be represented by a registry of ...ABCABC..., where the B layers shift by 1/3 and the C layers shift by 2/3 of a unit cell (both along the (110) crystal direction) with respect to the A layers. The 3R structure is shown in figure 2-3c.

Both natural and synthetic graphites have turbostratic stacking and 3R registered intergrowths in a predominantly 2H structure.

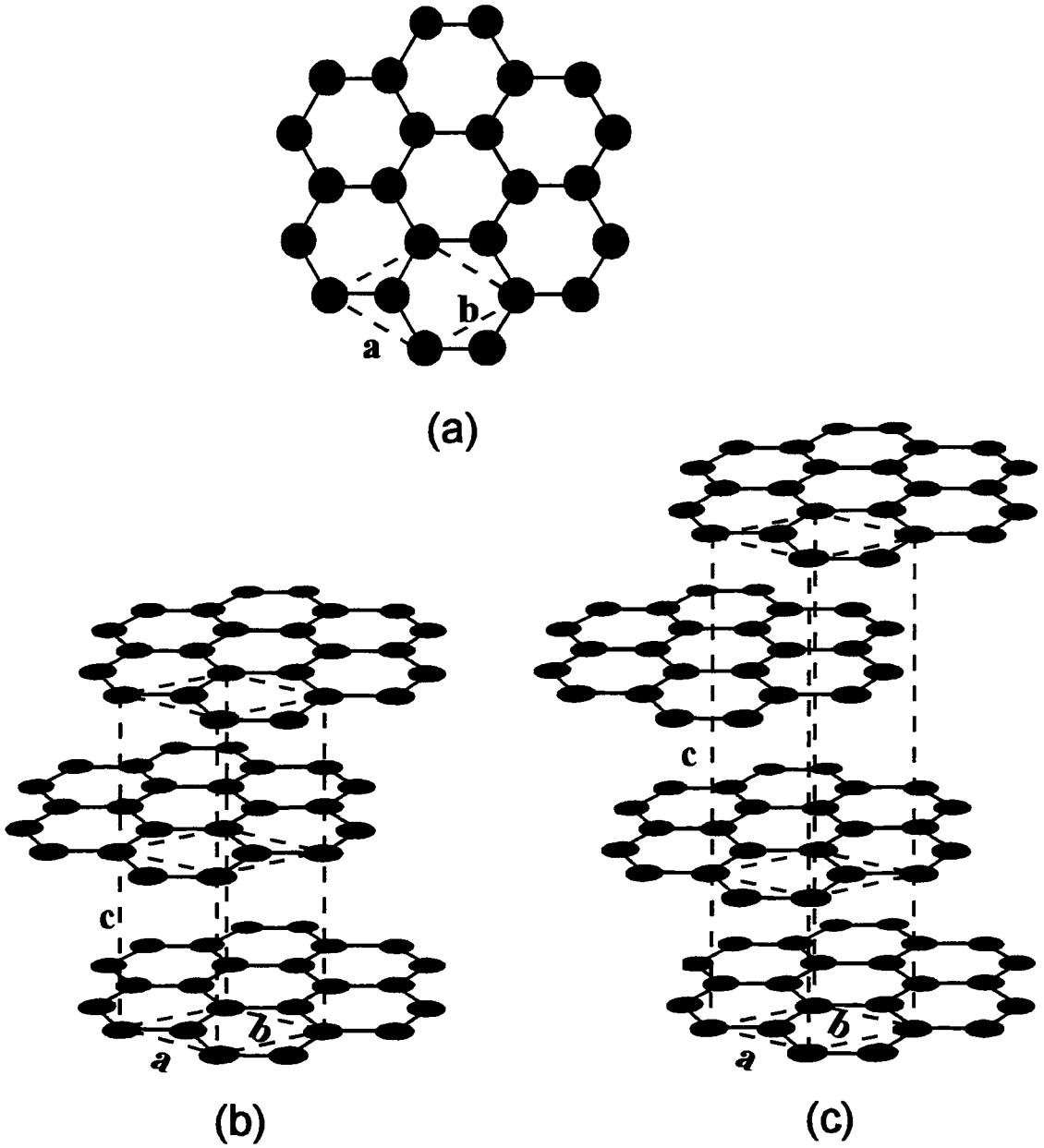

Figure 2-3. (a) basal view of a single graphene layer and a unit cell, (b) 2H structure of graphite, and (c) 3R structure of graphite. Dashed lines in (b) and (c) label unit cells.

2.4.3 Structure of Graphitic Carbons

Graphitic carbon normally refers to soft carbon heated above about 2100°C. The probability of finding turbostratic disorder begins to decrease as the heat-treatment temperature increases to above 2100°C. When the heating temperature reaches above

3000°C, graphite forms. Conceptually, graphite is a graphitic carbon with no or very little turbostratic disorder.

In graphitic carbon, the in-plane structure of graphene layers is almost the same as in graphite except the lateral extent of the layers increases with heat-treatment temperature. However, the distance between layers (d_{002}), where the turbostratic disorder occurs, is slightly larger than that in graphite.

Turbostratic disorder critically affects the structure and properties of graphitic carbons. Because of this, structural models have been developed to describe graphitic carbon. In chapter 5, the details of the structural models will be discussed.

2.5 Hydrogen-Containing Carbons — Region 2

Hydrogen-containing carbons in region 2 are made from both soft and hard carbon precursors. As organic precursors are heated to near 700°C, the carbonaceous materials formed consist of graphene layers with predominantly hydrogen-terminated edges. Although such materials may contain other elements, such as oxygen, nitrogen, and sulfur, carbon and hydrogen are the largest constituents on an atomic percent basis. Therefore we call these carbonaceous materials hydrogen-containing carbons.

2.5.1 Hydrogen Complexes in Carbon

Carbonaceous materials are pyrolyzed residues of organic compounds. Hydrogen complexes in carbons (Puri, 1970) are present as chemisorbed water, aliphatic hydrogen and aromatic hydrogen. The aliphatic hydrogen exists in the form of aliphatic chains or alicyclic rings attaching to the periphery of the aromatic structure of the graphene layer. The aromatic hydrogen atoms are combined directly with carbon atoms at the periphery of aromatic platelets through trigonal bonding. This carbon-hydrogen bonding is so strong that the aromatic hydrogen is held more firmly than the aliphatic hydrogen, and other complexes, such as oxygen, sulfur, *etc.*.

During pyrolysis of organic precursors in inert gas, the chemisorbed water is removed from carbons at low temperatures (> 100°C). Then the aliphatic hydrogen is lost and tarry materials are formed. The carbon-hydrogen bond is broken and aromatic hydrogen is emitted (as gasses containing hydrogen in significant amounts) only when precursors are heated to temperatures between 600 and 800°C. The aromatic hydrogen is eliminated continuously to almost zero in carbonaceous materials as the temperature is raised to ~1200°C.

2.5.2 Structure of Hydrogen-Containing Carbons

When carbonaceous materials are heated to about 700°C, hydrogen atoms are incorporated predominantly as aromatic hydrogen. The H/C atomic ratio in carbon samples depends on the "shell number" of the single graphene layers. In figure 2-4, different numbers of carbon rings are associated with each other to form different aromatic structures. For a one-shell carbon fragment, six carbon atoms and six hydrogen atoms are found, giving $H/C = 1$; a two-shell carbon fragment contains 24 carbon atoms and 12 hydrogen atoms, giving $H/C = 0.5$; a three-shell fragment contains 54 carbon atoms and 18 hydrogen atoms, giving $H/C = 0.333$. Although the graphene layers shown in figure 2-4 are perhaps more regular in shape than those in real samples, we can still calculate the H/C atomic ratio based on the shell numbers in carbonaceous samples as follows:

$$\text{Number of shells} \approx \frac{L_a}{4.9} + 0.5,$$

where L_a is lateral dimension of the graphene layers, and then,

$$\text{H/C atomic ratio} = 1/(\text{number of shells}).$$

The graphene layers terminated with edge hydrogen form BSUs in carbons. The lateral extent of single graphene layers in BSUs is from about 10Å to about 40Å. In soft carbons, a few of the graphene sheets are stacked in a more or less parallel fashion in each BSU. In hard carbons, most of the BSUs only contain single graphene layers. Therefore,

most graphene layers are not stacked in a parallel way, instead, they are more or less arranged like in a "house of cards".

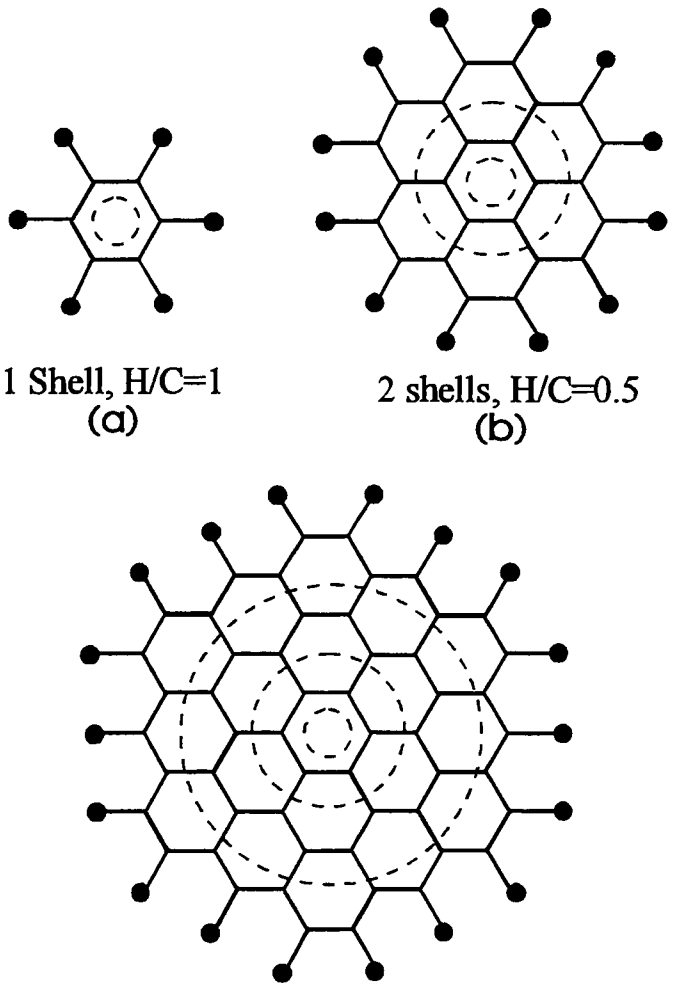

Figure 2-4. H/C atomic ratio for single graphene layers. Hydrogen atoms are represented by dots. (a) $H/C = 1$ *for one carbon shell (6 atoms) with* $L_a \approx 2.45 Å$*; (b)* $H/C = 0.5$ *for two carbon shells (24 atoms) with* $L_a \approx 7.4$ *Å; (c)* $H/C = 0.333$ *for three carbon shells with* $L_a \approx 12.4$ *Å. The dashed circles indicate the shells.*

Schematic drawings of the structure of hydrogen-containing carbons heated near 700°C are shown in figure 2-5. Figure 2-5a shows a soft carbon with preferred local BSU orientations. Figure 2-5b shows a hard carbon with BSUs including mostly single

graphene layers stacked at arbitrary angles to form a structure similar to a "house of cards".

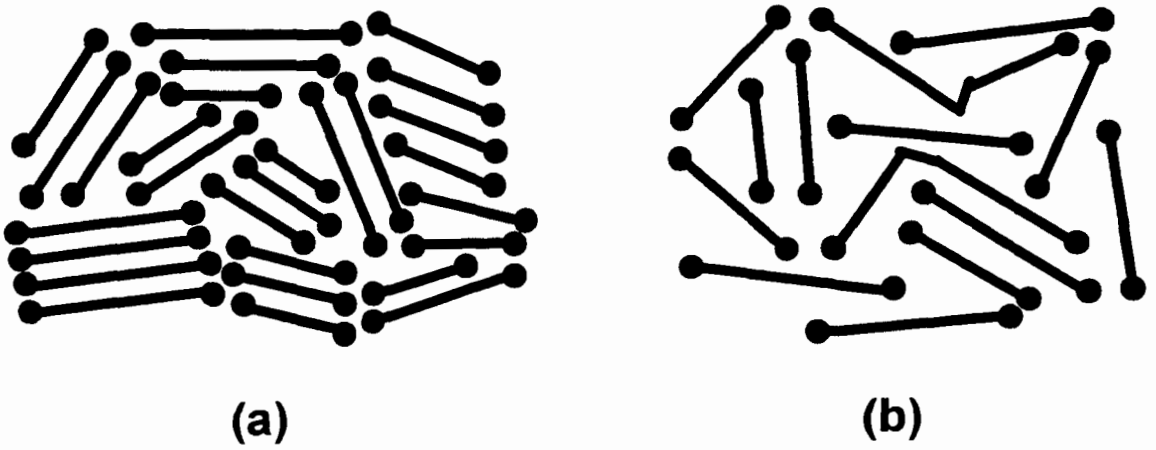

Figure 2-5. Schematic drawing of hydrogen-containing carbons heated at 700℃. Solid lines represent graphene layers and dots represent hydrogen atoms bonding aromatically at the edges. (a) for soft carbon, (b) for hard carbon.

2.6 Hard Carbons with Large Amounts of Monolayers — Region 3

Carbons in region 3 tend to be hard carbons, produced by the pyrolysis of hard carbon precursors around 1000°C in inert gas. The hard carbons retain the structure of figure 2-5b, but the hydrogen atoms are predominantly eliminated in the bulk, as indicated in figure 2-6.

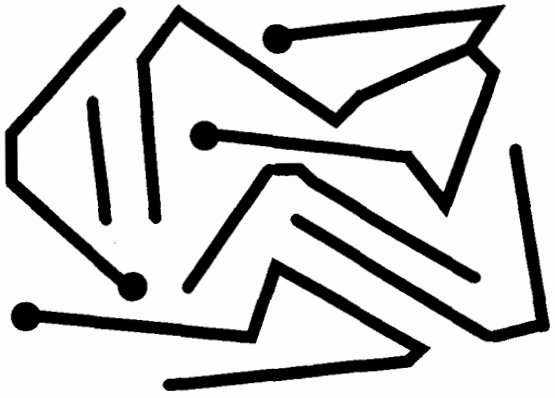

Figure 2-6. Hard carbon heated around 1000°C, the hydrogen atoms (dots) are predominantly eliminated in the bulk. The cross-links are more extensive and stronger.

2.6.1 "Importance" of heteroatoms

In the raw materials used for making carbonaceous materials, as well as low temperature heated carbons, a number of atoms other than carbon can be found. These heteroatoms include oxygen, hydrogen, nitrogen, chlorine and sulfur *etc.*. They strongly influence the pyrolysis yield of carbon from the precursor. During the pyrolysis, the heteroatoms react with carbon atoms to form different gases reducing the yield of carbon. On the other hand, some heteroatoms can creat cross-linking in the heated precursors which can reduce the reactions between other heteroatoms and carbon atoms to increase the carbon yield.

The heteroatoms also significantly affect the structure of the carbons. It is well-known that hard carbons are not completely converted into graphite at temperatures in excess of 3000°C (Franklin, 1950; Franklin, 1951a). This is due to extensive cross-linking created during the formation of hard carbons. We briefly review the crucial roles of a few heteroatoms in the formation of hard carbons below.

Oxygen is often present in functional groups attached to the edge of aromatic structures in carbonaceous precursors. During pyrolysis, these functional groups react with each other or with added agents to form cross-links between the BSUs. The more oxygen, the stronger the cross-linking (Chermin, 1957; Fitzgerald, 1959). In most cases, the cross-linking is extensively formed by 400°C. The cross-linking reduces the mobility of the BSU. Therefore a high content of oxygen in the precursor often leads to hard carbons after pyrolysis.

The role of hydrogen in carbons is two-fold (Oberlin, 1989). The aliphatic hydrogen is the source of suspensive media for the BSU. The aromatic hydrogen saturates the dangling bonds when the BSUs are free radicals, and it prevents bonding between two neighboring BSUs. This dual role favors the formation of soft carbons. This argument is consistent with the fact that less hydrogen is found in hard carbons than in soft carbons heated at the same temperature above 700°C (See table 6-1 in chapter 6).

Nitrogen and sulfur are not present in all carbonaceous precursors. However, most nitrogen and sulfur in stable functional groups attached to the periphery of graphene layers in carbons aid cross-linking in a similar way to oxygen.

Heteroatoms can also be used as additives to influence the structure of carbons formed during pyrolysis. A typical example is a hardening agent added during the production of hard carbon. The heteroatoms in the hardening agent react with the functional groups at the edges of aromatic structures to form cross-links. Liu et al (Liu, 1996) showed that epoxy novolac resins were hardened by phthalic anhydride at 120°C. Then the hardened resins were pyrolysed at 1000°C in inert gas, leading to hard carbon.

2.6.2 Structure of Hard Carbons in Region 3

The structure of hard carbons do not change significantly with heat-treatment temperature between 700°C and 1100°C except that the heteroatoms, especially hydrogen atoms, attached to the edges of graphene layers, are continuously eliminated. Therefore it is expected in hard carbon that the cross-links between BSUs are more extensive and stronger as heating temperatures approach 1000°C. It is believed that the skeleton of the structure of hard carbons in region 3 is quite similar to figure 2-6.

CHARACTERIZATION OF CARBONACEOUS MATERIALS

There are many ways to characterize the structure and properties of carbonaceous materials. Among these methods, the CHN test, powder X-ray diffraction, small angle X-ray scattering, and the Brunauer-Emmett-Teller (BET) surface area measurement are most useful and are described here.

3.1 CHN Test

The CHN test determines the weight percentages of carbon, hydrogen, and nitrogen in the samples. Samples were combusted in pure oxygen in a quartz tube. Then the combustion products, including CO_2, H_2O, and N_2, *etc.*, were carried by a pure argon stream to a gas chromatograph and quantified. Small amounts (about 20 mg each) of our samples were sent to Canadian Microanalytical Service Ltd. (Delta, BC, Canada) for the CHN test. The accuracy of the test is $\pm$ 0.3% by weight.

3.2 Powder X-Ray Diffraction

Carbon samples used for powder X-ray diffraction were obtained by grinding the as-made carbons. If carbon samples are supplied in powder form, they can be measured directly. Some of the powder samples used in chapter 5 are heated mesocarbon microbeads. These samples consists of an enormous number of spherical particles with completely random orientation.

3.2.1 Experimental Methods

Powder X-ray diffraction patterns for each carbonaceous material were collected using a Siemens D5000 powder diffractometer equipped with a copper target X-ray tube

and a diffracted beam monochromator. The diffractometer operates in the Bragg-Brentano geometry. The samples were packed into a rectangular well 25 mm long (parallel to the X-ray beam) × 20 mm wide × 2 mm deep in a stainless steel holder. During the measurement, the sample is fixed, and the tube and detector arms move simultaneously in opposite directions at the same speed. Therefore, if the tube arm moves through an angle of θ_B, the detector arm also moves through an equal angle, leading to a scattering angle of $2\theta_B$.

The divergence and antiscatter slits we normally used were 0.5°. For most disordered carbon samples, we selected a 0.6 mm receiving slit. These choices lead to an instrumental resolution of about 0.15° in $2\theta_B$. However, for graphitic carbons, we selected a 0.2 mm receiving slit to obtain higher resolution. All the measurements were made between 10° and 120° in scattering angle.

3.2.2 Scherrer Equation to Estimate the Size of Organized Regions

Imperfections in the crystal, such as particle size, strains, faults, *etc*, affect the X-ray diffraction pattern. The effect of particle size on the diffraction pattern is one of the simplest cases and the first treatment of particle size broadening was made by Scherrer in 1918 (Scherrer, 1918). Since the Scherrer equation has been widely used in the structural analysis of carbonaceous materials, it is worth deriving the Scherrer equation from Bragg's law (Cullity, 1978).

Bragg's law is the theoretical basis of X-ray diffraction. It may be written in the following form

$$2d(\sin\theta_B) = \ell\lambda \qquad (3\text{-}1),$$

where d is the distance between two parallel lattice planes, $2\theta_B$ is the scattering angle, ℓ is an integer, and λ is the X-ray wavelength, as shown in figure 3-1. When Bragg's law is satisfied, the diffracted intensity is maximum. (This is not true for very broad peaks because of the form factor! But here we suppose the peak we are dealing with is not so broad.) For example, in figure 3-1, the incident rays, A, D, ..., and M (we suppose the

number of layers, m, is even for convenience) make exactly the Bragg angle, θ_B,, with the reflecting plane. Therefore, the maximum intensity is at a scattering angle, $2\theta_B$, as shown in figure 3-2, due to the constructive interference of the scattered waves, A′, B′, ..., and M′.

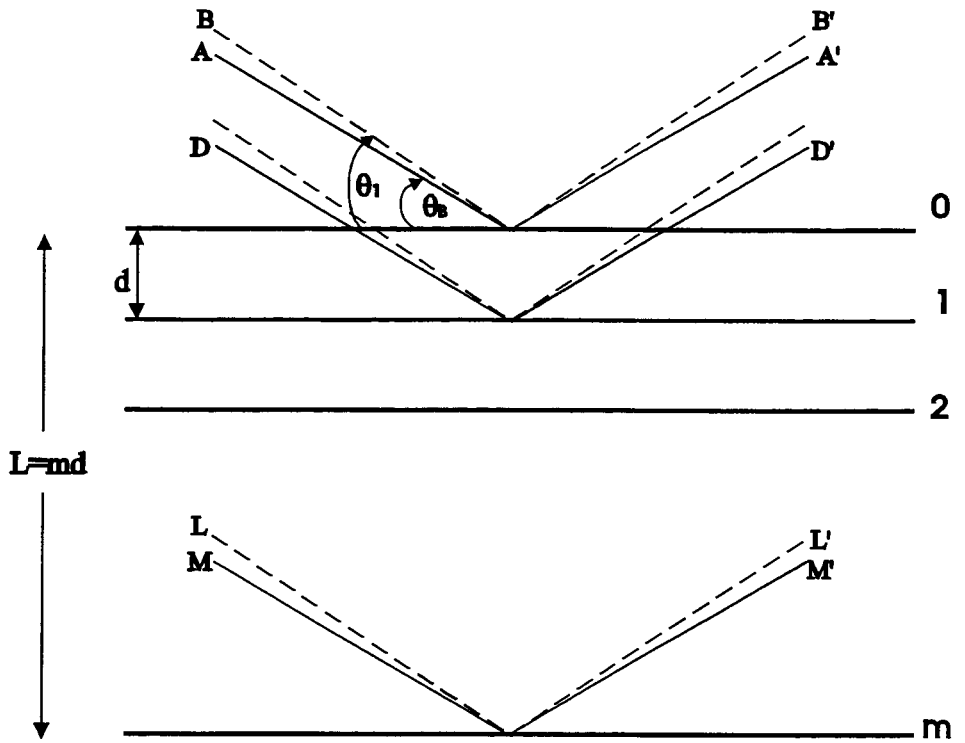

Figure 3-1. X-ray diffraction from a crystal with limited dimension.

Now consider the closest destructive interference to the central maximum, assumed to be at $2\theta_1$. For example, rays B, ..., and L make a slightly larger incident angle than θ_B so that the ray L′ scattered from the mth plane will have a phase shift of $2\pi(m+1)$ compared with ray B′. At θ_B the phase shift is $2\pi m$. It follows that the $(\frac{m}{2})$th plane, in the center of the particle, will scatter a ray with a phase shift of $2\pi(m/2+1/2)=\pi m+\pi$ with respect to ray B′. Since m is even, this ray will cancel ray B′ due to destructive interference. In other words, the rays scattered from the planes between 0 and m/2 in the particle will cancel the scattering from the planes between m/2

and m in the particle. Therefore, a minimum intensity at scattering angle $2\theta_1$ is observed as shown schematically in figure 3-2. A similar argument explains the minimum intensity at a slightly smaller angle, $2\theta_2$,.

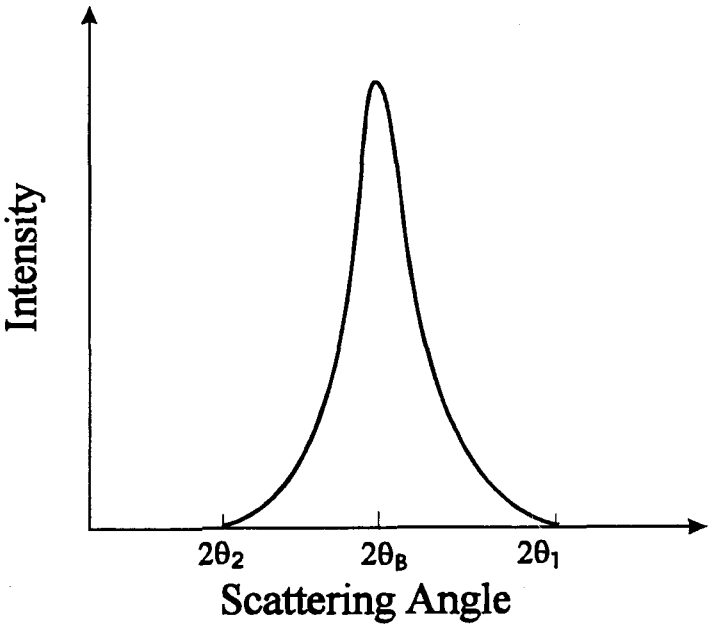

Figure 3-2. Schematically showing an X-ray peak profile from a particle with finite size.

The sharpness of an X-ray diffraction peak is characterized by its half width at half maximum intensity. We suppose that B is given by,

$$B = \frac{1}{2}(2\theta_1 - 2\theta_2) = \theta_1 - \theta_2 \qquad (3\text{-}2).$$

Then, B can be easily obtained from the above argument. Summing

$$2(md)(\sin\theta_1) = (m+1)\lambda,$$

and,

$$2(md)(\sin\theta_2) = (m-1)\lambda,$$

we have,

$$2(md)(\cos\frac{\theta_1+\theta_2}{2})(\sin\frac{\theta_1-\theta_2}{2}) = \lambda.$$

We approximate,

$$\frac{\theta_1 + \theta_2}{2} = \theta_B,$$

and,

$$\sin(\frac{\theta_1 - \theta_2}{2}) = \frac{\theta_1 - \theta_2}{2},$$

to obtain,

$$(md)(\cos\theta_B)B = \lambda.$$

Letting $L = md$ represent the dimension of the particle, we obtain,

$$L = \frac{\lambda}{B\cos\theta_B}.$$

A more exact derivation by Warren (Warren, 1941) showed that,

$$L = \frac{K_s\lambda}{B\cos\theta_B} \qquad (3\text{-}3),$$

now known as the Scherrer equation. He showed that the constant K_s is 1.84 (Warren, 1941), for two-dimensional peaks, and is 0.89 for three-dimensional peaks (Warren, 1990).

For carbonaceous materials, the lateral extent of the graphene layers and the number of stacked layers can be estimated using the Scherrer equation with the appropriate shape constant. Usually, the (002) or (004) reflection is used to estimate the carbon crystallite (i.e., BSU for low-temperature heated carbon) dimension perpendicular to the basal graphene layer, $L_{c,}$, and the (100) or (110) reflection is used to estimate the lateral dimension of the graphene layers, L_a.

3.2.3 Structure Refinement Program for Carbons

The X-ray diffraction pattern of carbon can be complex to interpret due to the complicated structural disorder of carbons. Recently, Shi *et al*(Shi, 1993a; Shi, 1993b) developed a structure refinement program for heated carbons. The program is ideally suited to studies of the powder diffraction patterns of soft carbons heated between 2000°C and 3000°C. By performing a least squares fit between the measured diffraction pattern

and a theoretical calculation, parameters of the model structure are optimized. For soft carbons heated above about 2200°C, the structure is well described by stacked two-layer packages in *AB* registry. The stacking of these packages is performed with the following probabilities:

a) a turbostratic shift or rotation between adjacent packages with probability P';

b) a registered shift between adjacent packages with probability, P_t', to describe local order *AB/CA/BC etc.*;

c) no shift between adjacent packages to obtain the stacking *AB/AB/AB etc.* with probability $(1-P'-P_t')$.

Thus, if $P'=0$ and $P_t'=0$, 2H graphite is obtained, if $P'=1$ and $P_t'=0$, turbostratic graphite (50%) is obtained, and if $P'=0$ and $P_t'=1$, 3R graphite is obtained. It is more convenient to use the stacking probabilities per layer, $P=P'/2$ and $P_t=P_t'/2$, and we will use these through this thesis.

In this thesis, the structure refinement program will be used to determine the structural parameters of graphitic carbons in region 1 of figure 2-1, as shown in chapter 5.

3.3 Small-Angle X-Ray Scattering

Small-angle X-ray scattering (SAXS) has been widely used to investigate the inhomogeneous electron density in materials. In carbonaceous materials, porosity is commonly encountered. The pores form and provide escape routes for gases produced during the pyrolysis process.

3.3.1 Experimental Methods

Small-angle X-ray scattering (SAXS) data was collected on the carbon samples using the Siemens D5000 diffractometer. This diffractometer is generally used for flat-sample powder diffraction which was performed in reflection geometry. In order to perform SAXS, it was necessary to make the measurement in transmission mode (see figure 3-3). To this end, the samples were filled in a rectangular frame with kapton

(fluorinated polyamide) windows on both sides. The frame was held vertically. The incident and antiscatter slits were both 0.1° and the receiving slit was 0.1 mm. The empty frame with kapton windows showed negligible signal when there was appreciable scattering from the carbons. Therefore we neglected the background signal from the frame in our analysis of the SAXS data from the pyrolyzed coals, pitches and sugar. The mass of sample held in the frame was recorded.

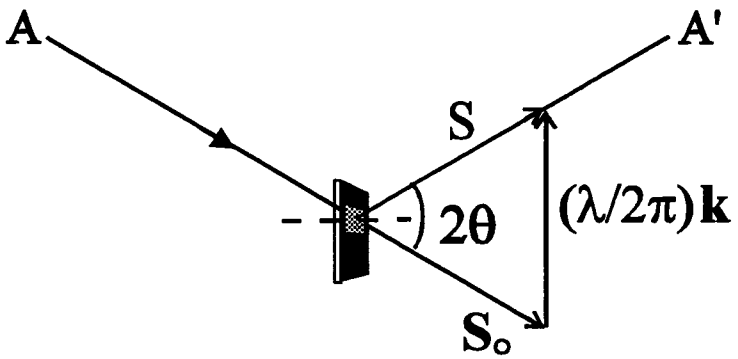

Figure 3-3. Schematic showing the SAXS measurement on the Siemens D5000 diffractometer. The wave-vector, **k**, *is determined as* $(2\pi/\lambda)(\mathbf{s}-\mathbf{s}_0)$.

For some samples, the attenuation of the X-ray beam by the sample was measured by comparing the number of detector counts registered with and without the sample in the beam path while the detector was set at 0°. This procedure was performed for some special purposes as we describe in chapter 7.

3.3.2 General Theory of SAXS

Consider a single object with electron density distribution $\rho(\mathbf{r})$. The amplitude, $F(\mathbf{k})$, of the scattering in a certain direction which is specified by wave-vector, **k**, is the Fourier transform of the electron density distribution of the object. That is,

$$F(\mathbf{k}) = \iiint dV \cdot \rho(\mathbf{r}) e^{-i\mathbf{k}\mathbf{r}} \qquad (3\text{-}4).$$

The wave-vector is determined as shown in figure 3-3,

$$\mathbf{k} = (2\pi/\lambda)(\mathbf{s}-\mathbf{s}_0),$$

where **s** and $\mathbf{s}_o$ are the unit vectors defining the directions of the scattered and incident radiation respectively. The intensity $I(\mathbf{k})$ is the absolute square of the amplitude, $F(\mathbf{k})$.

Now, let us consider a collection of identical pores embedded in a carbonaceous material of constant electron density ρ_0. Only the density difference will contribute to the scattering. If the pores are separated from one another such that there is no interaction between them, it is plausible to assume that they will make independent contribution to the intensity of diffraction (Porod, 1982). In this case, each pore can be treated separately, and then the intensities from all pores are simply added to give the total scattered intensity.

The simplest case is that of pores showing spherical symmetry. Suppose a spherical pore has radius, R_0. Then,

$$I(\mathbf{k}) = \left| \iiint dV\{(-\rho_0)\cos(\mathbf{k}\cdot\mathbf{r})\}\right|^2$$

$$= \left|\rho_0 \int_0^{R_0} dr \cdot 2\pi r^2 \cdot \int_0^{\pi} d\theta \cdot \sin\theta \cdot \cos(kr\cos\theta)\right|^2 \qquad (3\text{-}5)$$

The integration over θ in equation (3-5) is,

$$\int_0^{\pi} d\theta \cdot \sin\theta \cdot \cos(kr\cos\theta) = 2\frac{\sin(kr)}{kr} \qquad (3\text{-}6).$$

Therefore,

$$I(\mathbf{k}) = \left|\rho_0 \int_0^{R_0} dr \cdot 4\pi r^2 \frac{\sin(kr)}{kr}\right|^2$$

$$= \left(\frac{4\pi\rho_0}{k}\right)^2 \left(\int_0^{R_0} dr \cdot r\sin(kr)\right)^2$$

$$= 9(\rho_0)^2 V^2 \left(\frac{\sin(kR_0) - kR_0\cos(kR_0)}{(kR_0)^3}\right)^2 \qquad (3\text{-}7).$$

This result was first be given by Rayleigh (Rayleigh, 1911). Though this derivation is for spherical symmetry, a very special case, formula (3-7) gives common features for the scattering from a system with not too much anisotropy. If $k = 0$ in formula (3-7), then

$$I(0) = (\rho_0)^2 V^2 = (\Delta n_e)^2,$$

where Δn_e is the total electron deficiency of the pore. The intensity of the scattering is proportional to $(\Delta n_e)^2$. This must be true for any dilute distribution of pores in carbon, irrespective of size and shape.

When kR_0 is very small, formula (3-7) can be expanded using Taylor's approximation,

$$I(\mathbf{k}) = (\rho_0)^2 V^2 \left(1 - \frac{(kR_0)}{10}\right)^2 \qquad (3\text{-}8a).$$

The function,

$$I(\mathbf{k}) = (\rho_0)^2 V^2 \cdot e^{-k^2 R_{02}/5} \qquad (3\text{-}8b),$$

gives the same result as equation (3-8a), when expanded to first order in R_0^2. Equation (3-8b) results from Guinier's equation (Guinier, 1955),

$$I(\mathbf{k}) = (\rho_0)^2 V^2 e^{-k^2 R_g^2/3} \qquad (3\text{-}9),$$

where R_g is the radius of gyration which is defined as

$$R_g^2 = \frac{\int d^3r \cdot r^2 \rho(r)}{\int d^3r \cdot \rho(r)} \qquad (3\text{-}10).$$

Using equation (3-10) for a spherical pore of radius R_0, gives $R_g = \sqrt{\frac{3}{5}} R_0$.

If $kR_0 >> 1$, then equation (3-7), tends to Porod's law (Porod, 1951),

$$I(\mathbf{k}) \approx \frac{2\pi S(\rho_0)^2}{k^4} \qquad (3\text{-}11).$$

where S is the surface area of the pore. When $kR_0 >> 1$, $\cos(kR_0)$ changes very fast over a very small range of $\mathbf{k}$, therefore we take the average of this cosine function in obtaining equation (3-11). Any reasonable distribution of sphere radius will smooth out the oscillation in the cosine function.

Debye et al. (Debye, 1957) studied SAXS on inhomogeneous solids. They showed that the scattered intensity could be written as follows,

$$I(\mathbf{k}) = 2\pi S(\rho_0)^2 \frac{1}{\left(k^2 + \frac{6}{R_g^2}\right)^2} \qquad (3\text{-}12).$$

The above equation yields Porod's law if $kR_0 >> 1$, and is consistent with the first order term in the expansion of the Guinier's equation when $kR_0 << 1$.

When there are more than one type of pores in the carbonaceous material (Kalliat, 1981), for example macropores and nanopores, intensity of diffraction is,

$$I(\mathbf{k}) = \sum_n \frac{A_n}{k^4} + \sum_m \frac{B_m}{\left(\frac{6}{R_m^2} + k^2\right)^2} + C \qquad (3\text{-}13),$$

where A_n and B_m are constants related to the surface area of each type of pores, C is a background constant, and R_m is radius of gyration obtained from the Debye expression for each type of pore.

3.4 Surface Area Measurements

The Brunauer-Emmett-Teller (BET) method is the most widely used procedure for determining the surface area of porous materials. In this thesis, the single-point BET surface area measurement was performed using a Micromeritics Flowsorb II 2300 surface area analyzer. This method is quantified by measuring the gas adsorbed as a single layer on the surface of a sample. A mixture of nitrogen in helium (30:70 mol. %) is used, which is a favorable condition for the formation of a monolayer of adsorbed nitrogen, at atmospheric pressure and at the boiling temperature of liquid nitrogen. Before the test, the carbon sample was placed in a U-shaped glass holder, weighed, and degassed at 140°C under the mixed gas for about 15 to 20 minutes. The sample holder was then immersed in liquid nitrogen for adsorption, and after that, in room-temperature water for desorption. The adsorption or desorption was considered to be complete when the change of the BET result was less than 0.05 m^2/sec. The final result of the single-point BET measurement was taken from the desorption data.

3.5 Thermal Gravimetric Analysis/Residual Gas Analysis

A computer controlled TA instruments #51 thermal gravimetric analyzer (TGA) was used to measure the relative weight loss of precursors versus temperature during pyrolysis. Powder samples were held in a platinum pan and heated to 1000°C at a heating rate of 5°C/min in an argon flow. Residual gas analysis (RGA) was carried out with a Leybold Quadrex 200 residual gas analyzer (mass spectrometer). A small stream of TGA exhaust gas was sampled by the mass spectrometer which was operated under vacuum. Measurements were conducted at a base pressure of 2×10^{-5} Torr. All gas flow lines were heated above 100°C so that no water vapor or other gases of interest could condense in the lines before they reached the mass spectrometer. The data were recorded by a computer.

EXPERIMENTAL TESTING OF ELECTROCHEMICAL PROPERTIES OF CARBONACEOUS MATERIALS

There are many ways to study the electrochemical properties of carbonaceous materials. To study lithium insertion in carbonaceous materials, the electrochemical lithium/carbon coin cell is the most convenient test vehicle.

4.1 Introduction to the Lithium/Carbon Coin Cell

The voltage of a lithium-ion cell is the difference between the chemical potential of the lithium atoms in the two electrode hosts. Here, we define the chemical potentials of lithium atoms in the cathode and the anode as $\mu_{cathode}$ and μ_{anode} respectively.

The chemical potential of lithium in the electrode is

$$\mu = \frac{\partial G(N,T,P)}{\partial N},$$

where μ refers to either $\mu_{cathode}$ or μ_{anode}, G is the Gibbs free energy, N is the number of lithium atoms in the electrode, T is the temperature and P is the pressure in the cell. In our case, T and P can be regarded as fixed parameters during the cell charge or discharge. Therefore,

$$\mu = \frac{dG}{dN}.$$

During the discharge of a lithium-ion cell, ΔN lithium atoms are moved from the carbon anode, through an ionically conducting electrolyte to the cathode. The total change in the free energy (ΔG), combining changes in both electrodes, is

$$\Delta G = \Delta N \cdot (\mu_{cathode} - \mu_{anode}).$$

At the same time, ΔN electrons are moved through the external circuit into the cathode material. The work done on these electrons in the external circuit is

$$W = -(\Delta N)eV,$$

where V is the cell voltage, and e is the magnitude of the electron charge. This work is equal to the total change in the free energy, leading to

$$-eV = \mu_{cathode} - \mu_{anode},$$

i.e.,

$$V = -\frac{(\mu_{cathode} - \mu_{anode})}{e},$$

which is the same as equation (1-1) in chapter 1. The same result can be obtained for the cell charge process.

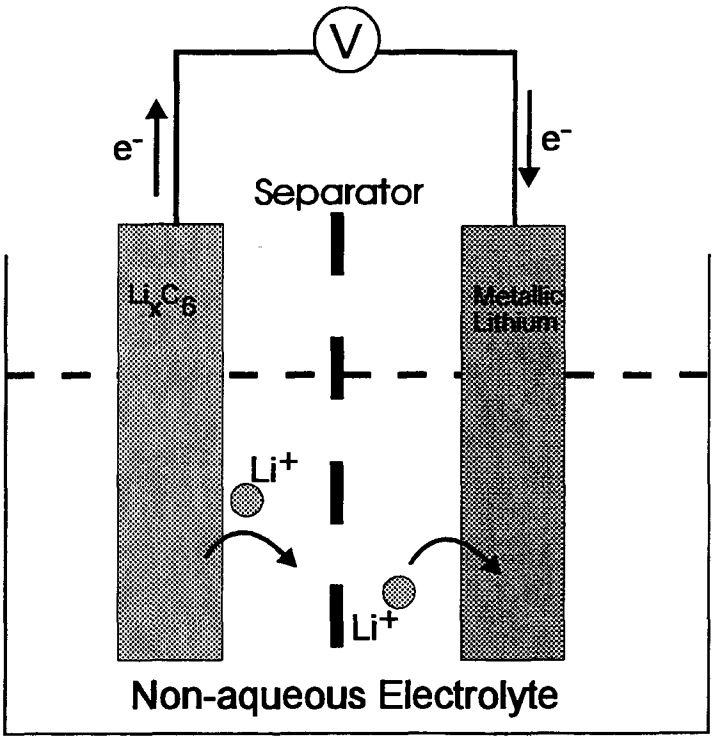

Figure 4-1. Schematically showing a lithium/carbon electrochemical test cell. The cell is being charged.

For convenience and simplicity, the electrochemical study of electrode materials is normally made in lithium/(electrode material) cells. For carbonaceous materials, a lithium/carbon cell is made to study electrochemical properties, such as capacity, voltage, cycling life, *etc.*. Lithium/carbon coin cells use metallic lithium foil as the anode and a

particular carbonaceous material as the cathode as schematically shown in figure 4-1. The purpose of using such cells rather than lithium-ion cells is that the chemical potential of lithium atoms in metallic lithium is fixed. Therefore, the cell voltage measures the chemical potential of lithium atoms within the carbonaceous material. In a lithium-ion cell, the chemical potential of lithium in both electrodes changes at the same time. This makes it difficult to study the carbon electrode alone.

Lithium/carbon cells are typically made as coin cells which we describe next.

4.2 Cell Construction and Testing

The lithium/carbon coin cell consists of several parts, including electrodes, separator, electrolyte and cell hardware. To construct a coin cell, we first must prepare each part separately. Successful cells will lead to meaningful results.

4.2.1 Electrodes and Electrolyte

The lithium/carbon coin cells used metallic lithium foil as the anode and a carbonaceous material as the cathode. The metallic lithium foil, with a thickness of 125 μm, was provided by Moli Energy (1990) Ltd.. The lithium foil is stored in a glove-box under an argon atmosphere to avoid oxidation.

The cathode is made by coating a slurry. The slurry is a mixture of the carbon powder (90% by weight), Super S carbon black (Chemetals Inc.) (5% by weight), and a binder solution of 9.4% by weight of Polyvinylidene fluoride (PVDF) in 1-Methyl-2-Pyrrolidinone (NMP) (~50% by weight). Excess NMP is added to the mixture to obtain a syrupy consistency. The slurry is then spread in a 150-μm thick layer on a copper foil substrate using a doctor blade spreader. After coating, the electrode is dried in an oven overnight at a temperature of 105 to 110°C in air. The NMP evaporates and a flat and adhering film of the electrode material is obtained on the copper. The electrode is pressed between two flat plates at about 1000 kPa for about one minute before it is used for

for making cells. The pressure increases the connections between powder particles, leading to good conductivity of the electrode.

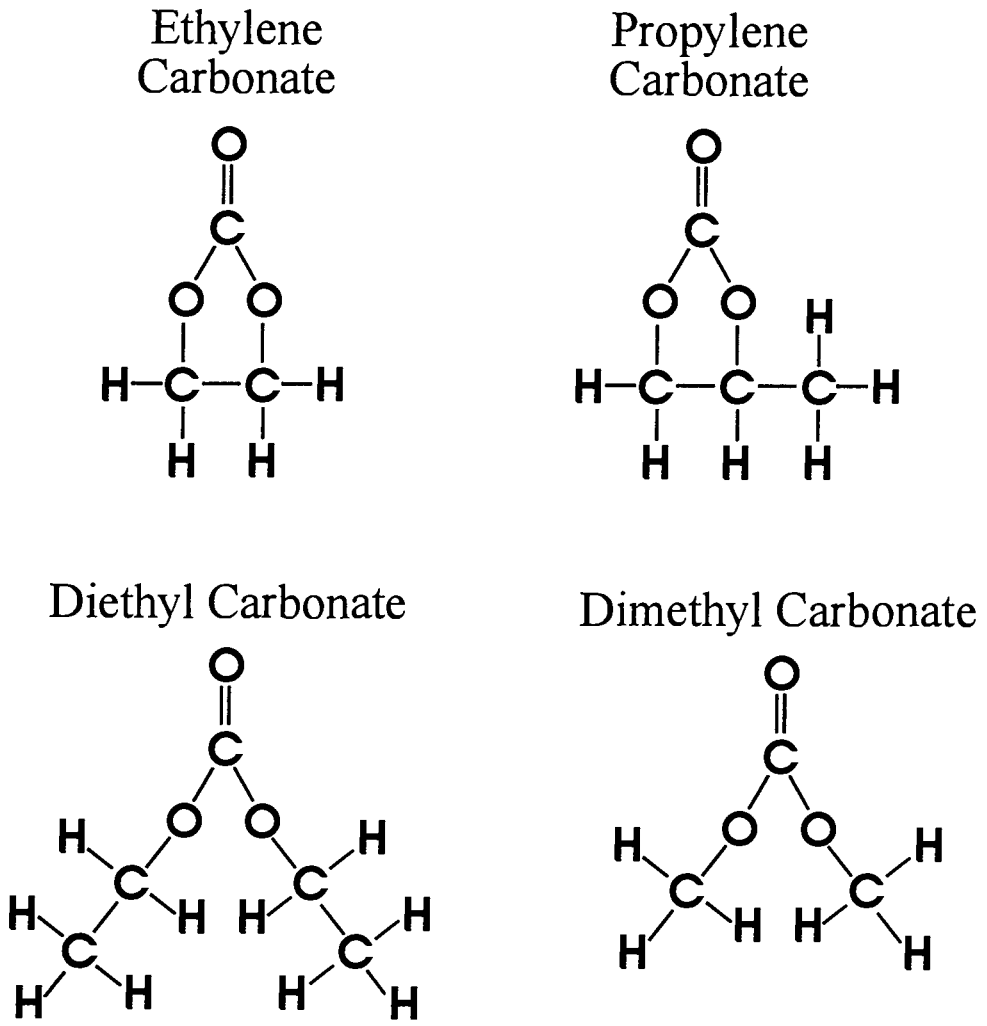

Figure 4-2. Schematic drawing of the molecular structure of EC, PC, DEC and DMC. The length of C—C, C—N, and C—O bonds are about 1.4 Å, a C—H bond is about 1.1Å, a C=O bond is about 1.2Å.

Two different electrolytes were used in this thesis, due to improvements in electrolytes with time and because of other considerations, such as compatibility with the hardware of certain electrochemical cells. The first electrolyte used was 1 molar $LiPF_6$ (Hashimoto) dissolved in a 25:25:50 volume % mixture of propylene carbonate (PC), ethylene carbonate (EC), and dimethyl carbonate (DMC). For this electrolyte, it is

necessary to "pressure wet" the separator and the carbon electrode before assembling the cell. The PC in the electrolyte can cause cointercalation, which refers the intercalation of each lithium-ion combined with a few PC molecules (making up the ion's solvation cloud) into the van der Waals space between adjacent graphene layers of the carbon electrode (Dahn, 1993). The cointercalation leads to more electrolyte decomposition due to exfoliation of the carbon. Therefore this kind of electrolyte was not used often. The second electrolyte used is 1 molar $LiPF_6$ dissolved in a mixture of 30% EC and 70% diethyl carbonate (DEC) by volume. This electrolyte is easier to use because it will self-wet the separator and electrodes at atmospheric pressure. The two electrolytes are kept under an argon atmosphere in the glove-box.

Figure 4-2 schematically shows the structure of the electrolyte solvents. These molecules have in-plane dimensions of about (4 Å × 5 Å) to (6 Å × 7 Å). These molecules are normally larger than the openings of the nanopores formed in the hard carbons of region 3 in figure 2-1 as discussed in chapter 7.

4.2.2 Cell Assembly

The carbon electrode is cut into unit squares 12 mm long × 12 mm wide using a stainless steel ruler with 12 mm width, and a surgical blade. Then these squares are weighed. The weight of the copper substrate square is known to be 13.3 mg. The active electrode mass is finally obtained by correcting for the weight of the substrate, the weight of the binder, and the weight of the Super S carbon black (the so-called dead mass in the electrode). Typically, the active electrode mass is around 10 mg.

Celgard 2502 microporous film is used for the separator. The film is obtained from Moli Energy (1990) Ltd. and then is stamped into unit circles of 21 mm diameter with a brass cutter.

Electrochemical cells are assembled in the glove-box. The cell is a 2320-type coin cell (23 mm OD and 2.0 mm thickness) as schematically shown in figure 4-3. The cell includes the electrolyte, the cell cap and can which are stainless steel, a polypropylene gasket used to seal the cell, the two electrodes, the separator between the electrodes, as

well as a stainless spacer and a mild steel disc spring which are used to increase the pressure on the electrodes.

If an electrolyte of 1 M $LiPF_6$ in PC/EC/DMC (25:25:50 vol. %) is used in the cell, it is necessary to "pressure wet" the carbon electrode and the separator so the pores in each fill with electrolyte. During this process, the carbon electrode and the separator are put in electrolyte in a vial placed in a sealed container. Vacuum is applied for about 3 to 5 minutes to remove the air from the carbon electrode and the separator pores. Then the vacuum is released and a pressure of about 120 kPa is applied for another 5 to 10 minutes to force the electrolyte into the separator and the carbon electrode.

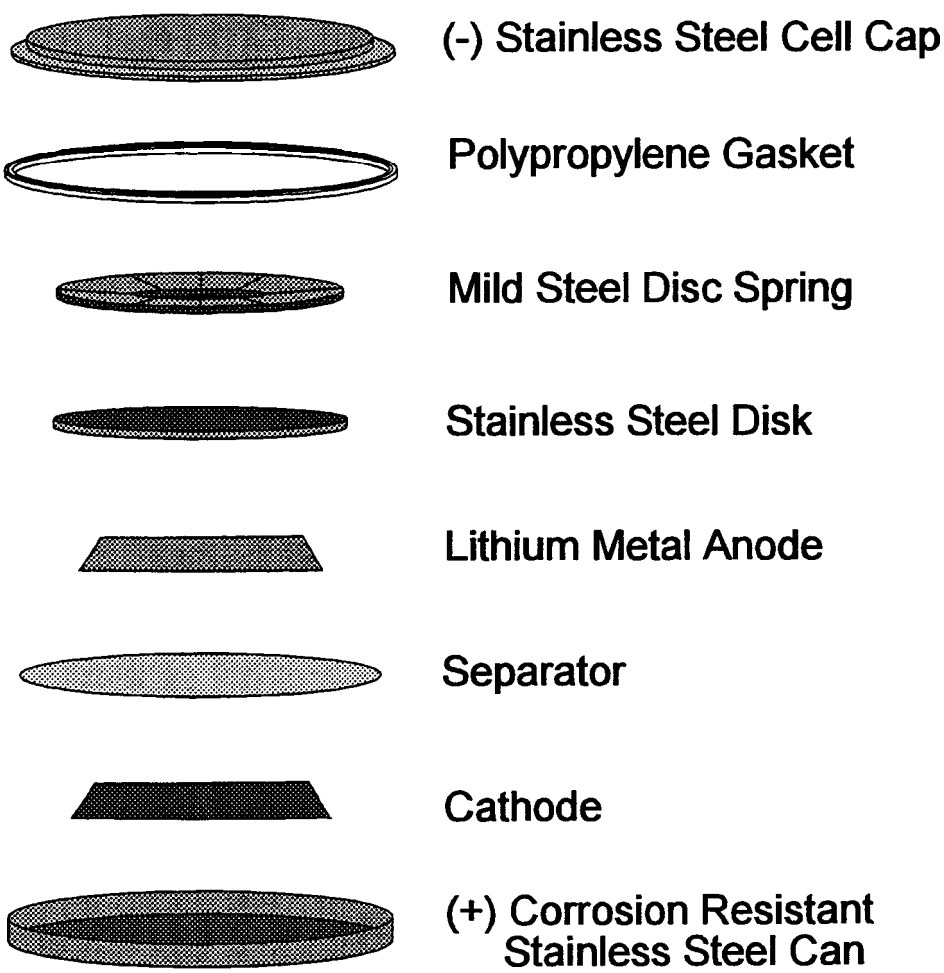

Figure 4-3. Exploded view of a 2320-type coin cell.

Once the cell is assembled in the right order, the cell is sealed by a pressure crimper inside the glove-box.

4.2.3 Cell Testing

Freshly assembled lithium/carbon coin cells typically have voltages between 2.8 and 3.4 volts. The cells are in their fully charged state which means that no lithium is inserted in the carbon anode. Then the coin cells are tested with computer-controlled constant-current cyclers (whose circuits are schematically shown in figure 4-4) having currents stable to ± 1%. The cells are placed in thermostats at a particular set temperature which is stable to ± 0.1°C during the test. Most of our cells were tested at 30°C. Some cells were tested at 50 and 70°C for special purposes.

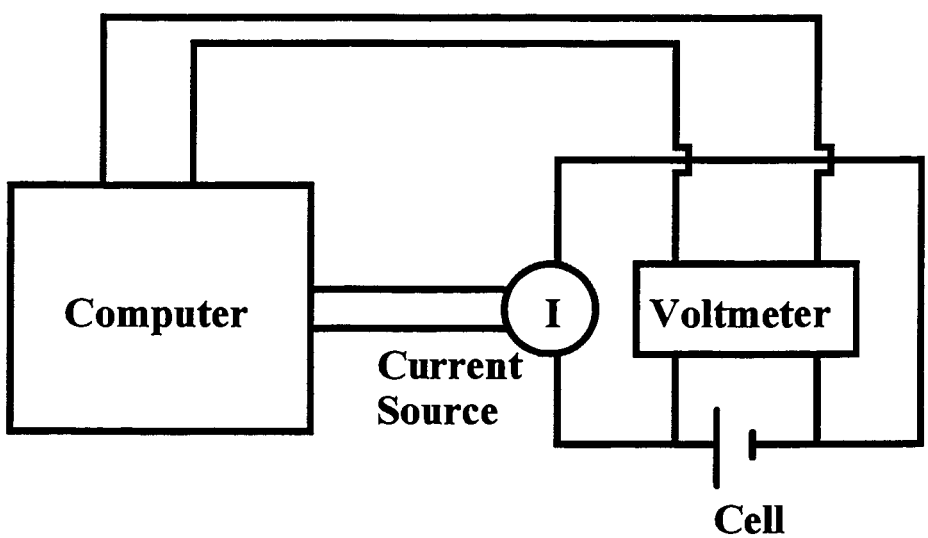

Figure 4-4. Schematic drawing of the computer-controlled cycler

The current for charge and discharge is selected based on the active mass of the carbonaceous electrode. A 50-h-rate current applied to the cell corresponds to a change $\Delta x = 1$ in Li_xC_6 in 50 hours (for a typical cell with 14-mg active carbon mass, the current is 104 μA). The parameter x is the concentration of lithium in the carbonaceous electrode.

4.3 Electrochemical Testing of Lithium/Carbon Cells

During the electrochemical test, the cell is typically cycled between high and low voltage trip points with a constant current which changes sign from charge to discharge. The cell will be cycled a number of times depending on the experiment. The voltage of the cell is measured as a function of time, and all the information we need is obtained from this data.

4.3.1 Voltage Profiles

The cell voltage as a function of time, V(t), can be analyzed in different ways. In our case, it is usually converted to a plot of voltage versus specific capacity, Q, for lithium, V(Q), using the formula:

$$Q = \frac{I \times t}{m}$$

where I is the current in mA which is applied on the cell, t is the time in hours, and m is the active mass of carbon electrode in grams. Hence, the specific capacity is measured in mAh/g.

Sometimes, instead of converting V(t) to V(Q), we convert to V(x), which is the change of the cell voltage as a function of the lithium concentration in the carbonaceous electrode. The following equation

$$x = Q/C_m$$

is used. C_m in this equation is the specific capacity of graphite, which is often called the "magic number". The magic number for carbonaceous materials is 372 mAh/g, corresponding to $x = 1$ in Li_xC_6 for graphite, which is calculated as

$$C_m = \frac{1}{6} \cdot \frac{N_a}{12g/mol} \cdot e \cdot \left(\frac{1000mA}{A}\right) \cdot \left(\frac{1hr}{3600s}\right),$$

where N_a is Avogadro's number. 12g is the weight of 1 mole of carbon, and e is the magnitude of the electron charge. Both V(Q) and V(x) curves have the same shape and contain similar information.

A graph of the discharge and charge capacities versus cycle number is called the capacity fade curve. This plot illustrates the loss of capacity (if any) versus cycle number. The materials we are looking for are expected to have little capacity loss with cycling, hence long cycle life.

4.3.2 Differential Capacity

Lithium insertion in carbonaceous materials is complicated. During discharge and charge, phase transitions in the intercalated host are often observed (McKinnon, 1980). Assume that, for a certain region of x, the Gibbs free energy has two minima which correspond to two single phases (phase 1 and phase 2) as shown in figure 4-5. For any x between x_1 and x_2, the material contains domains of both phases. Increasing x causes the domains of phase 2 to grow at the expense of phase 1. Such a phase transition is a first-order transition because the two phases coexist and have the same chemical potential during the transition. Therefore, a first-order phase transition in an intercalated carbon electrode appears as a plateau in the voltage profile as shown in the bottom panel of figure 4-5.

First-order phase transitions can be subtle if the difference between x_1 and x_2 is small, causing slight changes in the voltage profile. However, such slight changes are easier to observe if the data is differentiated and $-\left(\partial x/\partial V\right)_T$ versus V is plotted. Plateaus in V(x) appear as peaks in the differential capacity, $-\left(\partial x/\partial V\right)_T$. The subscript T will be dropped in the following.

In figure 4-5, the cell voltage is constant in the region of coexisting phases, and hence $-dx/dV$ diverges. In a practical cell however, kinetic effects yield a peak in $-dx/dV$ rather than a divergence (McKinnon, 1980).

A plot of differential capacity, $-dx/dV$, versus voltage also gives the density of sites, or capacity, in the electrode for hosting lithium, as a function of voltage. The total capacity in a particular voltage range is proportional to the area under the $-dx/dV$ curve.

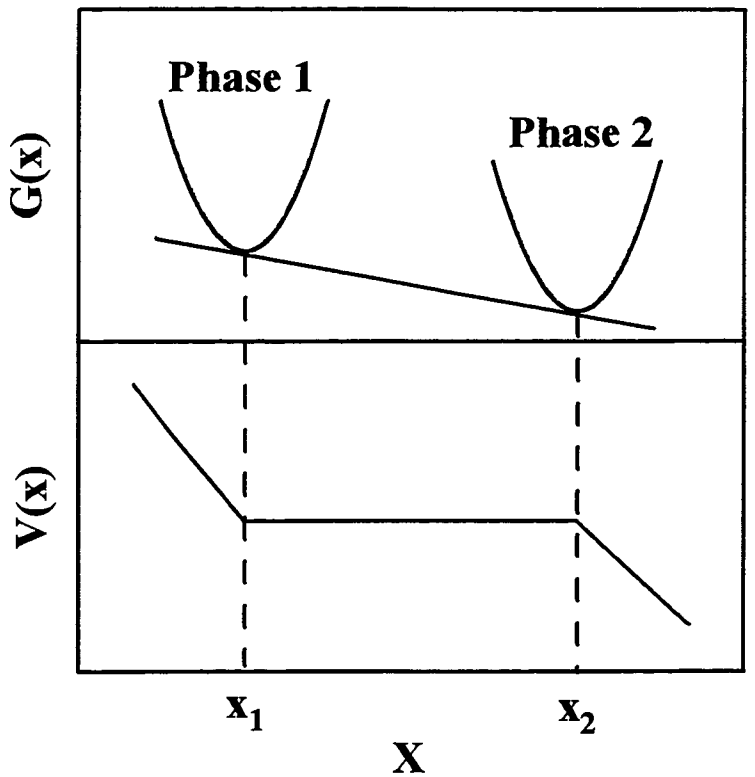

Figure 4-5. First-order transition leading to a plateau in V(x).

4.3.3 Comparison of Differential Capacity obtained by Constant Current Methods to that obtained by Cyclic Voltammetry

Another common way to test electrochemical cells is cyclic voltammetry. In this method, the voltage across the cell is changed linearly in time, and the resulting current is measured. Since

$$I = \frac{dQ}{dt} = \frac{dQ}{dV} \cdot \frac{dV}{dt} = C_m \frac{dx}{dV} \cdot \frac{dV}{dt},$$

where C_m is the magic number mentioned in section 4.3.1, and $^{dV}/_{dt}$ is constant, I is proportional to $^{dx}/_{dV}$ in this measurement, neglecting kinetic effects. The only advantage of cyclic voltammetry is that electrochemists are familiar with it. In a real coin cell however, we have to consider the effects of the internal resistance, R, which can be considered as a constant during the measurement. In cyclic voltammetry, the current changes with voltage, causing a variable shift in voltage of the differential capacity curve. Another disadvantage of cyclic voltammetry is that an equal amount of time is spent in each voltage interval. This is unlike the constant current measurement which spends more time on the peaks of the differential capacity curve which are more interesting to us.

4.3.4 "Open Circuit Voltage" Measurement Using the Macpile Charger

Open circuit voltage measurements were carried out using a MacPile Multichannel Galvanostat/Potentiostat (Bio-logic Co., France). This measurement was used to study the hysteresis during lithium insertion in the hydrogen-containing carbons. The cell is charged or discharged for a while, then the current is stopped and the cell is allowed to relax, before it is charged or discharged again. In this thesis, cells are charged or discharged for 2 or 4 hours with a constant current before the current is stopped. Then the cell is left in the open circuit state until the magnitude of the change in the voltage with time, $\left|^{dV}/_{dt}\right|$ is less than 0.3 mV/h.

4.4 In-Situ X-Ray Diffraction

In-situ X-ray diffraction can be used to probe the structure changes in the electrode during the insertion of lithium (Dahn, 1982). This technique is very important for understanding the intercalation process during cell discharging and charging.

In-situ X-ray diffraction employs a lithium/carbon cell equipped with a beryllium X-ray window. The structure changes in the carbon are studied by X-ray diffraction through the beryllium window while the cell is charged or discharged.

4.4.1 In-Situ X-Ray Cell Construction

Figure 4-6 schematically shows the construction of an in-situ X-ray cell. The cell is fundamentally similar to the coin cell which was described in section 4.2. The cathode

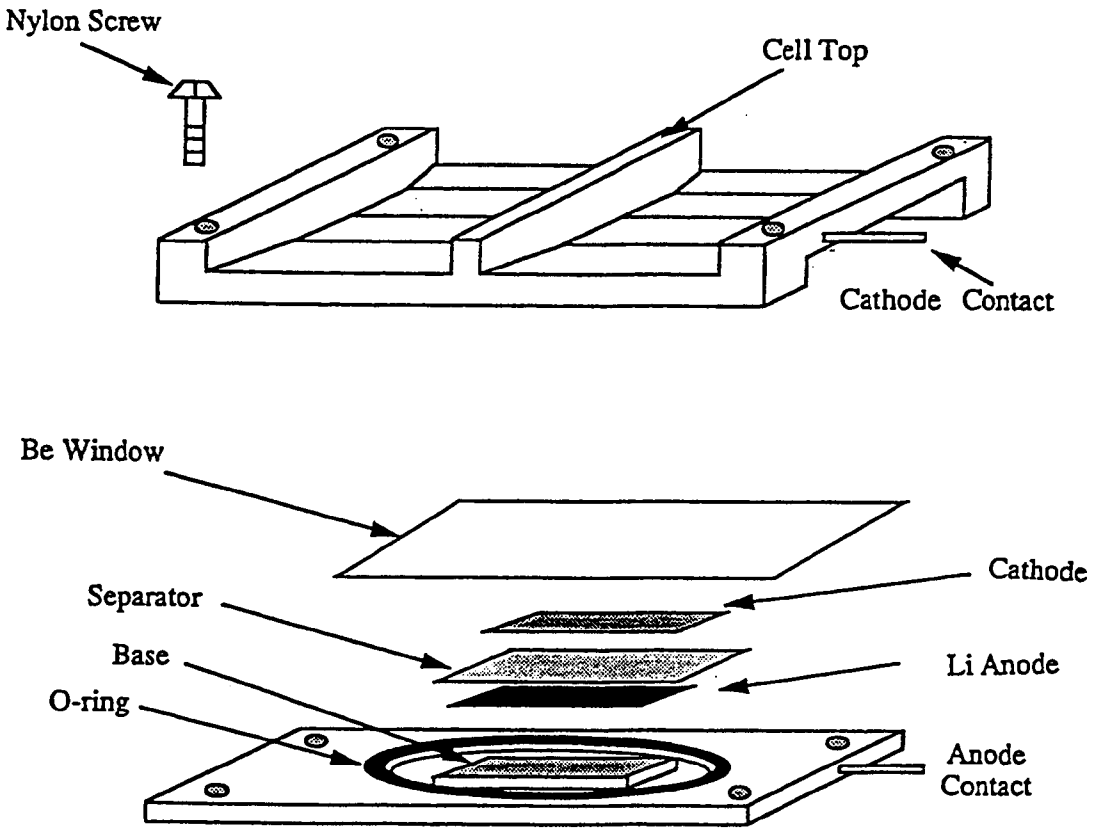

Figure 4-6. Exploded view of the in-situ X-ray cell.

is made by spreading the carbon slurry onto a piece of beryllium foil of dimensions 25 mm × 25 mm × 250 μm. The slurry is the same as described in section 4.2.1. The cathode is then put in the oven overnight at 110°C. After drying, the carbon material is about 100 to 150 μm thick and adheres to the beryllium window. The cell is assembled in the argon-filled glove box. The electrolyte used for the cell is 1 molar $LiPF_6$ in PC/EC/DMC

(25:25:50 vol.%) which is compatible with the silicone O-ring which we used for sealing the cell. The separator is cut into a square of dimensions 14 mm × 14 mm. Both the separator and the electrode (carbon adhering to the beryllium window) must be "pressure wetted" before assembling the cell to allow sufficient penetration of electrolyte. Once the parts of the cell are put in order, nylon or electrically isolated stainless steel screws are used to tighten the cell. The cell top and the base are made of stainless steel which are both electrically isolated by a thin plastic film.

4.4.2 In-Situ X-ray Cell Testing

The in-situ cells are discharged or charged by Keithley 236 source-measure units at room temperature. The cell is fixed at a particular voltage and once the current has decayed to less than 100 nA, representing quasi-equilibrium, a diffraction pattern is collected. The cell voltage is then switched to a new value. In-situ X-ray data were collected using the Phillips diffractometer with a 0.5° divergence slit and a 0.2 mm receiving slit, or using the Siemens D5000 diffractometer with 0.75° divergence and antiscatter slits and a 0.2 mm receiving slit.

4.4.3 Off-Axis Displacement

When the diffractometer is used to perform the in-situ X-ray measurement, the X-ray tube and the detector are on the measuring circle. The plane of the carbon electrode is placed perpendicular to the measuring circle, lying on a diameter of the circle. Our diffractometers operate in the Bragg-Brentano pseudofocusing geometry as shown in figure 4-7. Off-axis displacement is caused by a parallel shift of the carbon electrode from the correct position A (on the goniometer axis) to position B (see figure 4-7). The thickness of the lithium anode and the separator results in the upward shift of the cathode which adheres to the beryllium window. The carbon cathode is shifted upward with respect to the cell base which is aligned at the on-axis position, A, during the measurement.

For the case of the carbon cathode at the correct position A, the incident ray, Ra, makes an angle, θ_B, with the plane of the carbon cathode. The diffracted ray, Ra′, also makes an angle θ_B with respect to the sample. If the position of the cathode is shifted to B, the diffracted ray becomes Ra″ which causes an error, $\Delta 2\theta$, in the measured scattering angle.

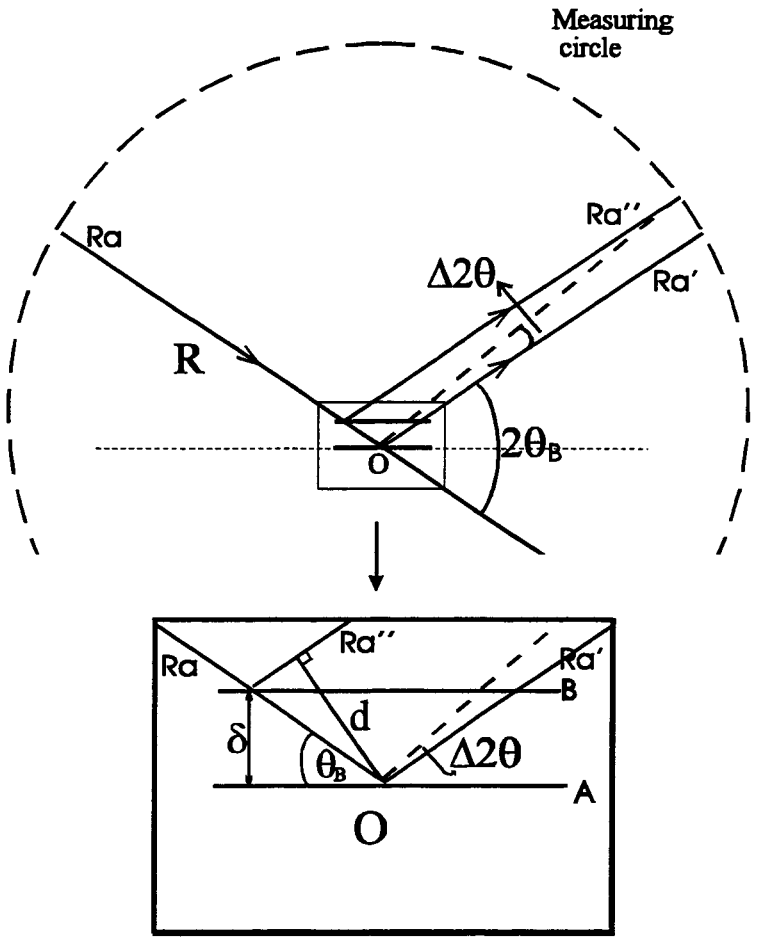

Figure 4-7. Schematic showing the off-axis displacement in the in-situ X-ray measurement.

In this work, we carefully prepare the in-situ X-ray cells to minimize the off-axis displacement, because a small displacement can cause a large error in scattering angle. For example, in figure 4-7, there is a vertical shift δ for the carbon electrode. This displacement will cause an error in scattering angle $2\theta_B$,

$$\Delta 2\theta = \frac{d}{R} = \frac{(\delta / \sin\theta_B)\sin 2\theta_B}{R},$$

where R is goniometer radius (205 mm for the Siemens, and 173 mm for the Phillips), and d is the distance between the two diffracted rays Ra′ and Ra″. If $\Delta 2\theta$ is small, then the error in scattering angle is

$$\Delta 2\theta = 2\frac{\delta \cos\theta_B}{R} \qquad (4\text{-}1).$$

The (002) peak of graphite is at about 26.5° of scattering angle. Hence, for the Siemens, a 0.5 mm off-axis shift will cause an error of $\Delta 2\theta \approx 0.27°$, i.e., the peak will shift to a higher angle, to about 26.8°.

Therefore, it is very important to minimize the off-axis displacement during the measurement of in-situ X-ray diffraction data. When we deal with the experimental data, the correction for this displacement is a priority. This can be done considering the (002) peak position of the graphitic carbon used to make the electrode. This peak position is then compared to the peak position obtained from scans of the freshly assembled in-situ cell to measure $\Delta 2\theta$ and hence δ. Corrections to the measured angle from the cell using equation (4-1) are then subsequently applied.

LITHIUM INTERCALATION IN GRAPHITIC CARBONS

Graphitic carbon is now used as the anode material in lithium-ion batteries produced by Moli, Matsushita, Sanyo and A+T battery. It is important to understand how the structures and properties of graphitic carbons affect the intercalation of lithium within them.

5.1 Synthesis of Graphitic Carbons

Here, graphitic carbon refers to soft carbon precursors heated to between 2100 and 3000°C. Several types of graphitic carbon were used for this thesis. These samples are from four different sources. First, mesocarbon microbeads (MCMB) were obtained from Osaka Gas Ltd. This carbon sample had been heat treated to about 1000°C. Further heat-treatment was done at Moli. We used a Centorr (series 10) graphitizing furnace to further heat the carbons under flowing nitrogen to 2300°C, 2400°C, 2500°C, 2600°C, 2700°C and 2800°C. Each sample was treated for one hour at the final temperature. These samples are called MCMB2300,..., and MCMB2800 respectively. Second, a petroleum coke sample (type XP, from Conoco, Houston TX, USA) was heat treated to 2250°C and 2300°C in a similar manner. These samples are called Conoco2250 *etc.*. Finally, a commercially available graphite powder (JMI) from Johnson Matthey Inc., and a natural graphite powder (IMP) from Industrial Mineral Park Mining Corporation (Vancouver, BC) were studied. Powder X-ray diffraction shows that the IMP sample contains large amounts of impurities and is not suitable for structural studies.

5.2 Structural Parameters for Graphitic Carbons

The structure refinement program for disordered carbons, which was recently developed by Shi *et al* (Shi, 1993a; Shi, 1993b) is ideally suited to studies of the powder diffraction patterns of graphitic carbons. By performing a least squares fit between the measured diffraction pattern and a theoretical calculation, parameters of the model structure are optimized. For graphitic carbon, the structure is well described by the two-layer model which was carefully described in chapter 3.

Figures 5-1 through 5-5 show the changes which occur in the diffraction patterns of the heated graphitic carbon samples, and the excellent description of these patterns by the structure refinement program. The structural parameters, P, P_t, a, d_{002}, L_c and L_a for all the carbon samples are listed in table 5-1 (Zheng, 1995a).

P decreases as the heat-treatment temperature increases above 2200°C. The parameters which describe the size of the crystallite, L_c and L_a, also increase with the heat-treatment temperature. The capacity parameters x_{max}, x_{2max} and x_{21} in table 5-1 will be described and carefully discussed later in this chapter.

Table 5-1. Structural parameters and capacities (x_{max}, x_{2max} and x_{21}) for the carbon samples studied.

Name	HTT(°C)	d_{002}(Å)	P	P_t	a(Å)	L_c(Å)	L_a(Å)	x_{max}	x_{2max}	x_{21}
Conoco2250	2250	3.382	0.42	0.03	2.457	340	294	0.579	0.432	0.147
Conoco2300	2300	3.376	0.37	0.04	2.457	350	320	0.645	0.457	0.188
MCMB2300	2300	3.369	0.37	0.04	2.456	440	310	0.657	0.471	0.186
MCMB2400	2400	3.363	0.29	0.06	2.456	490	310	0.684	0.463	0.221
MCMB2500	2500	3.359	0.24	0.07	2.456	550	330	0.729	0.454	0.275
MCMB2600	2600	3.358	0.21	0.07	2.456	560	350	0.788	0.467	0.321
MCMB2700	2700	3.357	0.17	0.06	2.457	610	360	0.814	0.469	0.346
MCMB2800	2800	3.352	0.10	0.04	2.457	670	420	0.859	0.473	0.386
JMI	?	3.356	0.05	0.04	2.460	380	330	0.924	0.483	0.441

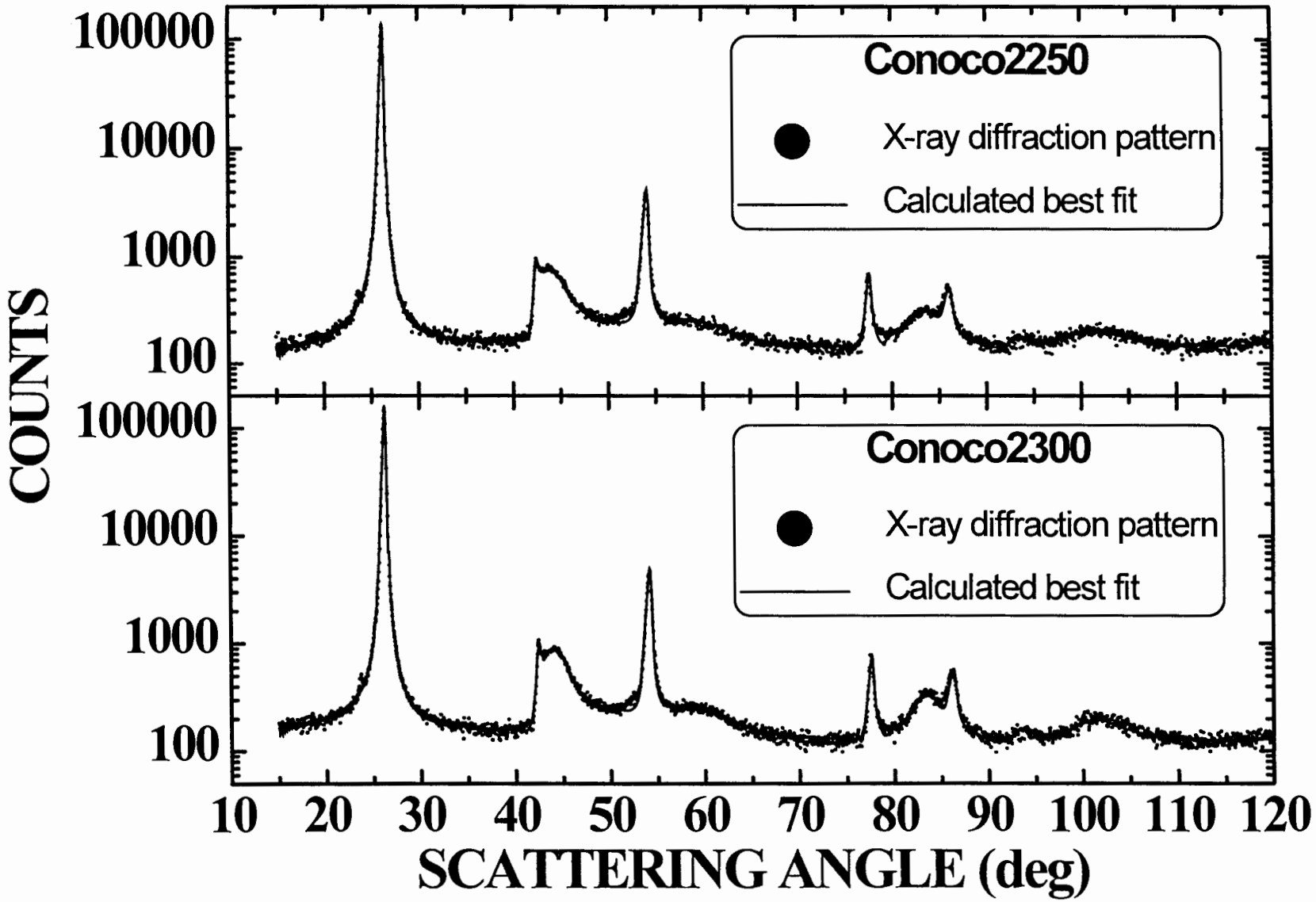

Figure 5-1. The X-ray diffraction patterns and calculated best fits from the structure refinement program for the samples Conoco2250 and Conoco2300.

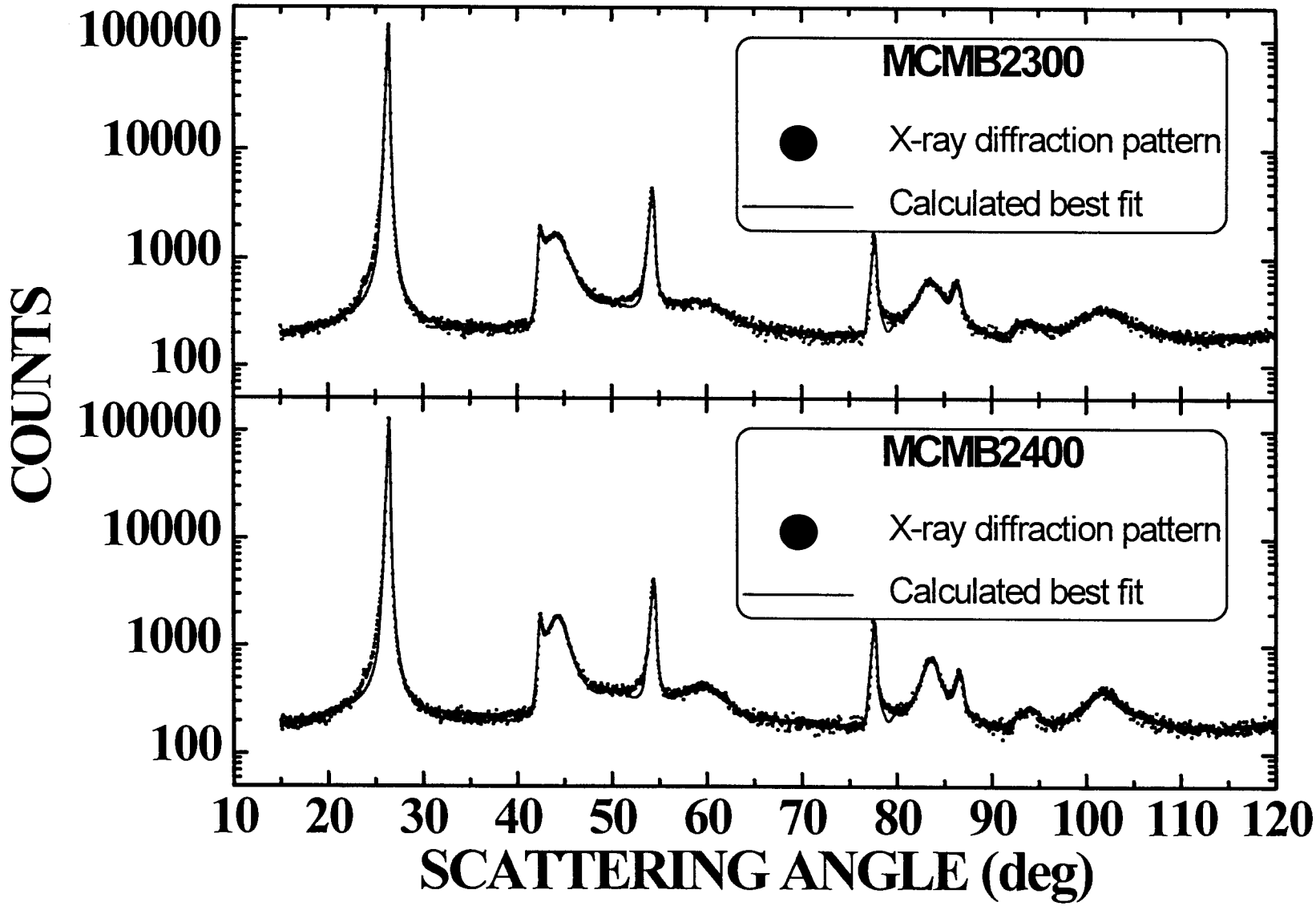

Figure 5-2. The X-ray diffraction patterns and calculated best fits from the structure refinement program for the samples MCMB2300 and MCMB2400.

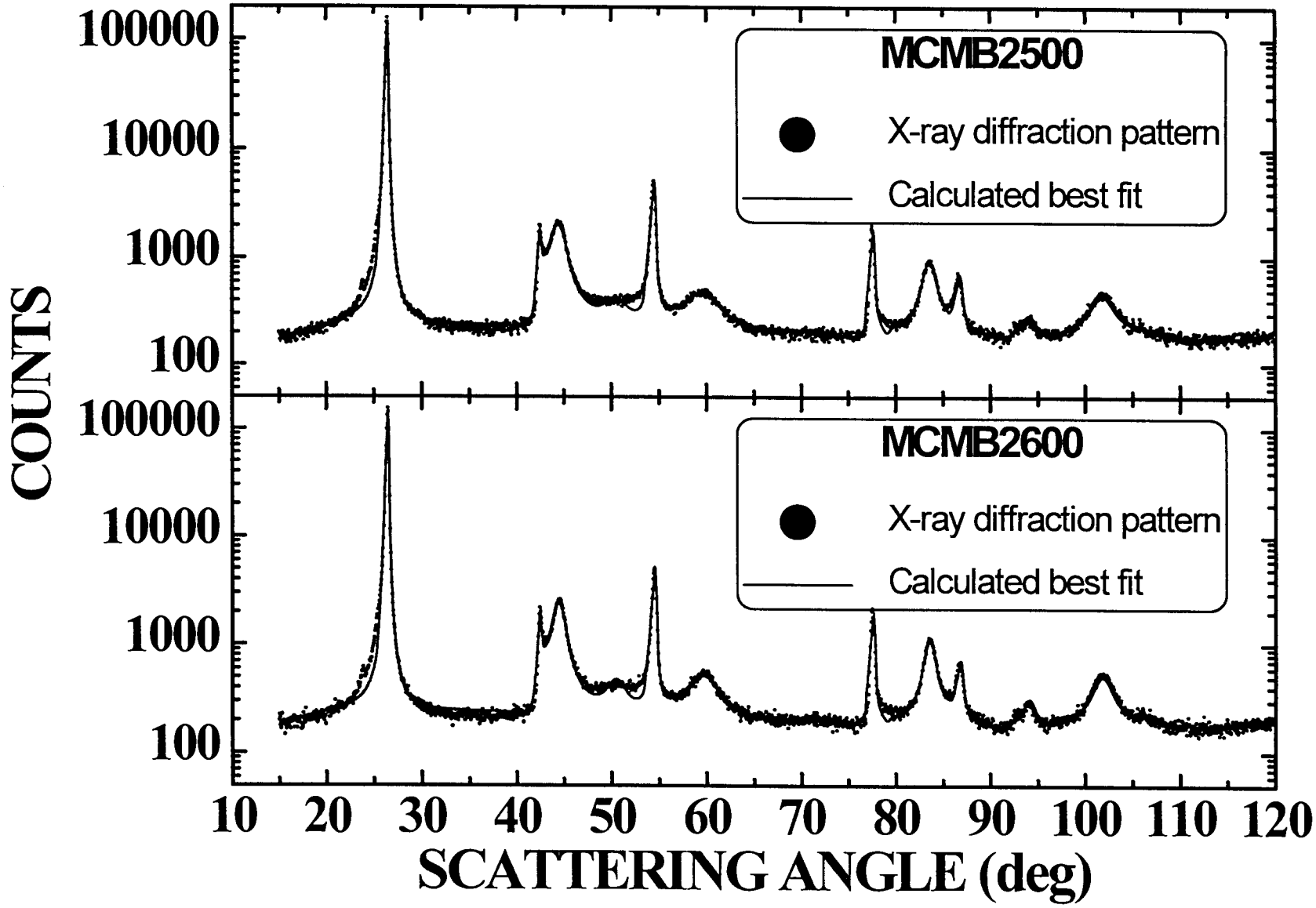

Figure 5-3. The X-ray diffraction patterns and calculated best fits from the structure refinement program for the samples MCMB2500 and MCMB2600.

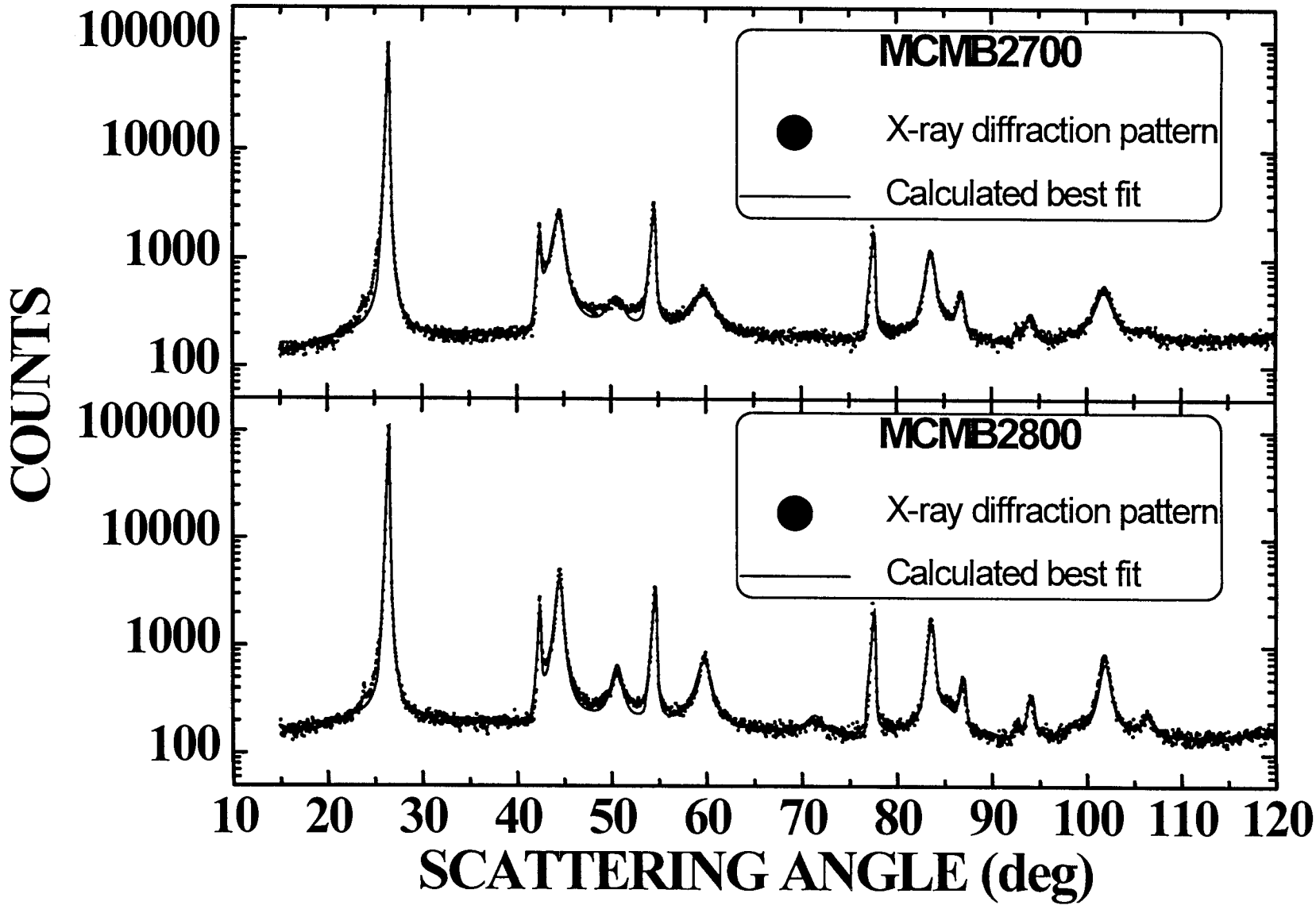

Figure 5-4. The X-ray diffraction patterns and calculated best fits from the structure refinement program for the samples MCMB2700 and MCMB2800.

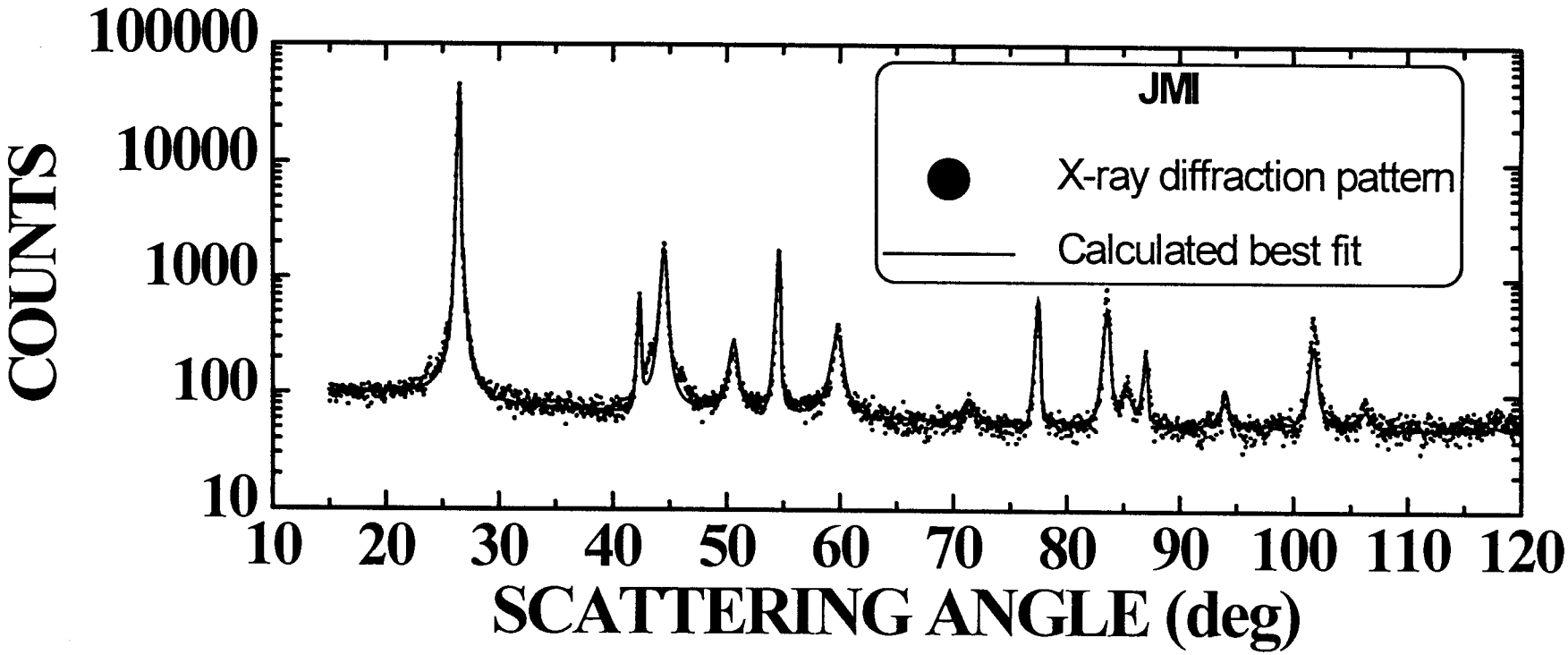

Figure 5-5. The X-ray diffraction pattern and calculated best fit from the structure refinement program for the sample JMI.

5.3 Lithium Intercalation in Graphite

Reviewing previous work on lithium intercalation in graphite is the starting point for studying lithium intercalation in graphitic carbons. In this section, the concept of intercalation is described first. Then we describe the phenomenon of "staging", which occurs during lithium intercalation with graphite. In lithium/graphite electrochemical cells, electrolyte decomposition occurs and passivating films form when lithium initially reacts with the graphite electrode. This causes a consumption of the lithium and graphite electrodes and leads to irreversible capacity as described later.

5.3.1 Intercalation, General Description of Lithium Intercalation in Graphite.

"Intercalation" is defined by McKinnon and Haering (McKinnon, 1983b) to be the "reversible insertion of guest atoms into host solids such that the structure of the host is not significantly altered". Lithium can intercalate in many materials with crystal or quasi-crystal structures, due to the activity and the small size of lithium atoms. In lithium intercalation compounds, like Li_xTiS_2 (Thompson, 1978), $Li_{1-x}Mn_2O_4$ (Tarason, 1993) and graphite intercalation compounds (GICs) (Dahn, 1991a), the host structures are basically unaltered over the range from $0 \leq x \leq 1$. There are no fundamental changes to the strong bond which holds these hosts together. The lithium simply fills interstitial sites and transfers some charge to the host. No significant hysteresis in charge-discharge behavior of lithium cells containing these hosts is observed.

Typically, intercalation hosts tend to be materials having either layered or tunnel structure to allow easy diffusion of intercalants, like lithium atoms, in the materials. It has been known for about 40 years that lithium can easily intercalate in graphite forming staged phases (Herold, 1955). Safran concluded that the staging phenomenon is the result of the competition between inter-layer repulsive and in-plane attractive interactions between the intercalated lithium (Safran, 1980). Stage-*n* order is a sequence of *n* graphite sheets and one intercalate layer. The layered structure of crystalline graphite and the

stage-2 and stage-3 phases of lithium intercalated graphite are schematically shown in figure 5-6.

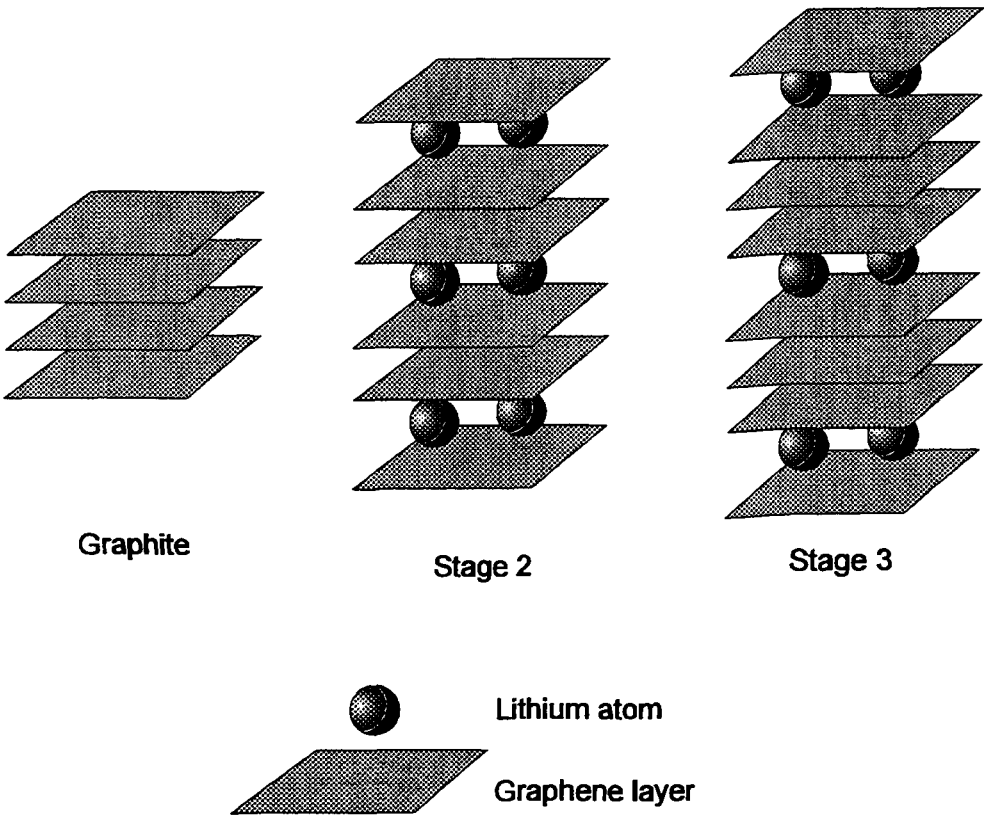

Figure 5-6. Schematic diagram of the layered structure of graphite and the stage-2 and stage-3 phases of lithium intercalated graphite

Daumas and Herold (Daumas, 1969) proposed a domain model to explain the stage transformations. This model is consistent with Safran's conclusion on staging phenomenon as mentioned above. The domains are stacked in columns to form ordered stages (see figure 5-7). Stage transformations only require a spreading out and rearrangement of the islands of intercalant without the necessity for occupied intercalated layers to be completely empty while others are filled (Marsh, 1987). This has been observed directly by Thomas et al. (Thomas, 1980) in graphite-$FeCl_3$ using lattice imaging with a transmission electron microscopy.

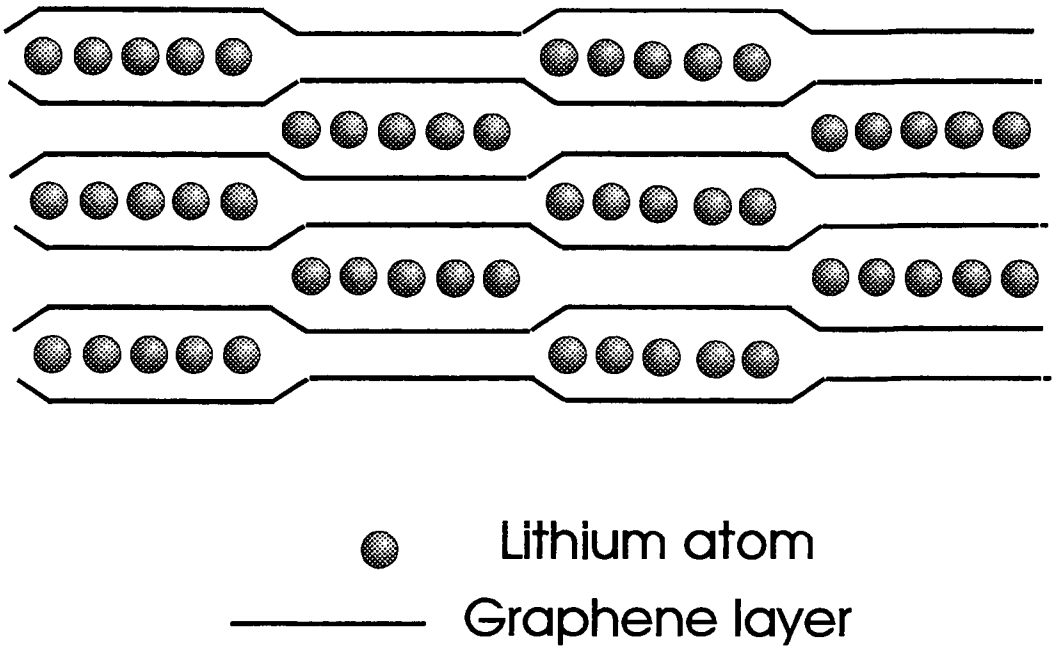

Figure 5-7. Stage-2 order in the Daumas-Herold domain model of staging

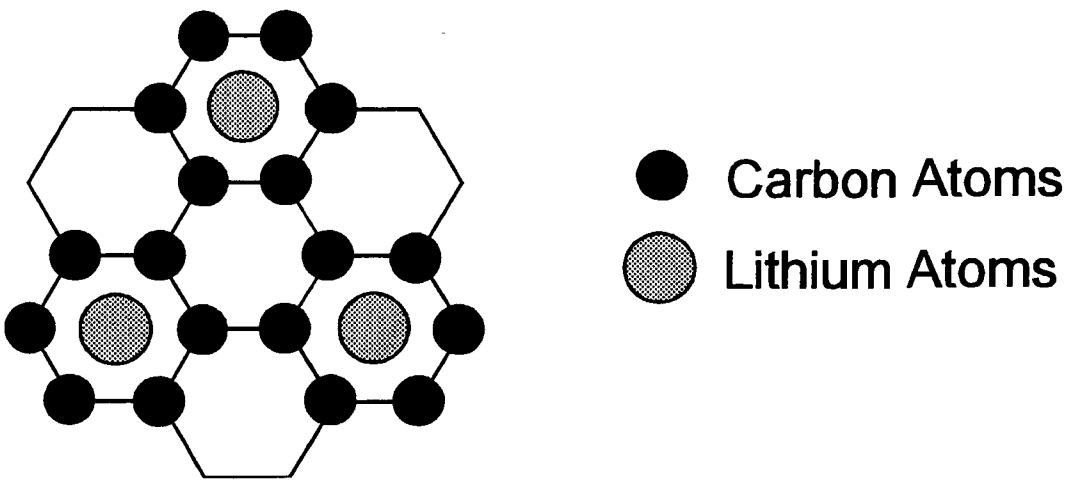

Figure 5-8. A basal view of LiC_6.

It is well known that graphite can intercalate up to 1 lithium atom per six carbon atoms under ambient conditions (Fischer, 1987), which leads to the stage-1 GIC, LiC_6. A basal view of this compound is shown schematically in figure 5-8. The lithium atoms occupy next-nearest neighbor sites (on one of the three $\sqrt{3}a \times \sqrt{3}a$ superlattices), separated by 4.25Å, within the Van der Waals space between every pair of carbon sheets

(Kambe, 1979). When the lithium is intercalated, it transfers most of its 2s electron to the carbon host and exists as a screened ion between the carbon sheets. The Coulomb repulsion between lithium ions in nearest-neighbor sites is apparently larger than the binding energy of the lithium to the graphite host so no lithium atoms occupy nearest-neighbor sites as shown in figure 5-8, However, when the extreme conditions of 280^0C and 50kBar lithium vapor pressure are applied, lithium atoms can move into nearest-neighbor sites (Nalimova, 1995).

When lithium intercalates between adjacent parallel carbon sheets, those sheets translate from "AB" registry (Harrison, 1989) into "AA" registry (Boehm, 1992) with honeycombs directly above one another "eclipsed". The lithium atoms are centered between honeycombs above and below.

5.3.2 Electrochemical Intercalation of Lithium in Graphite

5.3.2.1 Electrolyte Decomposition and Passivating Film Formation

During the first charge of a lithium-ion cell or discharge an electrochemical lithium/graphite cell, some of the lithium ions transferred through the separator onto the surface of the graphite electrode combine with electrons and react with the electrolyte. This reaction is called electrolyte decomposition and a passivating film is formed on the surface of the graphite electrode. This film is a solid electrolyte, and is electronically insulating but ionically conducting. It is often referred to as the solid electrolyte interphase (SEI) (Peled, 1979). The electrolyte decomposition reaction stops when the film is thick enough to prevent electrons tunneling across it to react with lithium ions and electrolyte.

The voltage profile of the first one and half cycles of a lithium/graphite cell is shown in figure 5-9. The anode is made from a natural graphite, IMP. The electrolyte used is a solution of 1 molar $LiPF_6$ in EC/DEC (30:70 vol. %). The difference between the first discharge and the first charge is defined as the irreversible capacity. The irreversible capacity caused by the SEI formation consumes lithium and occurs mainly

when the cell voltage is above 0.2 volts as shown in figure 5-9. This phenomenon can be observed in all cells made from carbonaceous materials. One goal in the research and development of lithium-ion cells is to minimize the irreversible capacity.

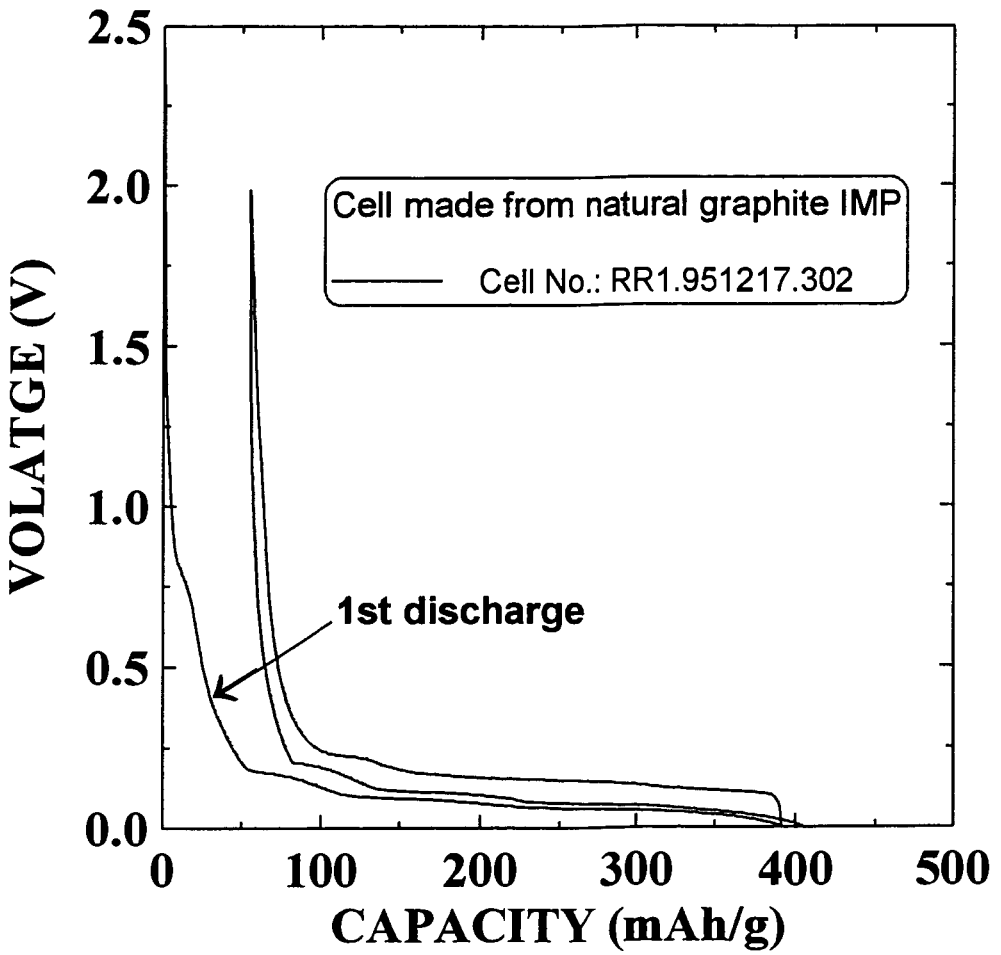

Figure 5-9. The first discharge and subsequent cycle of a lithium/graphite (IMP) cell.

5.3.2.2 Voltage Profile and Differential Capacity Curve of Lithium/Graphite cells

Staging phase transitions which occur as lithium intercalates into graphite are clearly shown in the voltage profile of an electrochemical lithium/graphite cell. A series of staged phases form as the concentration of lithium, x, increases (Dahn, 1991a). First, there is insertion of lithium into a dilute stage-1 phase, called stage 1′, followed by a first-order phase transition to a stage-4 phase. For a range of x, the dilute stage 1 and stage 4

phases coexist. In the coexistence region, the chemical potential of lithium in the two phases is equal, and a plateau in *V(x)* is observed.

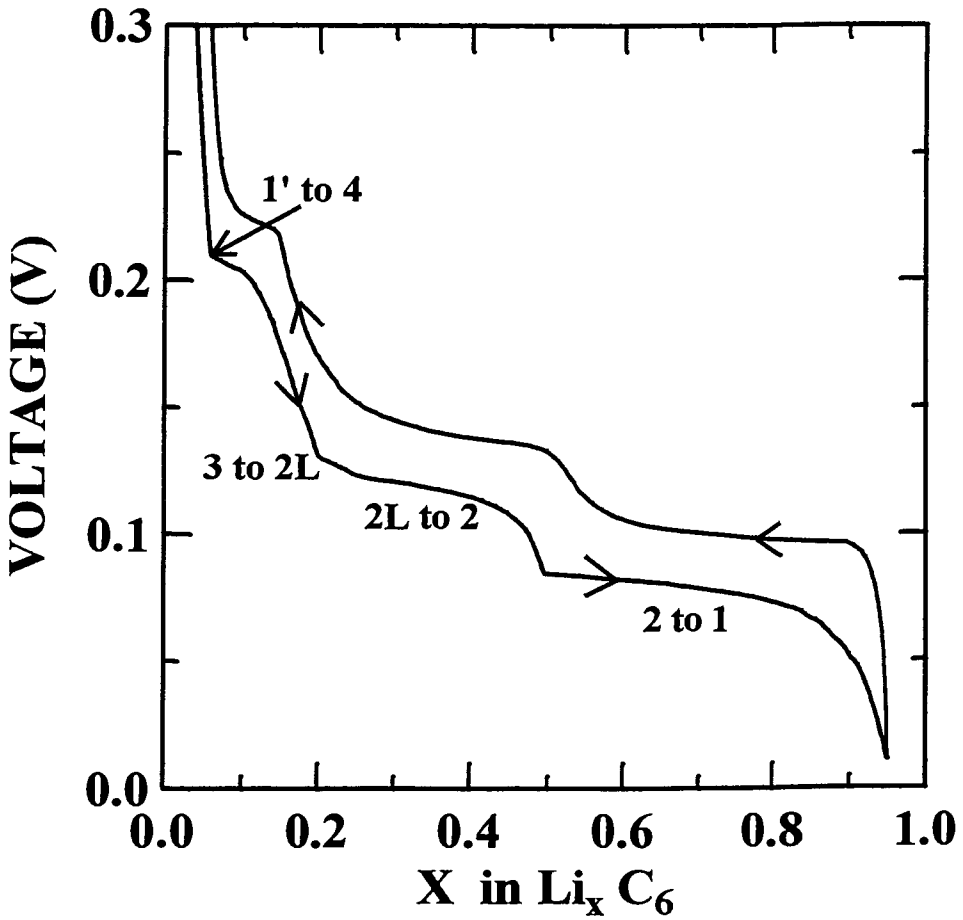

Figure 5-10. The voltage profile, V(x), of a Li/graphite cell. The graphite used is JMI. The correspondence between the plateaus and the transitions between staged phases has been indicated for the discharge.

Figure 5-10 shows *V(x)* for a lithium/graphite cell, where the two-phase regions have been labeled for the discharge curve following reference 40. The transition between stage 2 and concentrated stage 1 is especially easy to observe since it spans a range of almost $\Delta x = 1/2$.

Although several plateaus are visible in figure 5-10, the differential capacity, $-(dx/dV)_T$, showing peaks at the compositions where coexisting phases occur, is a more

sensitive probe. Figure 5-11 shows $-(dx/dV)_T$ for the above Li/graphite cell, where the two-phase regions are labeled.

Electrochemical methods are thus a very sensitive probe of the compositions of the staged phases and the widths of the two-phase regions.

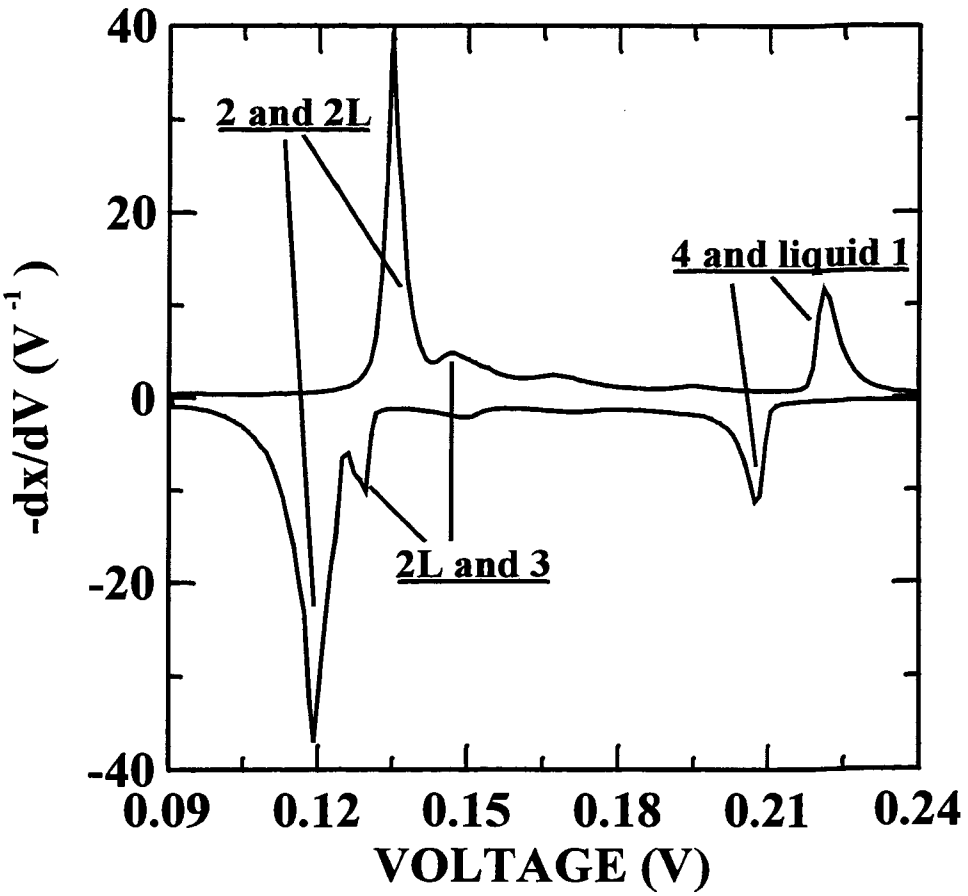

Figure 5-11. Differential capacity, $-(dx/dV)_T$, for the Li/graphite cell made from JMI. Two-phase regions are labeled.

5.4 Lithium Intercalation in Graphitic Carbons with Turbostratic Disorder

Graphitic carbon is presently one of the best candidates for anodes of lithium-ion batteries. The maximum amount of lithium which can be intercalated within the carbon, x_{max}, depends on the crystal structure of graphitic carbon (Dahn, 1993).

5.4.1. Reversible Capacity of Graphitic Carbons and Compositions of Stage-2 Materials

Two electrochemical coin-type cells were constructed for each of the graphitic carbons in table 5-1. The cell construction and testing were described in chapter 4. All cells were tested in the same manner. The first cycle (discharge and charge) of the cells was made using a current which corresponds to a 50 hour rate. A passivating film formed during the first discharge (Peled, 1979; Fong, 1990) and created about 20% irreversible capacity. Once the growth of passivating film reaches completion, the irreversible reactions apparently stop. Therefore, all careful measurements were made on the second and third cycles of these cells.

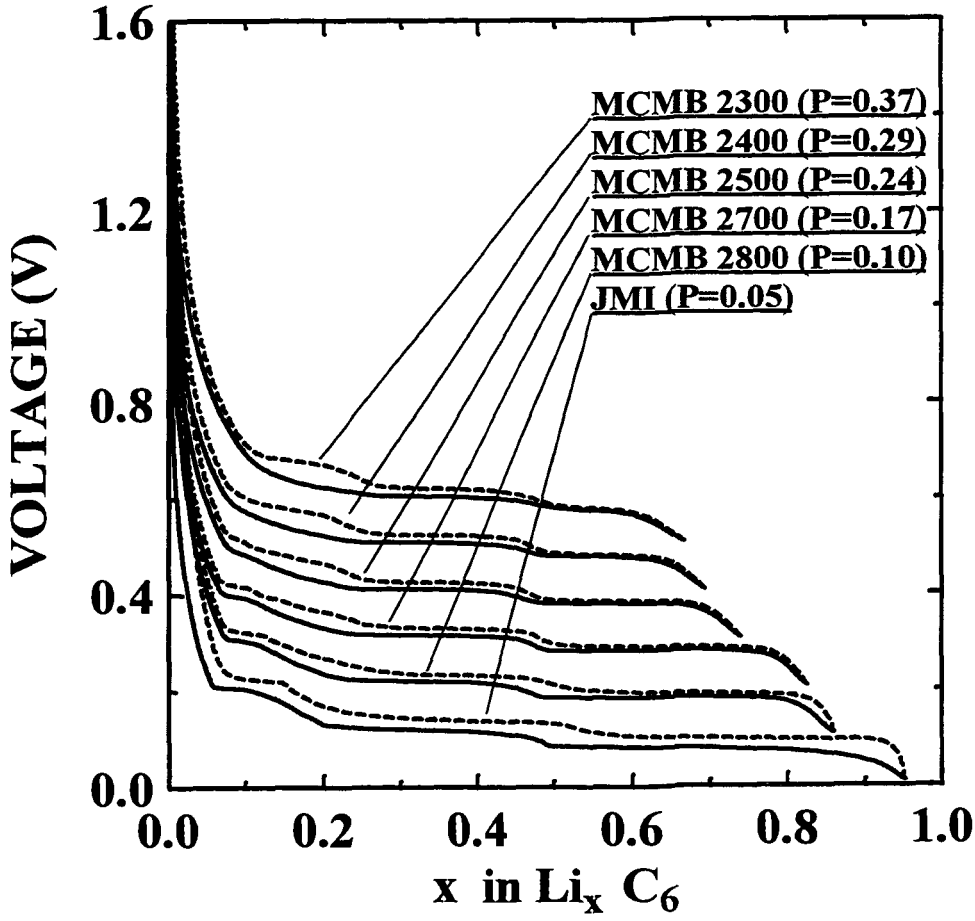

Figure 5-12. The voltage profiles of the graphitic carbon samples as indicated. The curves have been shifted sequentially by 0.1 V for clarity. Solid lines are for discharge and dashed lines are for charge.

The second cycle of the cells was made at a 400-hour rate to ensure quasi-equilibrium conditions, for examination of the staging transitions. At these small currents, there is an absolute error between the set current and the actual current which varies between channel to channel of our charger system. The currents are stable, but not accurately known. We then cycled all cells a third time, at a 50 hour rate, where the currents are accurate to 1% to determine the values of x_{max}. The data measured at the 400 hour rate was then normalized to the value of x_{max} determined at 50 hour rate.

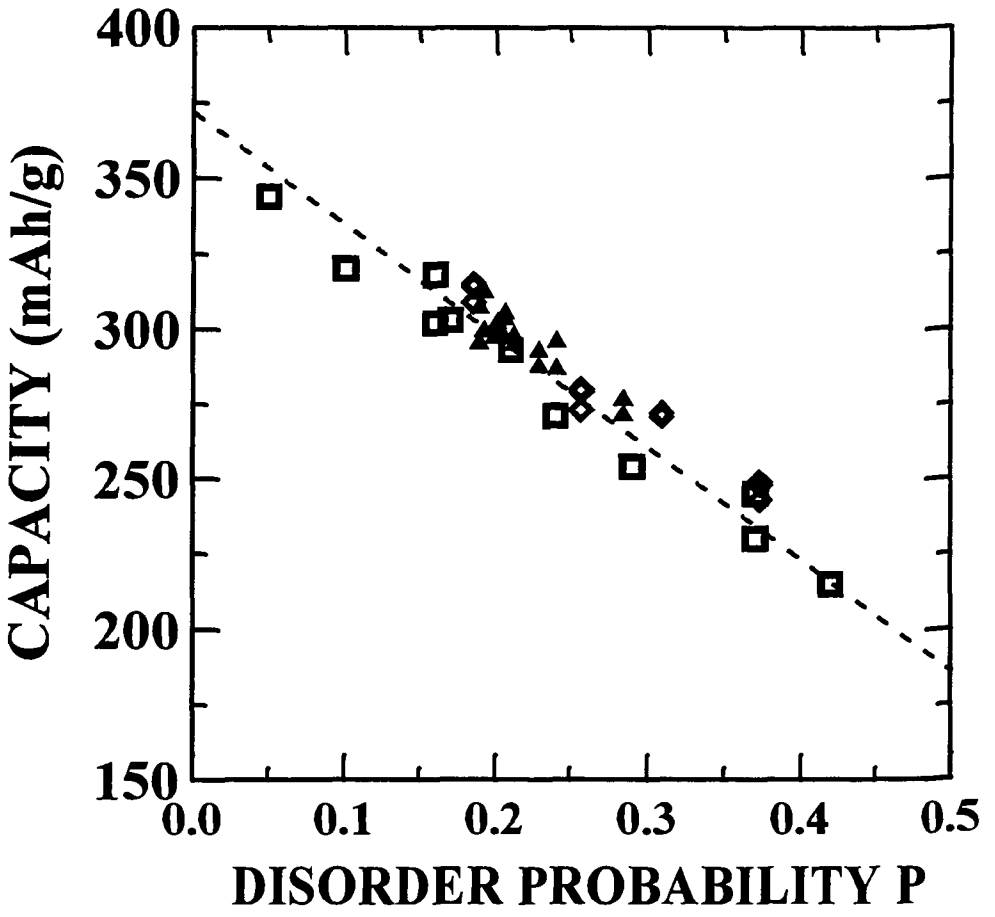

Figure 5-13. Capacities versus P for graphitic carbons. □: *included in table 5-1.* ◊ *and* Δ: *other carbons not included in table 5-1. The dashed line is a linear relationship described by* $x_{max}=1-P$.

Figure 5-12 shows voltage profiles, *V(x)*, for the second cycle of most of the graphitic carbon samples listed in table 5-1. The curves have been sequentially offset by

0.1 *V* for clarity. Most striking is a reduction of the maximum reversible capacity, x_{max}, as *P* increases. Most of this capacity loss is due to a shortening of the stage 2—stage 1 plateau.

Figure 5-13 shows x_{max} plotted versus *P* for all the carbons listed in table 1 and for many others. There is a linear relationship, well described by $x_{max}=1-P$, which is the straight line in the figure. This implies that little or no lithium is able to intercalate between randomly stacked parallel layers (Dahn, 1993). Therefore we call the space between these adjacent randomly stacked graphene layers, "blocked galleries".

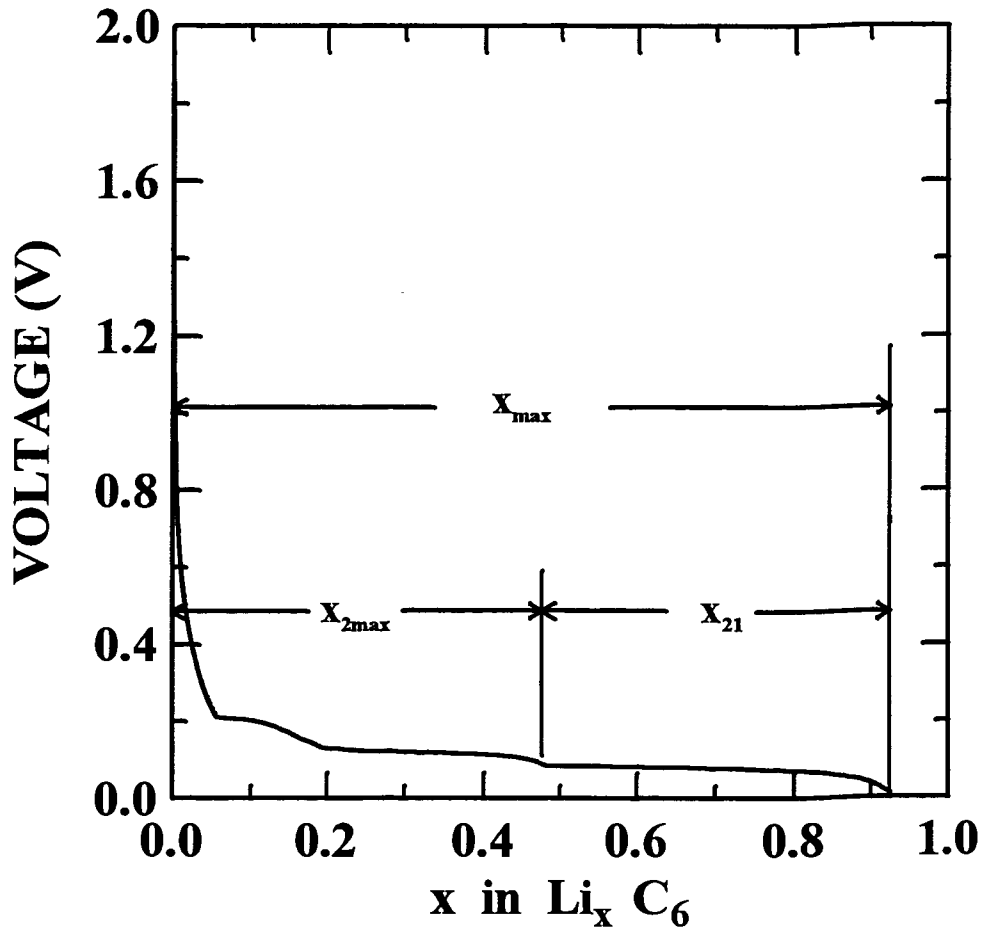

Figure 5-14. Schematically showing the definitions of the quantities x_{max}, x_{2max} and x_{21}.

Now it is time to analyze the results in figure 5-12 more carefully to learn about the length of the stage 2–stage 1 plateau, x_{21}, and the composition of stage 2 phase, x_{2max}. Figure 5-14 defines these quantities. Figure 5-15 shows x_{21} and x_{2max} plotted versus P for the carbon samples of table 5-1 and figure 5-12. Also shown is the prediction of the two models to be discussed later. It is clear that x_{2max} remains close to 0.5 independent of P, and that x_{21} is dramatically reduced as P increases. How can this be explained?

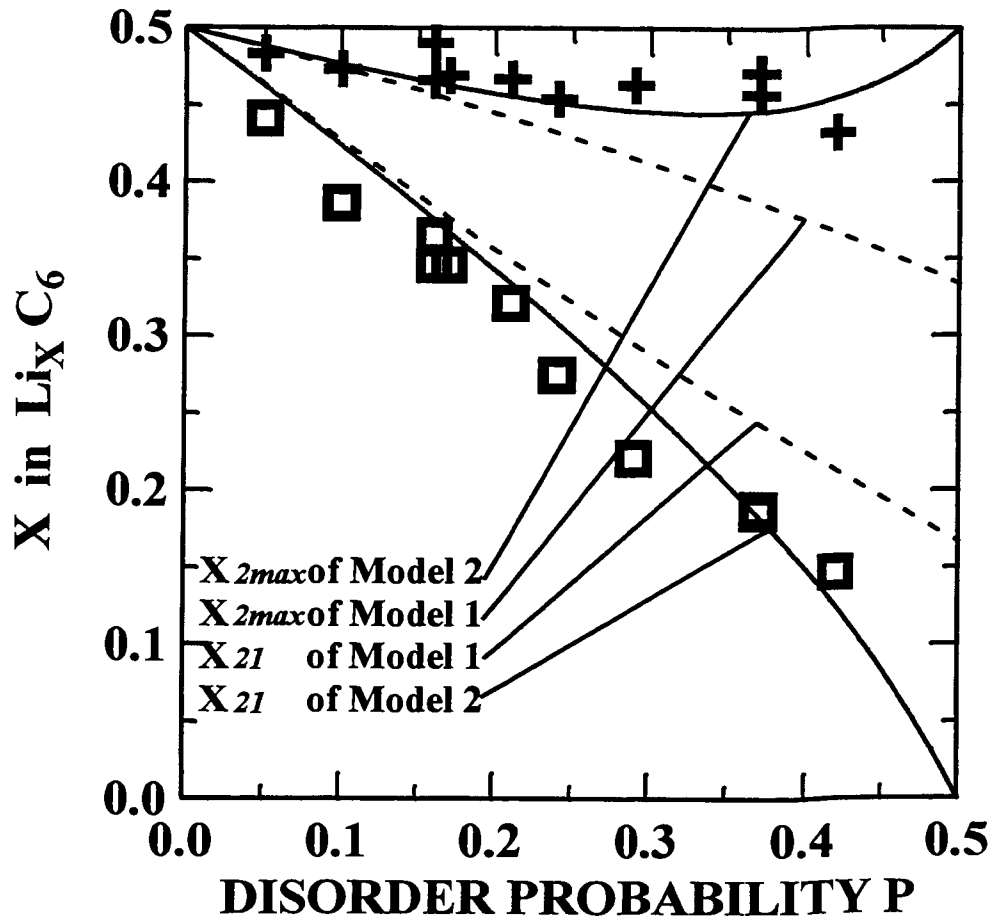

Figure 5-15. The variation of x_{2max} and x_{21} with P. Data points are from experiment. Dashed lines are for model 1 and solid lines are for model 2. □: experimental results for x_{21}; +: experimental results for x_{2max}.

The stage 2 phase forms because repulsion between intercalant islands in different layers make the lithium ions move as far apart as possible. When there are no blocked

galleries due to turbostratic disorder (P=0), the galleries are alternately full (F) and empty (E) as shown in figure 5-16a. As P increases, x_{max} decreases as $1-P$, suggesting that no lithium can be inserted within the galleries between turbostratic layers. We call these galleries blocked and designate them by B. We assume that at the stage 2 composition, full galleries cannot be adjacent. Then, figure 5-16b shows the stage 2 composition when P=0.33 for blocked galleries which are randomly positioned in the lattice. Figure 5-16c shows the situation for P=0.5.

MODEL 1: BLOCKED GALLERIES CAN BE ADJACENT

(a)		(b)		(c)	
F		B		B	
E		F		F	
F		E		E	
E		B		B	
F	P=0.0	F	P=0.33	B	P=0.5
E		E		F	
F	x_{2max}=0.5	F	x_{2max}<0.5	B	x_{2max}<0.5
E		E		F	
F		B		E	
E		B		B	
F		F		B	
E		E		F	

MODEL 2: BLOCKED GALLERIES NOT ADJACENT

(d)		(e)		(f)	
F		F		F	
E		E		B	
F		B		F	
E		F		B	
F	P=0.0	B	P=0.33	F	P=0.5
E		F		B	
F	x_{2max}=0.5	E	x_{2max}<0.5	F	x_{2max}=0.5
E		F		B	
F		E		F	
E		B		B	
F		F		F	
E		B		B	

F=Full Gallery, E=Empty Gallery, B=Blocked Gallery

Figure 5-16. : Schematic drawing of the stacking given by models 1 and 2 for the stage 2 phase when P=0.0, P=0.33 and P=0.5 as indicated.

Using a simple model (called model 1) we can predict the dependence of x_{2max} and x_{21} on P. We assume:

1) $x_{max}=1-P$ and no lithium is allowed in the blocked galleries;

2) Full galleries cannot be adjacent to full galleries;

3) The amount of lithium in the compound should be maximized subject to condition 2;

4) Blocked galleries are randomly positioned.

Using mathematical induction, and a matrix formalism, we obtain (see appendix 1)

$$x_{2max} = \frac{1-P}{2-P}, \text{ and } x_{21} = \frac{(1-P)^2}{2-P} = (1-P) - x_{2max}.$$

The details of the calculation are given in appendix 1. These expressions are plotted versus P in figure 15 as the dashed lines. The agreement is good at small P but poor as P becomes larger.

Since x_{2max} is near 1/2, even near P=0.5, we assumed next, without justification, that perhaps it is impossible for blocked galleries to be adjacent. This would mean that during the thermal treatment of soft carbon above 2100°C, turbostratic disorder is relieved in such a way that adjacent turbostratic defects are eliminated first, leaving a situation at P=0.5 where turbostratic shifts are found between every second set of adjacent layers. Figures 5-16d, e and f show the stage 2 compositions which would be obtained for P=0, P=0.33 and P=0.5 consistent with the assumption that blocked galleries cannot be adjacent. Notice that x_{2max}=1/2 when P=0.5 in this case.

We can calculate x_{2max} and x_{21} consistent with these assumptions (called model 2), which are:

1) $x_{max}=1-P$ and no lithium is allowed in the blocked galleries;

2) Full galleries cannot be adjacent;

3) Blocked galleries cannot be adjacent;

4) Blocked galleries are randomly positioned subjected to condition 3;

5) The amount of lithium in the compound should be maximized (as many full galleries as possible subject to the above conditions).

We find in this case (see appendix 1),

$$x_{2\max} = \frac{(1-P)^2}{2-3P}$$

and

$$x_{21} = (1-P) - x_{2\max} = \frac{(1-P)(1-2P)}{2-3P}.$$

These expressions are plotted as the solid lines in figure 5-15 and agree well with the data for $0 \leq P \leq 0.4$. This suggests that it is unlikely for blocked galleries to be adjacent!

If blocked galleries cannot be adjacent, then we expect a reasonably well ordered stage 2 structure to form when $P=0.5$ and $x_{2max}=0.5$. That is, superstructure peaks should be observable since the spacing between carbon layers bounding full and blocked galleries will differ. Using in-situ X-ray diffraction, we studied the MCMB2300 sample ($P=0.37$) carefully in the range near $x=0.5$.

The in-situ X-ray cell was equilibrated at V=0.100 *V*, corresponding to $x=0.47$ in figure 5-12 for the MCMB2300 charge curve. Figures 5-17a and b show the (002) peak for the carbon at $2\theta=25.1°$ and the (003) superlattice peak at $2\theta=38.2°$ due to the staged phase. The full width at half maximum of the superlattice peak is about 2° which corresponds to a correlation length for the staged order of about 40Å (obtained from Scherrer equation). If the blocked galleries were randomly arranged, it is unlikely that the correlation length could be so large. Therefore we believe that the blocked galleries tend not to be adjacent. This in turn, implies that turbostratic disorder in graphitic carbon is relieved in an unexpected way. That is, for *P* less than 0.5, it is unlikely to find two sequential layer pairs both with turbostratic shifts between them. The in-situ X-ray diffraction of the MCMB2300 cell will be carefully discussed later in this chapter.

The structure refinement program for graphitic carbons assumes that turbostratic shifts cannot be found between adjacent layer pairs because an *AB* stacked two-layer package is used as the basic unit in the model applicable to high temperature soft carbons. Based on our work above, it appears this assumption may be correct and perhaps this is part of the reason for the excellent agreement between the calculation and the data shown in figures 5-1 to 5-5.

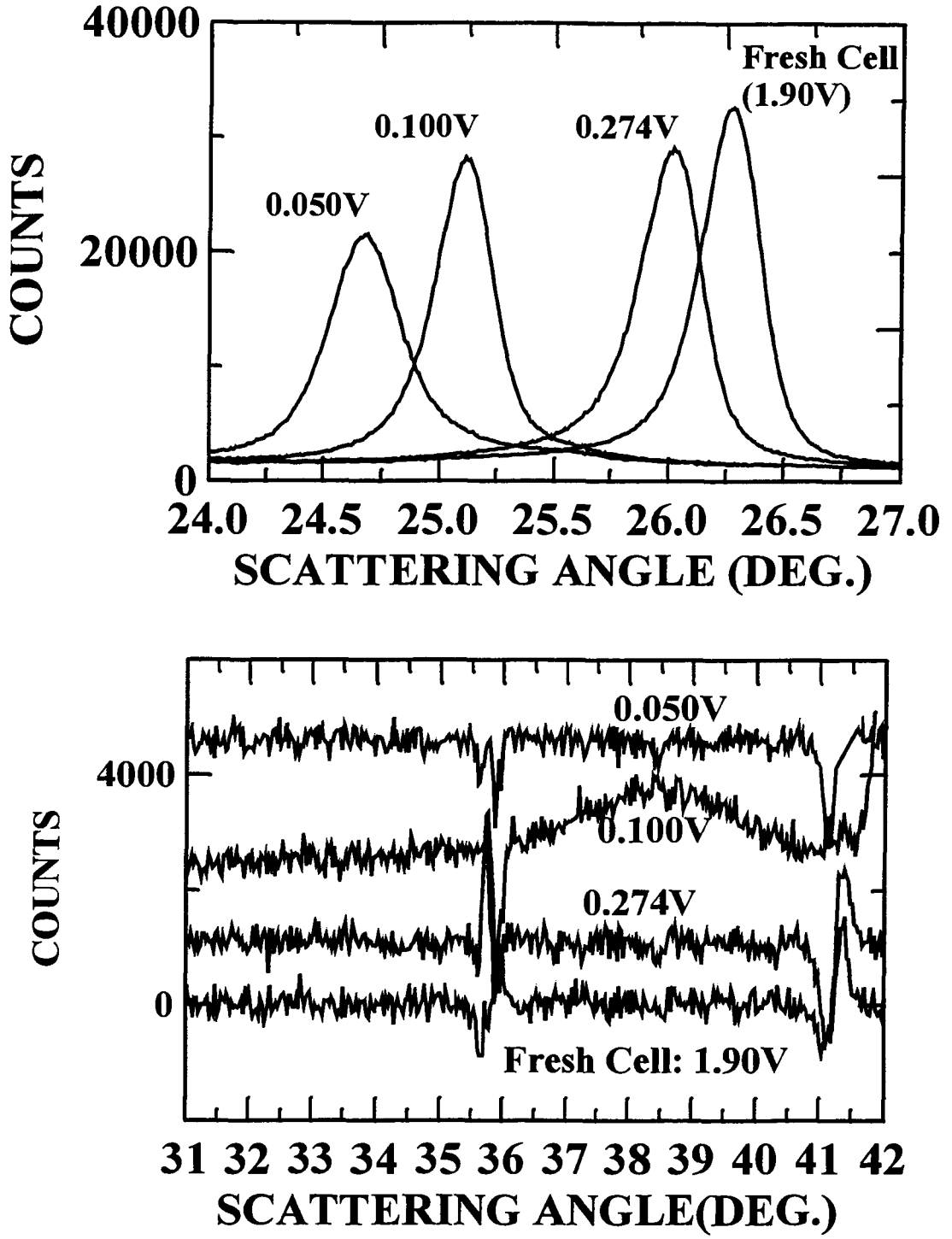

Figure 5-17. In-situ diffraction results at different voltages for the MCMB2300 sample. a) (002) Bragg peak, b) region of (003) superlattice peak (stage 2). The voltages correspond to the following phases: 1.90 V, no lithium added; 0.274 V, 1'; 0.100 V, stage 2; 0.050 V, stage 1. A second data set measured on the fresh cell has been subtracted from each of the data sets shown to reduce the background, and to eliminate peaks from Li (near 36.0°) and BeO (near 41.6°).

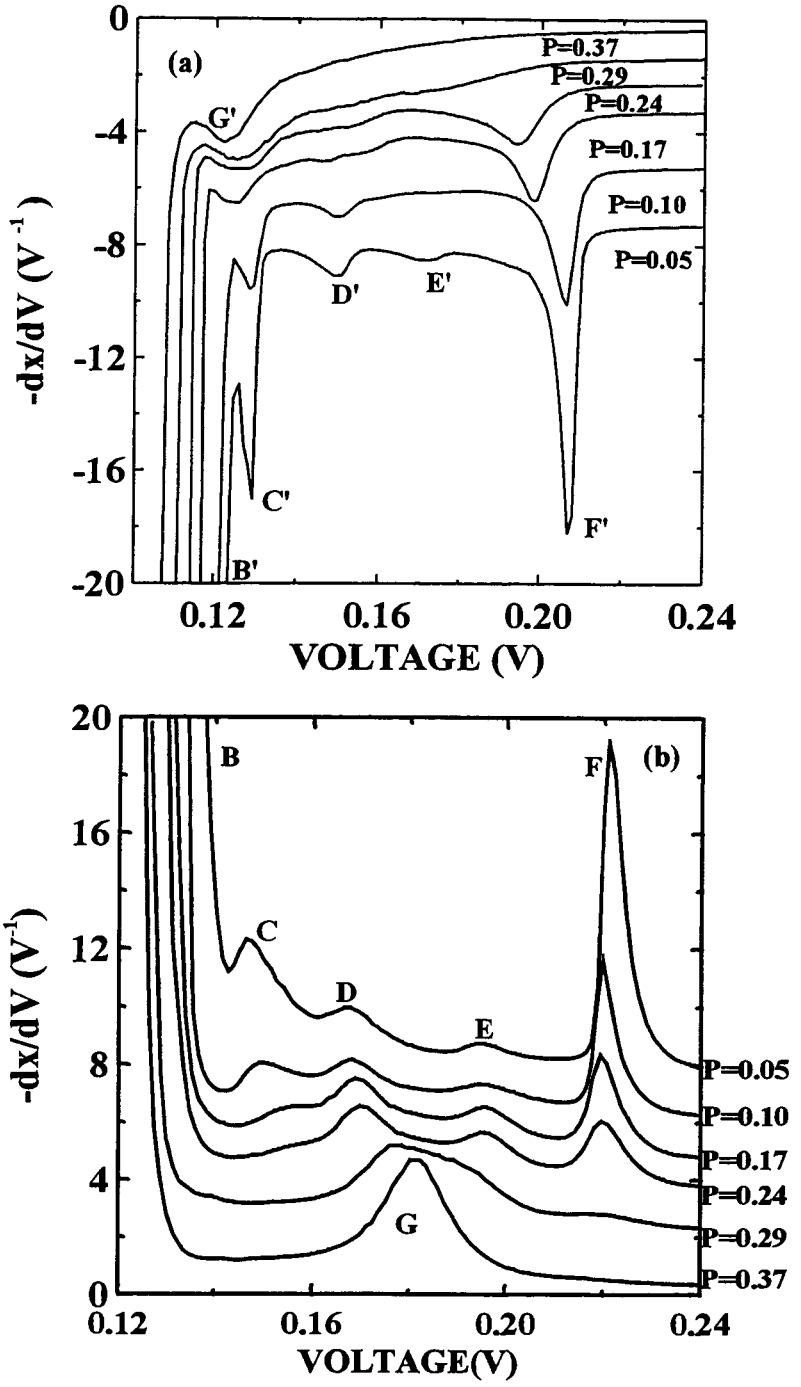

Figure 5-18. A portion of the derivative, $-dx / dV$ versus voltage corresponding to figure 5-12. The curves for MCMB2300, 2400, 2600, 2700, 2800 and JMI have been sequentially shifted for clarity. The shifts are $0V^{-1}$, $-1V^{-1}$, $-2V^{-1}$, $-3V^{-1}$, $-5V^{-1}$ *and* $-7V^{-1}$ *respectively for the discharge shown in figure 5-12a, and* $0V^{-1}$, $2V^{-1}$, $3.5V^{-1}$, $4.5V^{-1}$, $6V^{-1}$ *and* $7.5V^{-1}$ *respectively for the charge shown in figure 5-12b. The peaks for the JMI sample have been labeled. The peaks G' and G for MCMB2300 are also labeled.*

Based on the above results, we conclude as follows:

1) Lithium is not inserted in the Van der Waals space between layers which have a turbostratic shift between them. This conclusion was reached because $x_{max}=1-P$ was experimentally determined.

2) The majority of the reduction in x_{max} with P is caused by a reduction in the length of the stage 2–stage 1 plateau, x_{21}.

3) The composition of the stage 2 phase, x_{2max}, is weakly dependent on P. This can be explained if blocked galleries cannot be adjacent, which implies that turbostratic disorder is relieved in such a way that turbostratically stacked layers repel one another.

It is not surprising that it is difficult to insert lithium between parallel layers which are randomly stacked. When lithium intercalates between *AB* stacked layers, a shift to *AA* stacking occurs. It is likely that the turbostratically stacked layers are pinned by defects (which can only be removed near 2300°C!) preventing the rotation or translation to *AA* stacking. Thus, we can understand why x_{max} varies as $1-P$, the fraction of layers with *AB* registered stacking.

Lithium intercalation has proved useful in studying stacking disorder in host materials before. In 1984, Dahn and McKinnon (Dahn, 1984) showed how careful studies of the order-disorder transition in Li_xTaS_2 by electrochemical methods identified that stacking faults were present between about 10% of adjacent layer pairs. Our result suggesting that turbostratically aligned layer pairs repel one another during the graphitization process is an unexpected result and another example of the use of lithium intercalation as a probe of the disorder in the host.

5.4.2 Staging Phase Diagram of Lithium Intercalated Graphitic Carbons

5.4.2.1 Differential Capacities

The differential capacity, $-dx/dV$, plotted versus V corresponding to figure 5-12 is shown in figure 5-18 for both charge and discharge. The derivative curves change continuously as P varies. Peaks in $-dx/dV$ and plateaus in $V(x)$ occur at phase

transitions, so once we identify the transitions occurring, we can use electrochemical methods to determine the phase diagram (Berlinsky, 1979). We did in-situ x-ray measurements on the samples JMI, MCMB2700 and MCMB2300 to understand the peaks in figure 5-18.

For the synthetic graphite sample, JMI, the first in-situ x-ray measurement was made for the fresh cell. We then equilibrated the cell at sequentially smaller voltage points in the discharge direction. Dahn (Dahn, 1991a) reported earlier on another synthetic graphite material, KS-44 (obtained from Lonza Corporation). The JMI sample has smaller P than KS-44 ($P \approx 0.10$ for KS-44), and it gives sharper features in $-dx / dV$.

5.4.2.2 Studies of the Phase Transitions Using In-Situ X-Ray Diffraction

The in-situ cells were discharged or charged by Keithley 236 source-measure units. The cell was fixed at a voltage point and once the current decayed to less than 100 nA, a diffraction pattern was collected. Then the cell voltage was switched to a new value. We collected the in-situ X-ray data for the MCMB2700 and MCMB2300 samples using a Phillips diffractometer equipped with a copper target tube and a diffracted beam monochromator. The divergence slit was 0.5° and the receiving slit was 0.2 mm. Long counting times (120 seconds per point) were used to reduce noise and to get clear results for the superlattice peaks associated with the enlarged unit cell of the staged phases. An initial data set measured on the fresh cell was subtracted from each of the measurements of superlattice peaks at the different voltage points to eliminate spurious peaks from the cell holder itself. In particular, the metallic lithium anode of the cell gives a peak near 36°, which can still be seen in the subtracted data. We did very careful in-situ measurements on JMI graphite using the above Siemens D5000 diffractometer. The JMI in-situ cell was fixed on the sample holder of the diffractometer during the whole measurement process for a period of over three weeks. We used 0.75° divergence and

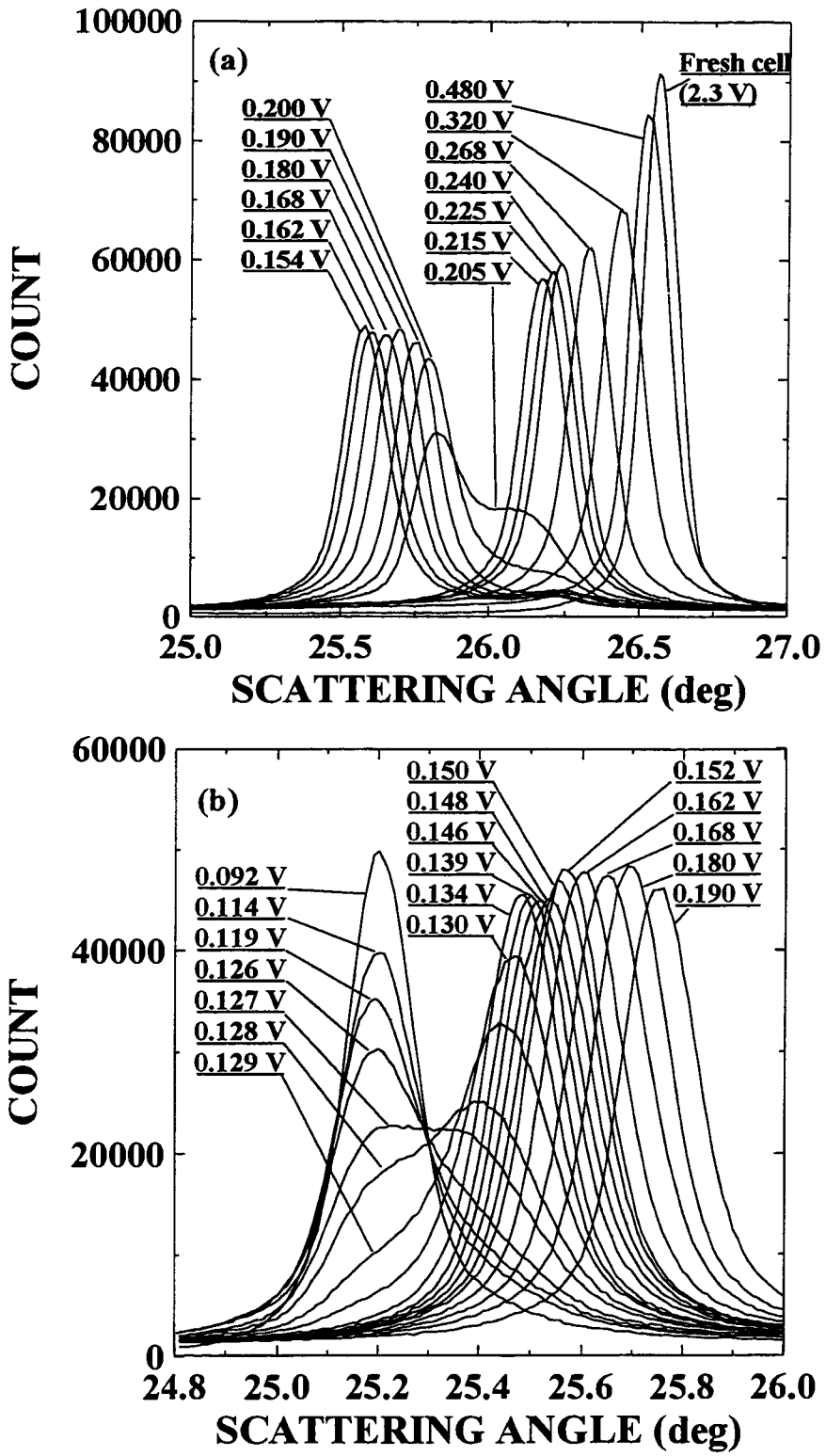

Figure 5-19. In-situ X-ray diffraction data for the (002) Bragg peak at different voltages during the discharge of the JMI sample. The cell voltage is indicated near each scan a) $V > 0.153$ volts and b) $V < 0.190$ volts.

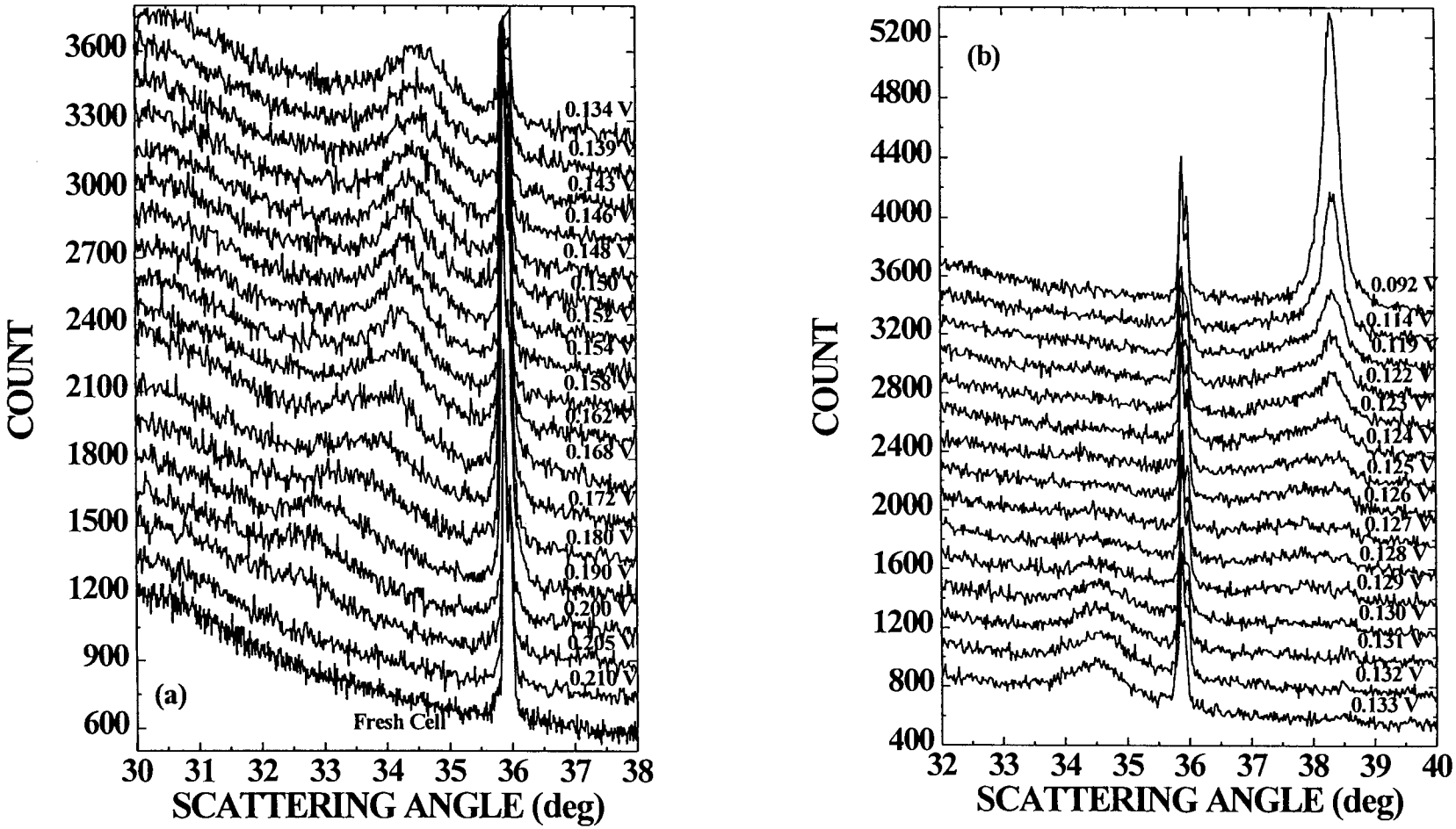

Figure 5-20. In-situ X-ray diffraction data for the superlattice peak at different voltages for the discharge of the JMI sample. The cell voltage is indicated near each scan. The scans have been sequentially offset for clarity. a) $V \geq 0.134$ volts and b) $V \leq 0.133$ volts.

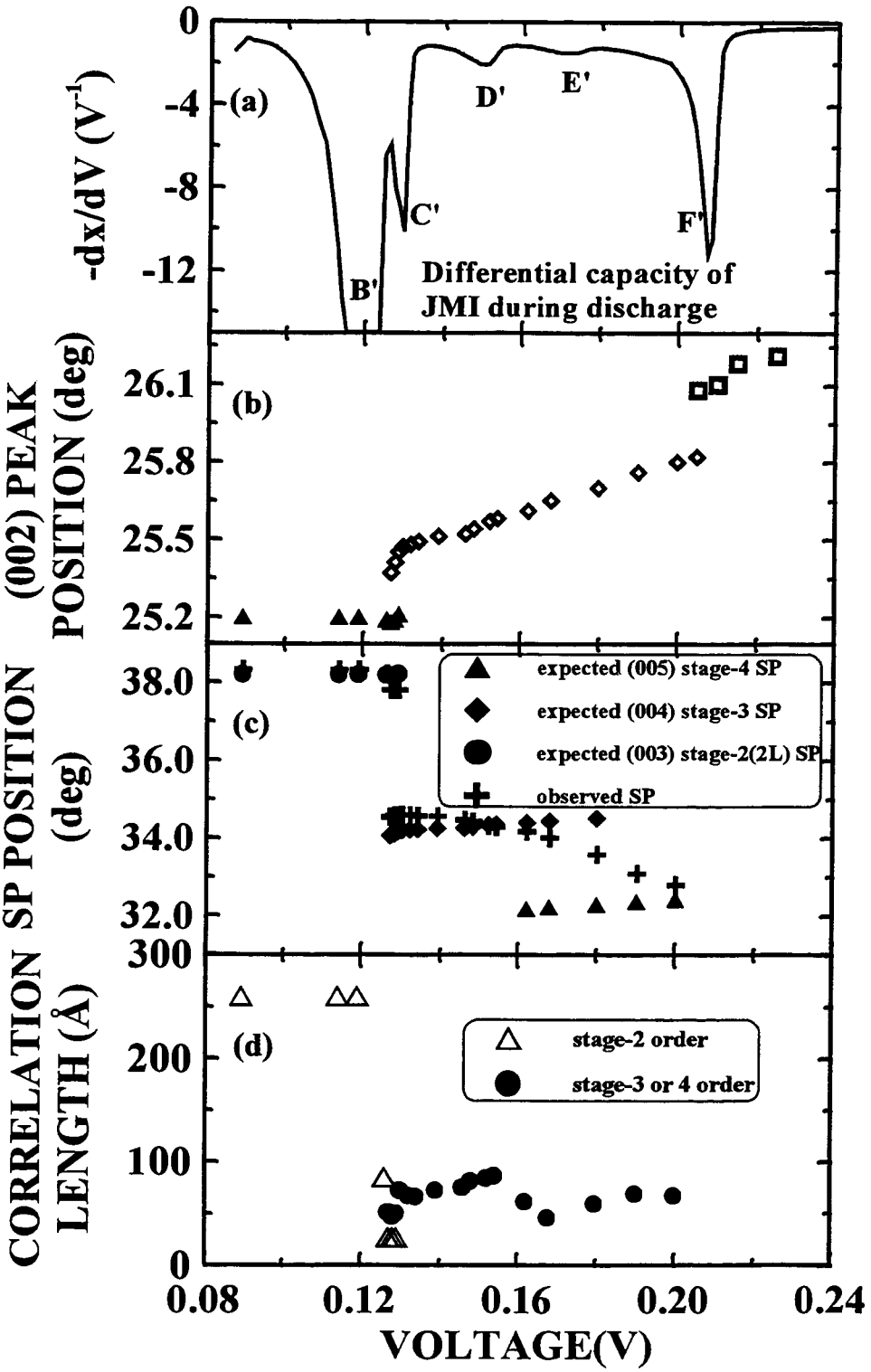

Figure 5-21. a) the differential capacity, b) the (002) peak position, c) the observed superlattice peak position and the expected superlattice peak positions for different staged phases as indicated, and d) the correlation length of the staged phases plotted as a function of cell voltage for JMI graphite, respectively.

Table 5-2. Summary of superlattice peaks for JMI during discharge.

Voltage (V)	x in Li_xC_6	(002) position* (±0.02°)	HWHM[+] of (002) peak	stage-4L (005) expected (±0.05°)	stage-3L (004) expected (±0.05°)	stage-2L or 2 (003) expected (±0.05°)	Observed SP**	HWHM of observed SP	CL*** of staged order (Å)	n[+++]
0.225	0.060	26.21°	0.08°							
0.215	0.064	26.18°	0.08°							
0.210	0.068	26.10°	0.09°							
0.205	0.104	26.08°, 25.82°	0.18°, 0.09°							
0.200	0.118	25.80°	0.09°	32.41°			32.78° ± 0.02°	0.61°	67	3.79
0.190	0.133	25.76°	0.09°	32.36°			33.08° ± 0.02°	0.59°	69	3.61
0.180	0.144	25.70°	0.09°	32.28°	34.50°		33.57° ± 0.03°	0.70°	59	3.35
0.168	0.158	25.65°	0.09°	32.22°	34.43°		34.00° ± 0.03°	0.90°	46	3.15
0.162	0.164	25.61°	0.09°	32.17°	34.38°		34.16° ± 0.02°	0.67°	61	3.08
0.154	0.172	25.58°	0.09°		34.34°		34.28° ± 0.02°	0.48°	86	3.02
0.152	0.175	25.57°	0.09°		34.32°		34.30° ± 0.02°	0.49°	84	3.01
0.148	0.181	25.54°	0.09°		34.28°		34.42° ± 0.02°	0.51°	81	2.95
0.146	0.184	25.52°	0.09°		34.25°		34.46° ± 0.02°	0.55°	75	2.93
0.139	0.192	25.51°	0.09°		34.24°		34.55° ± 0.02°	0.57°	72	2.90
0.134	0.197	25.49°	0.09°		34.21°		34.56° ± 0.02°	0.62°	66	2.89
0.132	0.200	25.48°	0.09°		34.20°		34.58° ± 0.02°	0.61°	67	2.88
0.130	0.210	25.47°	0.10°		34.19°		34.58° ± 0.02°	0.57°	72	2.87
0.129	0.216	25.45°, 25.21° (TP)[++]	0.12°, 0.11°		34.16°	38.21°	34.58° ± 0.02° for (004), 37.8° ± 0.5° for (003)	0.82°, 1.5°±0.5°	50, 27	2.86 2.07
0.128	0.225	25.41°, 25.19° (TP)	0.14°, 0.10°		34.10°	38.18°	34.57° ± 0.02° for (004), 37.8° ± 0.5° for (003)	0.88°, 1.5°±0.5°	47, 27	2.85 2.06
0.127	0.230	25.37°, 25.18° (TP)	0.16°, 0.10°		34.05°	38.17°	34.53° ± 0.04° for (004), 37.8° ± 0.03° for (003)	0.81°, 1.5°±0.5°	51, 27	2.84 2.06
0.126	0.234	25.19°	0.09°			38.18°	38.21° ± 0.03°	0.49°	85	2.00
0.119	0.338	25.20°	0.08°			38.20°	38.32° ± 0.02°	0.16°	260	1.98
0.114	0.418	25.20°	0.08°			38.20°	38.32° ± 0.02°	0.16°	260	1.98
0.092	0.479	25.20°	0.08°			38.20°	38.32° ± 0.02°	0.16°	260	1.98

*—Corrected for off-axis displacement of the cell electrode. [+]—Half width at half maximum.

**—Superlattice peak. [++]—Two (002) peaks merged.

***—Correlation length. [+++]—Stage number predicted by $2\theta_{(002)}$ and $2\theta_{(sp)}$.

antiscatter slits and a 0.2 mm receiving slit for all the in-situ measurements on the JMI specimen.

Figure 5-19 shows the scans over the (002) Bragg peak of the JMI cell at each voltage step during the discharge (adding lithium to the sample). The (002) peak position measures the average spacing between adjacent graphene sheets. Figure 5-20 shows the corresponding changes in the superlattice peaks which appear between $30° \leq 2\theta$ (scattering angle) $\leq 40°$. The superlattice peak (SP) gives information about staged phases (Dahn, 1991). A summary of the changes to the (002) peak and the superlattice peaks for the JMI sample during discharge is given in table 5-2. Peak positions and widths were obtained by least squares fits of pseudo-Voigt peaks to the data. The correlation lengths (CL) were obtained by applying the Scherrer equation, $CL = 0.89\lambda / (B\cos\theta_B)$. The instrumental resolution of about $\Delta(2\theta) = 0.12°$ was not deconvoluted from the measured peak widths.

When lithium was intercalated into JMI graphite above the first plateau in figure 5-12 (corresponding to peak F′ in figure 5-18), the (002) peak shifts smoothly towards small angle and no superlattice peaks are observed. This corresponds to a single phase region and lithium, at low concentration, is uniformly intercalated between all the graphene sheets. We call this region the stage-1' phase as discussed in section 5.3 of this chapter.

In an attempt to consolidate the information contained in figures 5-12, 5-18, 5-19 and 5-20 for the JMI sample, we plot the differential capacity, the (002) peak position, the observed superlattice peak position, and correlation length of the staged structure versus cell voltage in figures 5-21a through 5-21d respectively. Also plotted in figure 5-21c are the expected superlattice peak positions for the (005) peak from a stage-4 phase, the (004) peak from a stage-3 phase and the (003) peak from a stage-2 phase. These expected positions are derived from the (002) peak position $2\theta_{(002)}$, using the following equations

$$2\theta_{005} = 2 \cdot \sin^{-1}\left[\frac{5}{4} \cdot \sin\left(\left(2\theta_{002}\right)/2\right)\right] \quad (1),$$

$$2\theta_{004} = 2 \cdot \sin^{-1}\left[\frac{4}{3} \cdot \sin\left(\left(2\theta_{002}\right)/2\right)\right] \quad (2),$$

and

$$2\theta_{003} = 2 \cdot \sin^{-1}\left[\frac{3}{2} \cdot \sin\left(\left(2\theta_{002}\right)/2\right)\right] \qquad (3).$$

By comparing the measured superlattice peak position with those expected for the stage-4, stage-3 and stage-2 phases, we can determine which phases are present.

The superlattice peak indicating staged phases first appears below peak F′ in figure 5-21a. At 0.200 V, the peak is close to the position expected for pure stage-4. However, table 5-2 shows that the lithium composition is only $x = 0.118$ at this voltage, not $x = 0.25$ as expected for a filled stage-4 phase. As the voltage decreases further, the superlattice peak and the (002) peak shift continuously. At 0.180 V, the superlattice peak moves between the positions expected for pure stage-4 and 3 phases. So, it is believed that peak F′ corresponds to a transition from the stage-1′ phase to a mixed staged phase which includes both stage-4 and 3 orders. At 0.154 V, the superlattice peak is near the position expected for the pure stage-3. Between 0.180 V and 0.154 V, the material is best described as a mixed staged phase, containing regions of galleries hosting lithium separated by two or by three empty galleries. Apparently, the transition from stage-4 mixed with stage-3, near 0.180 V to stage-3, near 0.154 V is continuous. This may be caused by the presence of some turbostratic disorder ($P = 0.05$) in this sample.

Near 0.154 V, the correlation length of the staged phase shows a weak maximum (figure 5-21d). This coincides with the point where the superlattice peak position matches that expected for the pure stage-3. The lithium concentration at this point is $x = 0.172$ from table 5-2, not $x = 0.333$ expected for a filled stage-3 phase. As the voltage decreases to 0.130 V, the superlattice peak remains near the position expected for the stage-3 phase, but continues to shift slightly above the expected position for stage-3. This is due to an admixture of some stage-2 units within the predominantly stage-3 material. At 0.130 V, the composition is $x = 0.210$.

Why is the composition of the pure stage-3 phase so different from $x = 0.333$? The sites available for lithium within a gallery form a two-dimensional triangular lattice with a lattice spacing, $a \approx 2.45$ Å. However, at ambient temperature and pressure, lithium ions cannot occupy nearest-neighbor sites because of the Coulomb repulsion between them. Thus, the composition of a gallery is limited to 1/3 of the total number of sites.

The triangular lattice gas with large repulsive nearest-neighbor interactions is appropriate to describe the ordering which occurs in this system. For compositions less than 1/4 (at any temperature), the atoms randomly occupy sites on each of the three $\sqrt{3}a \times \sqrt{3}a$ superlattices, but for compositions larger than 1/4, they are found predominantly on one superlattice at low temperature (Schick, 1977; Berlinsky, 1979). We designate the random occupation of all superlattices as a liquid-like or L phase, like stage-4L, while the preferential occupation of one superlattice is designated as a "solid" phase like stage-3 or stage-2. For stage-4, we expect a liquid-like phase for values of x in Li_xC_6 less than 3/16, for stage-3, we expect a liquid-like phase for x less than 1/4 and for stage-2 we expect liquid-like phases for x less than 3/8.

Based on the argument above, the stage-4, the mixed stage-3 and 4 and the stage-3 phases are expected to have the lithium randomly occupying the three superlattices within each occupied gallery. Therefore, the region between 0.180 V and 0.154 V will be called the mixed stage-4L and 3L region, with predominantly stage-3L at 0.154 V. The region of peak F′ with voltage between 0.213 V and 0.180 V corresponds to the transition from stage-1′ to the above mixed phase. Although it is tempting to assign peak D′ in figure 5-21a to the stage-3L to 3 transition, this is unlikely because the composition only reaches about x = 0.200 at 0.132 V, below peak D′ and above peak C′. Based on the arguments above, we do not believe the solid stage-3 phase forms. The origin of peaks E′ and D′ are unknown.

As the cell voltage further decreases, peak C′ is encountered. Here, a two phase region is clearly observed, where stage-3L and stage-2L phases co-exist over a range of x. Figures 5-21b, 5-21c and 5-21d show that for three closely spaced voltages, peaks for the two phases could be simultaneously observed. Finally, the peak B′ is encountered, which is thought to correspond to the transition from the stage-2L phase to the solid stage-2 phase (Dahn, 1991a). The position of the superlattice peak is consistent with this interpretation.

The differential capacity of the MCMB2800 sample ($P = 0.10$) in figure 5-12

Table 5-3. Summary of superlattice peaks for MCMB2700 during charge.

Voltage (V)	x in Li_xC_6	(002) position* (±0.05°)	HWHM+ of (002) peak	stage-4L (005) expected (±0.05°)	stage-3L (004) expected (±0.05°)	stage-2L or 2 (003) expected (±0.05°)	Observed SP**	HWHM of observed SP	CL++ of staged order (Å)	n+++
0.239	0.066	26.26°	0.14°							
0.233	0.068	26.24°	0.14°							
0.228	0.071	26.23°	0.15°							
0.224	0.076	26.19°	0.18°							
0.219	0.095	26.01°	0.17°							
0.216	0.103	25.99°	0.15°	32.65°			33.98° ± 0.02°	2.02°	20	3.34
0.213	0.107	25.87°	0.14°	32.50°	34.73°		33.98° ± 0.02°	1.16°	35	3.27
0.204	0.119	25.85°	0.14°	32.47°	34.70°		34.03° ± 0.03°	1.15°	36	3.24
0.199	0.125	25.83°	0.14°	32.45°	34.68°		34.25° ± 0.03°	1.18°	35	3.15
0.192	0.140	25.78°	0.14°	32.38°	34.61°		34.54° ± 0.02°	1.02°	40	3.02
0.187	0.150	25.70°	0.14°		34.50°		34.59° ± 0.02°	0.80°	51	2.97
0.177	0.169	25.65°	0.14°		34.43°		34.79° ± 0.02°	0.74°	56	2.88
0.173	0.177	25.61°	0.15°		34.38°		35.00° ± 0.02°	0.62°	67	2.80
0.170	0.185	25.56°	0.16°		34.31°		35.07° ± 0.02°	0.71°	58	2.76
0.166	0.200	25.44°	0.17°		34.15°	38.57°	35.09° ± 0.02° for (004), 38.28°± 0.05° for (003)	1° to 2°, 1° to 2°	27, 28	2.71 2.04
0.160	0.215	25.36°	0.16°		34.04°	38.45°	38.13° ± 0.02°	0.80°	52	2.05
0.156	0.224	25.35°	0.15°		34.02°	38.43°	38.06° ± 0.02°	0.75°	55	2.06
0.151	0.233	25.29°	0.14°		33.94°	38.34°	38.07° ± 0.02°	0.70°	59	2.04
0.145	0.244	25.27°	0.13°		33.91°	38.31°	38.03° ± 0.02°	0.64°	59	2.04
0.134	0.287	25.25°	0.13°		33.89°	38.28°	38.06° ± 0.02°	0.61°	68	2.03
0.130	0.361	25.28°	0.13°			38.32°	38.33° ± 0.02°	0.60°	69	2.00
0.128	0.424	25.30°	0.13°			38.35°	38.37° ± 0.04°	0.60°	69	2.00
0.120	0.469	25.29°	0.13°			38.34°	38.43° ± 0.02°	0.54°	77	1.99
0.093	0.540	25.25°	0.17°			38.28°	38.51° ± 0.02°	0.63°	66	1.97

*—Corrected for off-axis displacement of the cell electrode. **—Superlattice peak.
+—Half width at half maximum. ++—Correlation length. +++—Stage number predicted by $2\theta_{(002)}$ and $2\theta_{(sp)}$.

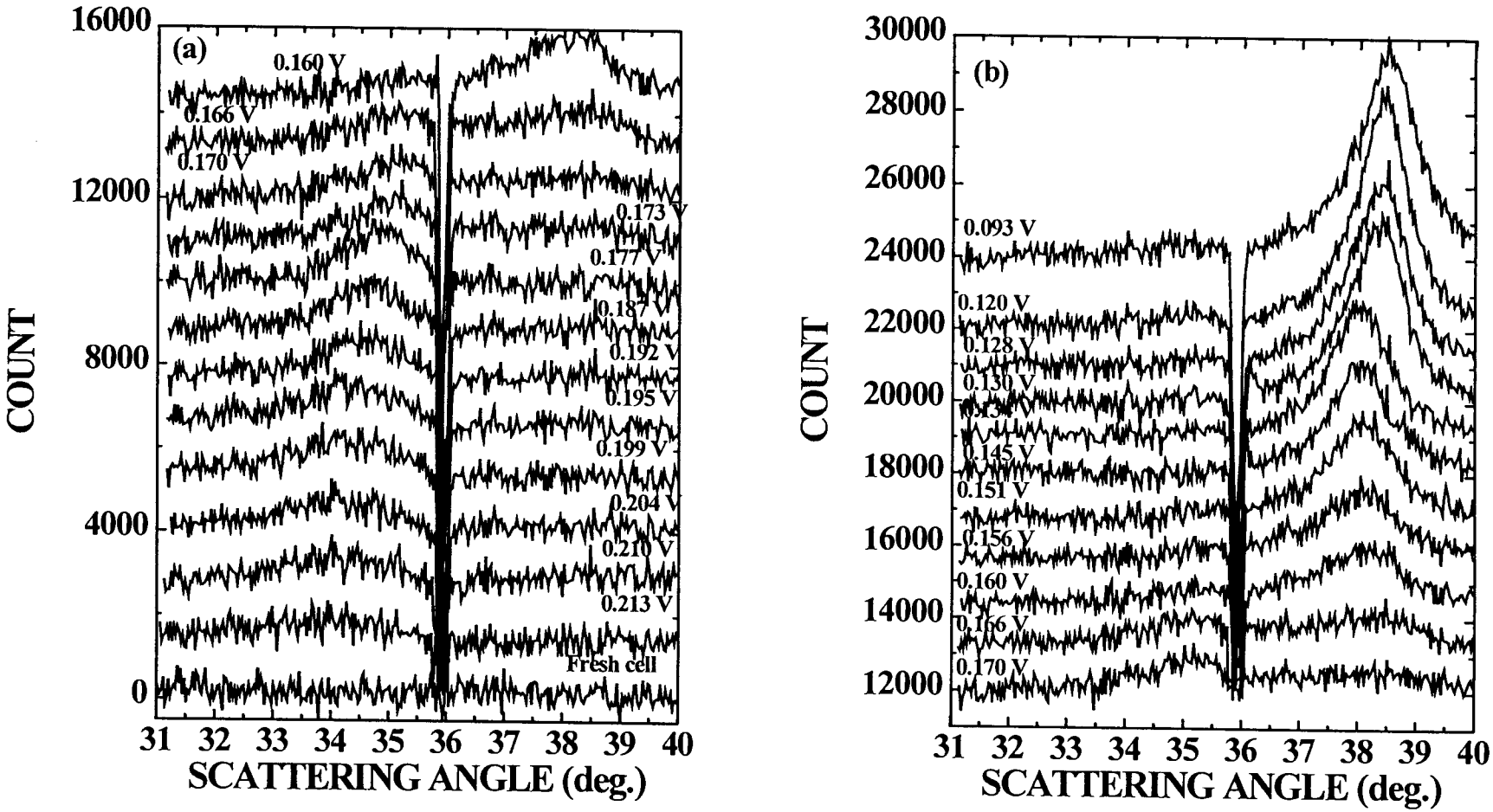

Figure 5-22. In-situ X-ray diffraction results for the superlattice peak at different voltages as indicated for the charge of the MCMB2700 sample. a) $V \geq 0.160$ volts and b) $V \leq 0.170$ volts. The scans have been sequentially offset for clarity.

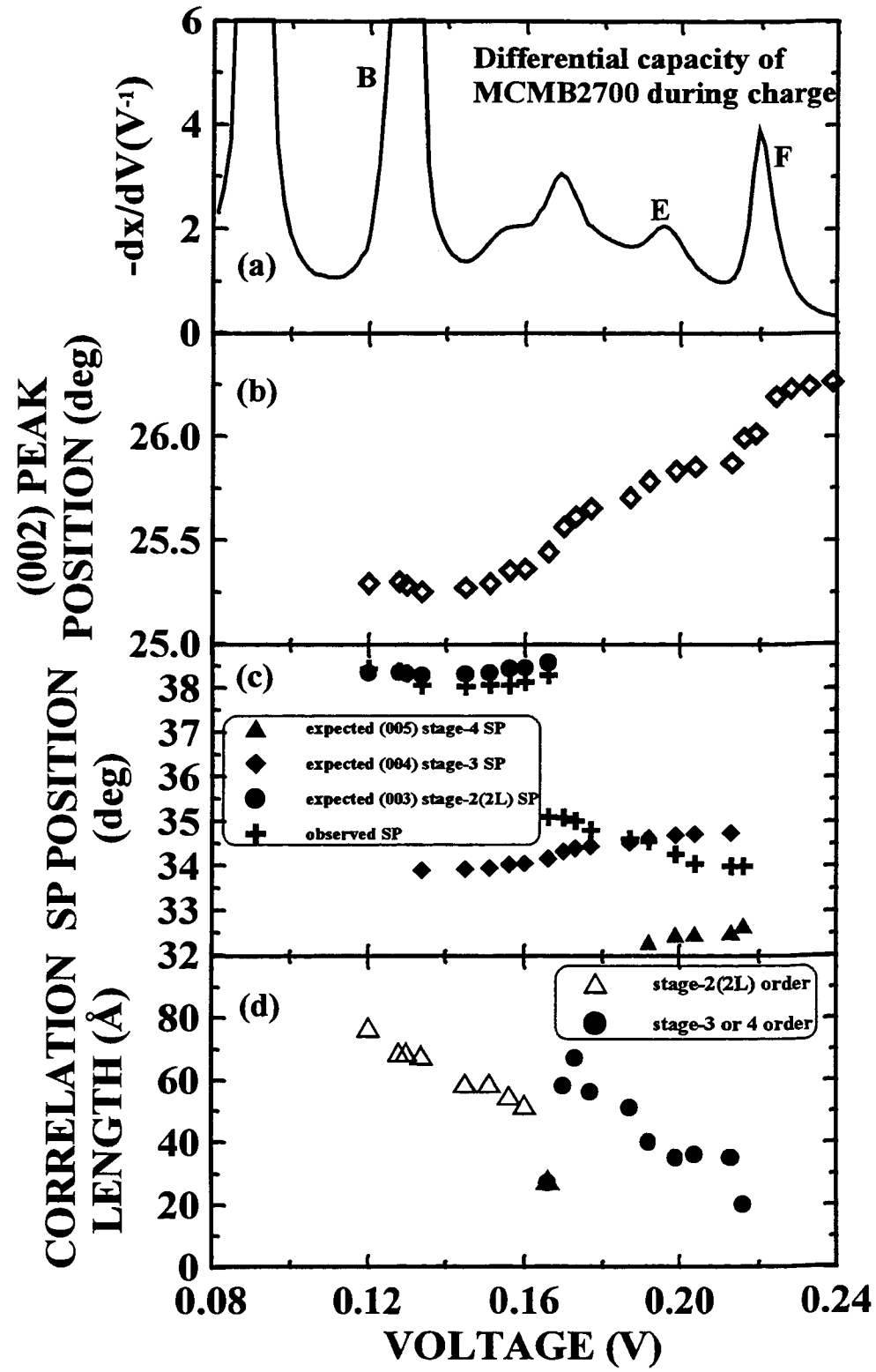

Figure 5-23. a) the differential capacity, b) the (002) peak position, c) the observed superlattice peak position and the expected superlattice peak positions for different staged phases as indicated, and d) the correlation length of the staged phases plotted as a function of cell voltage for the MCMB2700 sample, respectively.

shows similar characteristics compared to the JMI sample, except the peaks corresponding to the phase transitions are weaker. The synthetic graphite material, KS-44 with a similar P, was studied carefully before (Dahn, 1991a), and we will incorporate those results in the staging phase diagram in the P-x plane.

We next consider the results of in-situ X-ray measurements during the charge of the MCMB2700 sample ($P = 0.17$). Table 5-3 gives the measured (002) and superlattice peak positions and half widths versus cell voltage and lithium concentration x. The expected superlattice peak positions are also given. Figures 5-22a and 5-22b show the superlattice peak as a function of cell voltage and figure 5-23 consolidates all the information for the MCMB2700 sample, just as figure 5-21 did for JMI graphite. We can now clearly observe many of the effects of increased P. Even though the data in figures 5-22 and 5-23 is for the charge part, we start our description from high voltage, as we did for the JMI sample.

Above peak F, there is no evidence for superlattice peaks and the material is in the stage-1′ phase. Peak F corresponds to a transition from a staged phase to the stage-1′ phase. Figure 5-23c shows that the phases at 0.216 V are co-existing stage-1′ and mixed stage-3L, 4L phases. For this sample, the mixed stage-3L, 4L phase has more stage-3L character than stage-4L. As the voltage decreases below 0.216 V, the superlattice peak moves toward the position of pure stage-3, which is reached near 0.187 V. Below 0.187 V, the superlattice peak shows a small amount of stage-2L character mixed with stage-3L character, since its position is above the angle expected for pure stage-3L. The sharp peak encountered near 0.166 V during charge in figure 5-23a, corresponds to the transition from stage-2L to a phase predominantly made up of stage-3L. This is clearly shown by the behavior of the superlattice peak in this voltage range in figure 5-23c. Finally, the peak B corresponds to the solid stage-2 to liquid-like stage-2L transition.

The correlation length of the staged phases is always less than 80Å, even in the solid stage-2 phase. By contrast, the correlation length of the solid stage-2 phase for the JMI sample was at least 250Å. Presumably this difference is caused by the increased number of blocked galleries which are present in the MCMB2700 sample compared to the JMI graphite.

Table 5-3 and figure 5-23b show that the (002) peak moves smoothly for the MCMB2700 sample. There are no voltages or compositions where co-existing phases with different (002) plane spacings are observed. Instead, the width of the (002) peak increases slightly in those regions where co-existing phases with different (002) spacings were observed for the JMI sample. These increases in (002) peak width occur near peak F (near 0.22 V) and near the sharp peak in figure 5-23a at 0.166 V.

One major difference between the MCMB2700 and JMI samples is that the former shows no superlattice peak for a pure stage-4L order. However, the peaks F in figure 5-18 for samples JMI and MCMB2700 are similar in shape, although the peak for MCMB2700 is reduced in intensity compared to the peak for the JMI sample. Peaks F and F′ correspond to a transition between a mixed stage-3L, 4L phase and a dilute stage-1 phase. The proportion of stage-4L sequences in the mixed staged phase is reduced as P increases, which apparently weakens the strength of the transition. We expect increases in the number of blocked galleries to frustrate the formation of higher stages before lower stages. The blocked galleries can interfere with the sequence of full and empty galleries by being positioned where a full gallery is needed. Since the interactions which cause the formation of the staged phases become weaker with stage number (Safran, 1980), the blocked galleries will frustrate the higher stages first. We believe this is why the superlattice peak for pure stage-4L order is absent for MCMB2700, even though it is present for the JMI sample.

In figure 5-18, the differential capacity of the MCMB2600 sample ($P = 0.24$) is similar to that of the MCMB2700 sample. Though the phase transition peaks tend to be weaker and broader for the MCMB2600 sample, the positions of the peaks are coincident. We believe that the phase transitions are similar for both samples. As P increases, peaks C′, D′, E′, F′, and peaks C, D, E, F vanish, while new peaks G′ and G appear respectively in the discharge and the charge for samples heated at 2400 and 2300°C. This emphasizes that the attributes of materials heated at 2400 and 2300°C are different from those of graphitic carbons heated at higher temperatures. The MCMB2300 sample with $P = 0.37$ has similar but sharper features compared with MCMB2400 ($P = 0.29$). We decided to study the MCMB2300 sample (Zheng, 1995b) next and the results are presented in table

5-4. Figure 5-24 shows in-situ X-ray diffraction scans over the region of the superlattice peak as the voltage of the cell was stepped sequentially upward. Figure 5-25 shows $-(dx/dV)$, the (002) peak position, the superlattice peak position and the correlation length of the staged phase as a function of voltage. Figure 5-25c also shows the expected (003) superlattice peak position of the stage-2 or 2L phase.

Figure 5-25a shows that $-(dx/dV)$ differs dramatically from that for JMI or MCMB2700. Figures 5-24 and 5-25c show that peak G corresponds to a transition from a stage-2L phase to a stage-1′ phase. The transition appears continuous, because the (002) peak moves smoothly and the superlattice peak intensity vanishes smoothly. However, we believe the transition is really a first-order one broadened by disorder, because the peaks G and G′ in figure 5-18 show large hysteresis in voltage. This hysteresis would not be expected for a continuous transition.

The peak B for MCMB2300 is again consistent with a transition between phases with predominantly stage-2 character. We identify it with the solid stage-2 to liquid-like stage-2L transition.

The correlation lengths in figure 5-25d are even smaller than those for the MCMB2700 sample. The maximum correlation lengths appear when the superlattice peak is closest to the position expected for pure stage-2.

To understand the phase transitions which occur during the intercalation of lithium in graphitic carbon samples, we consider the variation of the average stage number, n, as a function of x in Li_xC_6. The average stage number is defined here by

$$\frac{n+1}{n} d_{(sp)} = d_{(002)} \qquad (4).$$

Solving for n, we obtain,

$$n = \frac{\sin(\theta_{(002)})}{\sin(\theta_{(sp)}) - \sin(\theta_{(002)})} \qquad (5),$$

where the subscripts (sp) and (002) correspond to the observed superlattice and (002) peaks respectively. Therefore n can be calculated from the positions of the observed

Table 5-4. Summary of superlattice peaks for MCMB2300 during charge.

Voltage (V)	x in Li_xC_6	(002) position* (±0.02°)	HWHM^{+} of (002) peak	stage-2L or 2 (003) expected (±0.03°)	Observed SP** (±0.03°)	HWHM of observed SP	CL^{++} of staged order (Å)	n^{+++}
0.238	0.090	26.15°	0.16°					
0.208	0.106	26.01°	0.16°					
0.188	0.134	25.83°	0.17°					
0.177	0.183	25.55°	0.18°	38.74°	37.81°	3.18°	13	2.15
0.167	0.213	25.41°	0.16°	38.53°	38.04°	1.21°	34	2.08
0.160	0.225	25.35°	0.16°	38.43°	38.11°	1.24°	34	2.05
0.150	0.239	25.32°	0.15°	38.38°	37.91°	0.97°	43	2.07
0.136	0.258	25.31°	0.15°	38.37°	37.98°	1.16°	36	2.06
0.120	0.405	25.26°	0.15°	38.29°	38.76°	1.66°	25	1.93
0.100	0.477	25.24°	0.15°	38.26°	38.92°	1.36°	31	1.91
0.078	0.577	24.97°	0.21°					
0.049	0.635	24.83°	0.19°					

*—Corrected for off-axis displacement of the cell electrode. **—Superlattice peak.
$^{+}$—Half width at half maximum. $^{++}$—Correlation length.
$^{+++}$—Stage number predicted by $2\theta_{(002)}$ and $2\theta_{(sp)}$.

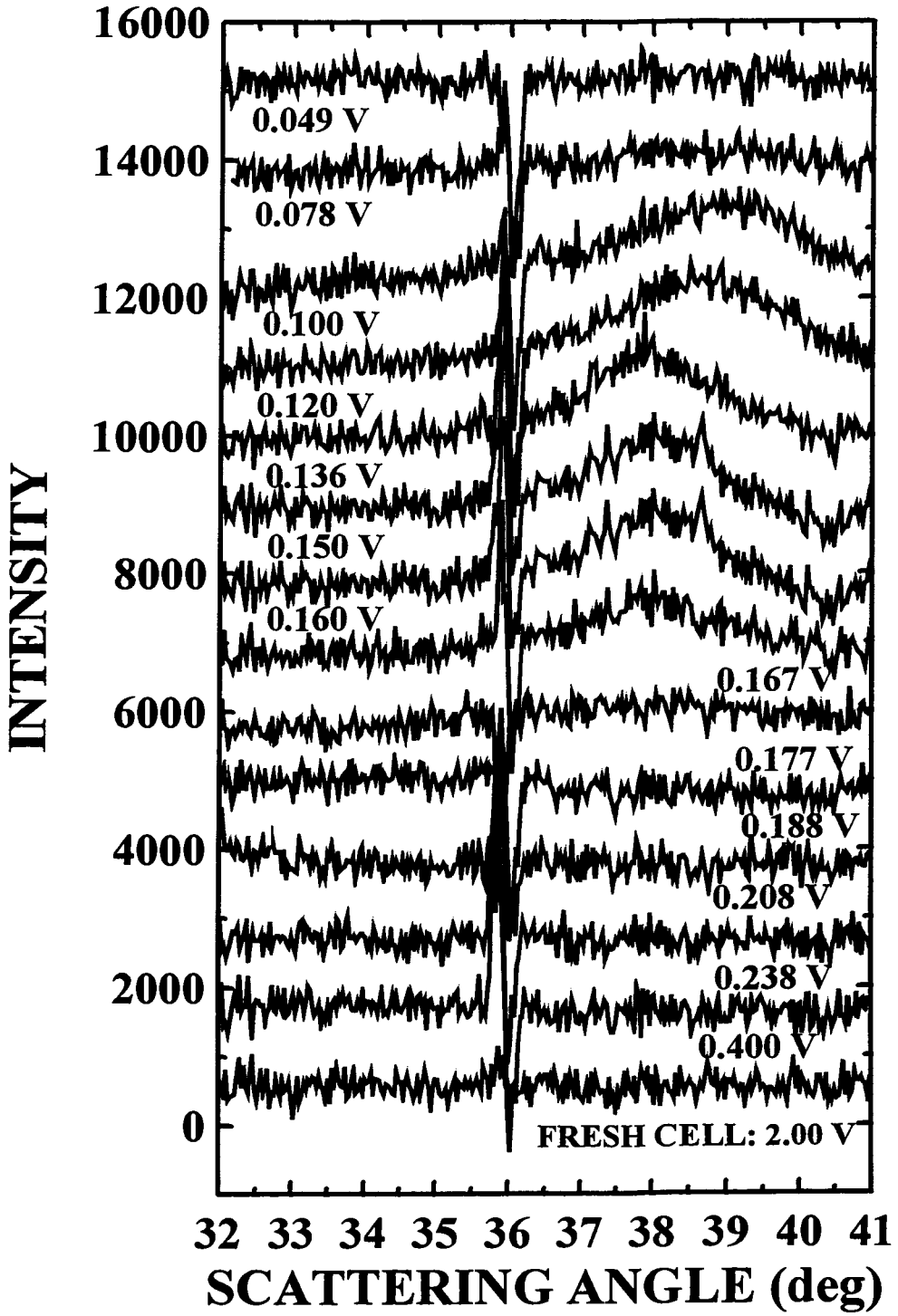

Figure 5-24. In-situ X-ray diffraction results for the superlattice peak at different voltages during the charge of the MCMB2300 sample. The scans have been sequentially offset for clarity.

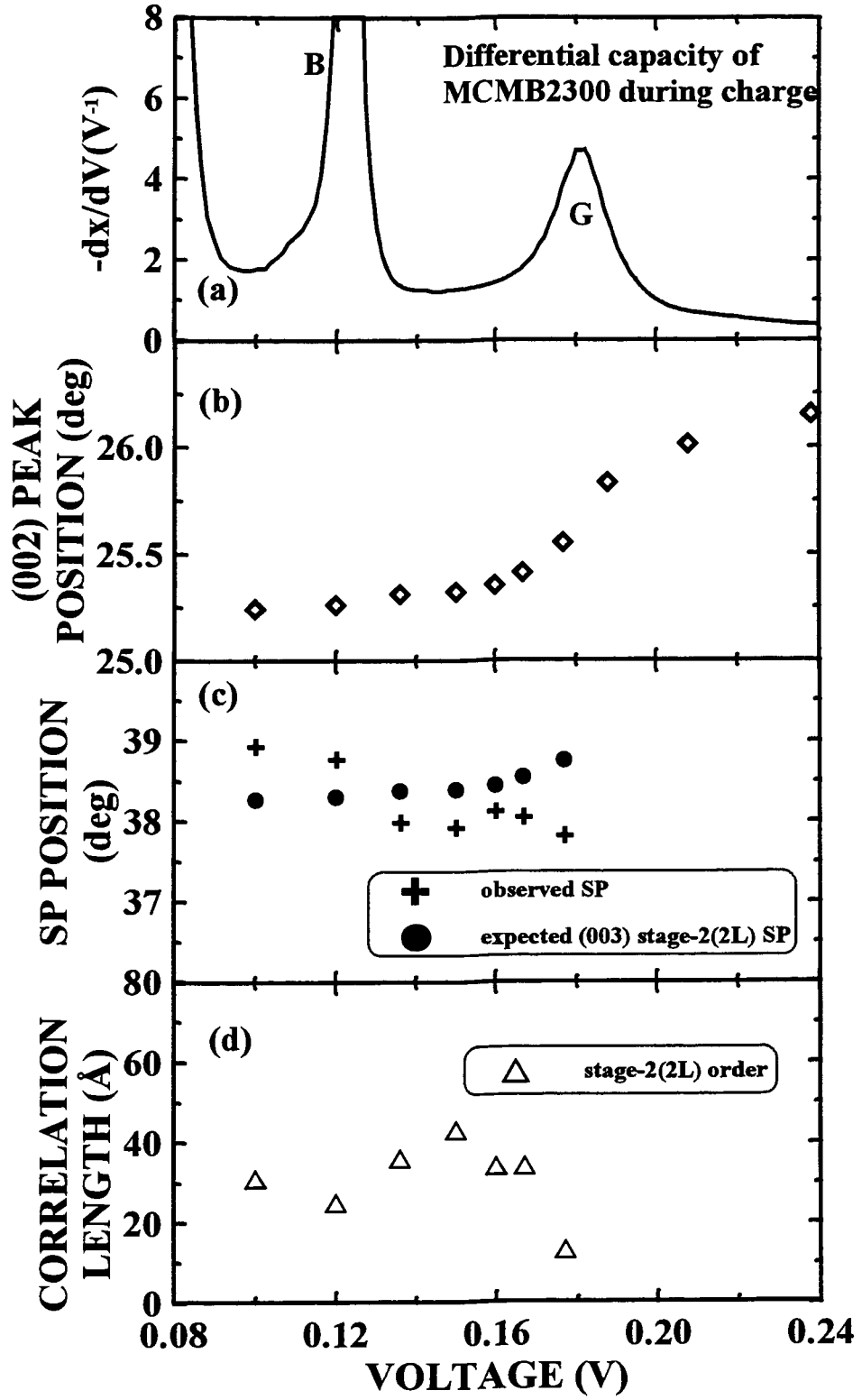

Figure 5-25. a) the differential capacity, b) the (002) peak position, c) the observed superlattice peak position and the expected superlattice peak position for a stage-2 or 2L phase, and d) the correlation length of the staged phase plotted as a function of cell voltage for the MCMB2300 sample, respectively.

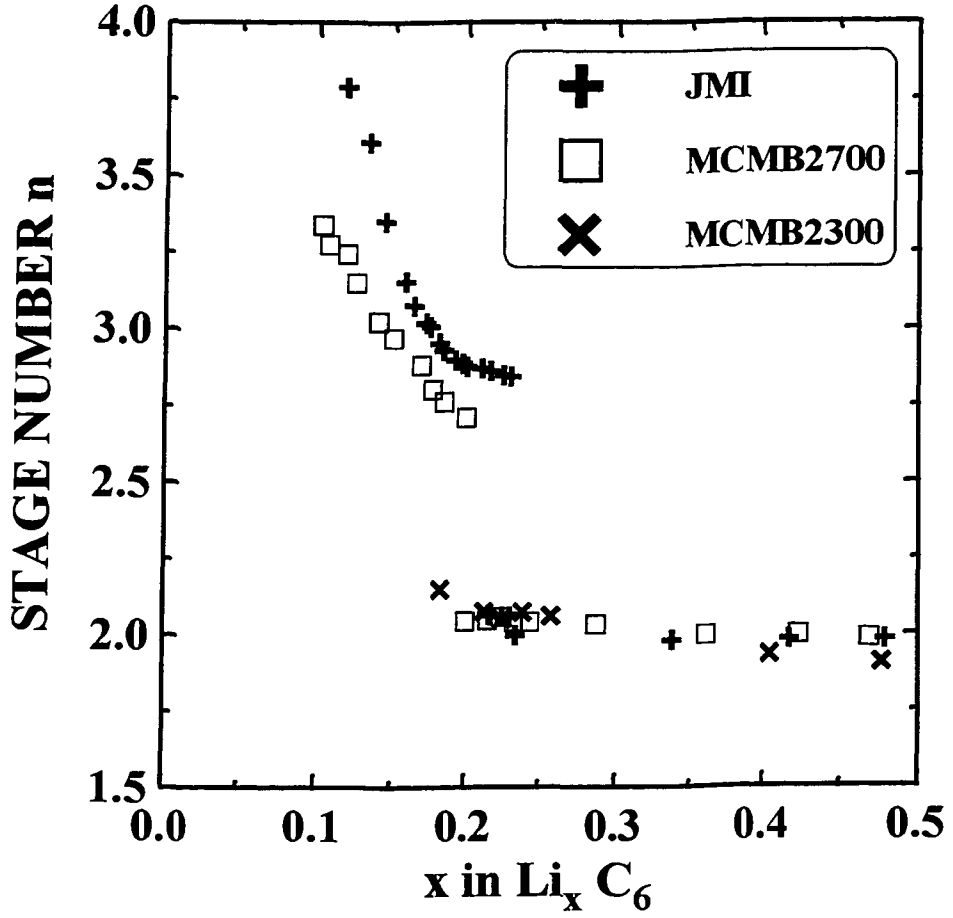

Figure 5-26. The average stage number, n, plotted as a function of x in Li_xC_6 for the JMI sample during discharge, and for MCMB2700 and MCMB2300 samples during charge, respectively.

(002) and superlattice peaks. The average stage numbers for the JMI sample measured during discharge, and for the MCMB2700 and MCMB2300 samples measured during charge have been calculated and are listed in tables 5-2, 5-3 and 5-4 respectively. Figure 5-26 shows n versus x for JMI during discharge, and MCMB2700 and MCMB2300 during charge. For JMI, the superlattice peak begins to appear with n approximately equal to 3.79, which means that the stage-1′ phase co-exists with a staged phase with predominantly stage-4L order. This is consistent with what we had described earlier above. Then n changes in a more or less smooth way as x in Li_xC_6 increases up to $x \approx 0.210$. Then n changes from 3 to 2 when the transition between stage-3L and 2L

phases occurs. The stage number stays at about $n = 2$ during the transition from stage-2L to stage-2. One difference between the JMI and MCMB2700 samples is that the latter first begins to show a superlattice peak with $n = 3.34$, much smaller than $n \approx 3.8$ for the JMI sample. This corresponds to the mixed stage-3L, 4L order. Then n decreases smoothly to near $n \approx 2.7$ and the transition to stage-2L occurs. For MCMB2300, the stage number at $x = 0.183$ during charge is larger than 2, then it continuously decreases to slightly below 2 as x increases. Stage-2L and stage-2 orders are predominant in the MCMB2300 sample.

5.4.3 Phase Diagram and Conclusions

It is now possible to summarize the effects of increases in P on the staged phases which form in lithium intercalated graphite (Zheng, 1996b). As P increases, higher stages are eliminated first. Based on the electrochemical data in figure 5-18, for $P \geq 0.30$, the peaks F and F′ are eliminated and the mixed staged phase (stage-3L, 4L) no longer forms. For higher P, the peaks G and G′ are formed and only the stage-1, stage-2, stage-2L and dilute stage-1 phases exist. The correlation length of the staged sequence decreases as P increases, as we expected.

Figure 5-27 shows our attempt to place this information on a staging phase diagram for Li_xC_6 in the P-x plane at room temperature. Figure 5-27a is for samples produced as lithium is intercalated (discharge) and figure 5-27b is for samples produced as lithium is removed (charge). The electrochemical information in figures 5-12 and 5-18 and the in-situ X-ray diffraction data presented throughout this paper have been used to construct this diagram, as described below.

The peaks in the differential capacity curves in figure 5-18 represent coexisting phases. For the discharge (figure 5-12), the first point where $^{dx}/_{dV}$ near peak F′, begins to deviate from the background, is the end point of the pure stage-1′ phase. The phase labeled M represents the mixed stage-3L, 4L phase. The area under the peak F′ during discharge or F during charge is the width of the stage-1′—M coexistence region. The

single-phase regions of stage-2L, 2, and stage-1 phases are narrow, of maximum width $\Delta x = 0.03$; these are denoted as heavier lines in figure 5-27. The x positions of these single-phases are determined from the compositions corresponding to the minima in $^{dx}/_{dV}$ between peaks corresponding to coexisting phases in figure 5-18. The minimum point at the left base of peaks F or F′ in figure 5-18 gives the low x composition of the M phase. Peaks C and C′ correspond to a phase transition between phase M and stage-2L. Their area can be used to extract the width of the two-phase regions. The minimum point between peaks C and B or C′ and B′ corresponds to the composition of the line phase of stage-2L. By considering the compositions of the positions of the minima in $^{dx}/_{dV}$ and the area of the peaks in $^{dx}/_{dV}$ in this way, the phase diagram can be determined. Data from reference 40 were used to identify the peaks in MCMB2800, which has a similar P to KS-44.

When P is small ($P \leq 0.10$), the transition from stage-1′ to M is to a phase which is predominantly stage-4L. As P increases, the amount of stage-3L in this phase increases. Eventually, even stage-3L cannot form (near $P = 0.3$) and the mixed staged phase, M, vanishes for $P > 0.3$.

The shaded region at the right hand side of the diagram represents compositions that cannot be prepared because lithium cannot be inserted into "blocked" galleries. The data that define this region come from section 5.4.1.

Figure 5-27 shows a phase diagram which a meaningful theory of lithium intercalation in graphite must be able to reproduce. Turbostratic disorder is present in most synthetic graphites, and hence affects experimental results. Furthermore, the voltage and $-(dx/dV)$ profiles in figures 5-12 and 5-18 must also be replicated by any theory considered to be viable. At the moment, all existing phenomenological theories for lithium intercalation in graphite cannot reproduce the experimental results shown here.

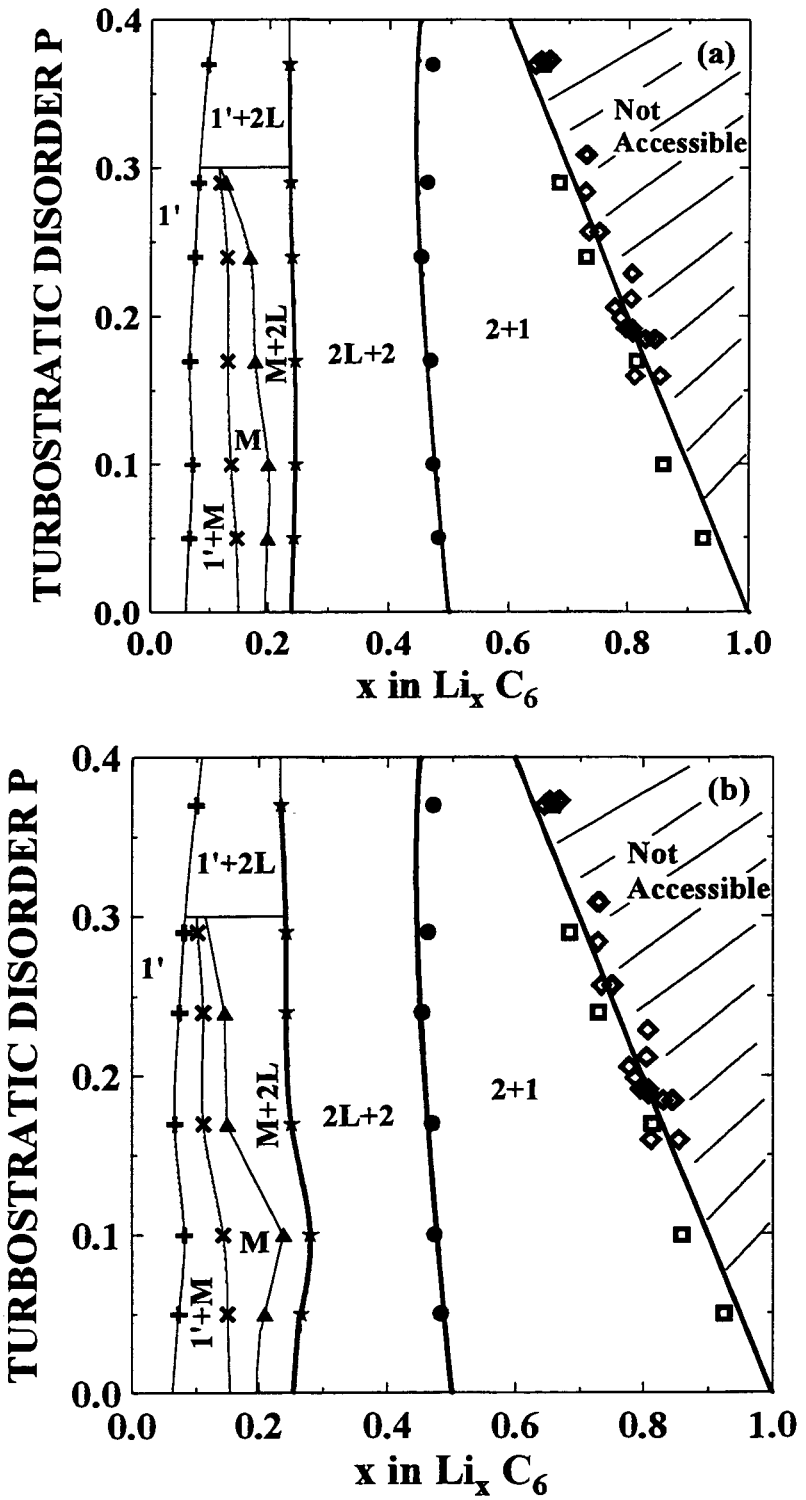

Figure 5-27. The room temperature phase diagram for lithium intercalated graphitic carbon in the P-x plane. a) discharge and b) charge. All symbols are from the results of electrochemical or in-situ X-ray measurements. The M phase is the mixed stage-3L, 4L phase. The stage-2L, 2 and 1 phases are depicted as line phases here (thick lines), although they have some small range of x. The solid lines are guides to the eye.

LITHIUM INSERTION IN HYDROGEN-CONTAINING CARBONS

A variety of materials have been pyrolysed at temperatures near 700°C which show behavior similar to that in figure 2-2 for the CRO550 sample (Yata, 1994; Mabuchi, 1994; Sato, 1994). Yata et al. (Yata, 1994) and Mabuchi et al. (Mabuchi, 1994) noticed that their carbons heated at these temparatures contain substantial hydrogen. However, they proposed that the large capacity and hysteresis was due to the storage of lithium in the pores of the materials. It was our idea that the hydrogen in these materials could be playing a crucial role. So we synthesized several series of materials at different temperatures and studied them.

6.1. Preparation of Carbonaceous Materials Heated at Low Temperatures

Petroleum Pitch, was obtained from Kureha Company (Japan). We call this sample the KS pitch. A second petroleum pitch was obtained from the Crowley Tar Company (U.S.A.). We call this sample the CRO pitch. Polyvinyl chloride (PVC) was obtained from the Aldrich Chemical Company (U.S.A.). These samples are all soft carbon precursors.

Oxychem phenolic resin (OXY) was supplied in powder form from Occidental Chemical Corp. (NY, USA). The powders were cured at 150 to 160°C for about 30 minutes in air to produce a solid lump. Epoxy novolac resin #DEN438 (poly[(phenyl glycidyl ether)-coformaldehyde]) was obtained from Dow Chemical Corporation (Midland, Michigan, U.S.A.). We used phthallic anhydride (Aldrich) as a curing agent to harden the epoxy samples prior to pyrolysis. Typically, between 15% and 30% curing agent by weight was added to the epoxy and mixed at 120°C. Curing was overnight at the same temperature, after which the samples were hardened. We will call these samples ENR here. These samples are hard carbon precursors. These samples were all reduced to powder before pyrolysis.

Table 6-1. Summary of the samples studied.

Sample	Heating temp. (°C)	Weight Percentages (%)			H/C Atomic Ratio (±0.03)	Yield (%)	BET surface area (m^2/g)	L_a (Å) (± 1)	(002) FWHM (deg.) (±0.2)	Reversible Capacity* (mAh/g) (±20)	Irreversible Capacity (mAh/g) (±20)	Capacity of one volt plateau* (mAh/g) (±20)
		C	H	N								
CRO550	550	93.5	3.2	0.2	0.41	49		20	3.6	880	450	570
CRO700	700	93.3	1.8	0.3	0.23	46	4.2±0.2	20	5.2	810	140	560
CRO800	800	95.1	1.3	0.3	0.16	45		27	4.9	590	180	350
CRO900	900	96.4	0.7	0.6	0.09	46		29	4.8	440	130	200
CRO1000	1000	95.5	0.3	0.5	0.04	45	4.5±0.2	33	4.3	340	100	100
KS550	550	95.1	3.2	<0.1	0.40	90		18	3.4	850	390	600
KS700	700	95.7	1.7	0.6	0.21	88	7.6±0.5	23	5.2	760	250	500
KS800	800	95.4	1.4	0.4	0.17	88		27	5.2	580	80	340
KS900	900	97.1	1.0	0.2	0.12	87		29	5.5	450	120	200
KS1000	1000	98.0	0.5	<0.1	0.06	86	7.9±0.5	33	5.2	350	60	120
PVC550	550	93.9	2.8	0.6	0.36	10		20	4.0	940	340	670
PVC700	700	94.6	1.6	0.7	0.20	10	24±1	19	3.9	770	160	500
PVC800	800	96.7	1.1	0.2	0.14	9		29	4.5	560	80	320
PVC900	900	97.9	0.7	0.4	0.09	9		29	4.8	400	70	170
PVC1000	1000	97.9	0.4	<0.1	0.05	8	25±1	37	3.9	340	80	110
OXY700	700	94.7	1.8	0.4	0.22	58	250±10	27	9.5	630	260	400
OXY800	800	95.8	0.9	0.7	0.11	57		29	8.5	540	210	230
OXY900	900	94.8	0.5	0.5	0.06	57		30	9.0	410	300	100
OXY1000	1000	97.4	0.4	1.4	0.05	56	240±10	32	9.0	540	200	80

Table 6-1 (Cont'd)

Sample	Heating temp. (°C)	Weight Percentages (%)			H/C Atomic Ratio (±0.03)	Yield (%)	BET surface area (m^2/g)	L_a (Å) (± 1)	(002) FWHM (deg.) (±0.2)	Reversible Capacity* (mAh/g) (±20)	Irreversible Capacity (mAh/g) (±20)	Capacity of one volt plateau* (mAh/g) (±20)
		C	H	N								
ENR700	700	93.3	1.3	<0.1	0.17	27	210±10	27	9.8	630	680	420
ENR800	800	91.7	0.9	<0.1	0.12	27		29	9.0	610	230	280
ENR900	900	93.4	0.5	<0.1	0.06	26		31	8.5	590	170	190
ENR1000	1000	93.1	0.2	0.6	0.03	26	220±10	31	9.0	570	150	150
SUG600	600	92.5	2.3	0.1	0.30					760	380	540
SUG700	700	93.8	1.4	0.2	0.18					720	270	430
SUG800	800	95.2	0.9	0.3	0.11					620	200	300
SUG900	900	95.5	0.6	0.4	0.07					570	180	190
SUG1000	1000	97.0	0.5	0.7	0.06					530	130	130
ASUG600	600	92.9	2.4	0.2	0.31					690	490	470
ASUG700	700	91.4	1.5	0.3	0.20					580	380	330
ASUG800	800	94.3	0.9	0.3	0.12					570	220	260
ASUG900	900	95.4	0.5	0.4	0.06					600	190	170
ASUG1000	1000	97.0	0.5	0.4	0.06					560	150	120

*obtained from the second cycles of voltage-capacity profiles.

Table 6-2. Some precursors used.

(1) Polyvinyl chloride (PVC)

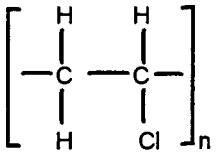

(2) Epoxy Novolac Resin (ENR)
Poly[(phenyl glycidyl ether)-co-formaldehyde]
DEN438 has average n=1.8

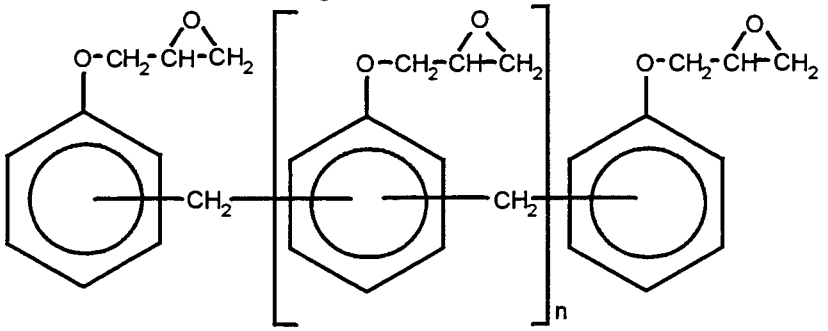

(3) Oxychem 29217 Resin (OXY)

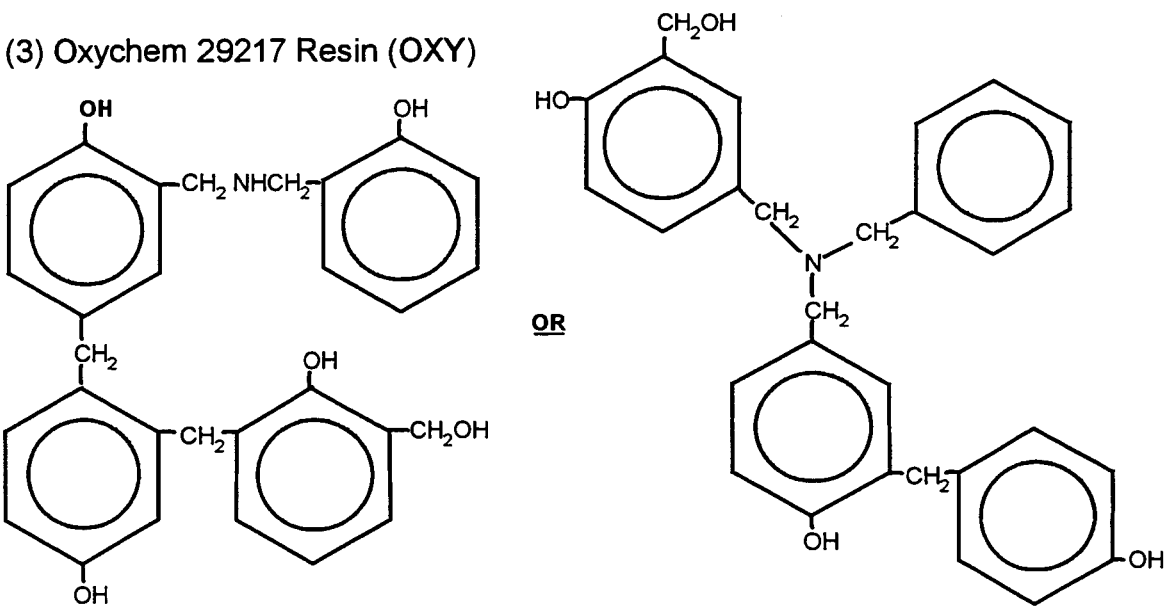

Pyrolysis was performed in tube furnaces equipped with quartz or stainless steel tubes. The tubes were fitted with end caps through which argon could flow. Typically, about 10 grams of the precursor was placed in an alumina boat and inserted into the furnace tube. Argon was flushed through the tube for at least one hour to remove all air

from the reaction tube. The samples were then heated at a rate of 16°C/min to the pyrolysis temperature which was maintained for one hour. An argon flow of 2 cc/sec was used during the pyrolysis. The samples were then cooled to room temperature under argon and weighed.. The product yield is the ratio of the sample mass before pyrolysis to the mass obtained after the heating. All samples made will be coded according to the starting material and pyrolysis temperature. For example, KS700 designates KS pitch pyrolyzed at 700°C, and ENR900 denotes epoxy novolac resin treated at 900°C. Table 6-1 lists the samples produced, and table 6-2 shows the chemical structures for some of the precursors. In addition, hard carbon samples made from sugar (SUG) and sulfuric acid-washed sugar (ASUG) are also included in table 6-1 (Xue, 1995b).

6.2 Characterization and Electrochemical Properties of As-Made Samples

6.2.1 Results of CHN Test and BET Measurement

The results of the CHN Test are listed in table 6-1. The quoted accuracy of the CHN test is ±0.3% by weight. The hydrogen to carbon atomic ratio was estimated by taking the ratio of the hydrogen to carbon weight percentages and multiplying by 12.

The single-point BET surface area measurement was used to check for open pores. The results for some soft and hard carbon samples heated at 700°C and 1000°C are presented in table 6-1 for comparison. The hard carbon samples studied here have about ten times more open porosity than the soft carbons.

6.2.2 Results of TGA and RGA Measurements

Figure 6-1 shows TGA and RGA data for the heating of CRO pitch. The sample powder was heated at 10°C/min. The data recorded by the RGA have a delay in time; this means the RGA data are shifted to higher temperature by about 100°C compared to the TGA data. Figure 6-1a shows that the weight loss occurs mostly around 500°C which is indicated by the peak of the derivative curve. The RGA data in figure 6-1b show that the

gas released at around 550°C contains methane (CH_4, mass 16). Hydrogen gas (H_2, mass 2) begins to be released mostly around 600°C. Based on visual examination of the pyrolysis tube, we expect that many heavy organic tarry species do not reach the RGA and hence are not detected.

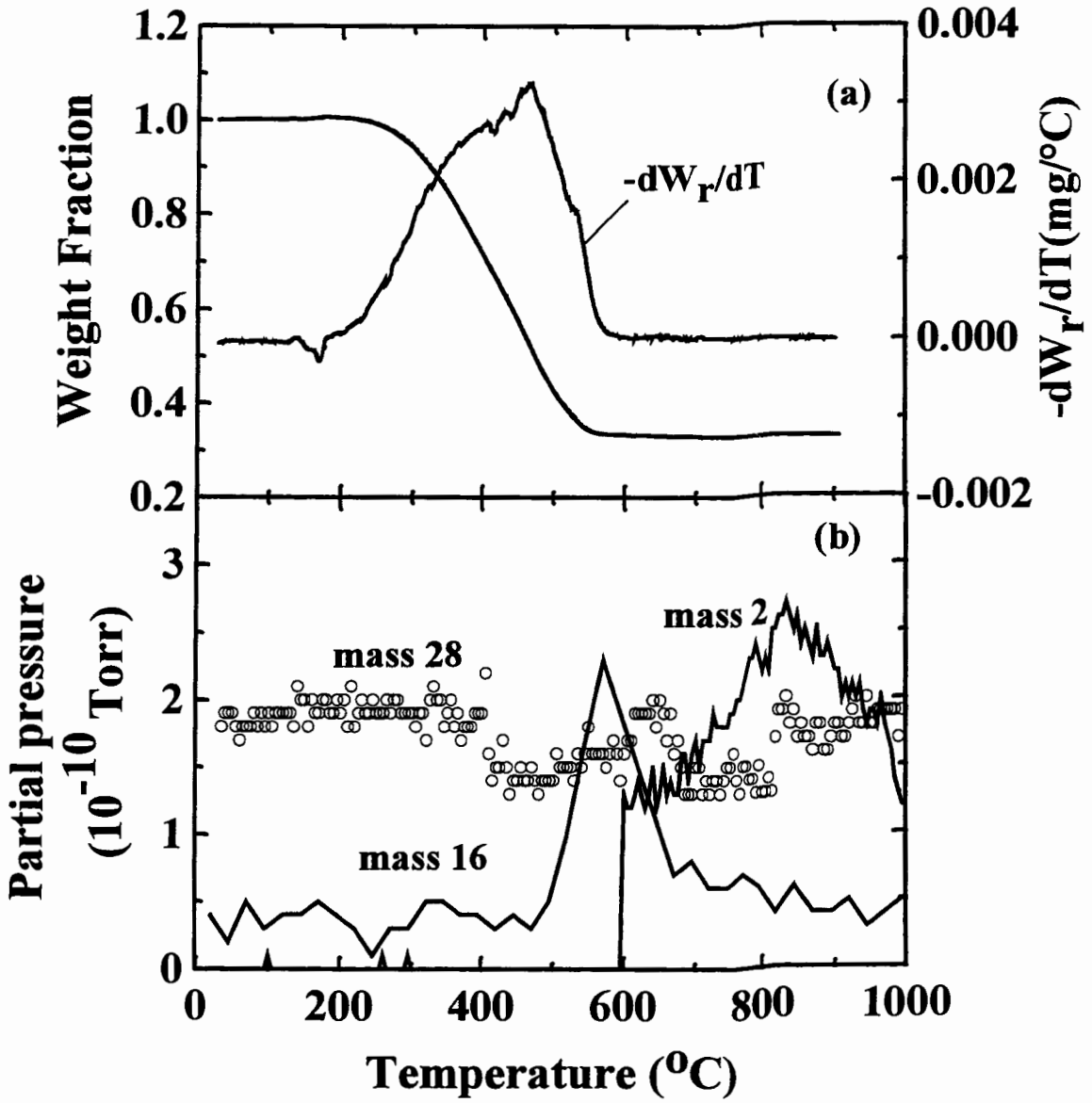

Figure 6-1. (a) TGA shows weight loss, and (b) RGA shows the partial pressure of CH_4, H_2, and CO versus temperature for the CRO pitch. The temperature recorded by the RGA is about 100°C higher than the TGA.

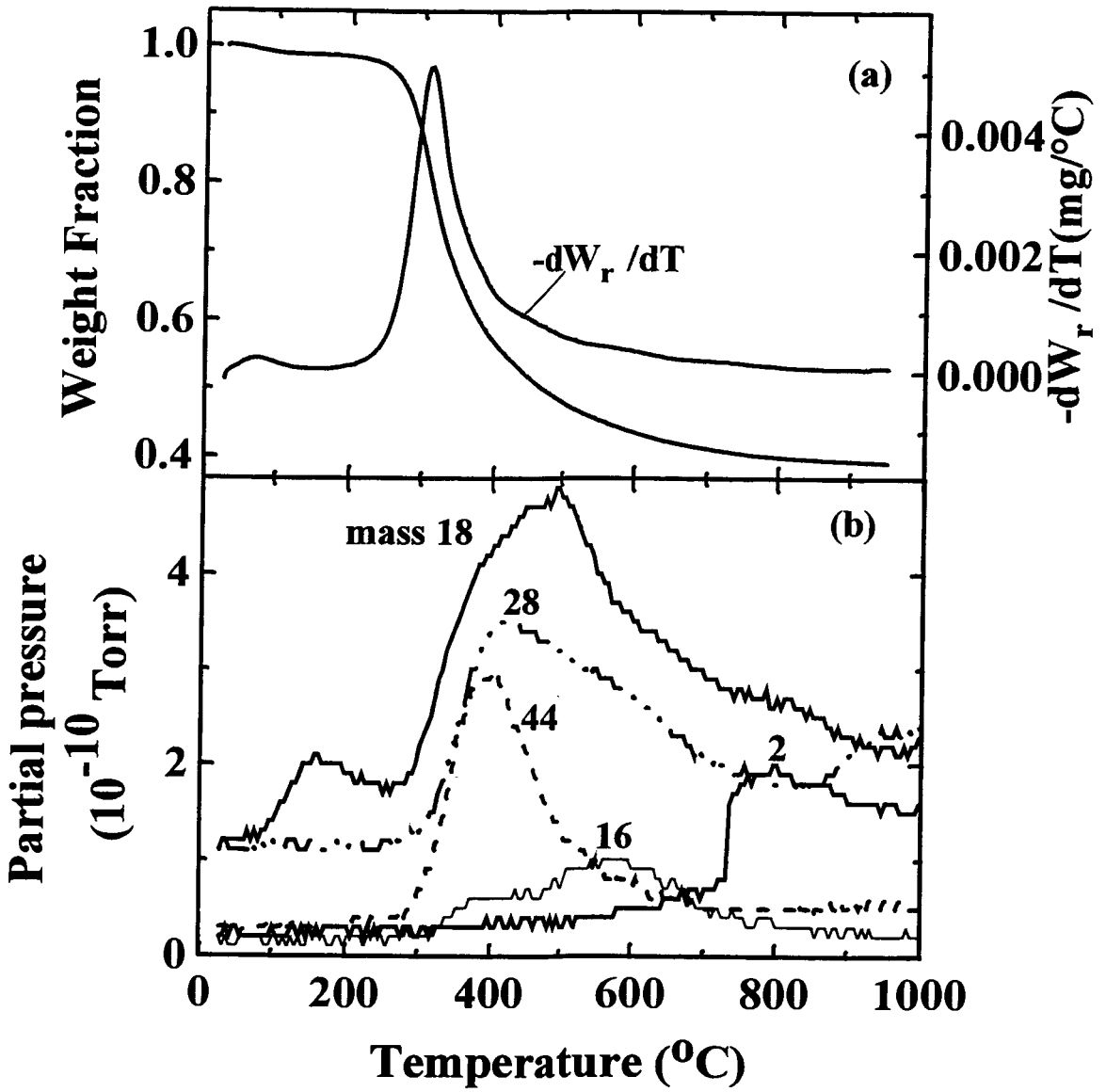

Figure 6-2. (a) TGA shows weight loss, and (b) RGA shows the partial pressure for some gases versus temperature for heated sugar. The temperature indicated by RGA is about 100°C higher than the TGA.

Figure 6-2 shows similar results for a sugar sample (Xing, 1996). Figure 6-2a shows that the sugar begins to lose weight at about 310°C. In figure 6-2b, the gases released at around 400°C are CO, CO_2, and H_2O, corresponding to mass 28, 44, and 18, respectively. Methane (CH_4, mass 16) begins to evolve at about 600°C and hydrogen gas (H_2, mass 2) evolves above 700°C.

When precursors are pyrolyzed around 700°C, the heteroatoms like oxygen and nitrogen are mostly lost but aromatic hydrogen is predominately left as we described in section 2.5. This is consistent with the results of the CHN test. The TGA and RGA works above show more evidence consistent with this argument. The aromatic hydrogen is eliminated continuously in carbonaceous materials as the temperature increases above 700°C.

6.2.3 Structure and Composition of Most Heated Samples

Figures 6-3 through figure 6-7 show the (002) Bragg peak region of most carbon samples studied. These figures give qualitative guidance about the differences between the samples. The lateral extent of the graphene sheets (L_a) was estimated from the (100) Bragg peak using the Scherrer equation, (refer to equation (3-3) in chapter 3)

$$L_a = \frac{1.84\lambda}{B\cos\theta_B}$$

where λ is the X-ray wavelength, θ_B is the Bragg angle, and B is the full width at half maximum of the peak in radians. The values of L_a for our samples are listed in table 6-1. We did not use the structure refinement program for disordered carbons (see chapters 3 and 5) for analysis of these very disordered materials. The (002) Bragg peak cannot be simply used to predict L_c (Franklin, 1951) for these highly disordered carbons. This is because some of the samples made from hard carbon precursors have significant fractions of single layers or unorganized carbon, which do not contribute to a peak in the (002) position, but add significantly to the background level there. (The structure of hard carbon will be carefully discussed in chapter 7.) We have chosen therefore to simply report the (002) peak full width at half maximum, measured after subtraction of a linear background. This still allows the trends in the samples to be quantified (see table 6-1).

The pitch samples (figures 6-3 and 6-4) and the PVC samples (figure 6-5) show well formed (002) peaks which first broaden, and then sharpen, as the heating

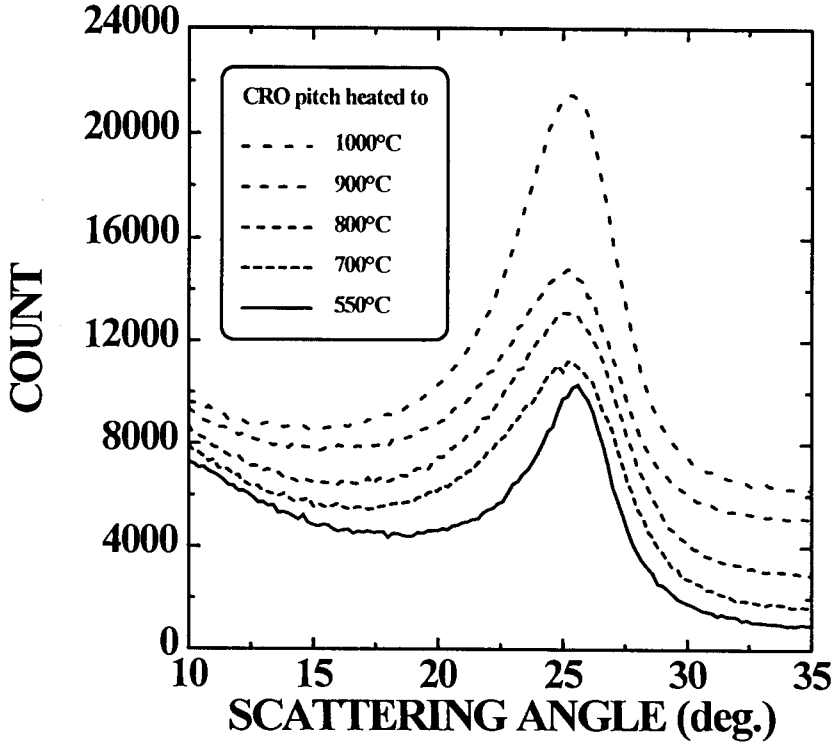

Figure 6-3. Powder X-ray diffraction pattern for the (002) peak of CRO pitch samples as indicated. The data sets have been offset sequentially by 0, 500, 2000, 4400 and 5400 counts for clarity.

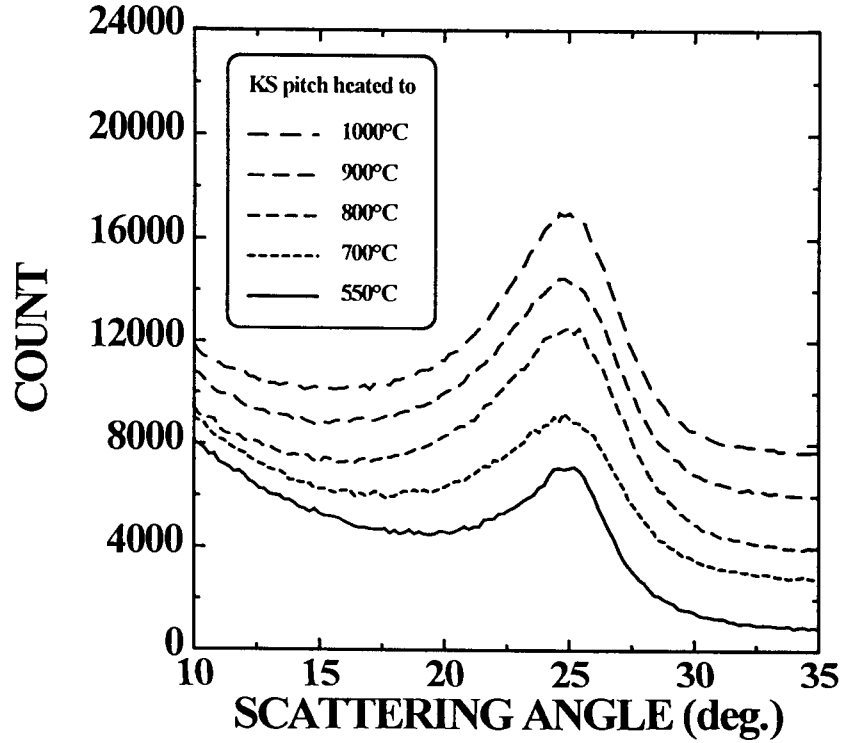

Figure 6-4. Powder X-ray diffraction pattern for the 002 peak of KS pitch samples as indicated. The data sets have been offset sequentially by 0, 2000, 3000, 5200 and 7000 counts for clarity.

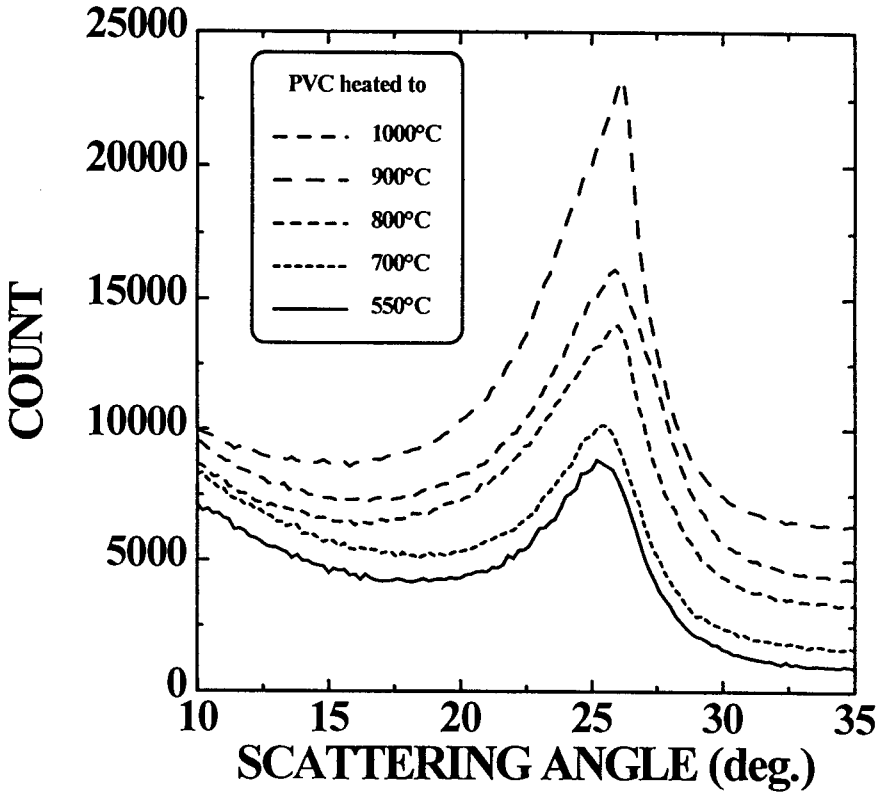

Figure 6-5. Powder X-ray diffraction pattern for the (002) peak of samples made from PVC as indicated. The data sets have been offset sequentially by 0, 600, 2500, 3500 and 5500 counts for clarity.

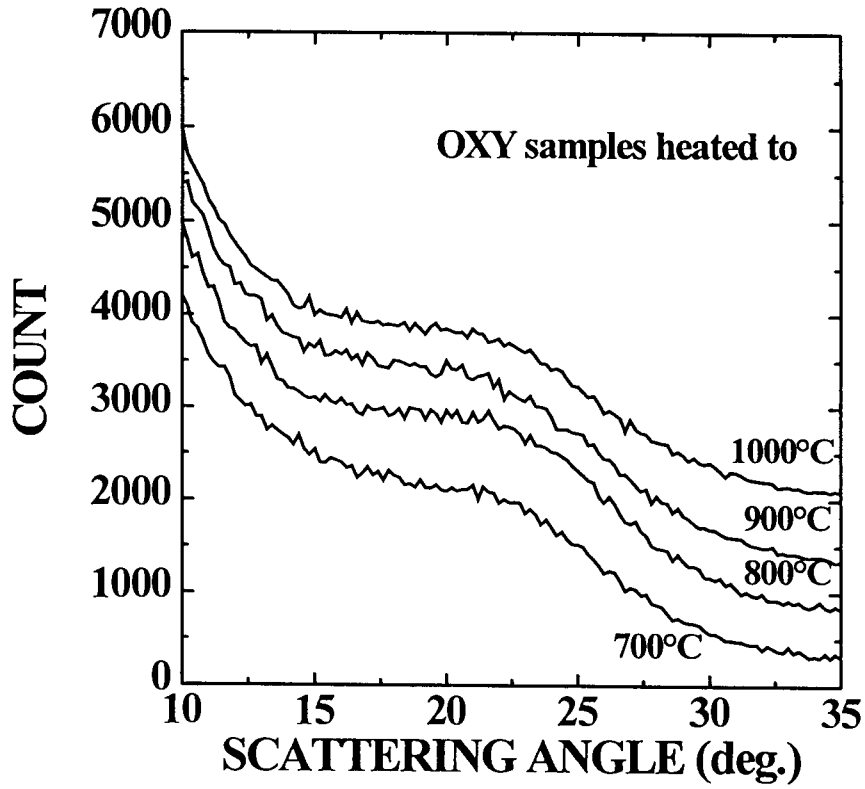

Figure 6-6. Powder X-ray diffraction pattern for the (002) peak of samples made from Phenolic resin (OXY) as indicated. The data sets have been offset sequentially by 0, 500, 1000 and 1900 counts for clarity.

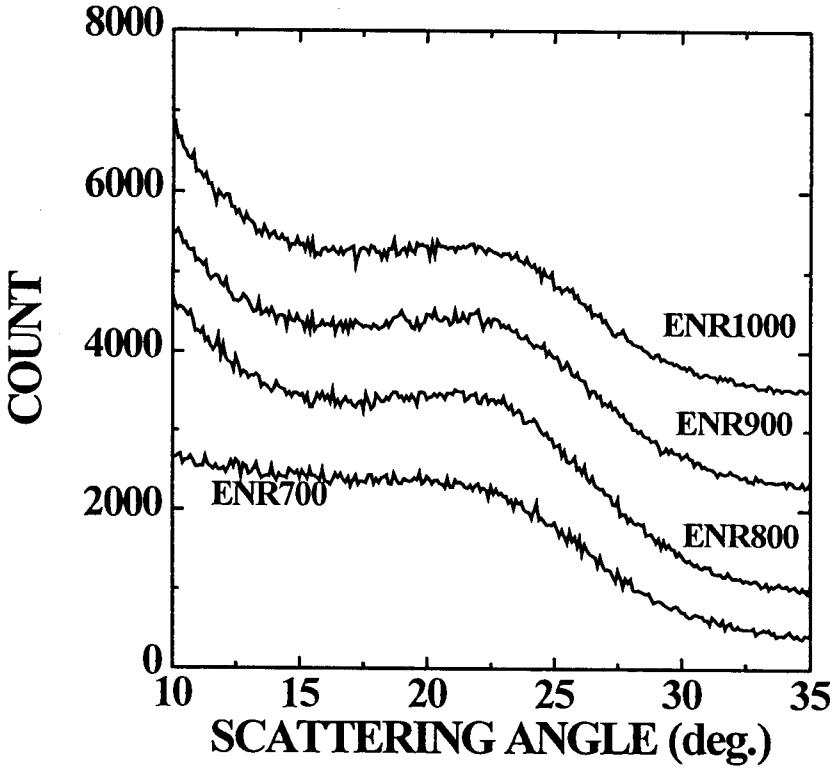

Figure 6-7. Powder X-ray diffraction pattern for the 002 peak of samples made from epoxy novolac resin (ENR) as indicated. The data sets have been offset sequentially by 0, 500, 1900 and 3200 counts for clarity.

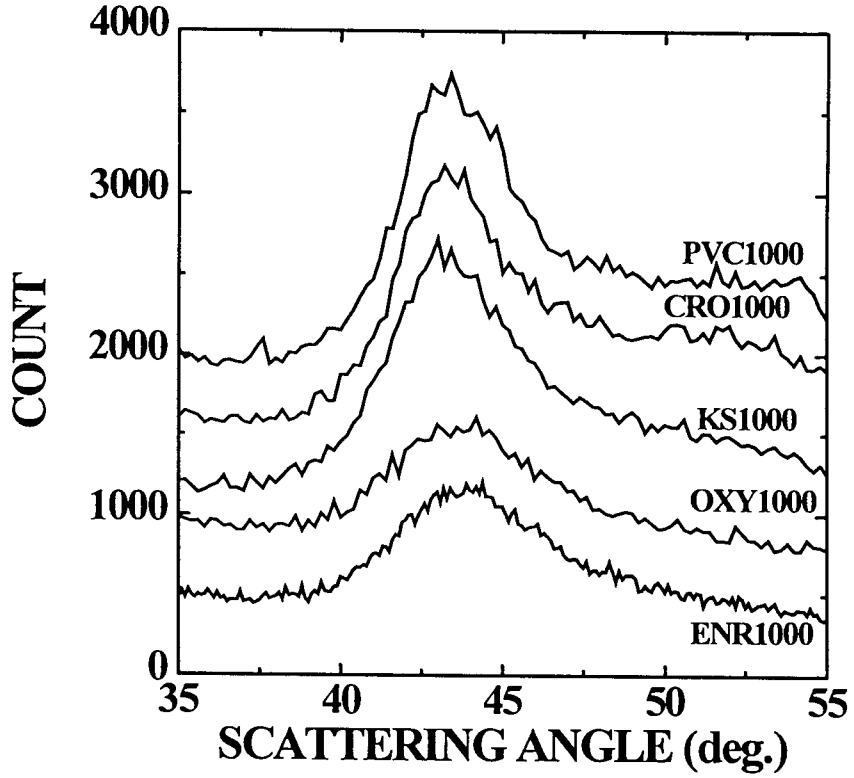

Figure 6-8. Powder X-ray diffraction pattern for the (100) peak of all samples made at 1000°C as indicated. The data sets have been offset sequentially by 0, 400, 500, 800 and 1200 counts for clarity.

temperature is increased. Diamond (Diamond, 1959) noticed this effect in his work on carbonization of coals. Figures 6-3, 6-4 and 6-5 show that the width and position of the (002) peaks do not change dramatically upon heating in this temperature range for the pitch and PVC samples. These peak widths are consistent with stacks of order 5 to 7 layers according to the Scherrer equation assuming $d_{(002)}$ is about 3.5Å.

The OXY (figure 6-6), and ENR (figure 6-7) samples have very weak (002) peaks with widths which are almost twice those of the pitch and PVC samples. This indicates that the samples contain significant fractions of single layer carbon sheets, which are stacked more or less like a "house of cards", containing significant nanoporosity. Again, the (002) peak of these materials changes little as the temperature is increased.

Figure 6-8 shows the (100) and (004) peak regions for samples made from each precursor heated to 1000 °C. The CRO1000, KS1000 and PVC1000 samples show some evidence for an (004) peak near 52° while the other samples do not. This is consistent with the behavior of the (002) peak for these samples. The (100) peaks do not differ greatly, indicating lateral layer extents of order 18 to 37Å for all samples (see table 6-1).

Structurally, the materials are grouped into two main classes, those (soft carbons) with predominantly stacked layers (CRO, KS and PVC) and those (hard carbons) which are predominantly made up of single layer sheets (OXY and ENR). All the samples show similar values of L_a when heated to a given temperature.

Figure 6-9 shows the SAXS measurements on the soft carbon samples CRO700 and CRO1000, and on the hard carbon samples OXY700 and OXY1000. All these samples were measured under the same conditions with about the same sample mass. The Guinier formula (referring to equation (3-9) in chapter 3) was used to qualitatively model these SAXS results. The SAXS intensity, $\mathbf{I(k)}$, from randomly located pores with homogeneous size is

$$\mathbf{I(k)} \propto NV^2 \cdot \exp\left\{-\frac{1}{3}\left(qR_g\right)^2\right\}$$

where R_g is the radius of gyration of the pore, N is the number of pores and V is the volume of one pore. A spherical pore of radius R_s has a radius of gyration R_g given by

$R_g = \sqrt{3/5} R_s$. Therefore, materials with large pores have small angle scattering intensities which fall off rapidly with k or with scattering angle, while those with small pores show a slower decline. Materials with significant porosity have higher SAXS intensities, while those with less porosity show lower intensities.

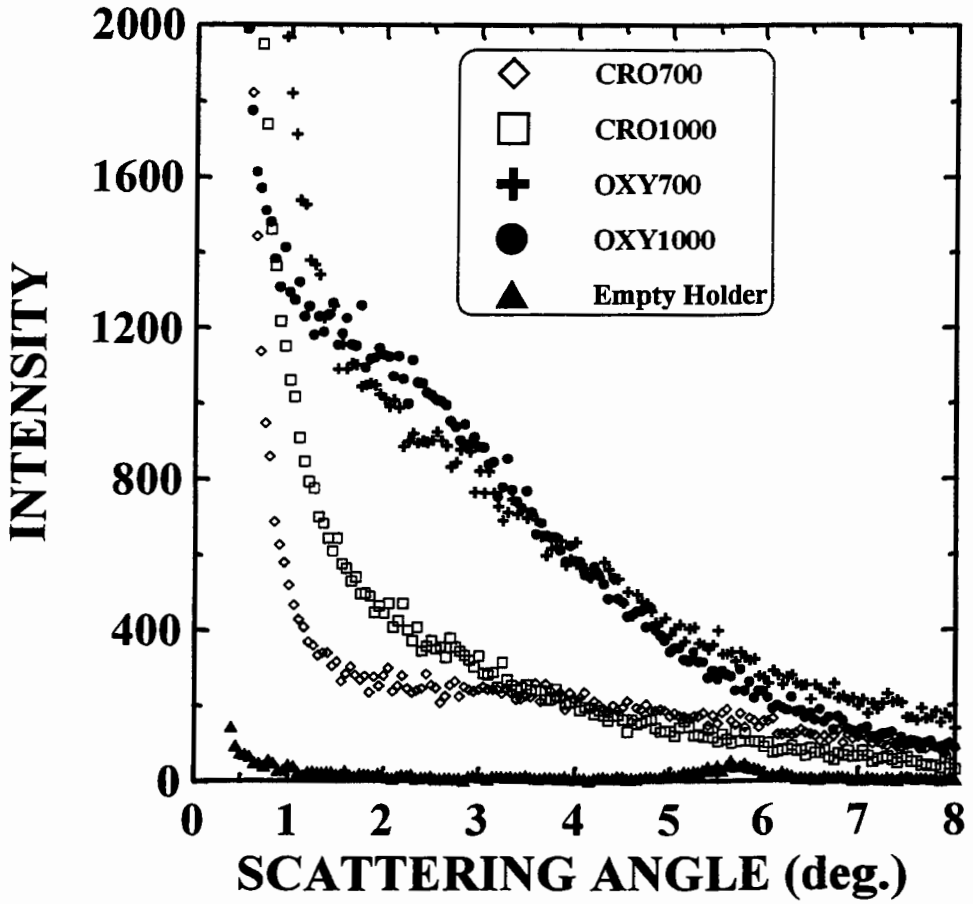

Figure 6-9. The small angle scattering intensity versus scattering angle for samples CRO700, CRO1000, OXY700 and OXY1000.

Figure 6-9 shows that the hard carbons OXY700 and OXY1000 show evidence for significant nanoporosity, while the CRO700 and CRO1000 samples contain substantially less nanoporosity. The high counts at very low angle (≤ 1°) in figure 6-9 are from larger pores which are typically larger than 50Å. We found that the hard carbon

samples all have significant nanoporosity, but that the soft carbon samples do not. This result is consistent with the results of powder X-ray diffraction.

In table 6-1, the H/C atomic ratio decreases monotonically for each of the samples as they are heated and all the samples approach pure carbon as the heating temperature is increased. Table 6-1 also gives the product yield for all the samples as a percentage of the starting weight of the precursor. The yields from the CRO, KS and OXY series are large, presumably because these precursors have large aromatic content and less heteroatoms. ENR shows intermediate behavior; it has less aromatic content and more heteroatoms. PVC shows the lowest yield of all presumably because it has no initial aromatic content.

6.2.4. Electrochemical Testing

Figure 6-10 shows the first discharge and charge of cells using electrodes made from the CRO pitch. Figure 6-10a shows an enlargement of the low voltage region of the data to show the initiation of lithium plating during discharge and the termination of lithium stripping during charge. The small vertical lines marked in each data set indicate the onset of plating and the end of stripping. The CRO550 and CRO700 samples have first charge capacities of about 900 mAh/g. There is a large hysteresis between discharge and charge, of about one volt. As the samples are heated to 800°C and above, the reversible capacity is reduced dramatically. The majority of the capacity reduction is due to a shortening of the low voltage (near zero volts) plateau during discharge and the one volt plateau during charge. That is, the portion of the voltage profile which displays hysteresis and is responsible for the large capacity, is removed as the samples are heated above 700°C. The irreversible capacity during the first cycle is taken as the difference between the capacity of the insertion reaction measured during discharge and charge, not including the capacity of lithium plating and stripping. Table 6-1 shows that the irreversible capacities for these samples are relatively small in comparison to the reversible capacity. Figure 6-9 shows the second cycle of the same cells. The

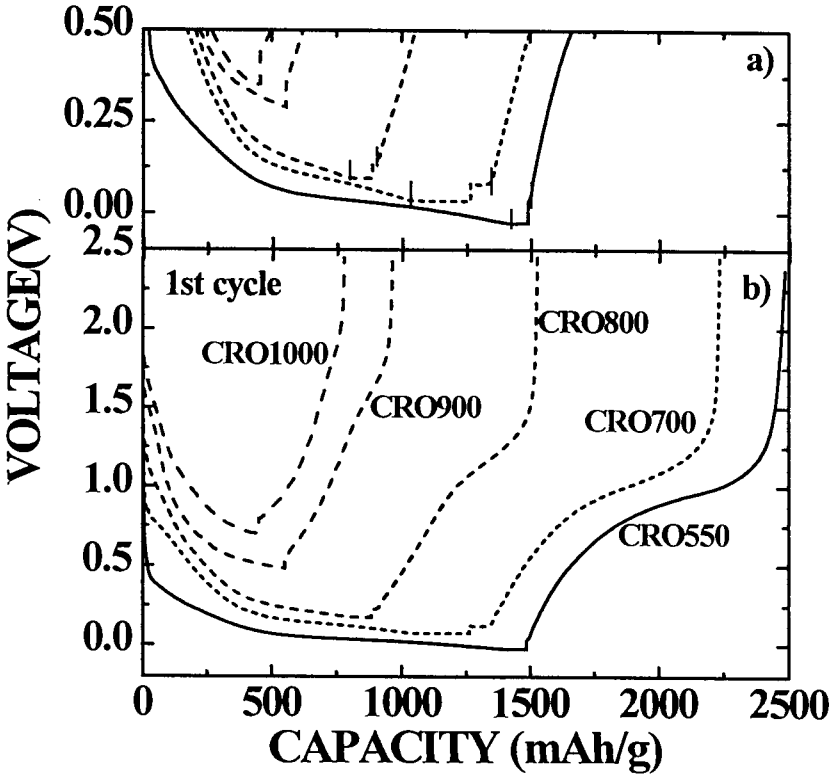

Figure 6-10. Voltage versus capacity for the first discharge-charge cycle of cells containing cathodes of CRO pitch as indicated. The upper panel (a) shows an enlargement of the low voltage region of the data. The vertical lines indicate the onset of lithium plating and the termination of lithium stripping. The data have been offset sequentially for clarity. The offsets are 0.0V, 0.06V, 0.12V, 0.30V and 0.40V in (a), and 0.0V, 0.10, 0.20, 0.50 and 0.75V in (b).

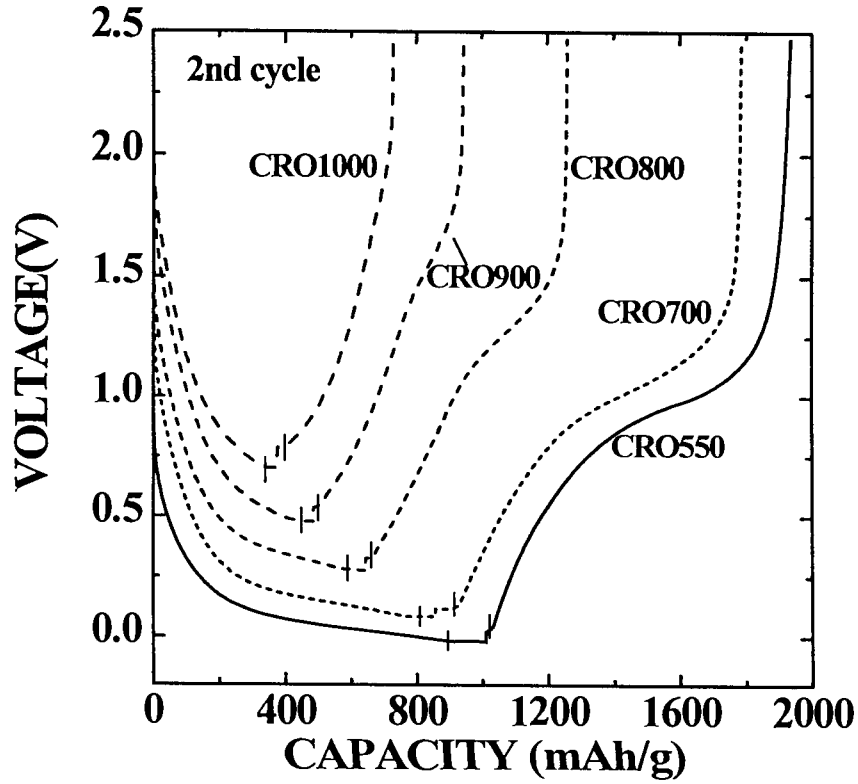

Figure 6-11. Voltage versus capacity for the second cycle of the CRO pitch samples. The data have been offset sequentially for clarity. The shifts are 0.00V, 0.10V, 0.20V, 0.50V and 0.75V. The vertical lines show the onset of lithium plating during discharge and the end of lithium stripping during charge.

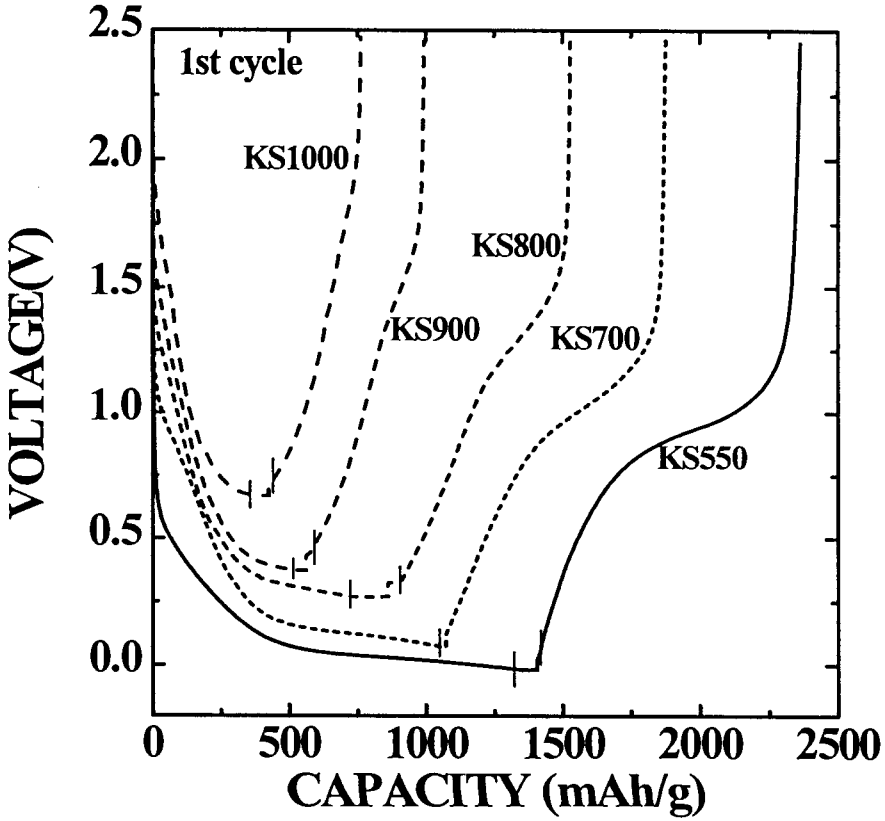

Figure 6-12. Voltage versus capacity for the first cycle of the KS pitch samples. The data have been offset sequentially for clarity. The shifts are 0.00V, 0.10V, 0.30V, 0.40V and 0.70V. The vertical lines show the onset of lithium plating during discharge and the end of lithium stripping during charge.

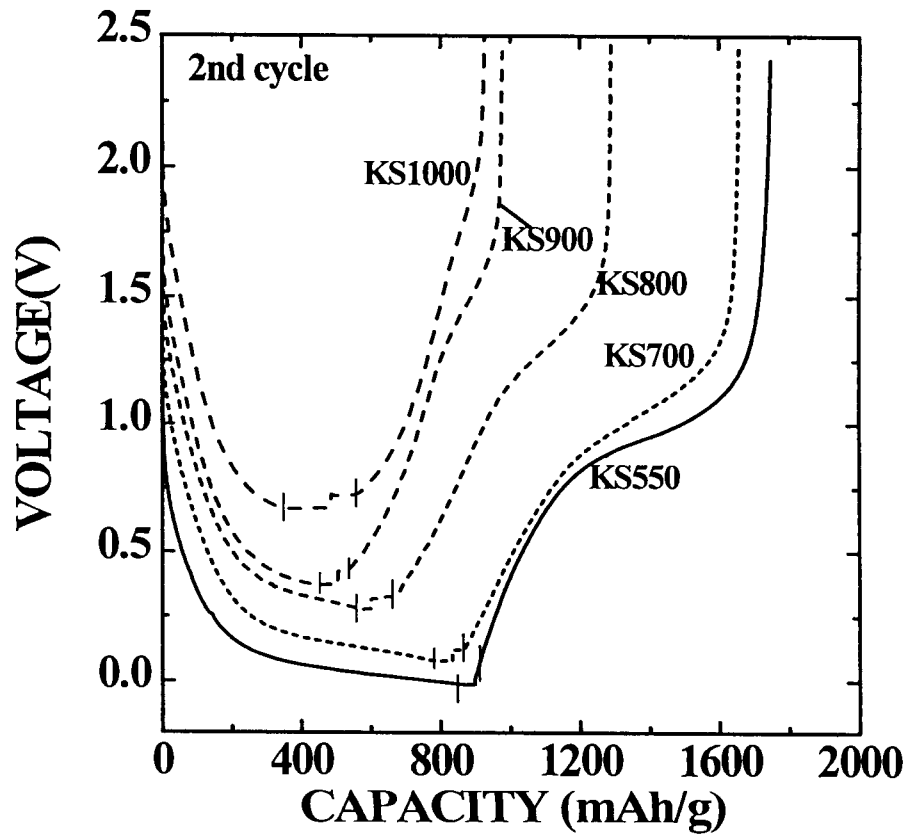

Figure 6-13. Voltage versus capacity for the second cycle of the KS pitch samples. The data have been offset sequentially for clarity. The shifts are 0.00V, 0.10V, 0.30V, 0.40V and 0.70V. The vertical lines show the onset of lithium plating during discharge and the end of lithium stripping during charge.

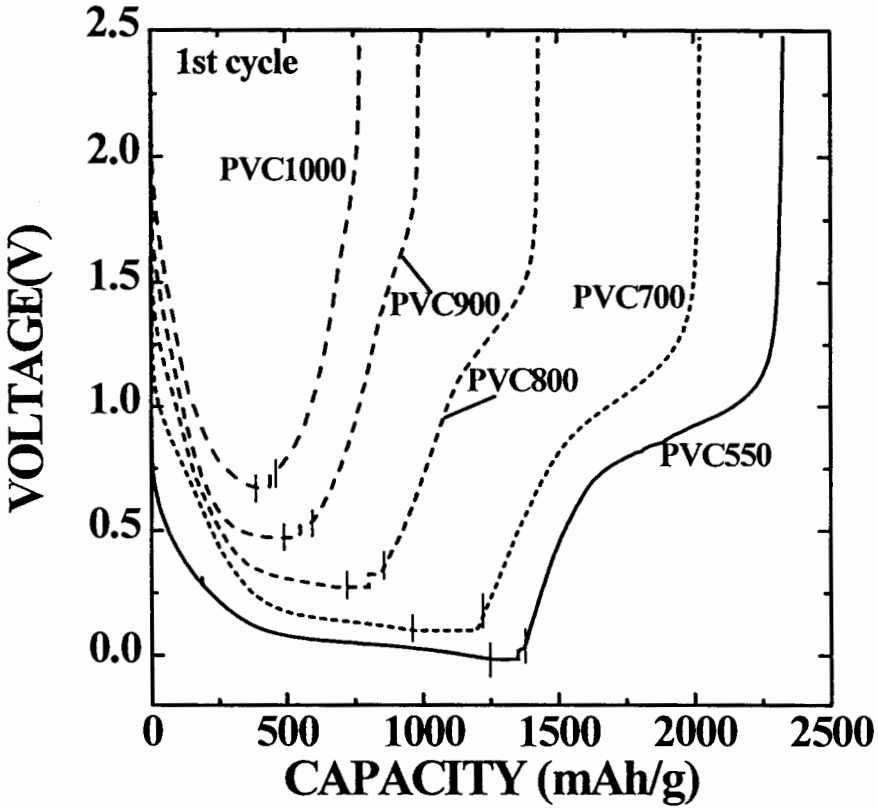

Figure 6-14. Voltage versus capacity for the first cycle of the samples made from PVC. The data have been offset sequentially for clarity. The shifts are 0.00V, 0.10V, 0.30V, 0.50V and 0.75V. The vertical lines show the onset of lithium plating during discharge and the end of lithium stripping during charge.

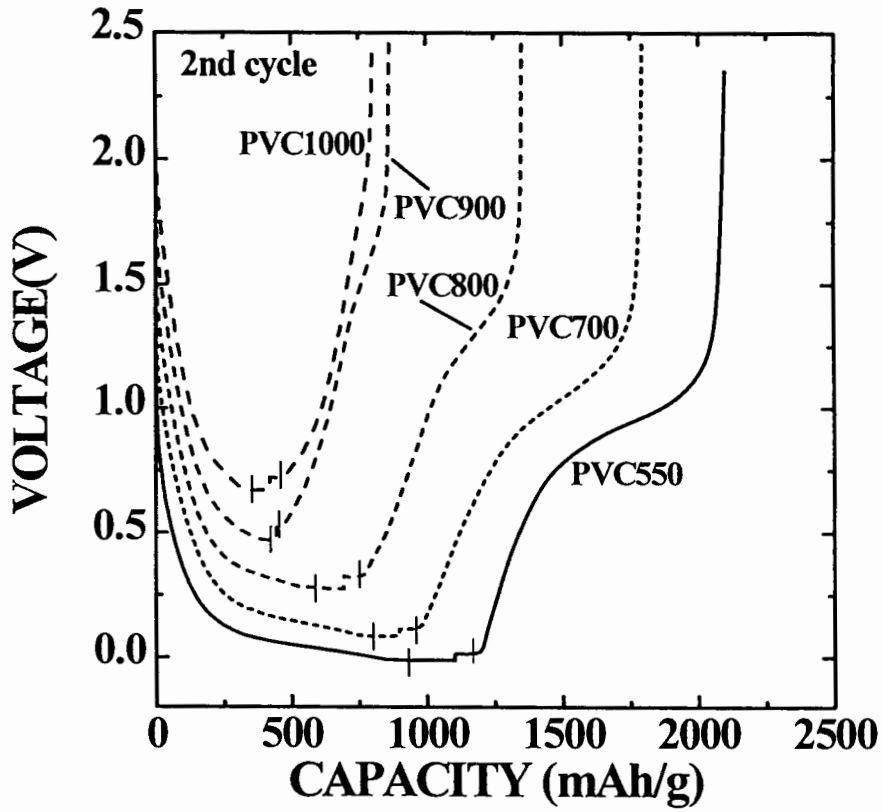

Figure 6-15. Voltage versus capacity for the second cycle of the samples made from PVC. The data have been offset sequentially for clarity. The shifts are 0.00V, 0.10V, 0.30V, 0.50V and 0.75V. The vertical lines show the onset of lithium plating during discharge and the end of lithium stripping during charge.

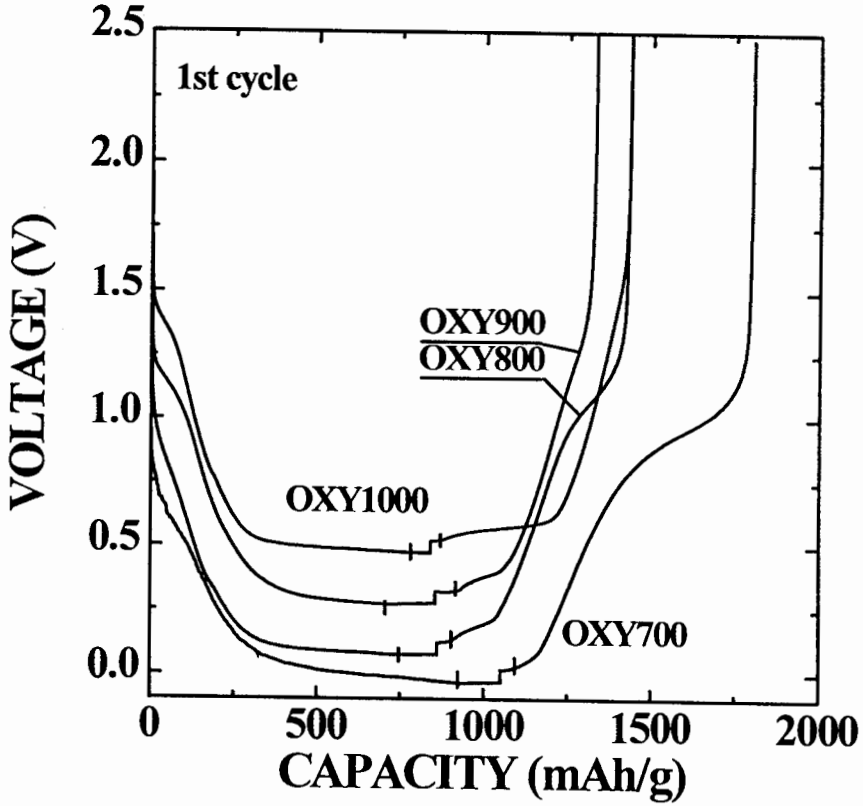

Figure 6-16. Voltage versus capacity for the first cycle of the samples made from OXY. The data have been offset sequentially for clarity. The shifts are 0.00V, 0.10V, 0.30V, and 0.50V. The vertical lines show the onset of lithium plating during discharge and the end of lithium stripping during charge.

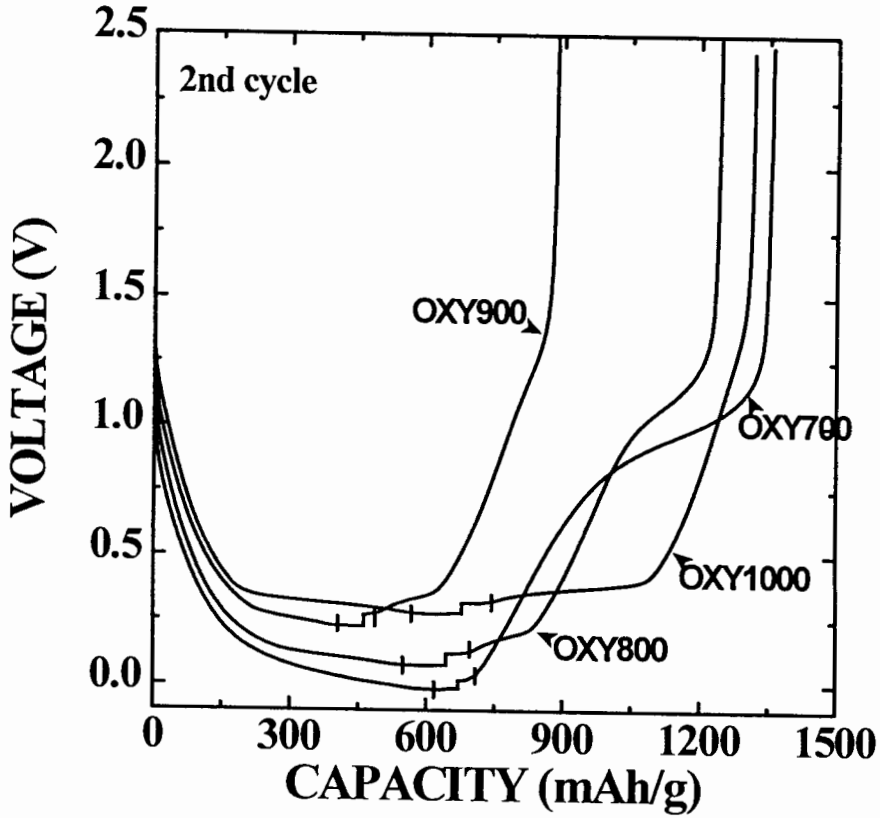

Figure 6-17. Voltage versus capacity for the second cycle of the samples made from OXY. The data have been offset sequentially for clarity. The shifts are 0.00V, 0.10V, 0.25V, and 0.30V. The vertical lines show the onset of lithium plating during discharge and the end of lithium stripping during charge.

elimination of the high capacity and the hysteresis is again evident as the samples are heated.

It is difficult to attribute the capacity reduction which occurs above 700°C to structural effects because the structure of the samples is not changed significantly, as indicated by our x-ray diffraction measurements on the CRO samples. On the other hand, the hydrogen content of the samples is dramatically reduced over this temperature range. To investigate the importance of the hydrogen content, we made a series of cells from the other samples.

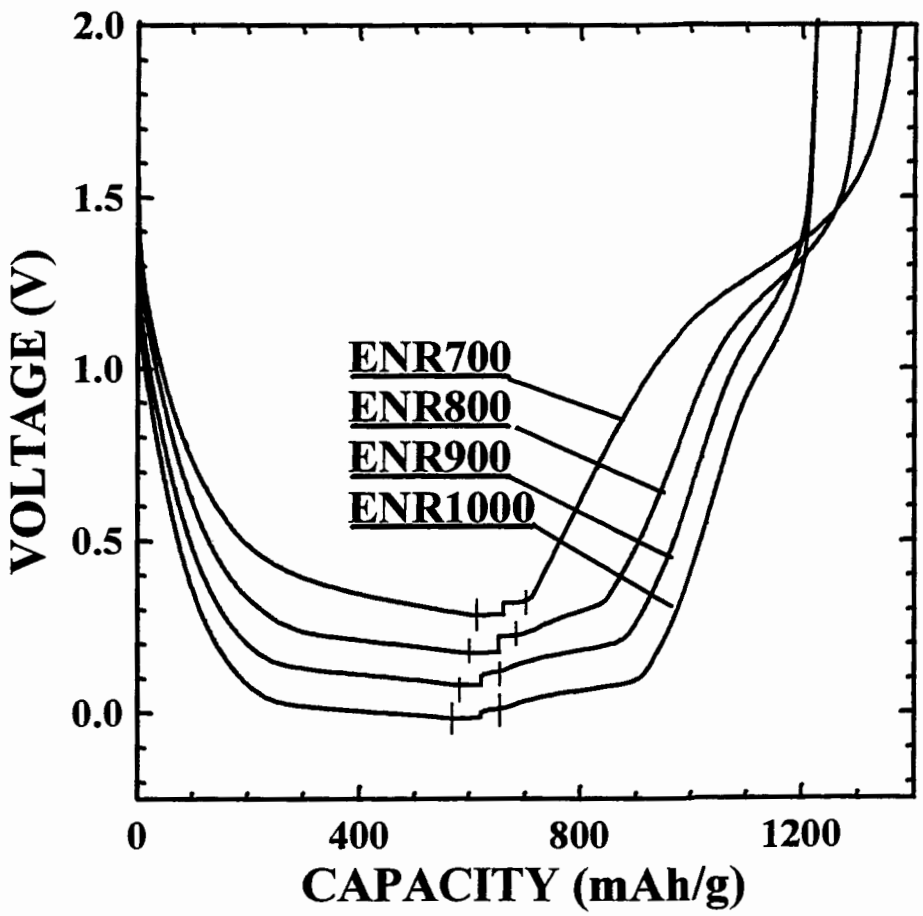

Figure 6-18. Voltage versus capacity for the second cycle of the samples made from ENR. The data have been offset sequentially for clarity. The shifts are 0.0 V, 0.10 V, 0,20 V, and 0.30 V. The vertical lines show the onset of lithium plating during discharge and the end of lithium stripping during charge for the samples.

Figures 6-12 and 6-13 show respectively the first and second cycles for the KS pitch samples, and figures 6-14 and 6-15 show respectively the first and second cycles for the PVC samples. These materials show a trend with heating temperature which is almost identical to the CRO pitch samples. Again, the large capacity and hysteresis in the voltage profiles are eliminated as the samples are heated above 700°C, even though little structural change to the samples occurs. On the other hand, the hydrogen content of the samples drops dramatically over this temperature range.

The OXY and ENR samples (hard carbons) show behavior similar to the CRO, KS and PVC samples (soft carbons) when their H/C ratio is large, but strikingly different behavior upon heating above 800°C.

Figures 6-16 and 6-17 show respectively the first and second cycles of the OXY samples and figure 6-18 shows the second cycle of the ENR samples. The results for the OXY1000, ENR900 and ENR1000 samples are more striking. (These samples will be discussed in chapter 7.) Figures 6-16, 6-17, and 6-18 show that the majority of the low voltage plateau is not caused by the plating and stripping of lithium, but by a reversible insertion process. These three figures also show how the voltage profile changes with heating temperature. At 700°C, where the H/C ratio is large, the hard carbon samples show basically an identical capacity and voltage profile to the soft carbon samples, even though these materials have very different structures. However, after further heating, the hard carbon samples evolve into high capacity, low hysteresis materials. We believe that when substantial hydrogen is present it dominates the reaction with lithium. But, when the hydrogen is removed the structural differences between the samples play an important role.

6.2.5 Discussion and Conclusions

Figure 6-19 compares the voltage-capacity profiles for the second cycle of lithium/carbon electrochemical cells made from OXY, a representative hard carbon, and those for samples made from CRO, a representative soft carbon. What impressed us most is a shortening of the one volt plateau during charge as the samples are heated above

700°C for both the soft and hard carbons. That is, the portion of the voltage profile which displays hysteresis is removed as the samples are heated above 700°C. The capacity of the one volt plateau (taken between 0.7 volts and 1.5 volts for all samples) is well correlated to the hydrogen to carbon atomic ratio of the samples as shown in figure 6-20. Changing the voltage limits of the one volt plateau to other values (e.g. 0.5 volts and 1.5 volts) does not significantly affect the correlation in figure 6-20. The solid line in figure 6-20 is expected if each lithium atom can bind near a hydrogen atom in the host and if a hydrogen-free carbon heated to higher than 1000°C does not have a one volt plateau. Mabuchi et al.'s data (Mabuchi, 1994) have also been included and fit the trend well. The hydrogen contained in carbonaceous materials heated at low temperatures (below 800°C) is clearly important.

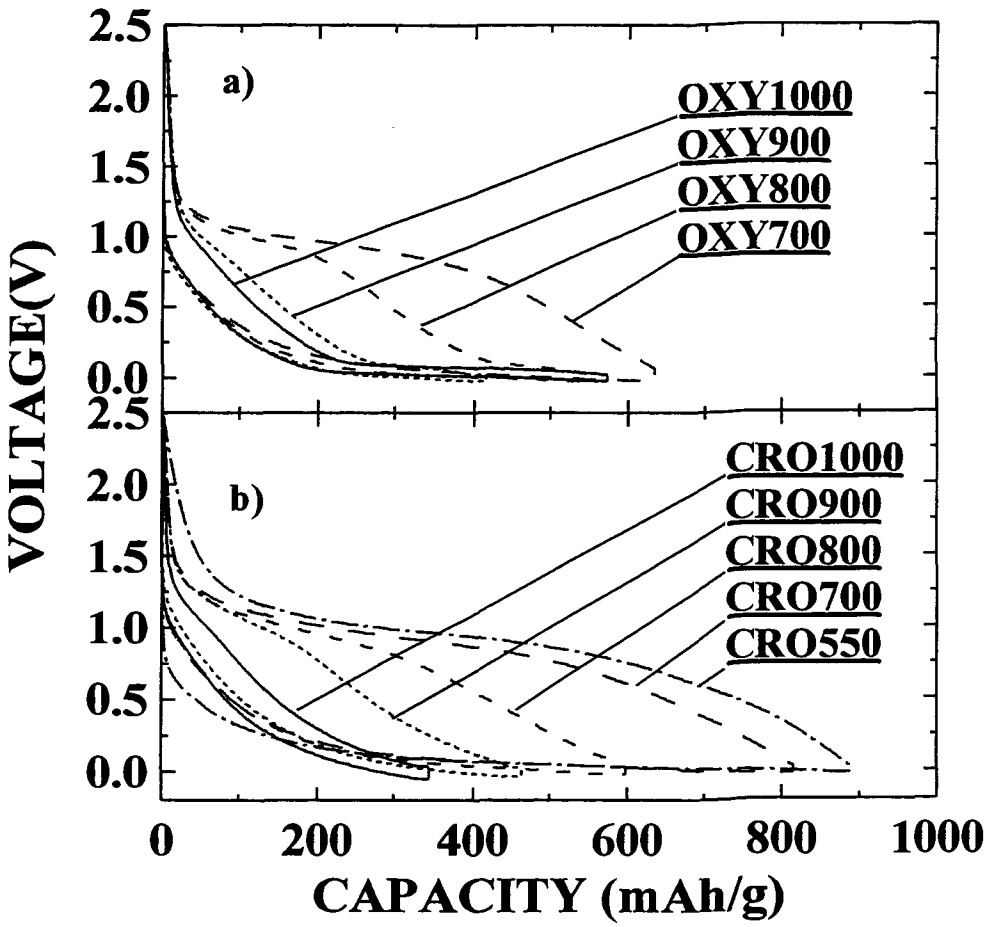

Figure 6-19. Voltage-capacity profiles for the second cycles of lithium/carbon cells made from a) OXY resin and b) CRO pitch at different temperatures as indicated.

Oxygen and nitrogen in the samples are not important. When any precursor is heated near 700°C, the heteroatoms like oxygen and nitrogen are predominantly eliminated except for aromatic hydrogen as described in section 2.5 and confirmed by the TGA/RGA measurements in section 6.2.2. Here we also point out that PVC contains no nitrogen or oxygen, so neither does its pyrolyzed product. Since pyrolyzed PVC shows the same behavior in figure 6-20 as the other samples, we believe the effects of oxygen and nitrogen in these materials to be negligible. The presence of hydrogen is the only common factor in all these samples with a variety of microstructures prepared from a variety of precursors.

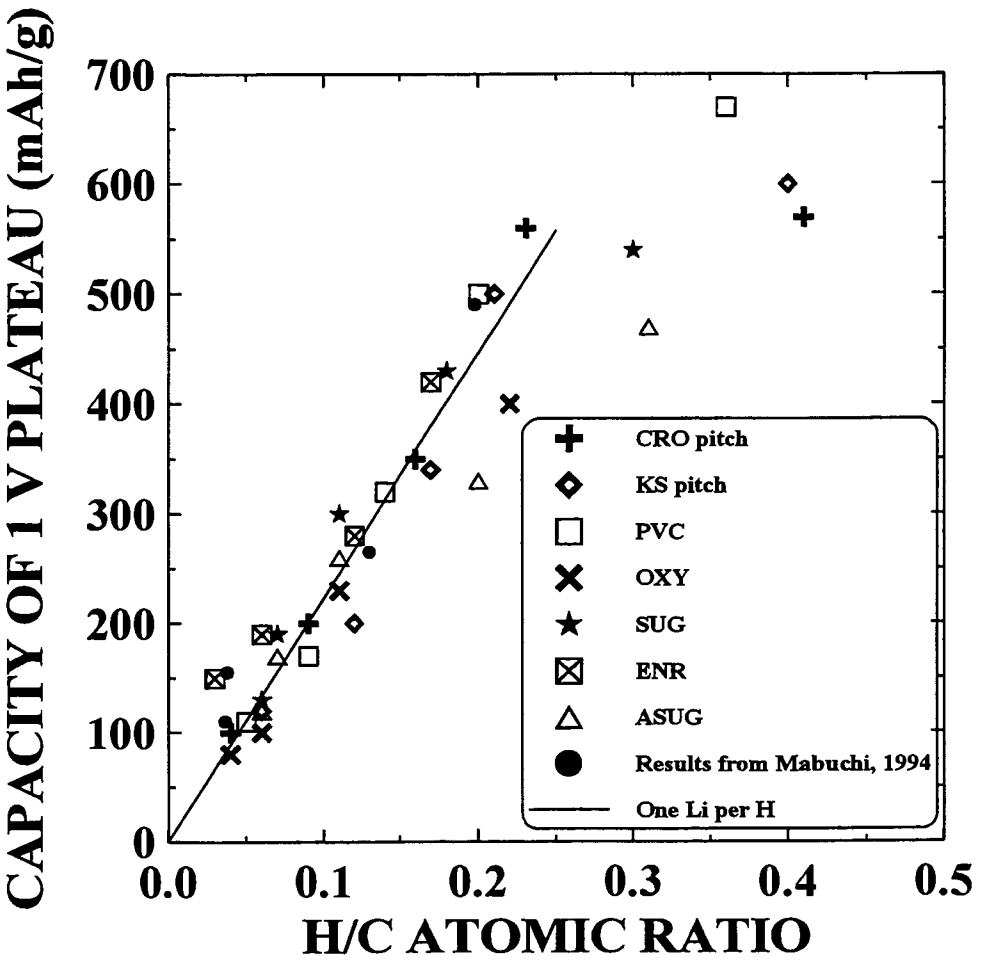

Figure 6-20. The capacity of the one volt plateau measured during the second cycle of several series of samples versus the H/C atomic ratio in the samples. The solid line suggests that each lithium atom binds quasi-reversibly to one hydrogen atom.

6.3 An Activated Process: Lithium Bonding near Hydrogen in Carbon

Hydrogen can affect lithium insertion in carbons. As an example, charge transfer from alkalis to hydrogen in carbons has been observed in ternary graphite-alkali-hydrogen materials (Enoki, 1990). In our hydrogen-containing samples, the lithium atoms may bind on hydrogen-terminated edges of hexagonal carbon fragments, with local geometries analogous to the organolithium molecule $C_2H_2Li_2$ (Papanek, 1996). If this is true, then the capacity for the insertion of lithium should strongly depend on the hydrogen content of the carbon materials as has been experimentally shown above. If the inserted lithium binds to a carbon atom which also binds a hydrogen atom, a corresponding change to the carbon-carbon bond from sp^2 to sp^3 occurs (Papanek, 1996). That is, the insertion and removal of the lithium atoms in carbons involves changes to the bonding in the host as shown schematically in figure 6-21. Bonding changes in the host have been previously shown to cause hysteresis in such electrochemical measurements. For example, hysteresis in lithium electrochemical cells was observed when Mo-S bonds in $LiMoS_2$ were broken due to the formation of Li-S bonds upon further insertion of lithium (Selwyn, 1987).

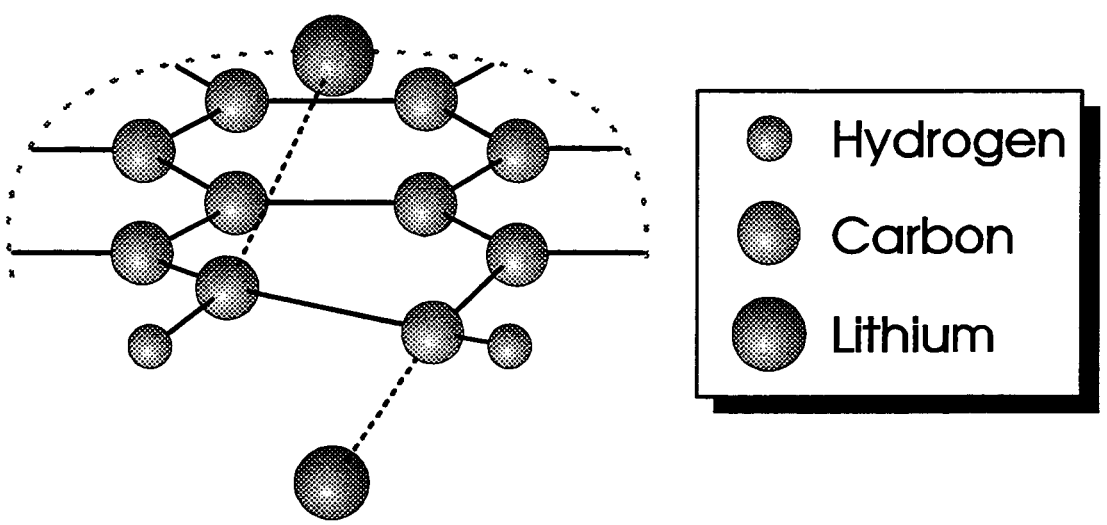

Figure 6-21. When lithium inserts in hydrogen-containing carbon, some lithium atoms bind on the hydrogen-terminated edges of hexagonal carbon fragments. This causes a change from sp^2 to sp^3 bonding.

Here, lithium/carbon electrochemical cells which were made from carbons containing substantial or little hydrogen were cycled at different temperatures and with different discharge/charge currents. We hoped that the results might give the additional information needed to understand more about carbonaceous materials pyrolyzed at low heat treatment temperatures. It was our goal to develop a simple qualitative model for the hysteresis which occurs in hydrogen-containing carbons, and to compare its predictions with experiment.

6.3.1 Model Development

It is our hypothesis that in hydrogen-containing carbon a process other than intercalation is involved. Intercalation refers to be the reversible insertion of guest atoms in host materials such that the structure of the host is not significantly altered. Therefore there are no fundamental changes to the strong bonds which hold the host together when intercalation occurs. No significant hysteresis in charge-discharge behavior of lithium cells containing such hosts is observed. However, we believe that the bonding environment near a hydrogen atom at the edge of a graphene ring changes from sp^2 to sp^3 when a lithium atom bonds nearby, as suggested by Papanek (Papanek, 1996). This is shown schematically in figure 6-21. This change is analogous to that which occurs when benzene is transformed to cyclohexane. Such bonding changes are normally activated process (Zumdahl, 1993).

To qualitatively understand the insertion of lithium in hydrogen-containing carbons, we will now consider a simple model, which will be shown to give predictions qualitatively consistent with experiment. First, assume that the hydrogen-containing carbon host has no lithium within it and that a lithium/carbon cell has just been constructed. Then, as the cell discharges, lithium intercalates into sites of energy, E_i, and its composition, x, within the carbon increases. The chemical potential, $\mu(x)$, of the inserted lithium increases with x. The voltage of the cell, V_m, is given by $V_m(x)=-\mu(x)/e$,

Figure 6-22a: Discharge

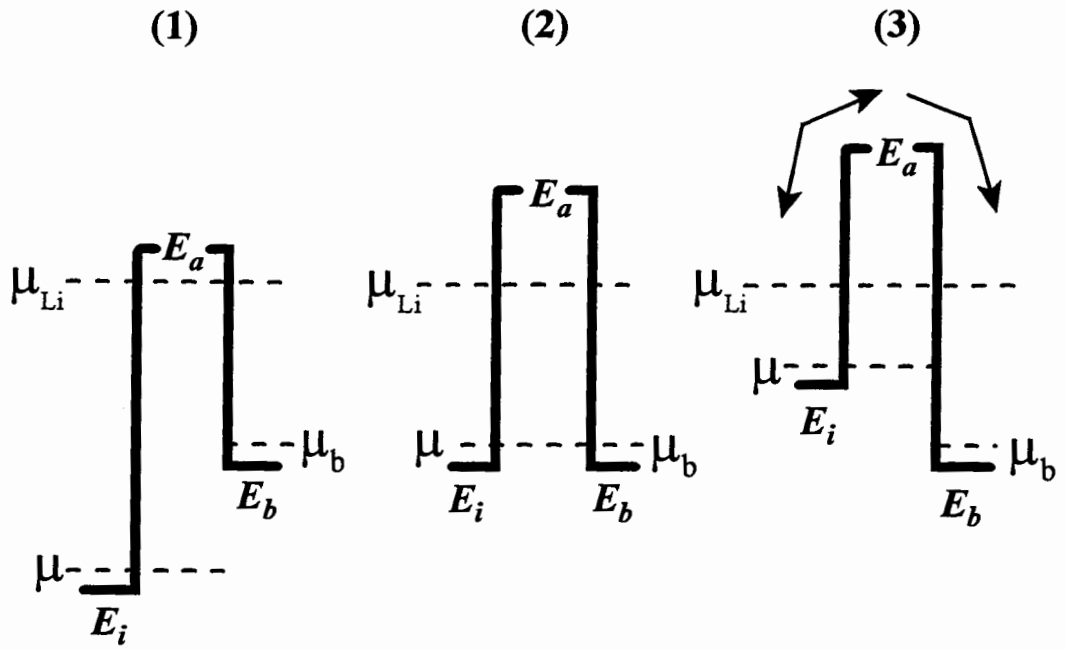

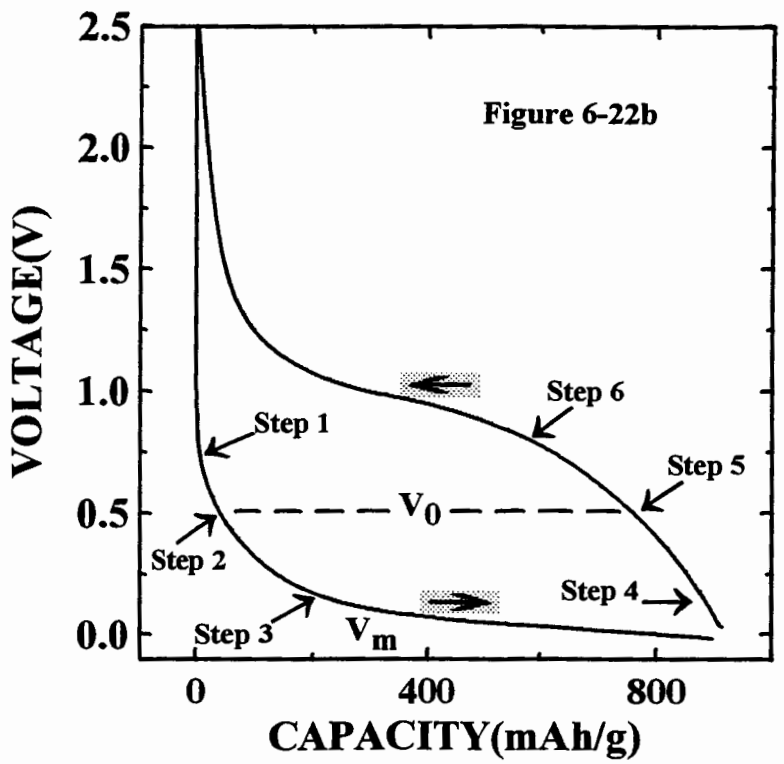

Figure 6-22c: Recharge

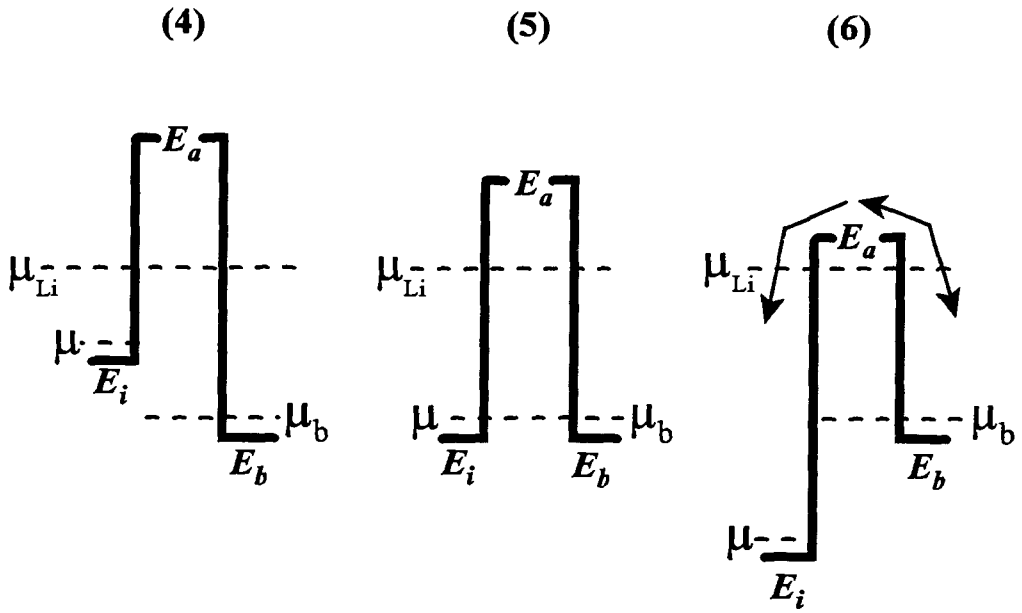

Figure 6-22. The simple model used to predict current rate and temperature dependent behavior for the electrochemical cells with hydrogen-containing carbon. (a) The energy levels of the 3 sites are shown at three steps of the discharge curve, indicated to correspond to the steps 1, 2 and 3 in figure 6-22b. In (a), chemical potentials are indicated by dashed horizontal lines. During discharge, the a-sites are in equilibrium with the i-sites, and so both are described by the same lithium chemical potential, μ, as suggested by the dashed line which extends under the a-sites. In step 3, the difference $E_a - \mu$ is small enough that reasonable amounts of lithium can occupy the a-sites as suggested by the double headed arrow. Lithium in the a-sites can empty into the b-sites, as indicated by the one-headed arrow. This arrow is one headed because the probability the lithium can return to the a-sites is negligible at this value of μ. (c) During charge, the a-sites are in equilibrium with the b-sites and both have chemical potential μ_b. In step 6 (refer to 6-22(b)) E_a is low enough that transfer to the i-sites begins. In all cases, the voltage of the cell measures μ.

where μ is measured with respect to the chemical potential, μ_{Li}, of lithium metal. The cell voltage, $V_m(x)$, therefore decreases. This is shown schematically in panel 1 of figure 6-22a and by corresponding "step 1" in figure 6-22b.

Next, we assume that there are sites available for lithium near hydrogen at the edges of the graphene sheets. For simplicity, we assume that lithium in these sites has chemical potential, μ_b, and fixed site energy, E_b, versus lithium metal. We call these sites "bonding sites". Intercalated lithium can enter the bonding sites only by passing through sites of higher energy, E_a, called activated sites. Thus, there is a barrier of height equal to $E_a - E_i$ which the lithium must overcome. If the barrier is relatively large, compared to kT, transfer to the bonding sites will hardly occur even when $\mu = \mu_b$. This is shown schematically in panel 2 of figure 6-22a and by the corresponding "step 2" in figure 6-22b. As μ increases from step 1 to step 2, figure 6-22a depicts that the energy barrier for transferring to the bonding sites decreases in magnitude.

Finally, as more lithium is intercalated, $\mu(x)$ increases to the point where transfer to the bonding sites begins to occur. This is shown schematically in panel 3 of figure 6-22a and by "step 3" in figure 6-22b. When intercalated lithium transfers to the bonding sites, heat is released. This heat is proportional to the difference, $\mu(x) - \mu_b$, and is expected for a process which shows hysteresis (McKinnon, 1983).

Now we develop a mathematical model for the process shown in figure 6-22. Assume the insertion of lithium into the carbon is made up of two parts: 1) intercalation and 2) activated bonding near hydrogen. For simplicity, take the variation of the equilibrium voltage, $V_i(x_i)$, for the intercalation process to be linear with the concentration, x_i, of intercalated lithium

$$V_i(x_i) = V_c - \frac{V_c}{x_t} \cdot x_i ;$$

$$\mu(x_i) = -eV_i(x_i) \qquad (6\text{-}1),$$

where x_t is the maximum amount of lithium which can be intercalated. This profile is shown in figure 6-23a. The equilibrium voltage profile for the bonding near hydrogen is

$$V_b(x_b) = V_0, \qquad 0 \le x_b \le x_m$$

as shown in figure 6-23b. The equilibrium voltage profile which includes both intercalation and bonding is shown in figure 6-23c. In order to make a rough match to

experiment, we set $x_t = x_m = 1$, and $V_c = 1.2$ V. The total amount of lithium in the carbon is given by

$$x = x_i + x_b .$$

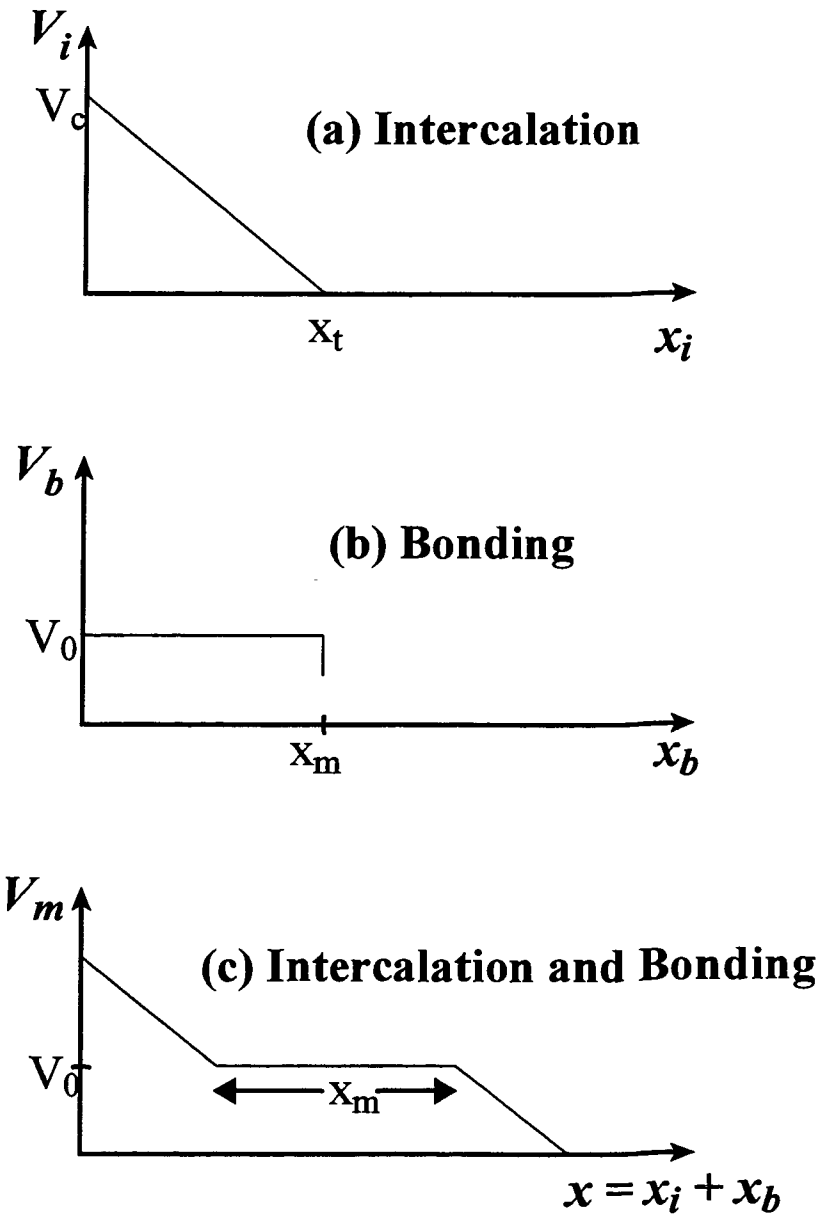

Figure 6-23. The insertion of lithium in hydrogen-containing carbon includes two parts: intercalation and activated bonding near hydrogen. (a) The equilibrium voltage, $V_i(x_i)$, changes linearly with the concentration, x_i, of intercalated lithium. (b) The equilibrium voltage, V_0, for the bonding of lithium near hydrogen. (c) The equilibrium voltage profile includes both intercalation and bonding.

Therefore

$$\frac{dx}{dt} = \frac{dx_i}{dt} + \frac{dx_b}{dt} \qquad (6\text{-}2).$$

During discharge, the chemical potential of lithium in the intercalated sites and in the activated sites is both equal to μ because they can interchange freely. The occupation of the a sites, x_a, will be given by

$$x_a = \exp\{-(E_a - \mu)/kT\}.$$

For the moment, let us assume that E_a depends on x_i through an unspecified interaction in a linear manner. Since μ has been taken to vary linearly with x_i, we set

$$E_a = E_{a0} + r\mu .$$

This is similar to the variation in the energy of activated sites proposed by Gerischer at al (Gerischer, 1978). In the simplest case of a fixed value for E_a, $r = 0$. However, r need not be zero in general. Figure 6-22a is drawn for $r = 1/2$.

Now assume that lithium in the activated sites crosses into the binding sites at a rate υ. Then

$$\frac{dx_b}{dt} = (1 - x_b)\cdot \upsilon \cdot x_a ,$$

$$\frac{dx_b}{dt} = (1 - x_b)\cdot \upsilon \cdot \exp\{-[E_{a0} - (1-r)\cdot \mu]/kT\} \qquad (6\text{-}3).$$

In the experiments with constant current to be described below, x varies at a constant rate. That is

$$x = at \qquad (6\text{-}4),$$

where a is a constant.

Then

$$\frac{dx_i}{dt} = a - \frac{dx_b}{dt} \qquad (6\text{-}5).$$

Equations (6-3) and (6-5) can be combined and integrated to give

$$x_i(t) = \int_0^t \{a - (1 - x_b)\cdot \upsilon \cdot \exp\{-[E_{a0} - (1-r)\cdot \mu]/kT\}\}dt \qquad (6\text{-}6).$$

The expression for x_i in equation (6-6) can then be inserted into equation (6-1) to obtain $V_m(x_i)$. The concentration of the intercalated atoms x_i, in the host, determines the cell voltage, so now we can calculate V_m, x_i, x_b and x as a function of time. This is done numerically, beginning with $x_i = 0$ and $x_b = 0$ at $t = 0$.

The treatment of the recharge is similar, though subtly different. During the recharge, the a sites are in equilibrium with the b sites, since lithium will interchange between them. This is shown in figure 6-23c. The rate at which lithium escapes from the b-sites will be the fraction of a-sites full, times the fraction of i sites empty, $(1 - x_i)$, times the rate at which lithium jumps from the a-sites to the i-sites (υ). Thus

$$x_a = x_b \cdot \exp\{-(E_a - E_b)/kT\},$$

and,

$$\frac{dx_b}{dt} = -\upsilon \cdot (1 - x_i) \cdot x_b \cdot \exp\{-[E_a - E_b]/kT\}.$$

If we again set

$$E_a = E_{a0} + r\mu,$$

then

$$\frac{dx_b}{dt} = -\upsilon \cdot (1 - x_i) \cdot x_b \cdot \exp\{-[E_{a0} - E_b + r\mu]/kT\} \qquad (6\text{-}7).$$

At the first glance, this is almost equivalent to equation (6-3) above. The factor $(1 - x_i)$ in (6-7) is not important because for reasonable parameters, x_b drops from one to zero over a small voltage range, so x_i does not change much during the variation of x_b.

The appearance of the factor r in equation (6-7), instead of $1 - r$ in equation (6-3), multiplying μ is an important point. In fact, the b sites empty only if the energy of the activated sites varies with μ in such a way that E_a decreases as x_i decreases. That is, the appearance of μ in equation (6-7) arises only from the μ dependence of E_a. Numerical calculations for the recharge are done in a similar manner to the discharge, except x_i and x_b are decreasing with t.

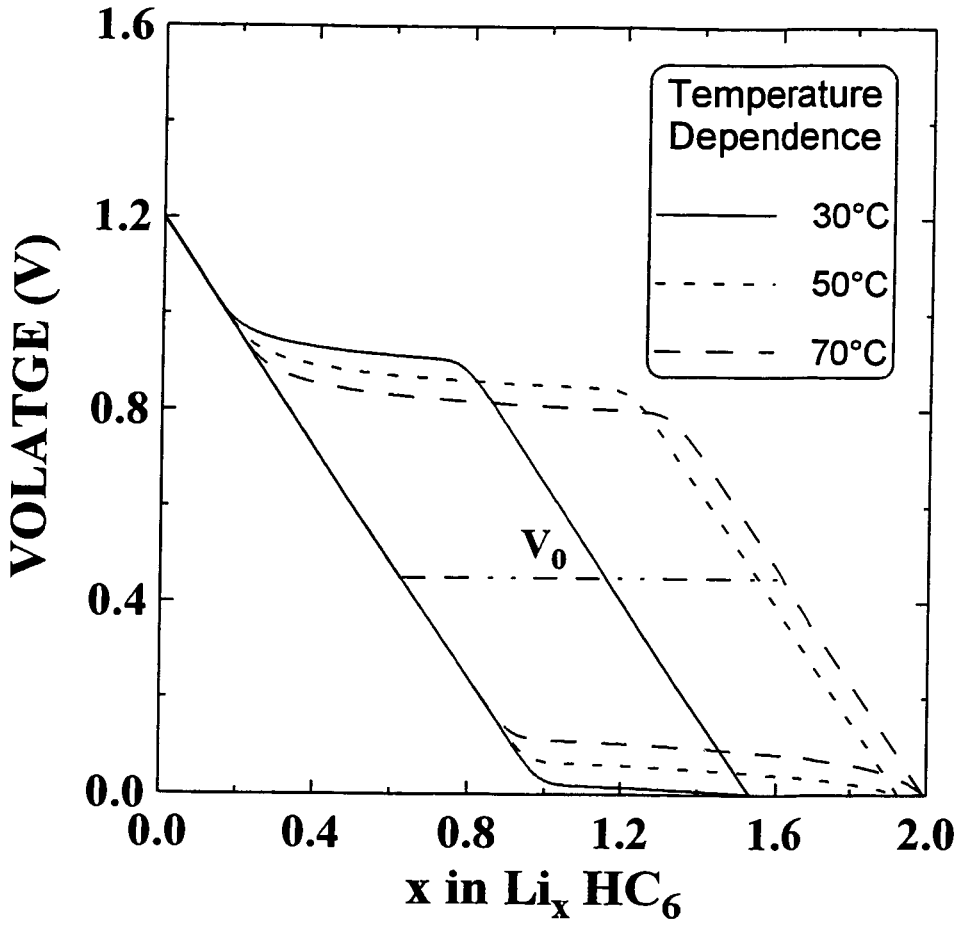

Figure 6-24. Cell voltage profiles calculated at three different temperatures, 30℃, 50℃ and 70℃, respectively. The calculation was based on a discharge/charge rate of C/25. The parameters used were $\upsilon = 1.0 \times 10^7$ / sec, V_c = *1.2 V,* V_0 = *0.45 V,* E_b = *–0.45 eV and* $x_m = x_t = 1$. $r = 1$, E_{a0} = *1.15 eV, and* $r = 0$, E_{a0} = *0.7 eV, were used for charge and discharge respectively.*

Figure 6-24 shows sample voltage profiles calculated at three temperatures for a current corresponding to a change $\Delta x = 1$ in 25 hours. The parameters used were $\upsilon = 1.0 \times 10^7$ / sec, $V_c = 1.2$ V, $V_0 = 0.45$ V, $E_b = -0.45$ eV. We used $r = 0$, $E_{a0} = 0.7$ eV for the discharge, and $r = 1$, $E_{a0} = 1.15$ eV for the charge. The choice of different E_{a0} keeps the parameter E_a the same at steps 2 and 5 in figure 6-22. While the choice of different r ensures that the difference between E_a and μ during discharge and E_a and E_b on charge both change at the same rate. For example, when $r = 0$ on discharge, E_a is fixed,

and when $r = 1$ on charge, E_a moves downward at the same rate as μ. At 30°C, the numerical calculation for the discharge part ended at 0.0 volts, with $x_i = 1.0$ and $x_b = 0.5338$, which is the starting point for the charge part. At 50°C, the discharge ended with $x_i = 1.0$ and $x_b = 0.9264$, and at 70°C, the discharge ended with $x_i = 1.0$ and $x_b = 1.0$. As shown in figure 6-24, the model produces a large hysteresis loop, similar to that seen in experiment. Although not shown in the figure, the separation in voltage between the charge and discharge scales with E_{a0}. As E_{a0} is increased (while the other parameters remain fixed) the hysteresis loop expands.

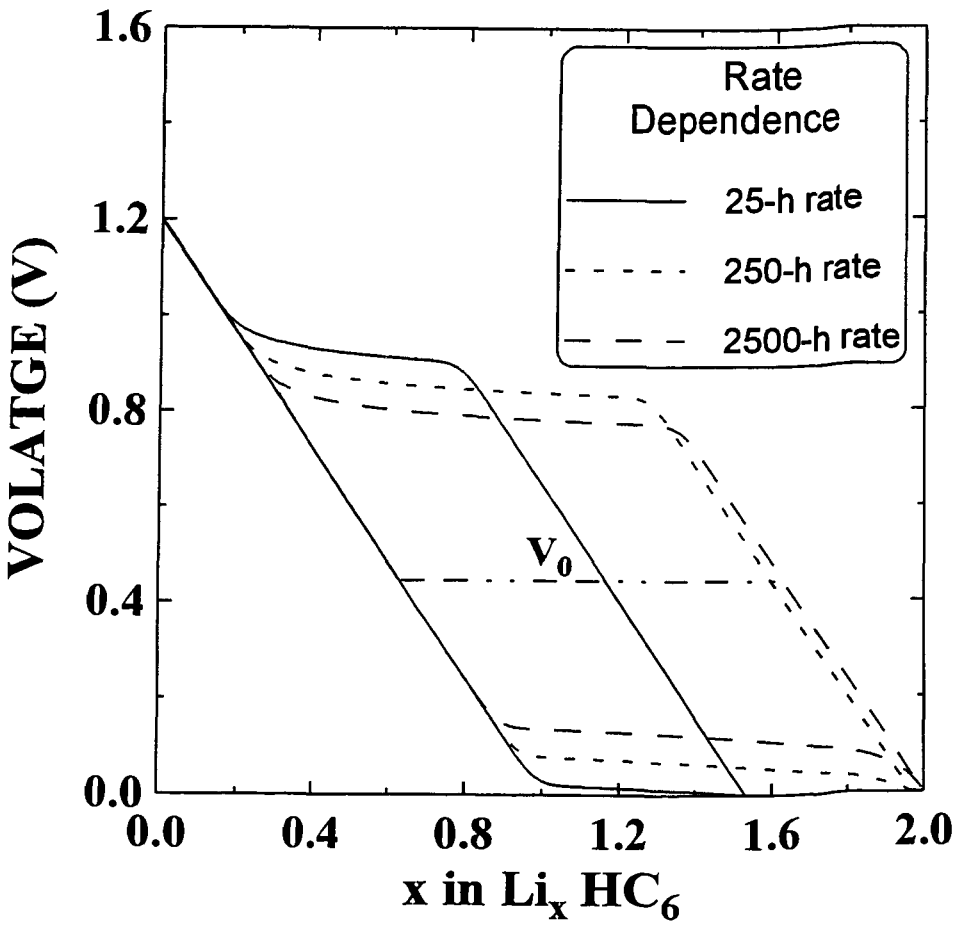

Figure 6-25. Cell voltage profiles calculated at 303 K (30 °C) for the same parameters as shown in figure 6-24, except for different discharge/charge rates, a, corresponding to C/25, C/250 and C/2500 respectively.

Figure 6-25 shows sample voltage curves calculated at 303 K for the same parameters as shown in figure 6-24, except for different values of a, corresponding to 25, 250 and 2500 hours rates. The hysteresis loop closes somewhat as the rate is slowed, but it is clear that impractical rates would be needed to measure the equilibrium behavior schematically shown in figure 6-23c. Similarly, "open circuit voltage" measurements obtained after partial discharge across the plateau, would need to wait for decades before relaxation to V_0 would occur. This is because E_{a0} is so large and υ is relatively small.

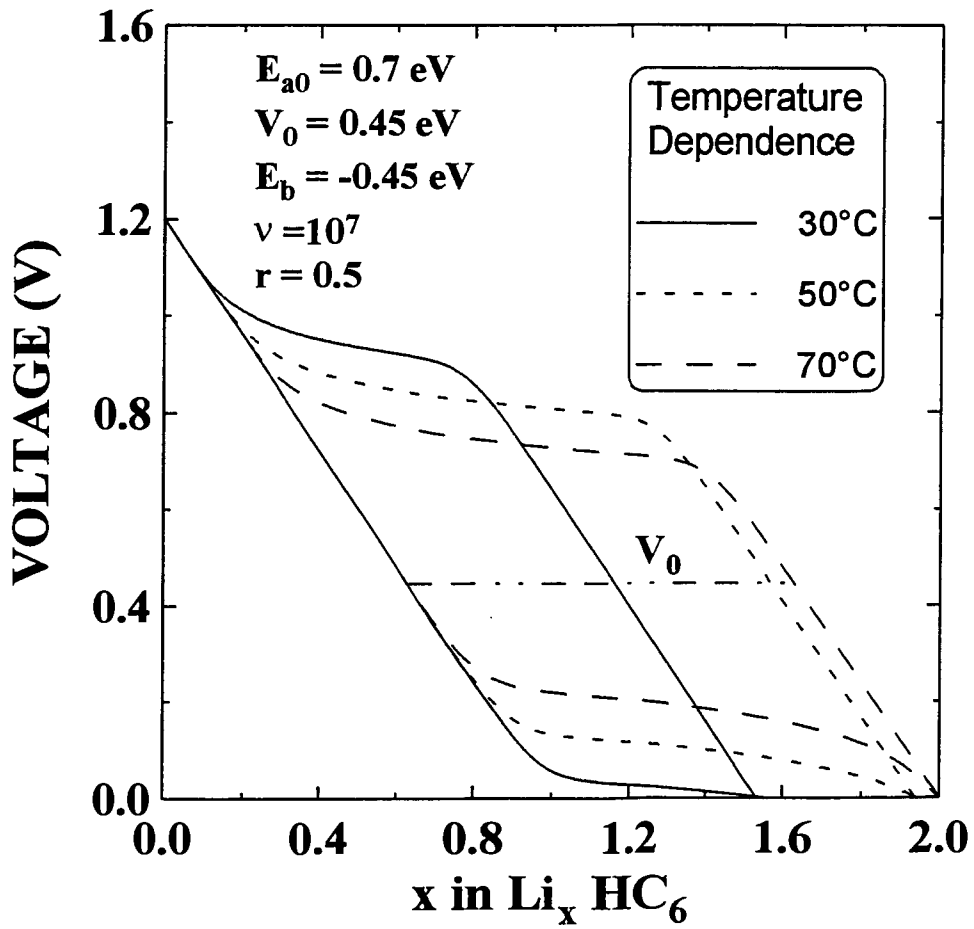

Figure 6-26. Cell voltage profiles calculated at three different temperatures, 30℃, 50℃ and 70℃, respectively. The calculation was based on the same parameters as shown in figure 6-24, except for $r = 1/2$, *and* E_{a0} = *0.7 eV for both charge and discharge.*

Of course, we do not expect r and E_{a0} to change between charge and discharge. Calculations for $r = 1/2$ and $E_{a0} = 0.7$ eV for both charge and discharge resemble those of figures 6-24 and 6-25. The calculations for $r = 1/2$ and $E_{a0} = 0.7$ eV are shown in figures 6-26 and figure 6-27, which have the same parameters as in figure 6-24 and 6-25 respectively. The plateaus in the hysteresis loop move towards $V_0 = -E_b / e$ at the same speed.

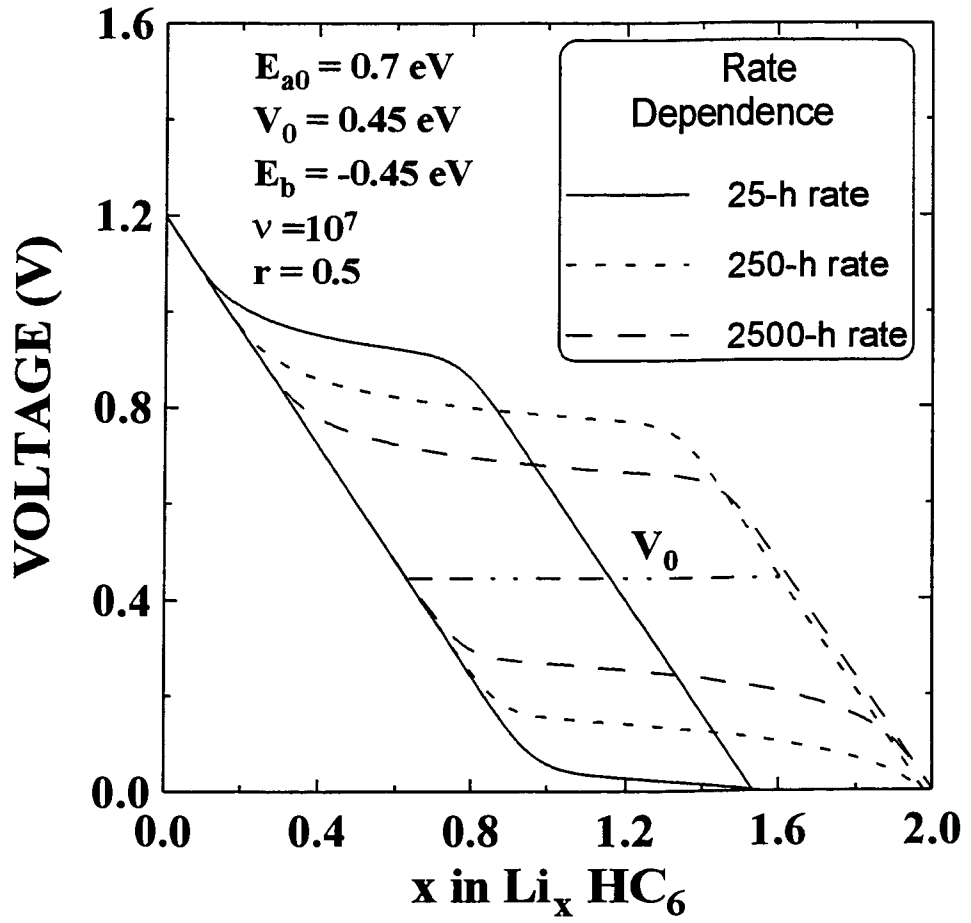

Figure 6-27. Cell voltage profiles calculated at 303 K (30℃) for the same parameters as shown in figure 6-25, except for $r = 1/2$, *and* $E_{a0} = 0.7$ *eV for both charge and discharge.*

However, if $r \neq 1/2$, then the hysteresis loop is no longer symmetric about $-E_b / e$. Figure 6-28 shows calculations for $r = 0.33$ and other parameters which will be

shown later to be consistent with experiment. For figure 6-28, we used E_{a0} = 1.16 eV $\upsilon = 10^{15}$ / sec, T = 303 K, V_c = 1.2 V, V_0 = 0.33 V, E_b = –0.33 eV, $x_m = x_t = 1$, and $r = 0.33$. One striking feature of this figure is that the charge plateau moves more rapidly than the discharge plateau as the rate shows. This is a general feature for $r < 1/2$. If $r > 1/2$ for both charge and discharge, then the discharge plateau moves more rapidly.

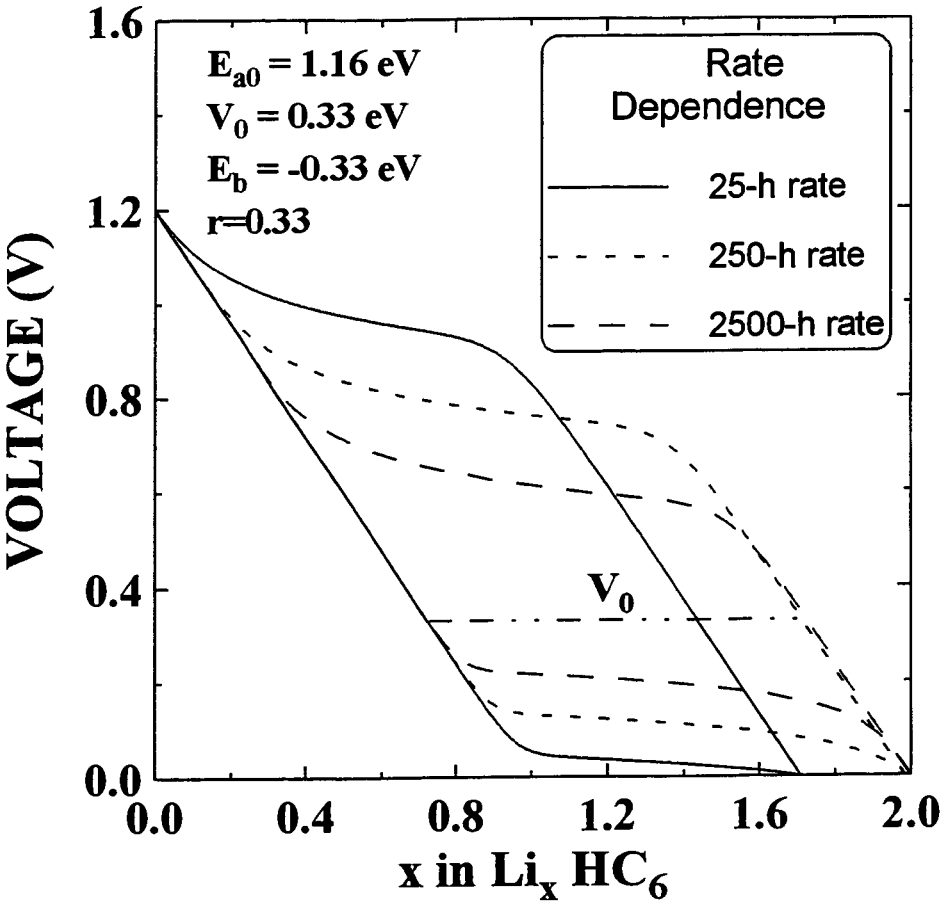

Figure 6-28. Cell voltage profiles calculated at 303 K for $r = 0.33$, and E_{a0} = 1.16 eV, $\upsilon = 1.0 \times 10^{15}$ / sec, V_c = 1.2 V, V_0 = 0.33 V, E_b = –0.33 eV. Three discharge/charge rates, a, corresponding to C/25, C/250 and C/2500 are shown.

The behavior in figures 6-24 to 6-28 suggests that the plateau voltage should depend on discharge rate and temperature in a relatively simple fashion. This can be

calculated as shown next. Equation (6-6) is substituted into equation (6-1) and then differentiated with respect to time to yield

$$\frac{dV_m}{dt} = -\left(a - (1-x_b)\cdot\upsilon\cdot\exp\left\{-\left[E_{a0} - (1-r)\cdot\mu\right]/kT\right\}\right)\cdot\frac{V_c}{x_t},$$

for $V_m < V_0$,

and,

$$\frac{dV_m}{dt} = -a\cdot\frac{V_c}{x_t}, \text{ for } V_m > V_0$$

Using the chain rule,

$$\frac{dV_m}{dx} = \frac{1}{a}\cdot\frac{dV_m}{dt} \qquad (6\text{-}8),$$

yields

$$\frac{dV_m}{dx} = -\frac{V_c}{a\cdot x_t}\left\{a - (1-x_b)\cdot\upsilon\cdot\exp\left\{-\left[E_{a0} - (1-r)\cdot\mu\right]/kT\right\}\right\} \qquad (6\text{-}9).$$

At the start of the plateau, when $x_b \cong 0$, $\frac{dV_m}{dx} \cong 0$ so we have

$$\frac{a}{\upsilon} = \exp\left\{-\left[E_{a0} - (1-r)\cdot\mu\right]/kT\right\} \qquad (6\text{-}10).$$

This can be solved for the plateau voltage, $V_p = -\mu_p / e$, as

$$V_p = \frac{kT}{(1-r)e}\ln(\upsilon/a) - \frac{E_{a0}}{(1-r)e} \qquad (6\text{-}11).$$

Equation (6-11) predicts that the plateau should shift by about 2.3×26 mV for each factor of 10 change in discharge rate if r is near zero. It also predicts that a graph of plateau voltage versus temperature should yield $\frac{-E_{a0}}{(1-r)e}$ as the intercept and $\frac{k}{(1-r)e}\ln(\upsilon/a)$ as the slope. Since $\upsilon >> a$, for any reasonable experiment, V_p will increase with temperature, as observed for the discharge in figure 6-24. For the recharge, we obtain a plateau voltage

$$V_p = \frac{kT}{re}\cdot\ln\frac{a}{\upsilon(1-x_{ip})} + \frac{E_{a0} - E_b}{er} \qquad (6\text{-}11a),$$

where x_{ip} is the value of x_i at the beginning of the recharge plateau. x_{ip} is normally close to zero, so we will neglect the factor $(1-x_{ip})$ in equation (6-11a). Now we must check these predictions with experiment.

6.3.2 Comparison of the Model with Experiment

Sample PVC700 and OXY700 have large hydrogen content, while sample OXY1000 does not. The composition of these samples is given in table 6-1. Six cells were made for each of the pyrolyzed materials. Two cells of each sample were placed in thermostats at 30.0°C, 50.0°C and 70.0°C respectively. Usually the cells were discharged to below zero volts until the plating of metallic lithium was observed. This corresponds to an equilibrium cell voltage of zero volts. During charging of cells, the plated metallic lithium was first stripped and then the inserted lithium was removed from the carbon materials.

Figure 6-29 shows the cell capacity versus cycle number for the first five cycles of cells with PVC700 electrodes. Figure 6-29a shows the results measured at 70°C, figure 29b shows the results at 50°C and figure 6-29c shows the results at 30°C. The cells were cycled at ± C/10 rates. Figure 30 shows corresponding results for OXY700. The cell capacity for PVC700 stabilizes near 800 mAh/g at 50°C and 70°C after 5 cycles, and near 600 mAh/g after 5 cycles at 30°C. For OXY700, the cell capacity stabilizes near 700 mAh/g at 70°C, near 650 mAh/g at 50°C and near 500 mAh/g at 30°C. The qualitative variation of cell capacity with temperature is expected based on figures 6-24 to figure 6-28.

After the first five cycles, the rate dependence of the hysteresis was studied at each of the three temperatures. The cells were cycled at a 10-h rate, a 20-h rate, a 10-h rate, a 40-h rate, a 10-h rate, an 80-h rate and finally a 10-h rate again. The 10-h rate cycles were included so that subtle changes, if any, in the voltage profile due to increased cycle number could be monitored.

Figure 6-31 gives a comparison of voltage profiles measured at a 10-h rate (the sixth cycle) for sample PVC700 at 30°C, 50°C and 70°C respectively. Larger capacities (as shown in figure 6-27) were found when the cells were cycled at 50°C and 70°C. The extra capacity appears as increased low voltage plateaus on discharge and increased one voltage plateaus on charge, and is attributed to the bonding capacity. Not all the bonding capacity is attained at 30°C, because the cells reach the point where lithium plating is observed, before the filling of the bonding sites is complete. At lower currents or higher temperatures, the discharge plateau voltage moves upward (as shown in figures 6-24 and 6-28) and the full capacity of the bonding sites can be accessed.

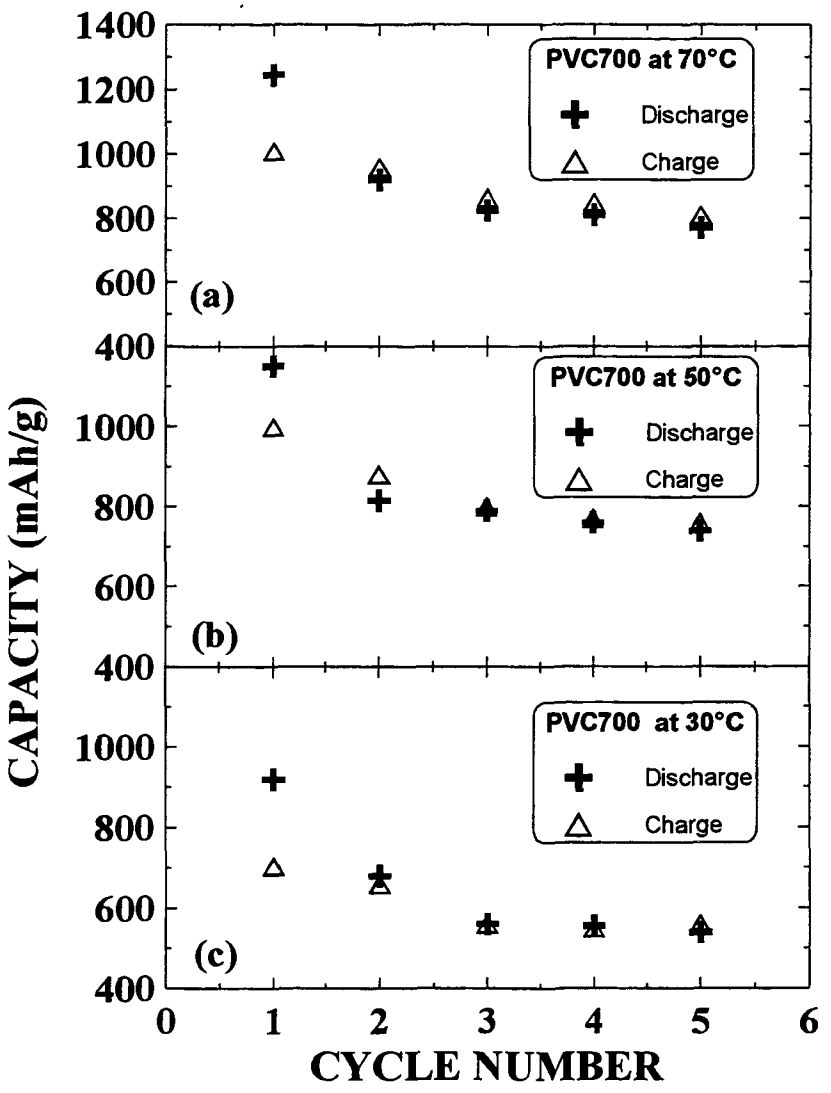

Figure 6-29. The capacities of the first five cycles for the cells made from the sample PVC700. The cells were measured at 30℃, 50℃ and 70℃, respectively.

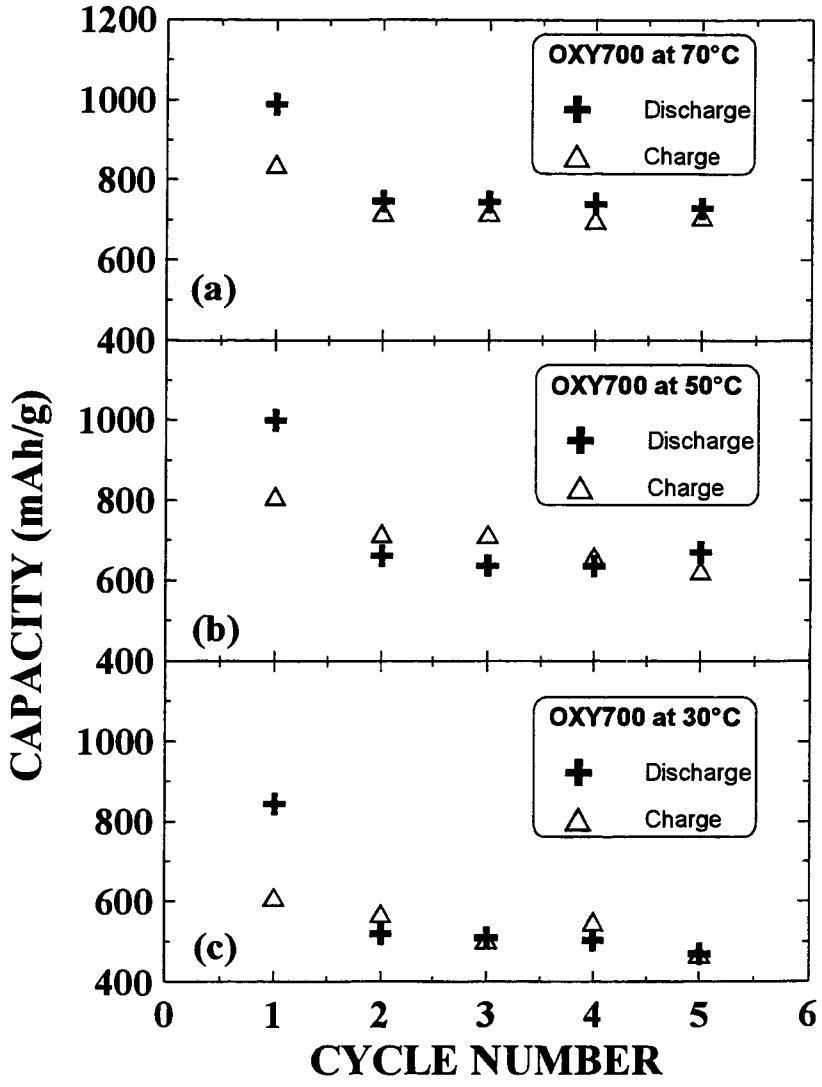

Figure 6-30. The capacities of the first five cycles for the cells made from the sample OXY700. The cells were measured at 30℃, 50℃ and 70℃, respectively.

A plateau in the voltage profile appears as a peak in the differential capacity curve. The capacity of the plateau is given by the area under the peak. The difference between the voltage profiles in figure 6-31 can be displayed more clearly in a plot of differential capacity, dx / dV, against voltage as shown in figure 6-32. The peak corresponding to the low voltage plateau on discharge moves to higher voltage and the peak corresponding to the one volt plateau on charge moves to lower voltage. A second

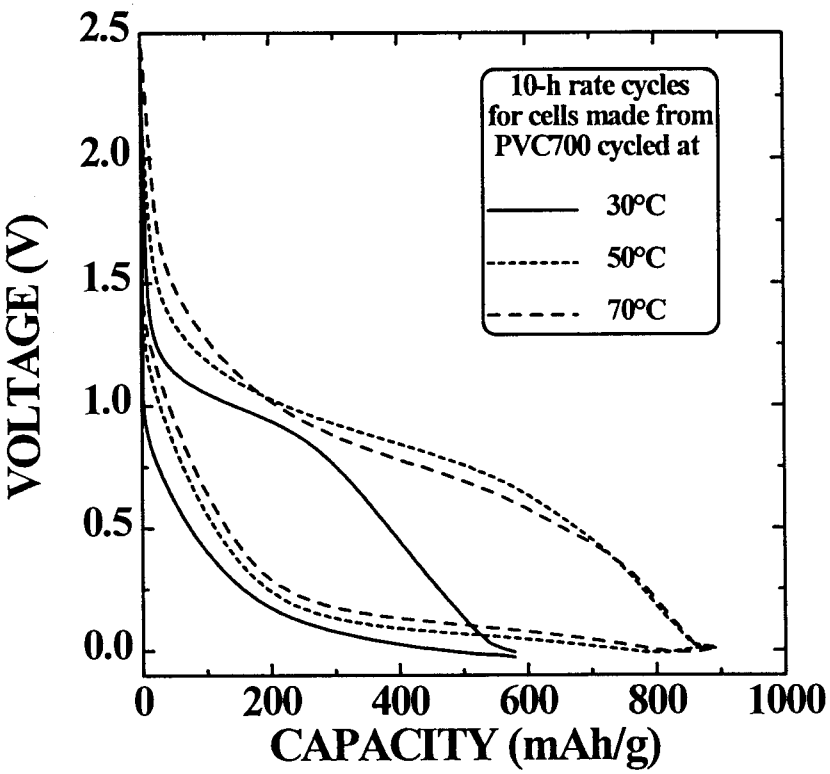

Figure 6-31. Voltage profiles for cells made from sample PVC700 tested at different temperatures, as indicated, with a 10-h rate current.

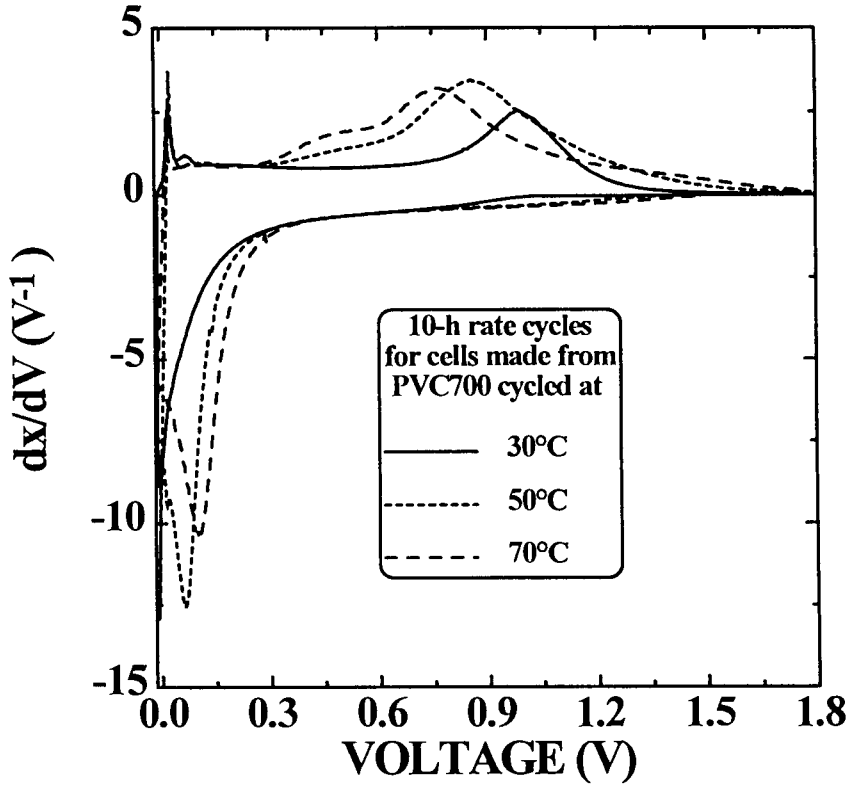

Figure 6-32. The differential capacity versus voltage for cells made from sample PVC700 corresponding to figure 6-28.

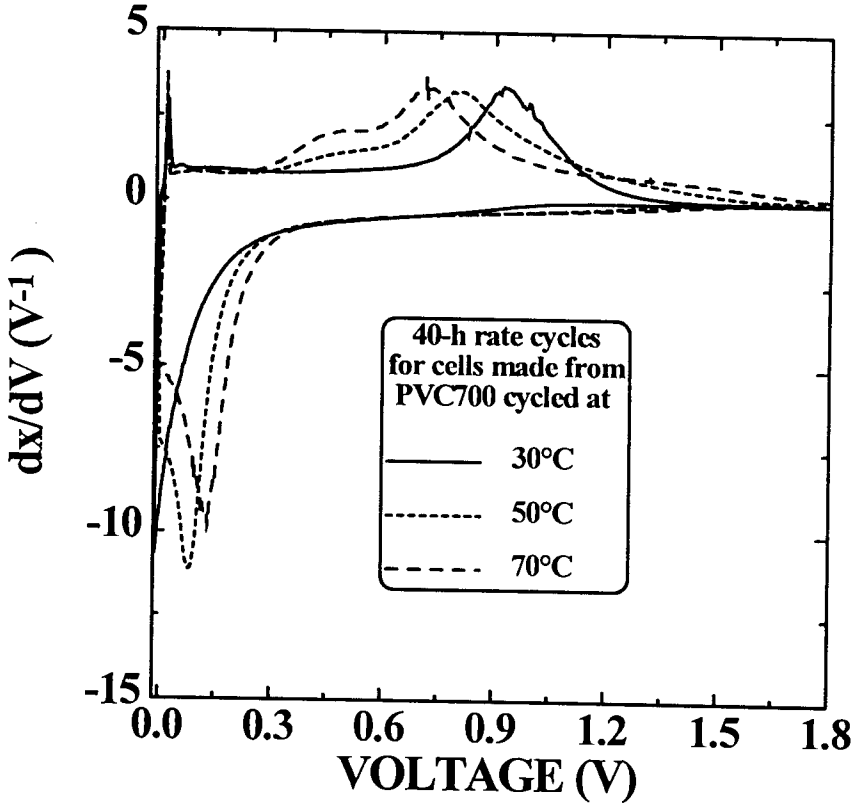

Figure 6-33. The differential capacity versus voltage for cells made from sample PVC700 tested at different temperatures, as indicated, with a 40-h rate current.

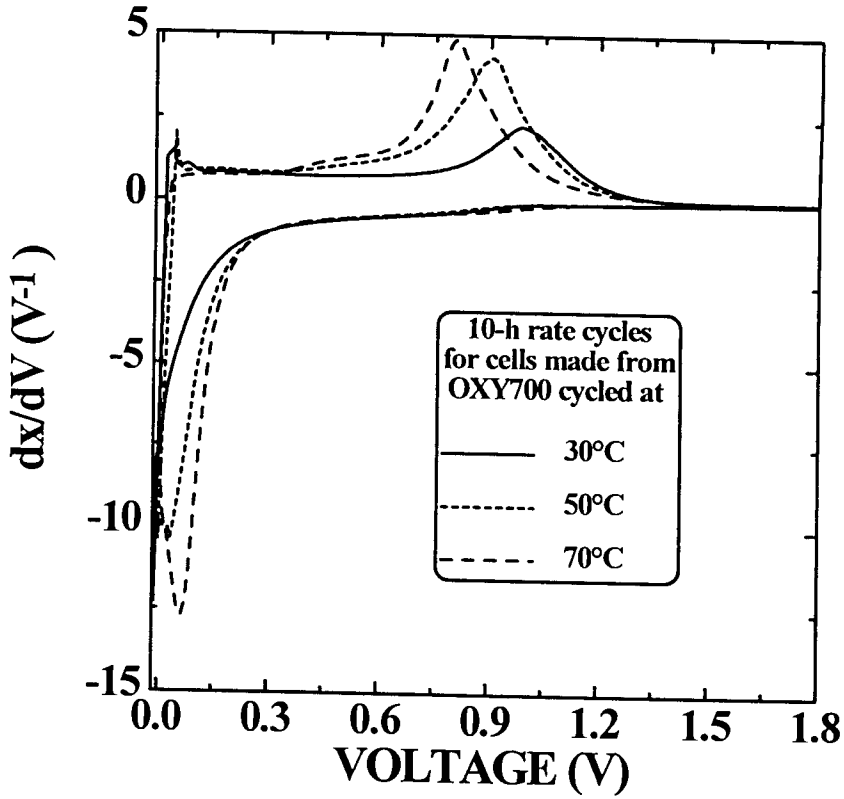

Figure 6-34. The differential capacity versus voltage for cells made from sample OXY700 tested at different temperatures as indicated, with a 10-h rate current.

peak, or shoulder, appears at the low voltage side of the charge peak at higher temperatures.

The differential curves for the 40-h rate cycles (the ninth cycles) at 30°C, 50°C and 70°C for cells using sample PVC700 are shown in figure 6-33. These display similar features to those of the 10-h rate cycles in figure 6-32. Figures 6-34 and 6-35 show, respectively, dx / dV versus voltage for cells using sample OXY700 cycled at a 10-h and a 40-h rate at the three temperatures. OXY700 shows the same features as the PVC700 sample. The behavior in figures 6-31 to 6-35 shows the same general trends as the model described by figures 6-24 to 6-28.

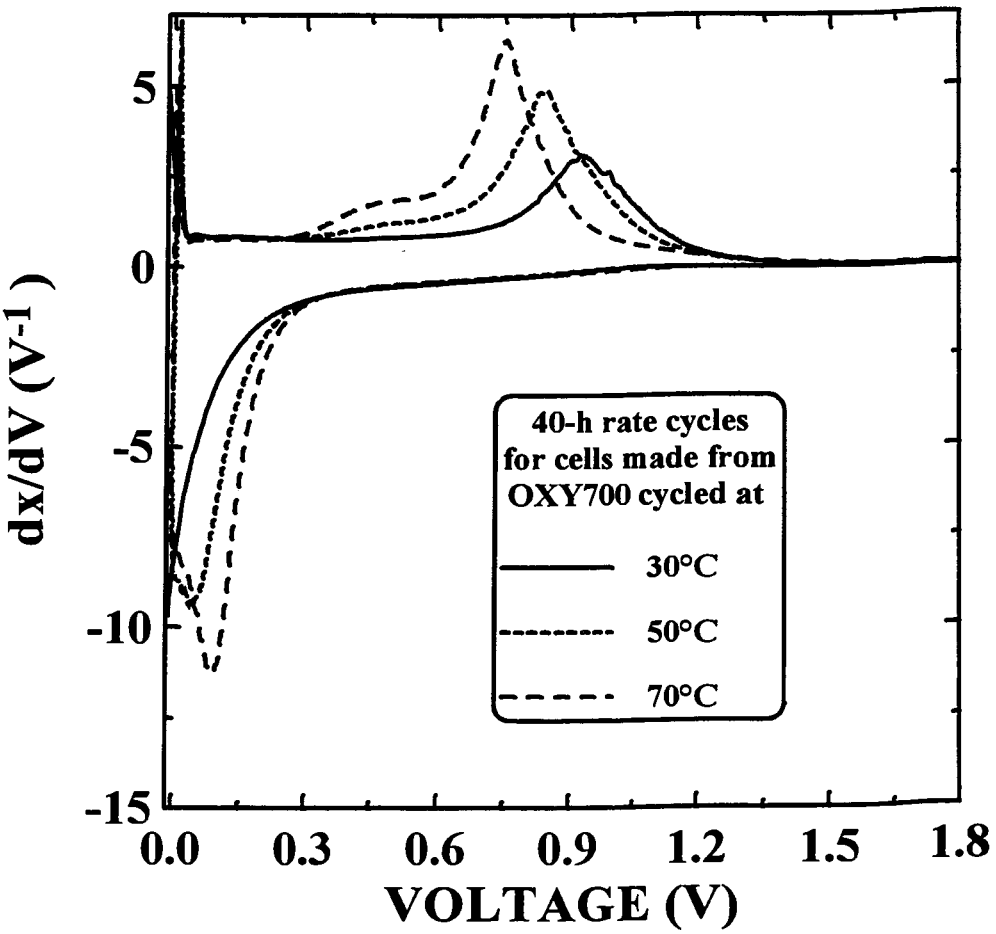

Figure 6-35. The differential capacity versus voltage for cells made from sample OXY700 tested at different temperatures as indicated, with a 40-h rate current.

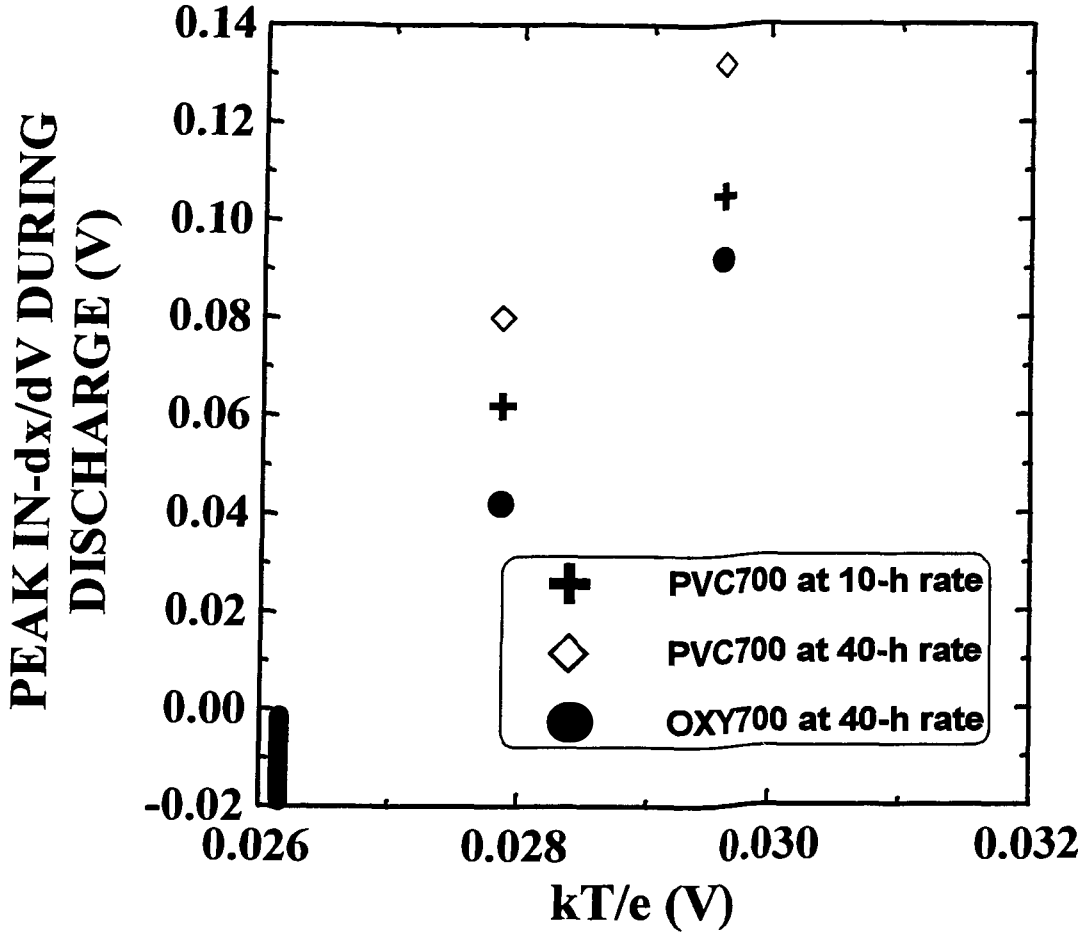

Figure 6-36. The voltage of the peak in dx / dV (low voltage plateau) versus kT/e for the discharge of cells made from the samples PVC700 and OXY700 cycled at 50°C and 70°C. The bar on the figure at 0.0261 eV represents the fact that the 30°C peak for these samples is below 0 volts.

We used the voltage of the peak in dx / dV as a measure of the position of the plateau voltage, V_p, in equation (6-11). Data of V_p versus temperature can be extracted from the measurements at 50°C and 70°C. The peak is below 0 volts for the 30°C data. The data in figures 6-32 to 6-35 can be used to estimate υ and E_{a0}. Figure 6-36 shows a graph of the voltage of the peak in dx / dV during discharge versus kT/e. The bar below zero volts represents where the 30°C peak is estimated to fall, if it could have been measured. The data points measured for the 10 hour rate (a = 1/36,000 sec^{-1}) and the 40 hour rate (a = 1/144,000 sec^{-1}) can be used to extract rough estimates of υ and E_{a0}. The

slope of an average line through the data is about 30 and yields $\upsilon \cong 10^{7\pm2}\,\mathrm{sec}^{-1}$ and the intercept with the y axis at T = 0 yields $E_{a0} = 0.7 \pm 0.2\,\mathrm{eV}$, assuming $r = 0$. There are large errors in these values due to the scatter in the data. We attach significance to the magnitude of these numbers only to point out they are similar to those used in the model calculations of figures 6-24 to 6-27.

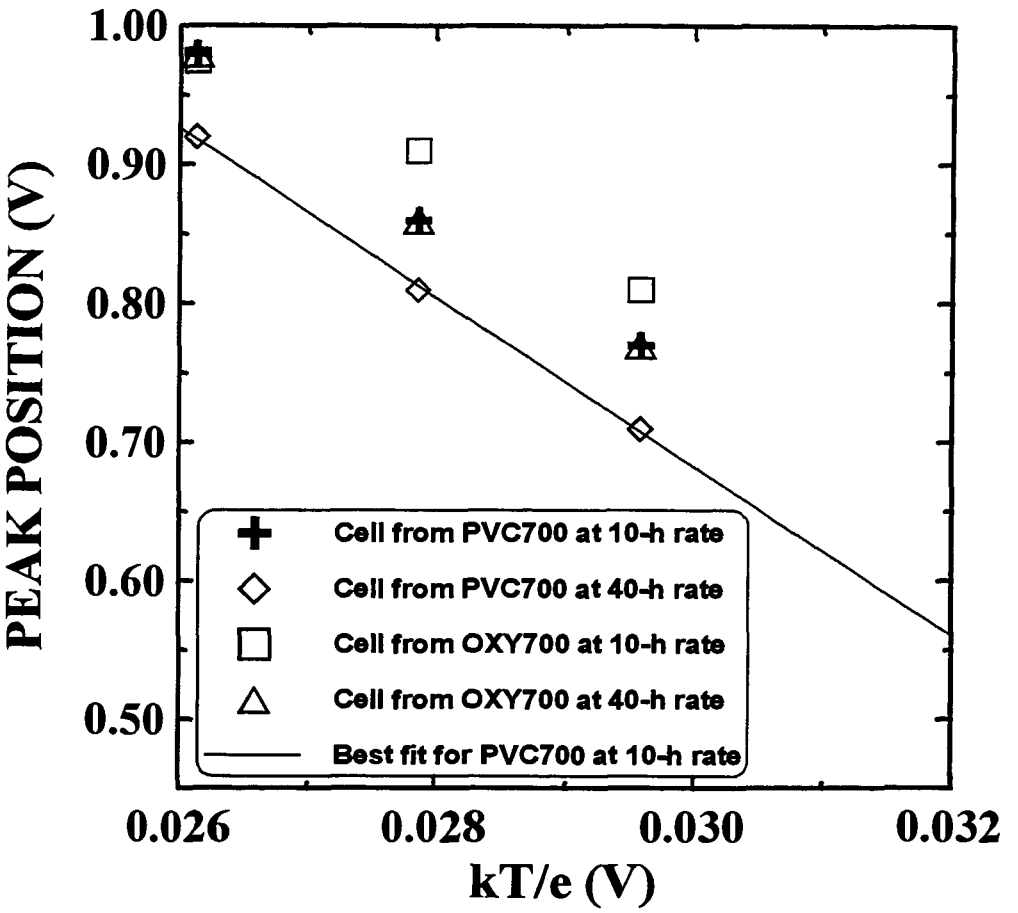

Figure 6-37. The voltage of the peak in dx / dV (one volt plateau in voltage profile) versus kT/e for the charge of cells made from the samples PVC700 and OXY700 cycled at 50 ℃ and 70 ℃.

The behavior measured during the charge is quite complex. A peak or shoulder near 0.45 V appears in all the data collected at the higher temperatures. This may indicate

that the dependence of E_a on x_i or μ is complex. We do not claim to understand this. Nevertheless, the position of the peak in dx/dV near 0.9 V on charge can be plotted versus temperature as is done in figure 6-37, and E_{a0} and υ extracted as before. The slope of the line in figure 6-34 is about –62. Assuming $r = 1$ for the charge, we obtain $E_{a0} \cong 1.6 \pm 0.3$ eV and $\upsilon \cong 10^{21\pm3}\,\text{sec}^{-1}$. These values are quite different from those obtained from the discharge. This is not surprising because the peak shifts about twice as far in voltage for the same change in temperature as the peak measured during discharge. This suggests that $r < 1/2$ for both charge and discharge.

Comparison of equations (6-11) and (6-11a) shows that the ratio of the slopes of the lines in figures 6-36 and 6-37 should be given by $\frac{-r}{(1-r)}$ for data collected at the same discharge rate, provided $x_{ip} \approx 0$. The slope of the curve for the discharge for figure 6-33 is about 30, while that for the charge is about –62. This gives $r = 0.33$, which was used in the sample calculation of figure 6-28.

We also studied the current rate dependence of the differential capacity when cells made from the PVC700 and OXY700 samples were cycled at a fixed temperature. Figure 38 shows dx/dV versus voltage for a cell of the OXY700 sample cycled at 70°C with different current rates. The data included cycles from the sixth to the twelfth with the first five cycles at a 10-h rate ignored. Although the capacity for the 10-h rate cycles was decreasing due to the demanding (70°C) cycling temperature, it is not hard to see that the discharge-charge cycle with a lower current always gave higher capacity. The two peaks corresponding to the plateaus associated with the bonding sites shifted towards each other as the discharge/charge current was reduced, as expected based on the model predictions of figures 6-24 to 6-28.

Equation (6-11) predicts that V_p should change as $-\frac{kT}{(1-r)e}\cdot\ln(a\cdot 1(\text{sec}))$ at fixed temperature during discharge. Using the peak position in dx/dV measured during discharge as V_p, figure 6-39a shows V_p plotted versus $\ln(a)$ for the discharge data of figure 6-38. The slope is –0.0281 V. Similarly, equation (6-11a) predicts that V_p should

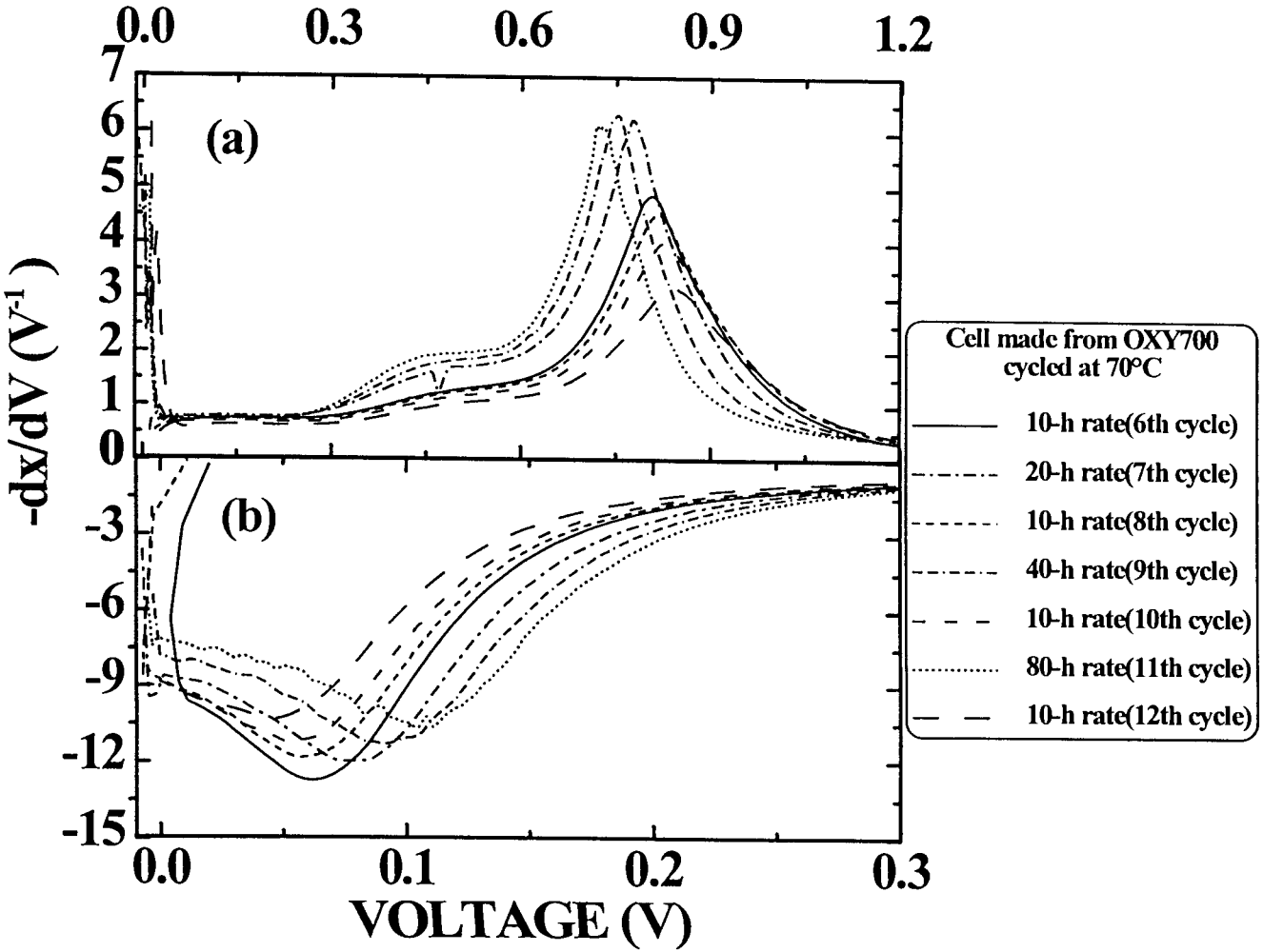

Figure 6-38. The differential capacity versus voltage for cells made from sample OXY700 cycled at 70°C with different currents as indicated. Only the sixth to the twelfth cycles are shown. The cell impedance is apparently increasing, judging by the shift in the 10-h rate data with successive cycles.

change as $\frac{kT}{re} \cdot \ln(a \cdot 1(\text{sec}))$ for the charge. Figure 6-39b shows the dependence of the peak in dx/dV on charge from figure 6-38 plotted versus ln(a). The slope is 0.0461 V. The ratio of the slopes in figure 6-36a and figure 6-36b should be $\frac{-r}{(1-r)}$, as given by a comparison of equations (6-11) and (6-11a). Solving for r, we obtain $r = 0.391$, which is in good agreement with $r = 0.33$ obtained from the temperature dependence of the plateau voltage. We stress that this agreement may be fortuitous because we have not corrected for the changes in dx/dV which are occurring with cycle number.

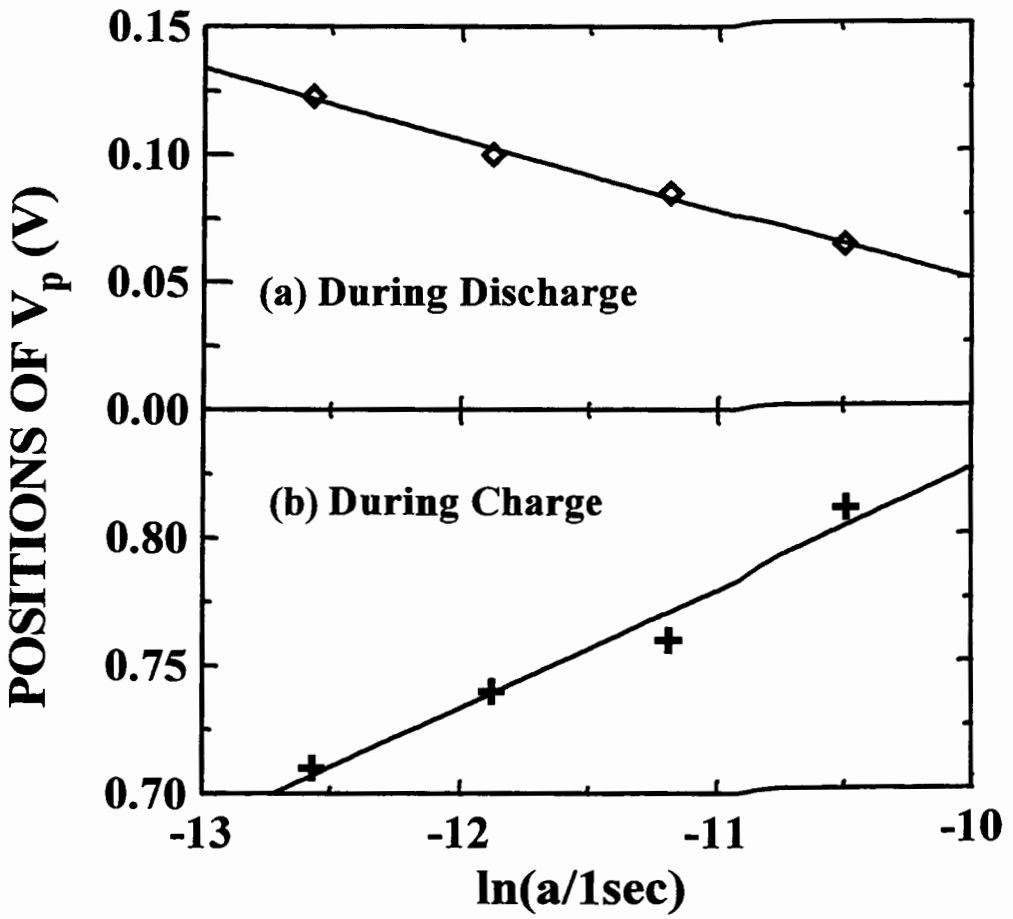

Figure 6-39. (a) The peak position in dx/dV measured during discharge, V_p, plotted versus ln(a) for the data from figure 6-38. Diamonds are measured data and the solid line is the best linear fit to the data. (b) The peak position in dx/dV measured during charge, V_p, plotted versus ln(a) for the data from figure 6-38. Crosses are measured data and the solid line is the best linear fit to the data.

The slopes and intercepts of figures 6-33, 6-34, 6-36a and 6-36b can now be used along with equations (6-11) and (6-11a) to obtain a consistent set of the parameters of E_{a0}, μ_b (or E_b or V_0) and r for hydrogen-containing carbon. We obtain $E_{a0} = 1.1 \pm 0.2$ eV, $E_b = -0.33 \pm 0.1$ eV, $V_0 = 0.33 \pm 0.1$ V, and $r = 0.36 \pm 0.03$. Figure 6-28 has been calculated with similar parameters and with $\upsilon = 10^{15}\,\mathrm{sec}^{-1}$.

Now we will examine the sample which has very little hydrogen, and hence should have few bonding sites. Figure 6-40 shows the differential capacity versus voltage for cells made from the OXY1000 sample cycled at different temperatures. The cells were cycled at a 10-h rate. Increasing the temperature to 50 or 70°C has little effect on the position and size of the peaks near zero volts. These peaks correspond to the low voltage plateaus on both discharge and charge, which are thought to result from the adsorption of lithium on internal surfaces of nanopores present in such a hard carbon (see chapter 7).

Changing the rate at which the cells were cycled had little effect on the peaks in the differential capacity, as shown in figure 6-41. Both figures 6-40 and 6-41 show evidence that the mechanism of lithium insertion in hard carbon without hydrogen(OXY1000) is different from that in hydrogen-containing carbons (like PVC700 and OXY700). However, in figures 6-40 and 6-41, small amounts of extra capacity were observed between 0.7 to 1.2 V on charge. This extra peak in the dx/dV curve showed a dependence on both temperature and current like the hydrogen-containing carbons. Since OXY1000 has H/C = 0.05 ± 0.03, we believe this peak is caused by the bonding sites near the residual hydrogen.

Figure 6-42 shows that the resistive overvoltage in our cells cycled at 70°C is very small. This is because the peak in dx/dV measured during discharge does not shift appreciably in position as the current is changed. During charge, the sharp peak near zero volts does not shift, while the higher voltage peak (near one volt), associated with emptying the bonding sites, shifts significantly. This proves that the effects seen in figure 6-35 are not due to changes in the resistive overvoltage, but are really caused by the rate dependence of filling and emptying the bonding sites.

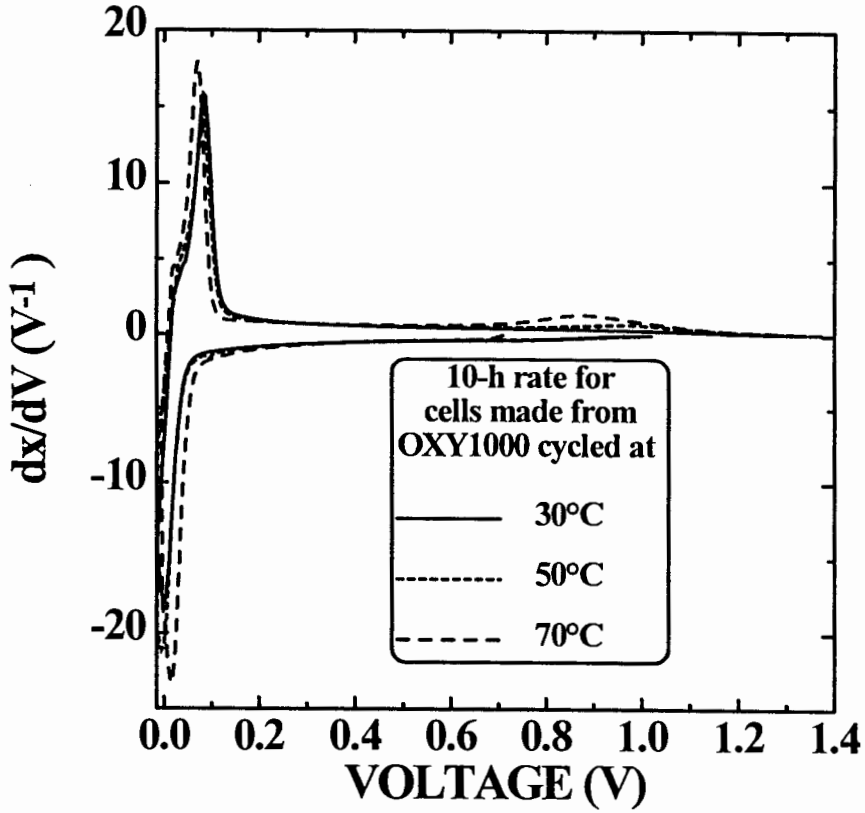

Figure 6-40. The differential capacity versus voltage for cells made from sample OXY1000 tested at different temperatures as indicated, with a 10-h rate current.

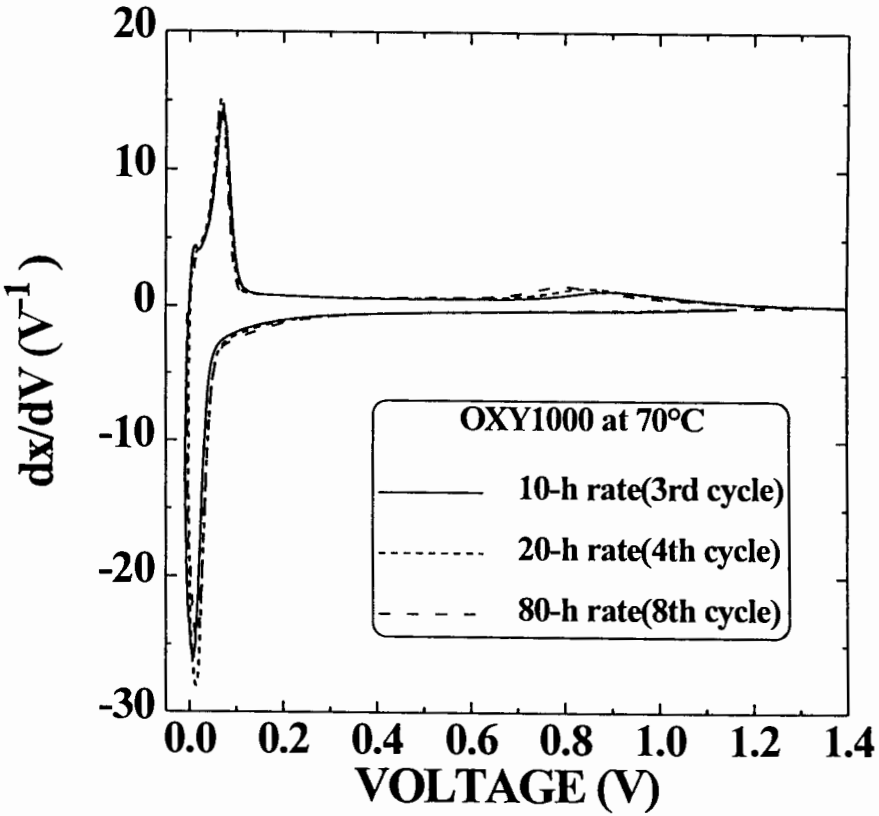

Figure 6-41. The differential capacity versus voltage for cells made from sample OXY1000 cycled at 70°C with different currents as indicated. Only the third, the fourth and the eighth cycles are shown with 10-h, 20-h and 80-h rate currents, respectively.

The simple model provides a conceptual framework that describes the overall features associated with the hysteresis observed during lithium insertion in hydrogen-containing carbons. Clearly, one could expect distributions in the energy of the activated sites, E_a, from place to place in the sample, and non-linear variations of E_a with μ. It is not our intention to investigate such possibilities here. The recharge of the hydrogen-containing carbons seems much more difficult to model than the discharge. In particular, the double peaks which appear during the charge at low rates and high temperatures is still a mystery.

6.3.3 Relaxation Experiments

A coin cell containing the PVC700 sample was studied with the MacPile charger at 30°C. The cell was first cycled once to eliminate the irreversible capacity prior to the relaxation study. The cell was discharged for 2 hours with a constant current (CC) corresponding to a 40-h rate before its relaxation. After the cell was tested for about 700 hours, a 4 hour discharge period was used for the CC discharge instead of a 2 hour period. (We thought this maight save time, but actually it did not as shown later.) During the charge, the cell was charged with CC for 4 hours before relaxation. Figure 6-42 shows the voltage plotted versus time for the open circuit voltage (OCV) measurement. The inset in figure 6-42 is the "boxed position" during discharge in the plotted voltage curve. The inset is divided into two parts by a straight line, which labels when the CC segment was changed from 2-h to 4-h long. It is clear that this change does not affect the relaxation data collected for the voltage profile of the OCV measurement.

The voltage profile for the OCV measurement of the PVC700 sample is shown in figure 6-43 compared to that measured with a 40-h rate CC. The voltage profile of the OCV measurement in figure 6-43 is approximately equivalent to that of a CC measurement with a very small constant current. The estimated magnitude of this current will be considered later below. In this figure, the low voltage plateau during discharge moves upward by about 0.10 volts compared to the CC data, and the one volt plateau during charge moves downward by 0.25 volts. The plateaus move with different speed.

The ratio of the shifts of two plateaus satisfies $\frac{r}{1-r} = \frac{0.10}{0.25}$ as described in section 6.3.2.

Therefore, r ≈ 0.29, in approximate agreement with r ≈ 0.33 which was obtained in section 6.3.2.

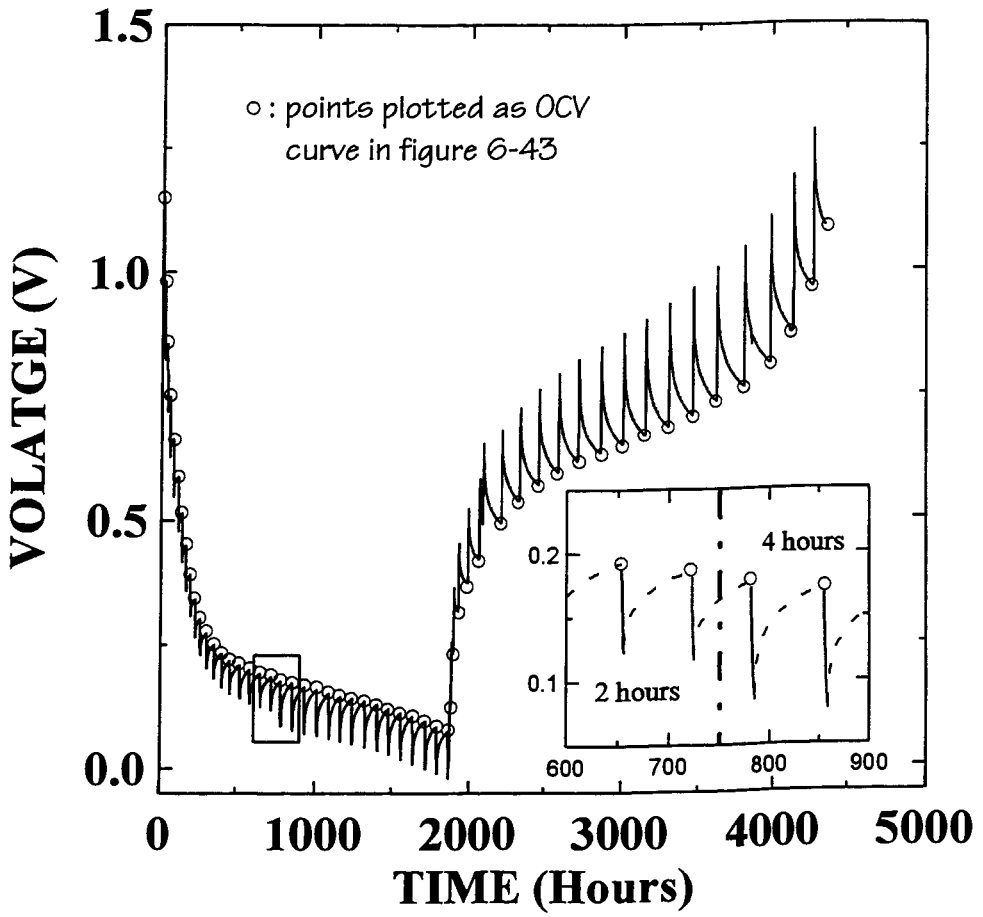

Figure 6-42. The voltage is plotted versus real time for the MacPile experiment. The inset enlarges the boxed portion at the left hand side of the figure. The solid lines in the inset show the CC discharge segments, and the dashed lines show the relaxation parts. The vertically dashed line in the inset labels where the CC segment was changed from 2-h to 4-h long.

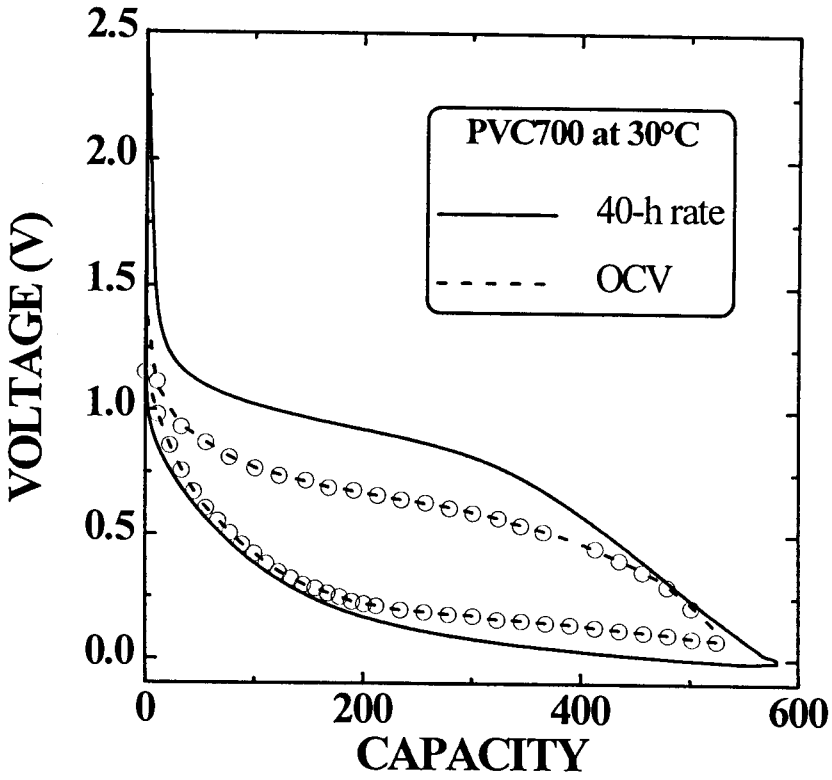

Figure 6-43. Voltage profiles for the OCV measurement and for a normal 40-h rate measurement with constant current. Open circles show recorded points, as shown in figure 6-42.

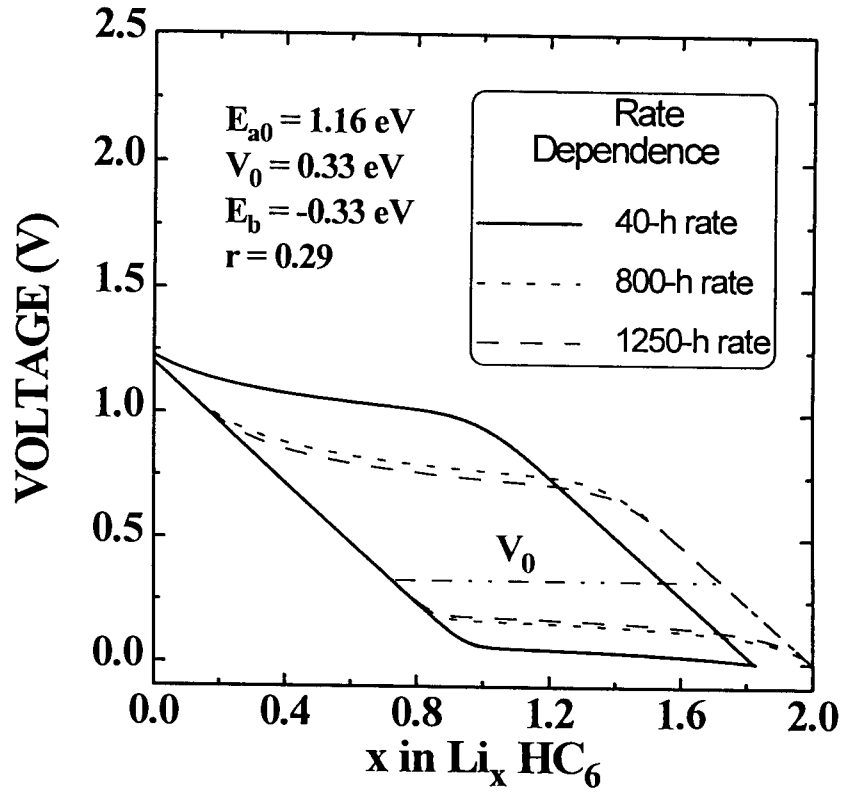

Figure 6-44. Cell voltage profiles calculated at 303 K for r = 0.29, *and* E_{a0} = *1.16 eV,* $\upsilon = 1.0 \times 10^{15}$ / sec, V_c = *1.2 V,* V_0 = *0.33 V,* E_b = *–0.33 eV. Three discharge/charge rates corresponding to C/40, C/800 and C/1250 are shown.*

Figure 6-44 shows calculated cell voltage profiles for CC measurements at 30°C, based on the model developed in section 6.3.1. The parameters used in this figure are $r = 0.29$, $E_{a0} = 1.16$ eV, $\upsilon = 1.0 \times 10^{15}$ / sec, $V_c = 1.2$ V, $V_0 = 0.33$ V, and $E_b = -0.33$ eV. The three discharge/charge rates shown correspond to C/40, C/800 and C/1250 respectively. The low voltage plateau moves up about 0.10 V for the C/800 case, and the one volt plateau moves down about 0.25 V for the C/1250 case. Therefore we expect that the OCV measurement approximately corresponds to a CC measurement with a 1000-h rate.

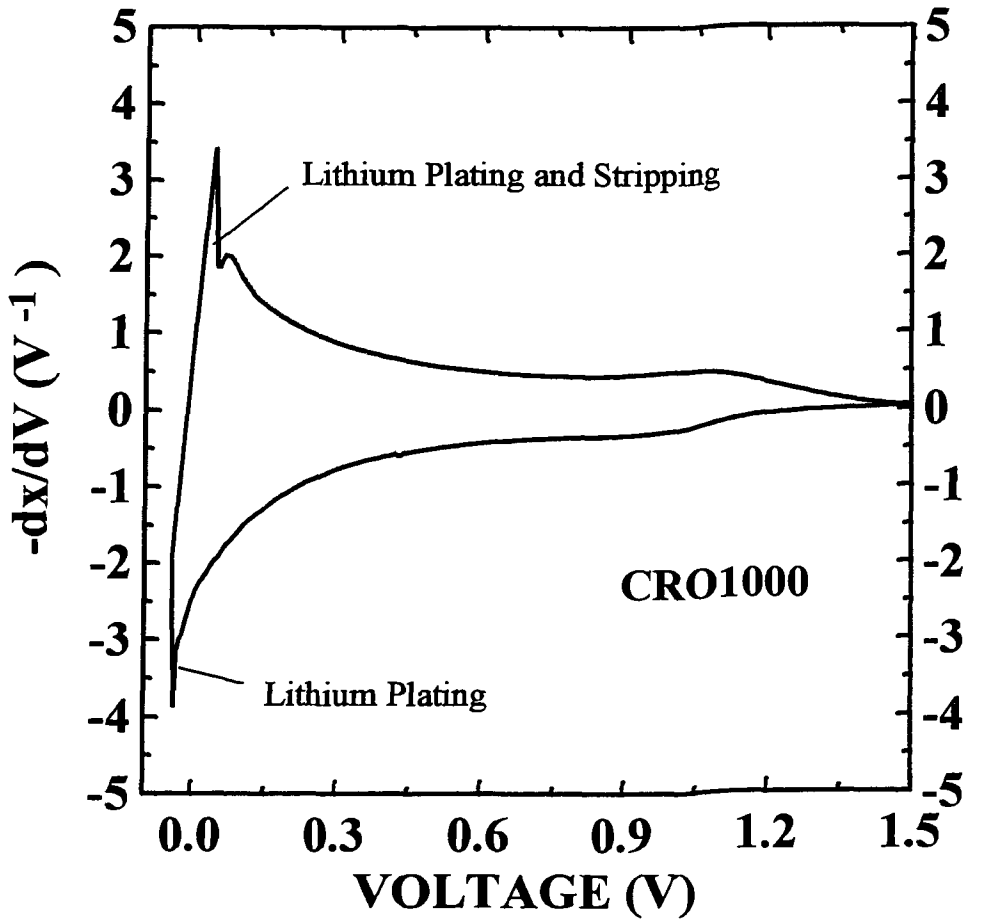

Figure 6-45. Differential capacity for the second cycle of a cell made from the CRO1000 carbon sample.

The OCV measurement took about six months. The relaxation period is stopped when the rate of change of the cell voltage is less then 0.3 mV/h, which means the OCV

measurement roughly corresponds to an 4000-h rate if the cell voltage changes linearly with x_i as described by equation (6-1). However, the intercalation capacity is not a linear function of voltage. For example, figure 6-45 shows dx/dV versus V for the CRO1000 sample, which is thought to roughly represent the intercalation capacity. The derivative, dx/dV, changes with voltage. Therefore, a 0.3 mV/h relaxation rate corresponds to different effective constant currents depending on the voltage where the relaxation takes place. Since the differential capacity is larger at low voltages, the corresponding effective currents at low voltages are larger than at high voltages. Hence, a more reliable estimate will give an effective CC rate three to five times larger than an 4000-h rate, i.e., about a 1000-h rate.

Figures 6-46 and 6-47 show selected relaxation curves, plotted as voltage versus time, for both discharge and charge respectively. These relaxation curves can be calculated from the model developed in section 6.3.1. During the relaxation period, $dx/dt = 0$. Therefore, $\frac{dx_i}{dt} + \frac{dx_b}{dt} = 0$.

From equations (6-1) and (6-3) for the discharge, the voltage versus time for the relaxation can be obtained,

$$\frac{dV}{dt} = \frac{V_c}{x_t} \cdot (1 - x_b) \cdot \upsilon \cdot \exp\left\{-\left[E_{a0} + (1 - r) \cdot eV\right] / kT\right\} \qquad (6\text{-}12).$$

To obtain equation (6-12), we assume that the variation in x_b during relaxation is small compared to 1 and can be neglected compared to the exponential term. Hence,

$$\frac{dV}{dt} \propto \exp\left\{-\left[E_{a0} + (1 - r) \cdot eV\right] / kT\right\}.$$

So,

$$\ln\left(\frac{dV}{dt}\right) = -\frac{(1 - r)}{kT} \cdot eV + const1 \qquad (6\text{-}13),$$

where the constant, const1, is about −10.6, if the parameters used in equation (6-12) are $E_{a0} = 1.16$ eV, $\upsilon = 1.0 \times 10^{15}$ / sec, $V_c = 1.2$ V, $V_0 = 0.33$ eV, $x_t = 1.0$, and $x_b = 0.6$.

Similar results can be obtained for the charge from equations (6-1) and (6-7) as follows,

$$-\frac{dV}{dt} = \frac{V_c}{x_t} \cdot (1 - x_i) \cdot x_b \cdot \upsilon \cdot \exp\left\{-\left[E_{a0} - E_b - r \cdot eV\right] / kT\right\} \qquad (6\text{-}14).$$

Hence,

$$\ln\left(-\frac{dV}{dt}\right) = \frac{r}{kT} \cdot eV + const2 \qquad (6\text{-}15),$$

where the constant, const2, is about –23.5, if the parameters used in equation (6-14) are $E_{a0} = 1.16$ eV, $\upsilon = 1.0 \times 10^{15}$ / sec, $V_c = 1.2$ V, $V_0 = 0.33$ eV, $x_t = 1.0$, $x_i = 0.2$, $x_b = 0.4$, and $E_b = -0.33$ eV.

Therefore, from equations (6-13) and (6-15), we predict that plots of $\ln\left(\frac{dV}{dt}\right)$ or $\ln\left(-\frac{dV}{dt}\right)$ versus V should be straight lines. These are shown in figures 6-48 and 6-49 for both the discharge and charge, which correspond to figures 6-46 and 6-47 respectively. Linearity is excellent after the rapid changes in dV/dt at small times due to the elimination of the voltage drop across the internal resistance. This can be clearly seen in figures 6-48 and 6-49.

The average of the gradual slopes for the discharge in figure 6-48 is –46 resulting in $r \approx -0.20$, and the average of the gradual slopes for the charge in figure 6-49 is 26 resulting in $r \approx 0.68$. These give inconsistent results! We believe the inconsistency may come from systematic measurement errors. This will modify equations (6-12) and (6-14) to be,

$$\frac{dV}{dt} = \frac{V_c}{x_t} \cdot (1 - x_b) \cdot \upsilon \cdot \exp\left\{-\left[E_{a0} + (1 - r) \cdot eV\right] / kT\right\} + f(V). \qquad (6\text{-}16),$$

and,

$$-\frac{dV}{dt} = \frac{V_c}{x_t} \cdot (1 - x_i) \cdot x_b \cdot \upsilon \cdot \exp\left\{-\left[E_{a0} - E_b - r \cdot eV\right] / kT\right\} + f'(V) \qquad (6\text{-}17).$$

In the above equations (6-16) and (6-17), the extra terms, f(V) and f'(V), will effect the slopes in both figures 6-48 and 6-49. Therefore, inconsistent values of r were obtained.

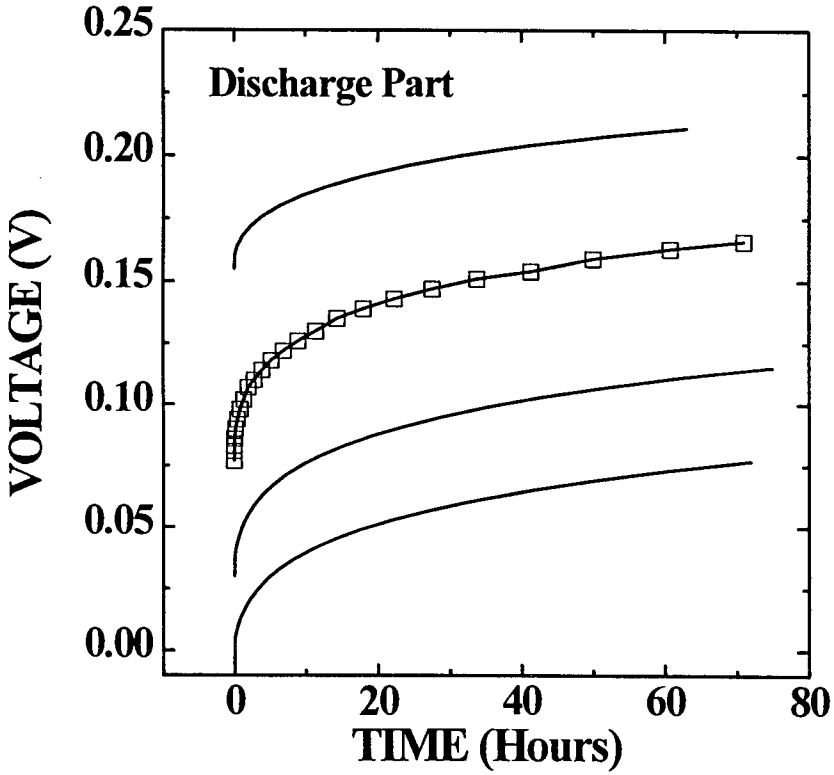

Figure 6-46. Selected relaxation curves plotted as voltage versus time for the discharge. Open squares show recorded data for one of the relaxation curves. The rapid changes in voltage for short times are due to the elimination of the voltage drop across the internal resistance.

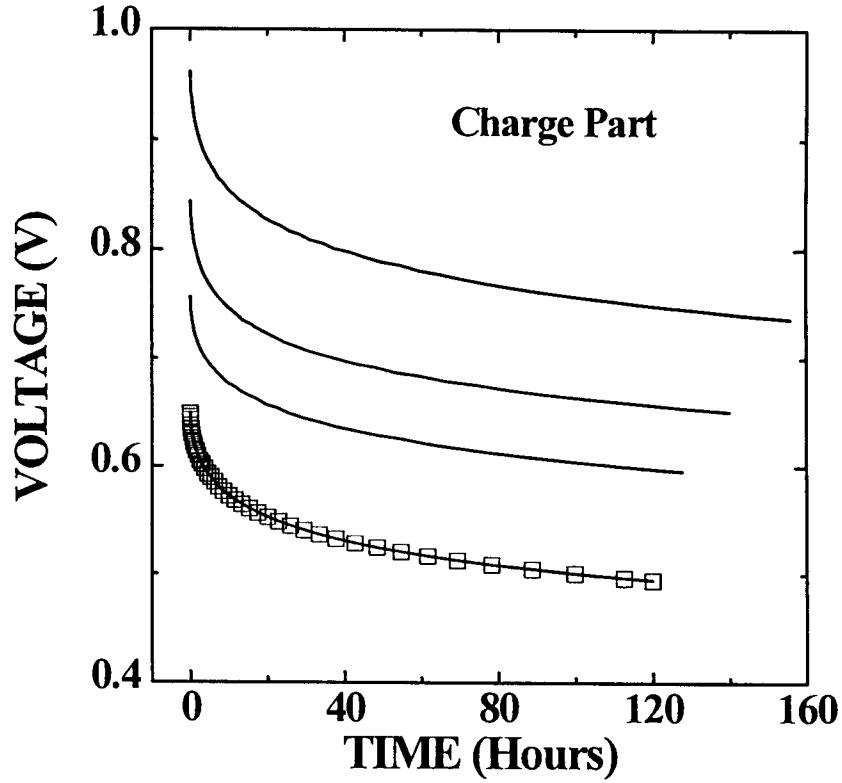

Figure 6-47. Selected relaxation curves plotted as voltage versus time for the charge. Open squares show recorded data for one of the relaxation curves. The rapid changes in voltage for short times are due to the elimination of the voltage drop across the internal resistance.

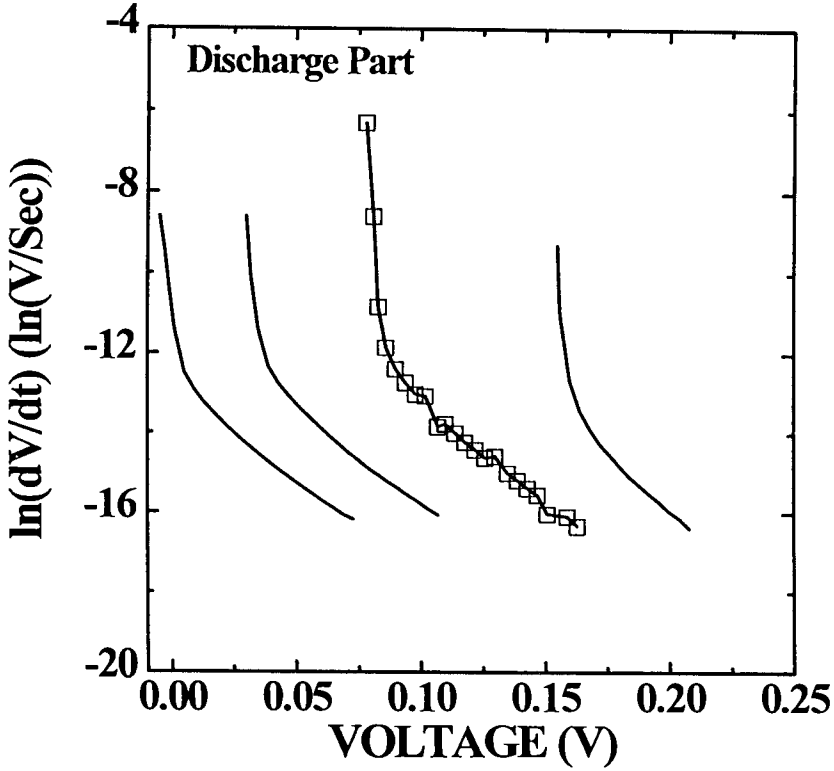

Figure 6-48. Semi-log plot for the selected relaxation curves obtained for the discharge process. Open squares show data points for one of the relaxation curves. The rapid changes for the first several points of the relaxation are due to the elimination of the voltage drop across the internal resistance.

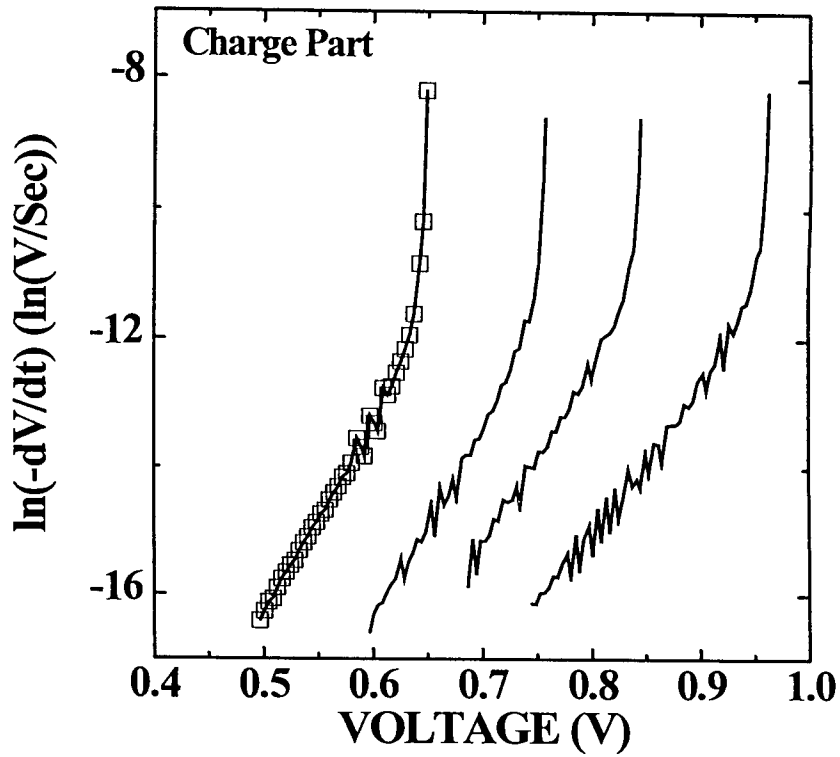

Figure 6-49. Semi-log plot for the selected relaxation curves obtained for the charge process. Open squares show data points for one of the relaxation curves. The rapid changes for the first several points of the relaxation are due to the elimination of the voltage drop across the internal resistance.

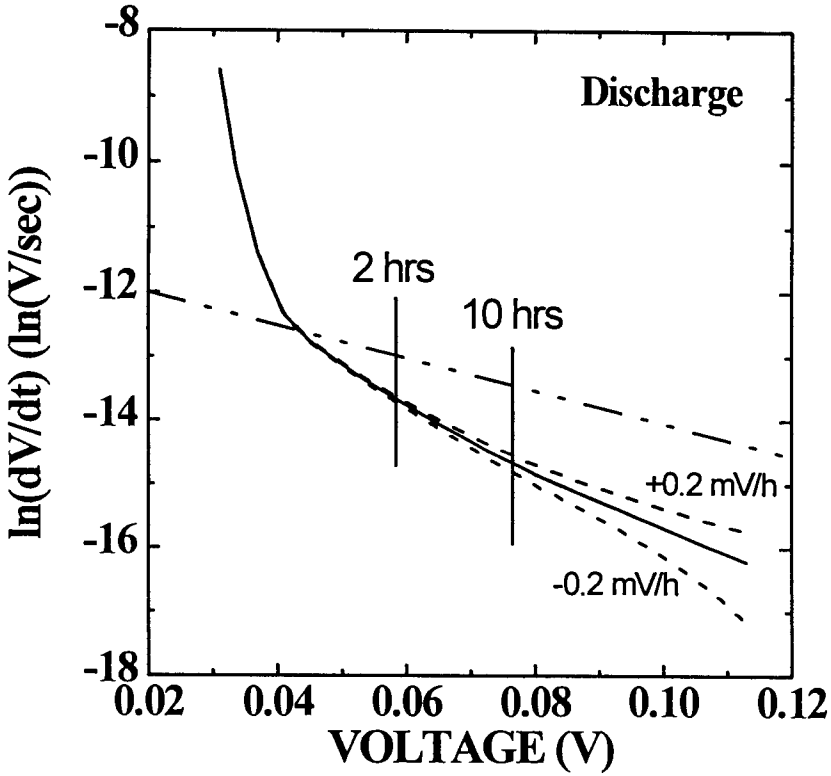

Figure 6-50. The experimental data is compared to the "corrected" data (dashed curves) for the discharge. A systematic drift of ± 0.2 mV/h is considered in two corrected curves respectively. The dashed straight line has the slope corresponding to r=0.33. Relaxation times of 2 hours and 10 hours are marked by two vertical lines.

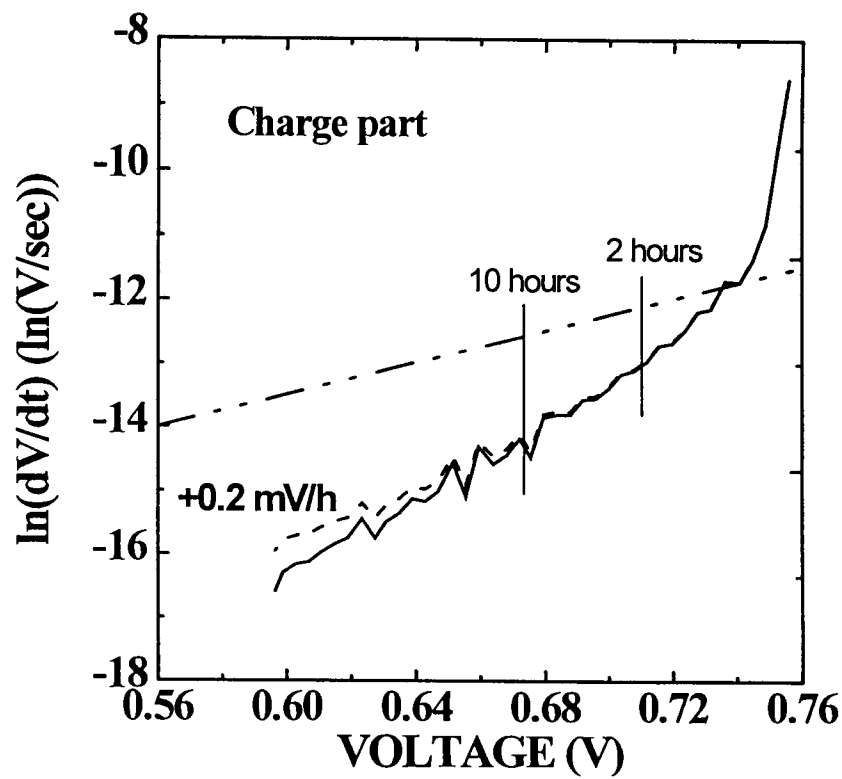

Figure 6-51. The experimental data is compared to the corrected data (dashed curve) for the charge. A systematic drift of + 0.2 mV/h is considered in the corrected curve. The dashed straight line has the slope corresponding to r=0.33. Relaxation times of 2 hours and 10 hours are marked by two vertical lines.

One simple case is that the extra term, f(V) or f'(V), is constant. This may be caused by side reactions in the cell which consume lithium or by self discharge of the cell. To examine the sensitivity of the measurement to small values of f(V), we considered -0.2 mV/h $<$ f(V) $<$ 0.2 mV/h.

Figure 6-50 shows two corrected curves, $\ln\left(\frac{dV}{dt}\right)$ versus V, during the discharge, where we suppose values of f(V) of $\pm$ 0.2 mV/h respectively. The experimental data, one selected curve from figure 6-48, is also included in figure 6-50 as a solid line for comparison. The experimental data has a with a slope of -42, and an intercept of -11.5 which corresponds well to const1 in equation (6-13). If a systematic drift due to side reactions is 0.2 mV/h, the data is tilted and its slope becomes -29.4. This slope gives $r \approx 0.23$, which is close to 0.33. Figure 6-50 also shows a straight dashed line with the slope corresponding to $r=0.33$. These considerations show that very small systematic voltage drifts in these cells are troublesome in these types of measurements.

Figure 6-51 shows the similar results for the charge. One curve from figure 6-49 is shown in the figure, compared with the corrected curve assuming 0.2 mV/h of systematic drift. The experimental data gives a slope of 27.6 and an intercept of -33. The corrected curve gives a slope of 20 and an intercept of -28. The slope of the corrected curve gives $r \approx 0.52$ which is much larger than 0.33. We need to do further work to understand these difficulties, but we expect that we are near the limit of self discharge rates and side reactions in these cells when drift rates of 0.3 mV/h are used.

6.3.4 Conclusions and Practical Considerations

Both soft and hard carbons heated around 700°C show large capacities for lithium with significant hysteresis. These samples contain substantial hydrogen. The hydrogen atoms presumably appear at the edges of planar aromatic sheets of carbon. These planar aromatic sheets are arranged in different manners in soft and hard carbons. Nevertheless, the hysteresis for both carbons showed similar temperature and current rate dependence.

A simple model was used to provide a conceptual framework to describe the hysteresis. This model assumes that intercalated lithium must overcome an energy barrier before it can be bonded near hydrogen. The model fits many aspects of the data qualitatively. To our knowledge, this represents the first attempt to model hysteresis obtained in an intercalation system.

Although the hydrogen-containing carbons show higher capacities, they all display a large hysteresis with lithium insertion in these carbons near zero volts and removal at one volt. The hysteresis will affect the efficiency of a real lithium-ion cell during charge and discharge. For example, the cell may charge at four volts and discharge at three volts. Therefore, efforts to produce industrially useful hydrogen-containing carbons for lithium-ion batteries should focus on reducing the energy barrier, for it controls the size of the hysteresis. If the barrier can be reduced, then excellent carbons for lithium-ion cells can be obtained.

The cycle life of the hydrogen-containing samples also appears to be limited as shown in figures 6-29 and 6-30. This is unacceptable for a practical application. The capacity loss is mostly due to the elimination of the excess capacity which exhibits hysteresis. Since this portion of the capacity appears related to the incorporated hydrogen, its elimination with cycling may not be unexpected. We do not understand this point fully yet.

LITHIUM INSERTION IN HARD CARBON

There have been a number of reports of carbons with voltage profiles similar to that of the region 3 material, single-layer hard carbon, shown in figure 2-2. Omaru et al. (Omaru, 1992), using pyrolyzed polyfurfuryl alchohol, Takahashi et al. (Takahashi, 1994), using unspecified precursors, Sonobe et al. (Sonobe, 1994), using pyrolyzed petroleum pitch and Liu et al. (Liu, 1996), using pyrolyzed epoxy novolac resin, have all prepared materials that show a low voltage plateau with a capacity of several hundred mAh/g, and little hysteresis. We believe that lithium can be adsorbed onto internal surfaces of nanopores formed by single, bi, and trilayer graphene sheets which are arranged like a "house of cards" (Zheng, 1995c; Zheng, 1995d; Liu, 1996) in the hard carbons (schematically shown in figure 7-1). Such hard carbons show promise for lithium-ion battery applications (Zheng, 1995c; Zheng, 1995d; Liu, 1996).

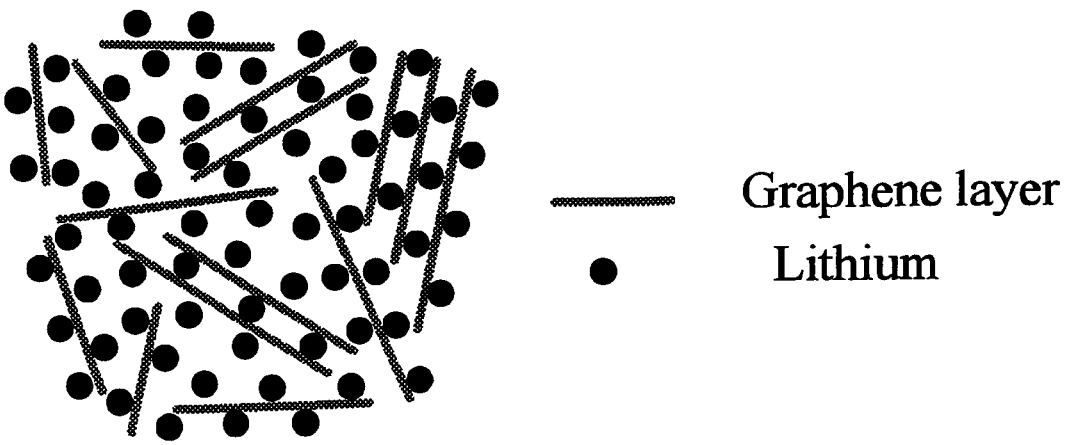

Figure 7-1. Adsorption of lithium on the internal surfaces of nanopores formed by single, bi, and trilayers of graphene sheets in hard carbon.

In lithium-ion battery applications, it is important to reduce the cost of electrode materials as much as possible. In this chapter, we will try to prepare hard carbons with

high capacity for lithium, from phenolic resins and coal. It is also our goal, to collect further evidence supporting the model in figure 7-1.

7.1 Higher capacity Carbons Prepared from Phenolic Resin

A hard carbon with high capacity can be made from epoxy novolac resin (Liu, 1996). The epoxy resins used (Liu, 1996) cost about US$2.50 per pound and give pyrolysis yields between 20 and 30%. However, it is well known that phenolic (or phenol-formaldehyde) resins can be pyrolyzed to give hard carbons with a yield of over 50% (Fitzer, 1969). In addition, these resins cost about US$1.00 per pound. Phenolic resins therefore offer significant cost advantages over epoxy resins, so we undertook a study of the electrochemical characteristics of hard carbons prepared by pyrolyzing both acid (novolac) and base-catalyzed (resole) phenolic resins.

7.1.1 Samples and their Electrochemical Testing

Three samples of phenolic resins were obtained, and designated as resin Ar, Br and Cr, as shown in table 7-1. The phenolic resin samples were all supplied in powder form. The powders were cured at 150 to 160°C for about 30 minutes in air to produce a solid lump. The lump was reduced to powder, then pyrolyzed in a tube furnace under flowing argon. Argon was flushed through the quartz furnace tube for at least one hour before heating to remove the air. Then the sample was heated from room temperature to the desired pyrolysis temperature in about three hours and soaked at the final pyrolysis temperature for one hour, under an argon flow of 2 cc/sec. The furnace power was then turned off and the samples cooled to near room temperature in a few hours at the same argon flow rate. Samples of resins Ar, Br and Cr were pyrolyzed at 700, 800, 900, 1000 and 1100°C. Those samples are designated Ar700, Ar800, ..., Br700,..., etc.. Table 7-2 summarizes these samples and their properties. The samples were all weighed before and after pyrolysis, to determine the yield. Resin Br was also pyrolyzed in smaller temperature

Table 7-1. The phenolic resins used.

Sample Designator	Manufacturer *	Product Number	Resin Type
Ar	Plenco	11760	resole
Br	Oxychem	29217	resole
Cr	Plenco	12116	novolac

* Plenco, Plastics Engineering Co., Sheboygan, WI, 53082-0758, U.S.A.; Oxychem, Occidental Chemical Corp., Durez Division, North Tonawanda, NY, U.S.A.

Table 7-2. Summary of the samples produced.

Sample	Heating temp (°C)	Weight Percentages (%)			H/C Atomic Ratio (±0.03)	Yield(%) (± 2%)	Reversible Capacity (mAh/g) (±20)	Irreversible Capacity (mAh/g) (±20)
		C	H	N				
Ar700	700	91.2	1.5	1.2	0.19	57	550	440
Ar800	800	93.1	1.0	1.3	0.13	55	510	280
Ar900	900	92.3	0.6	1.2	0.07	55	510	210
Ar1000	1000	94.2	0.4	1.9	0.05	54	450	160
Ar1100	1100	96.7	0.3	0.8	0.04	52	330	70
Br700	700	94.7	1.8	0.4	0.22	58	630	260
Br800	800	95.8	0.9	0.7	0.11	57	540	210
Br900	900	94.8	0.5	0.5	0.06	57	410	300
Br1000	1000	95.6	0.3	0.6	0.04	56	540	200
Br1100	1100	97.4	0.4	1.4	0.05	56	340	110
Cr800	800	95.7	0.9	0.6	0.11	64	530	210
Cr900	900	95.1	0.4	0.7	0.05	57	450	180
Cr1000	1000	96.5	0.3	0.8	0.04	58	450	130
Cr1100	1100	97.0	0.3	1.3	0.03	56	330	120
Arv1000	1000					58	520	270
Brv1000	1000					55	550	250
Crv1000	1000					57	550	220

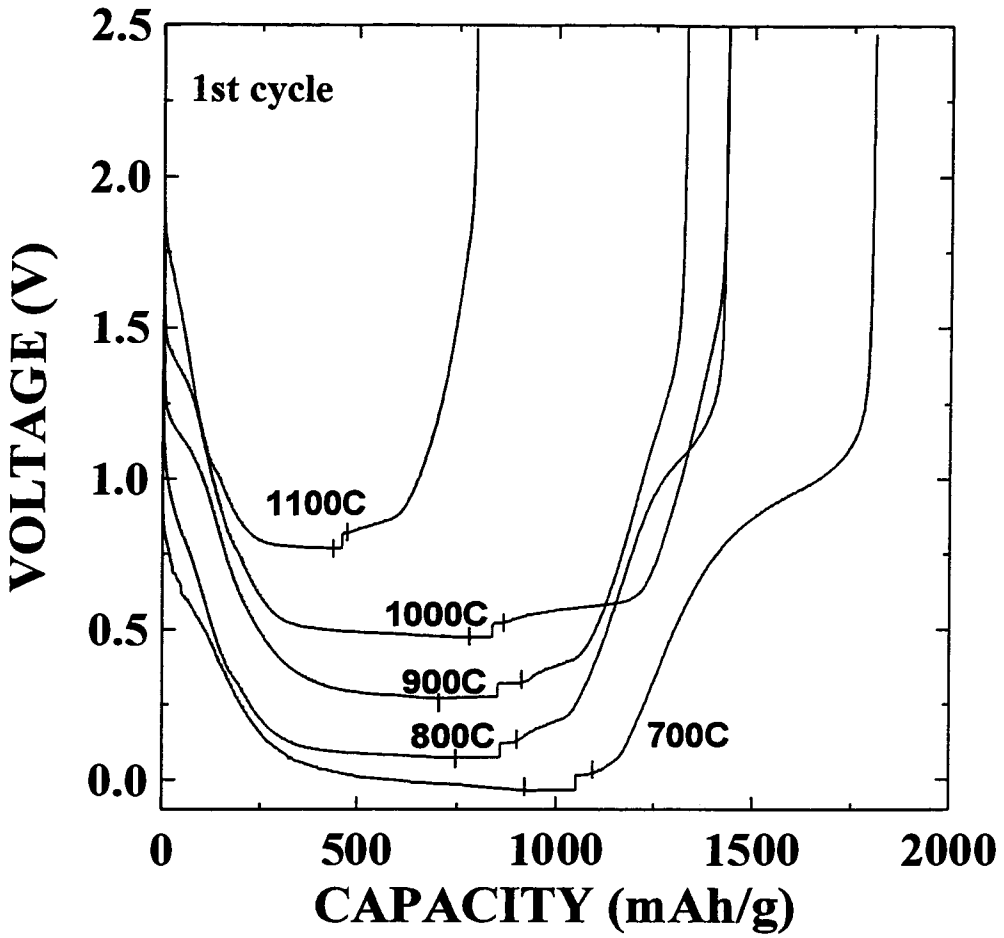

Figure 7-2. Voltage versus capacity for the first cycle of cells with lithium anodes and with cathodes made of Br-series samples. The curves have been sequentially offset for clarity. The shifts are: Br700, 0.0V; Br800, 0.10V; Br900, 0.30V; Br1000, 0.50V and Br1100, 0.80V. The vertical lines mark the onset of lithium plating during discharge and the termination of lithium stripping during charge.

increments between 900 and 1100°C. Those samples are designated in a similar way as Br940, Br970, Br1000, Br1030, Br1060 and Br1100.

Two electrochemical lithium/carbon cells were made for each of the pyrolyzed materials. The detailed methods of cell assembly and testing have been described previously in chapter 4. We used currents of 18.5 mA/g (20-hour rate) for the first three charge-discharge cycles and 37 mA/g (10-hour rate) for the extended cycling test.

Figure 7-2 shows the first cycle and figure 7-3 shows the second cycle for the Br-series carbonaceous materials. The voltage profiles of the Ar and Cr-series samples were similar to those of the Br-series samples and their second cycles are shown in figures 7-4 and 7-5 respectively. The reversible and irreversible capacities for all the samples are given in table 7-2.

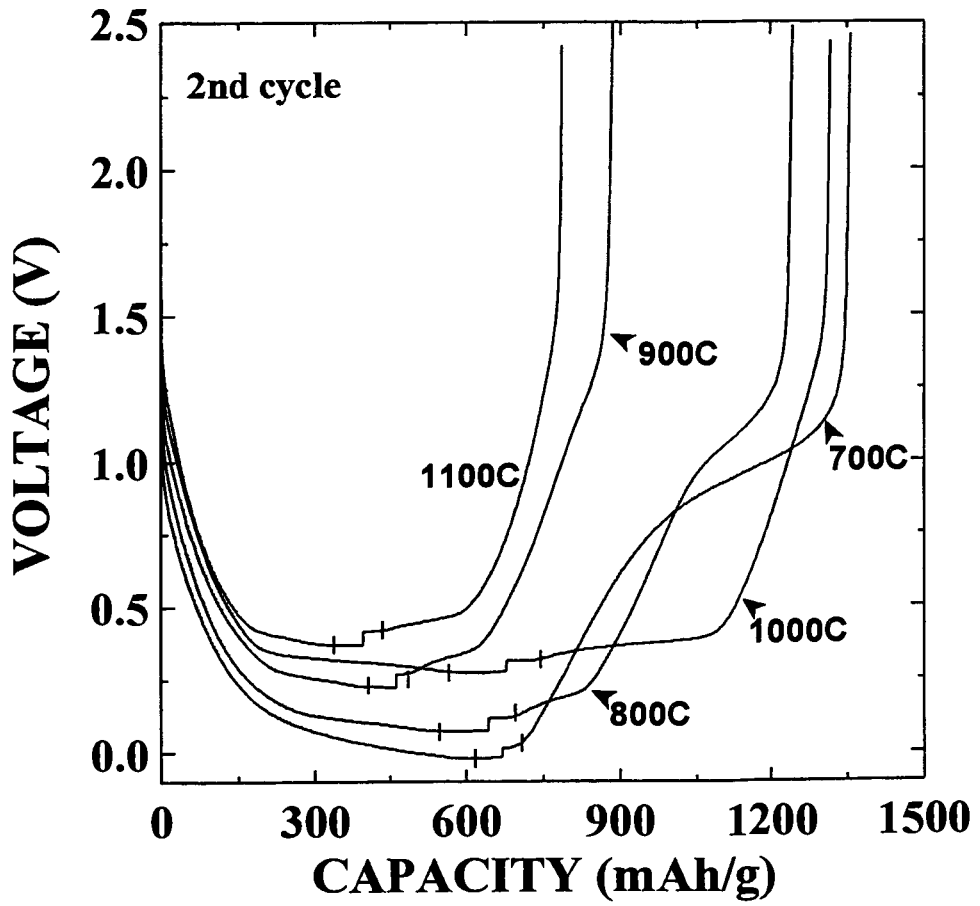

Figure 7-3. Voltage versus capacity for the second discharge and charge of cells with lithium anodes and with cathodes made of Br-series samples. The curves have been sequentially offset for clarity. The shifts are: Br700, 0.0V; Br800, 0.1V; Br900, 0.25V; Br1000, 0.30V and Br1000, 0.4V. The vertical lines mark the onset of lithium plating during discharge and the termination of lithium stripping during charge.

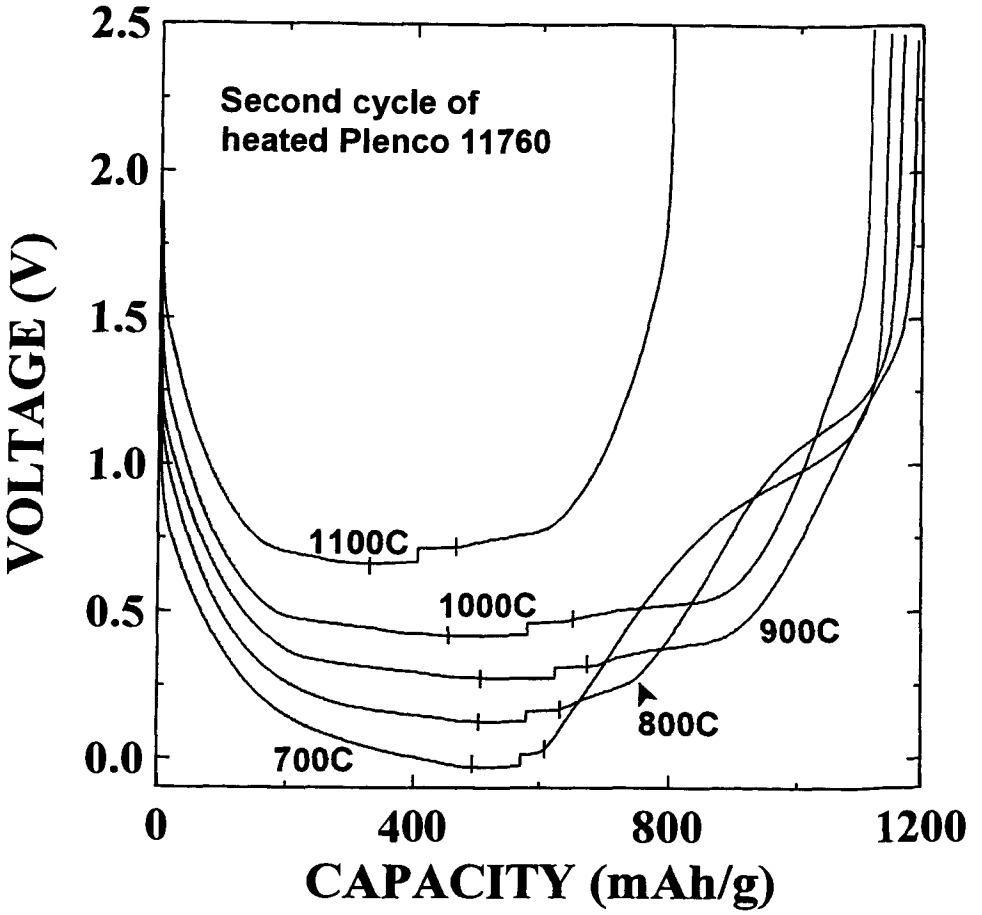

Figure 7-4 Voltage versus capacity for the second cycle of cells with lithium anodes and with cathodes made of Ar-series samples. The curves have been sequentially offset for clarity. The shifts are: Ar700, 0.00V; Ar800, 0.15V; Ar900, 0.30V; Ar1000, 0.45V and Ar1100, 0.70V. The vertical lines mark the onset of lithium plating during discharge and the termination of lithium stripping during charge.

All samples heated at 700 and 800°C show significant hysteresis; that is, lithium is inserted in the materials near zero volts and removed at about one volt. We have shown in chapter 6 that the amount of lithium which can be inserted in 700°C materials is directly proportional to their hydrogen (H) content. Table 7-2 shows that materials heated to 700 and 800°C retain substantial hydrogen. Upon heating to 900°C, the hydrogen is predominantly eliminated and so is the hysteresis. The samples then show substantial recharge capacity at low voltages. The vertical lines in figures indicate the onset of lithium plating during discharge and the termination of lithium stripping during charge.

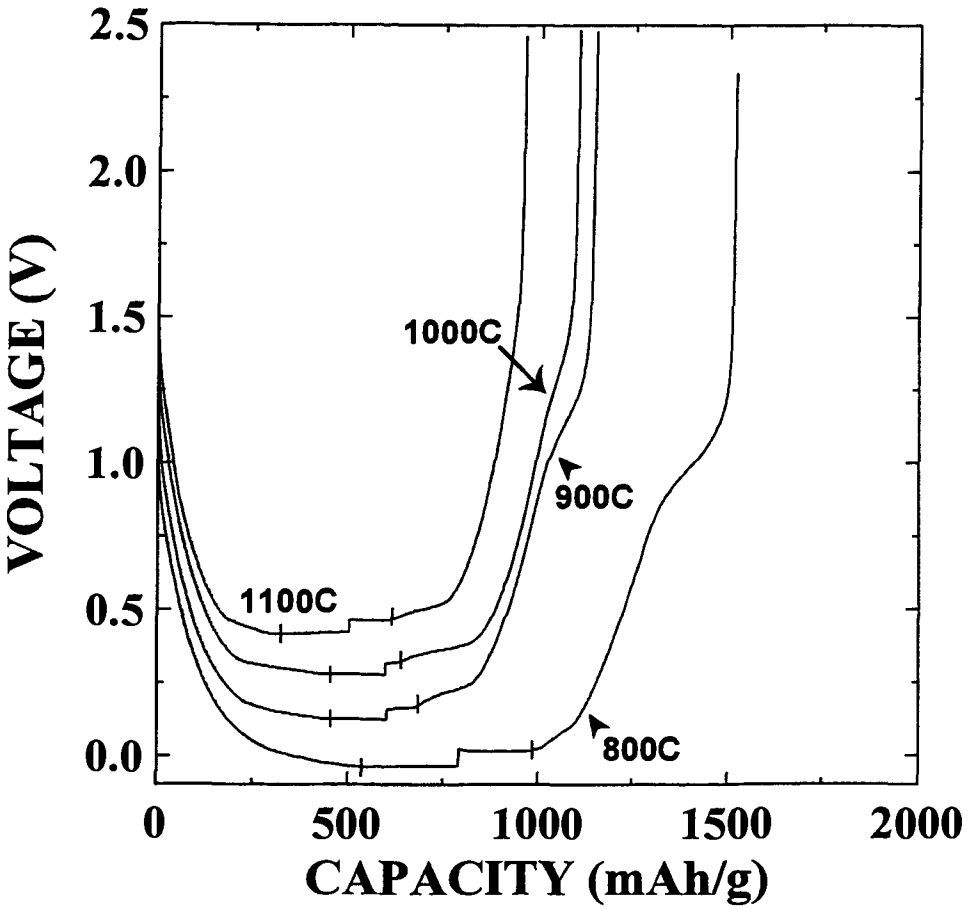

Figure 7-5. Voltage versus capacity for the second discharge and charge of cells with lithium anodes and with cathodes made of Cr-series samples. The curves have been sequentially offset for clarity. The shifts are: Cr900, 0.15V; Cr1000, 0.45V and Cr1100, 0.60V. The vertical lines mark the onset of lithium plating during discharge and the termination of lithium stripping during charge.

Table 7.3. Supplemental Br-series samples.

Sample	Irreversible Capacity (mAh/g) (±20)	Reversible Capacity (mAh/g) (±20)
Br900	300	410
Br940	160	470
Br970	160	550
Br1000	200	540
Br1030	140	540
Br1060	200	450
Br1100	110	340

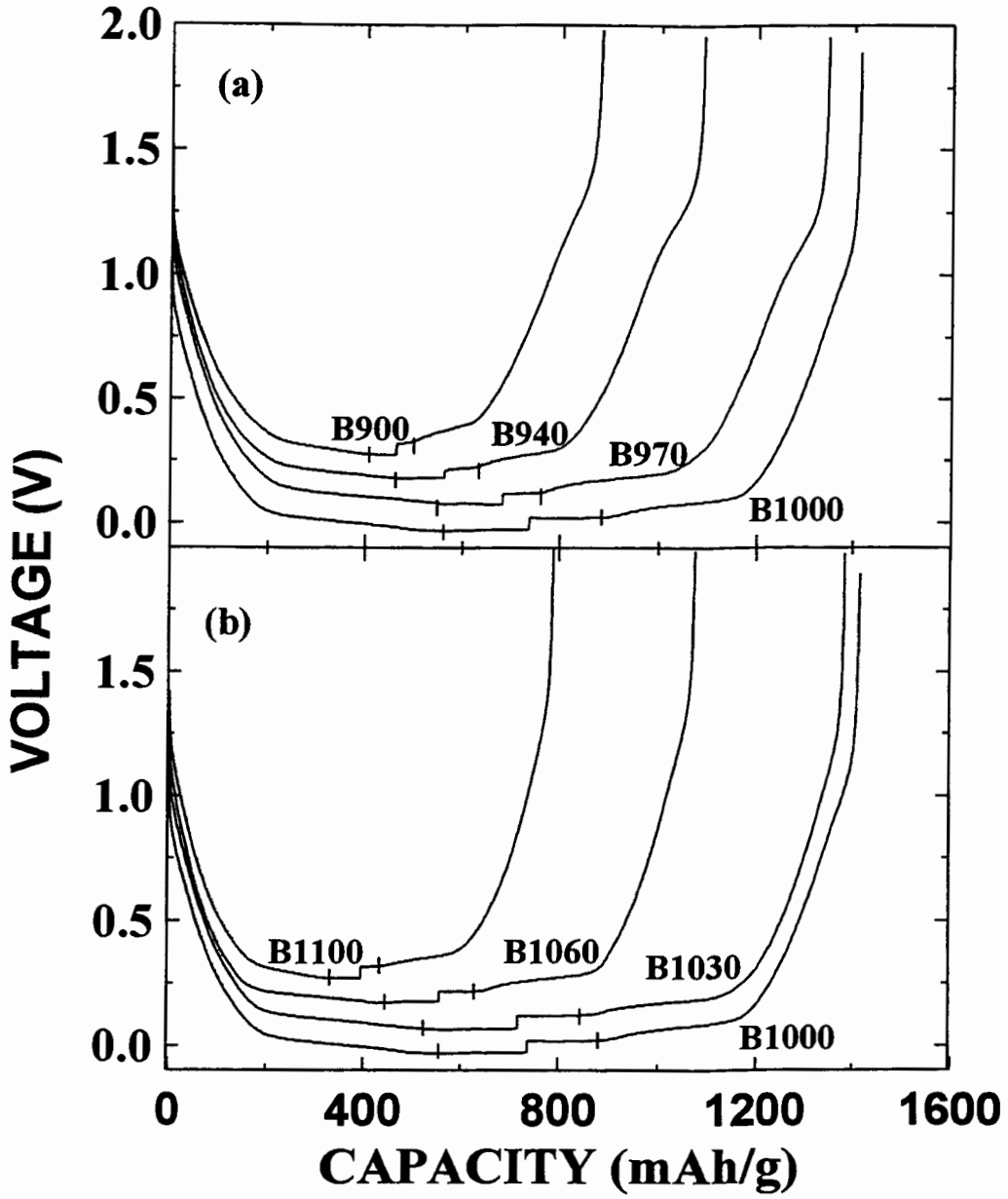

Figure 7-6. Voltage versus capacity for the supplemental Br-series samples. The curves are offset sequentially by 0.1V for clarity. The vertical lines mark the onset of lithium plating during discharge and the termination of lithium stripping during charge.

The cell made from Br1000 appears most promising. Its reversible capacity is about 540 mAh/g and it has a long low voltage plateau. Similar results were found for the second cycles of samples made from Ar and Cr resins, except that the capacities were

smaller. Why does the resin Br heated at 1000°C have larger capacity compared to the resins Ar and Cr? We will discuss this later.

The Br1000 sample was shown to have the highest reversible capacity with the longest low voltage plateau. In order to observe how the reversible and irreversible capacities varied in the temperature range around 1000°C, we prepared a series of samples from the Br resin at temperatures of 900, 940, 970, 1000, 1030, 1060 and 1100°C as described in table 7-3. These samples were pyrolyzed under similar conditions except at different pyrolysis temperatures. The materials were tested electrochemically as described above and their voltage profiles, irreversible capacities and reversible capacities were measured.

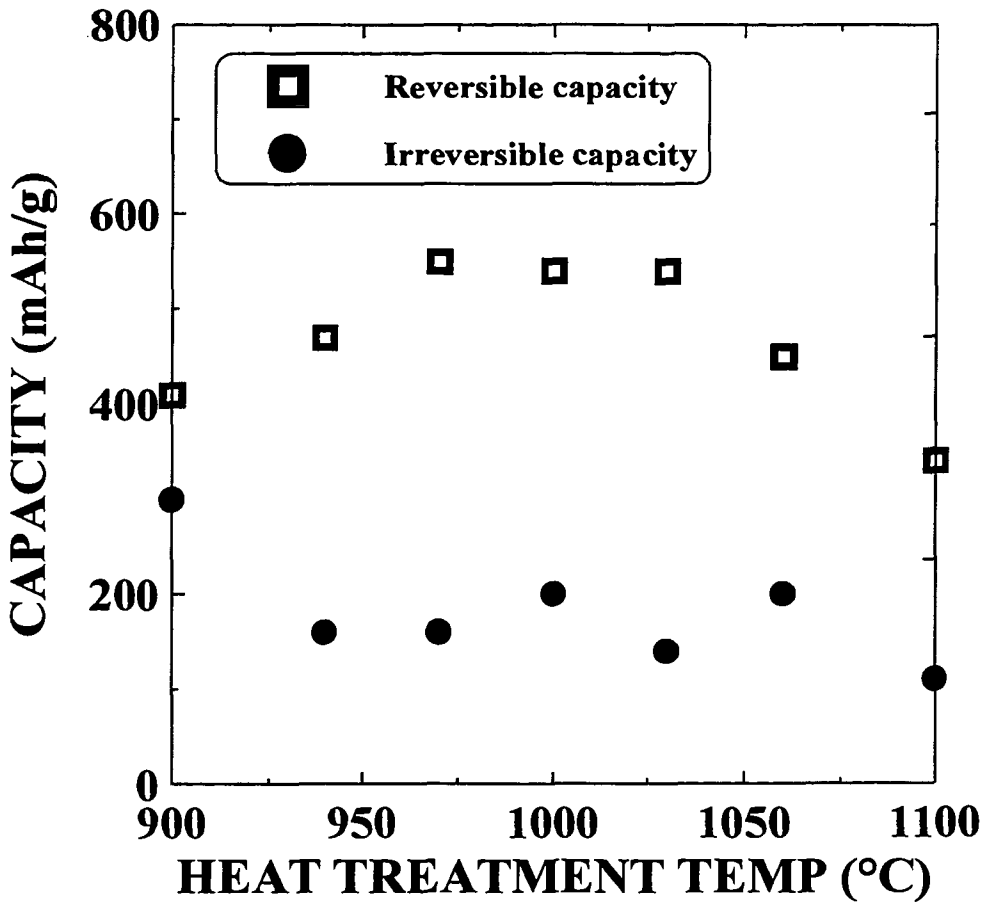

Figure 7-7. Both the reversible and irreversible capacities change as a function of temperature near 1000°C for heated Br-series samples.

Figure 7-6 shows the second cycles of these samples as indicated and the capacities are listed in table 7-3. There is a relatively narrow maximum in reversible specific capacity as a function of temperature, centered around 1000°C as shown in figure 7-7 which also includes the irreversible capacity versus temperature. Clearly, appropriate selection of the pyrolysis temperature is critical for optimizing the properties of these materials.

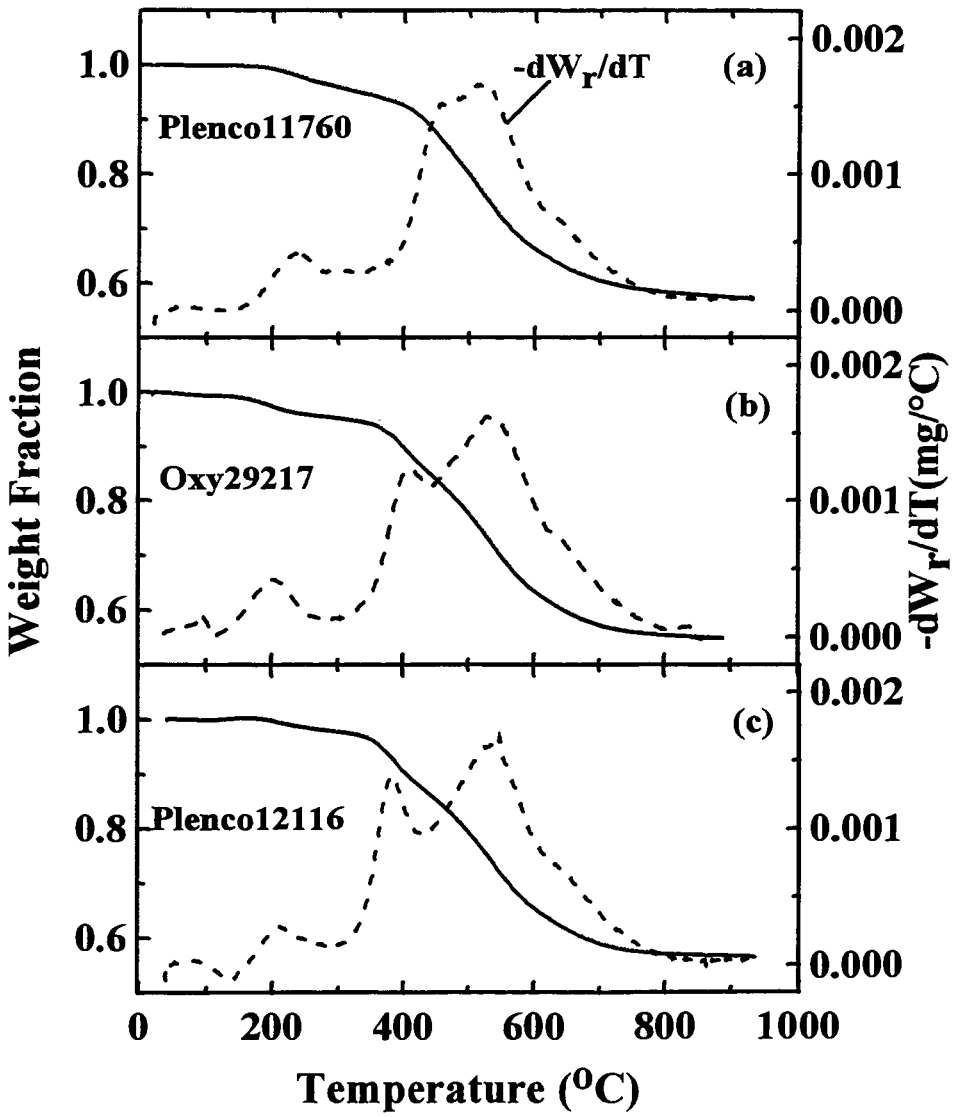

Figure 7-8. Weight fraction versus temperate from TGA and their derivatives for the three resins. (a) resin Ar, (b) resin Br, and (c) resin Cr.

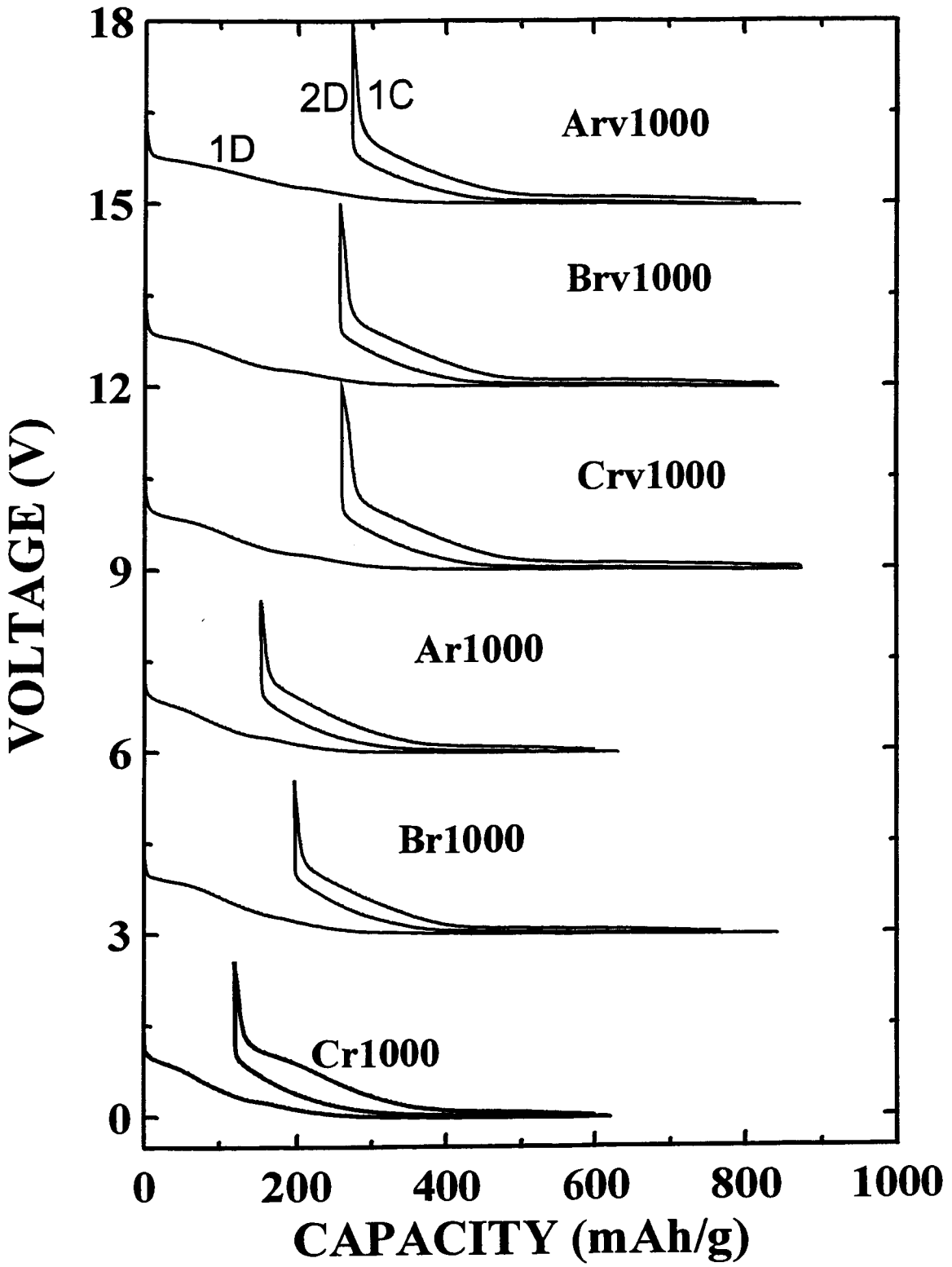

Figure 7-9 Voltage profiles of samples Arv1000, Brv1000, and Crv1000. They are compared with those of the samples Ar1000, Br1000, and Cr1000. The profiles have been offset by 3V sequentially.

Recent work by Xing et al. (Xing, 1996) showed that high capacity carbon can be made by pyrolysing sugar at ~1000°C under vacuum. During the pyrolysis of sugar, the vacuum environment reduces the reaction rate of residual gas, CO_2, produced during pyrolysis, with carbon to form CO. The reaction $CO_2 + C \rightarrow 2CO$ is called "carbon burnoff". Carbon burnoff has a dramatic effect on the insertion of lithium in these hard carbons (Xue, 1995a), because of an enlargement of nanopore openings which allows electrolyte penetration into the nanopores and results in large irreversible capacity for lithium insertion. Therefore, the pyrolysis gases including CO_2, should be rapidly removed during the pyrolysis of precursors to produce higher capacity carbon samples. We decided to make carbons from the three resins at 1000°C using vacuum pyrolysis.

It is useful to make TGA measurements on the three resins before the vacuum pyrolysis. The TGA curves and their derivatives for the three resins are shown in figure 7-8. Figure 7-8 indicates the release of pyrolysis gases from the precursors beginning near ~150°C. A pyrolysis scheme was then made for the resins based on figure 7-8. Each resin sample was heated slowly at 2°C/min from 100 to 850°C, and then a heating rate of 16°C/min was applied for the rest of the heating to 1000°C. The low heating rate was used so the vacuum pump could remove CO_2 as soon as it was produced, and hence to reduce the pressure of CO_2 gas in the tube during pyrolysis. The samples pyrolyzed under vacuum from resins Ar, Br and Cr are designated Arv1000, Brv1000, and Crv1000 respectively. The yields of these three samples are listed in table 7-2.

Two carbon/lithium cells for each vacuum pyrolysis sample were made. Figure 7-9 shows the voltage profiles of the first discharge (1D), the first charge (1C) and the second discharge (2D) for the samples Arv1000, Brv1000, and Crv1000, compared to that of the samples Ar1000, Br1000, and Cr1000. The irreversible and reversible capacities of the three vacuum pyrolyzed samples are listed in table 7-2. These three samples have similar voltage profiles. We noticed that the carbon samples Arv1000 and Crv1000 have much larger reversible capacity compared to the samples Ar1000 and Cr1000. However, the sample Brv1000 has almost the same reversible capacity as the sample Br1000. We also noticed that the vacuum pyrolyzed carbon samples have larger irreversible capacity, which

is not consistent with what we described above. More careful research on these samples is needed to understand these phenomena.

The cycling behavior of sample Br1000 was tested. Figure 7-10 shows the capacity versus cycle number for one Br1000 cell. This cell was cycled with a current corresponding to 37 mA/g (10-hour rate) after the first three cycles. There is little capacity loss upon cycling, and the materials show adequate rate capability.

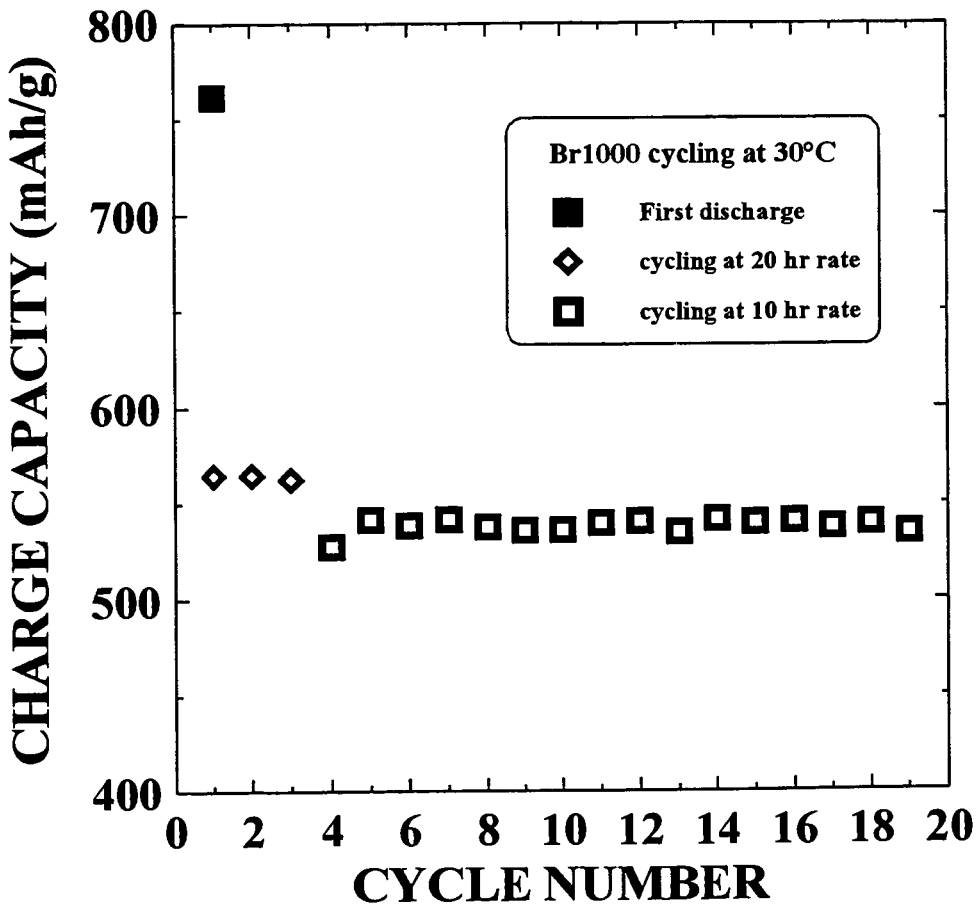

Figure 7-10. Capacity versus cycle number for a cell containing Br1000 as the electrode material. The test was made at 30 ℃.

The materials made near 1000°C from the three resins show high capacity (520 to 550 mAh/g), little charge-discharge hysteresis, and appear well-suited for application in

lithium-ion batteries. The mechanism for lithium insertion is believed to be the adsorption of lithium onto internal surfaces of nanopores formed by single, bi, and trilayer graphene sheets which are arranged like a "house of cards". Next we will show that these materials contain the nanopores implicitly required by such a microstructure.

7.1.2 Sample Nanoporosity

Powder X-ray diffraction and SAXS were employed here to explore the microstructure of hard carbon samples with high capacities. Powder X-ray diffraction measurements were made on all the samples listed in tables 7-2 and 7-3. We concentrate here on the patterns of the materials which appear most useful for battery applications, Br970, Br1000 and Br1030, shown in figure 7-11. The samples were measured overnight. Weak and broad (002) Bragg peaks (near 22°) are observed. Well formed (100) (at about 43.3°) and (110) (near 80°) peaks are also seen. The shapes of the (100) and (110) peaks are similar for three samples. The samples are predominantly made up of graphene sheets with a lateral extension of about 30Å (referring to table 6-1, applying the Scherrer equation to the (100) peaks). These layers are not stacked in a parallel fashion, and therefore, there must be small pores or voids between them. We used SAXS to probe these pores.

Figure 7-12a shows the result of SAXS on sample Br1000. We used the Guinier formula (see equation (3-9)) for the small angle scattering intensity, I(k), from randomly located voids with radius of gyration, R_g,

$$I(k) = (\text{const}) \cdot e^{-(kR_g)^2/3} \qquad (7\text{-}1).$$

A spherical pore of radius R_s has a radius of gyration R_g given by $R_g = \sqrt{3/5}R_s$, as shown in section 3.3.2. Although the above equation assumes a random distribution of pores with a homogeneous pore size, it fits our experimental data well. The slope of the solid line in figure 7-12b gives R_g = 5.5 Å and this value has been used for the calculated curve in figure 7-11a.. This suggests a relatively narrow pore-size distribution with an equivalent spherical pore size of about 14Å in diameter. Similar results were found for the

other B-series samples, except that the mean pore diameter changed from about 12 Å for samples made at 700°C to about 15 Å for samples made at 1100°C.

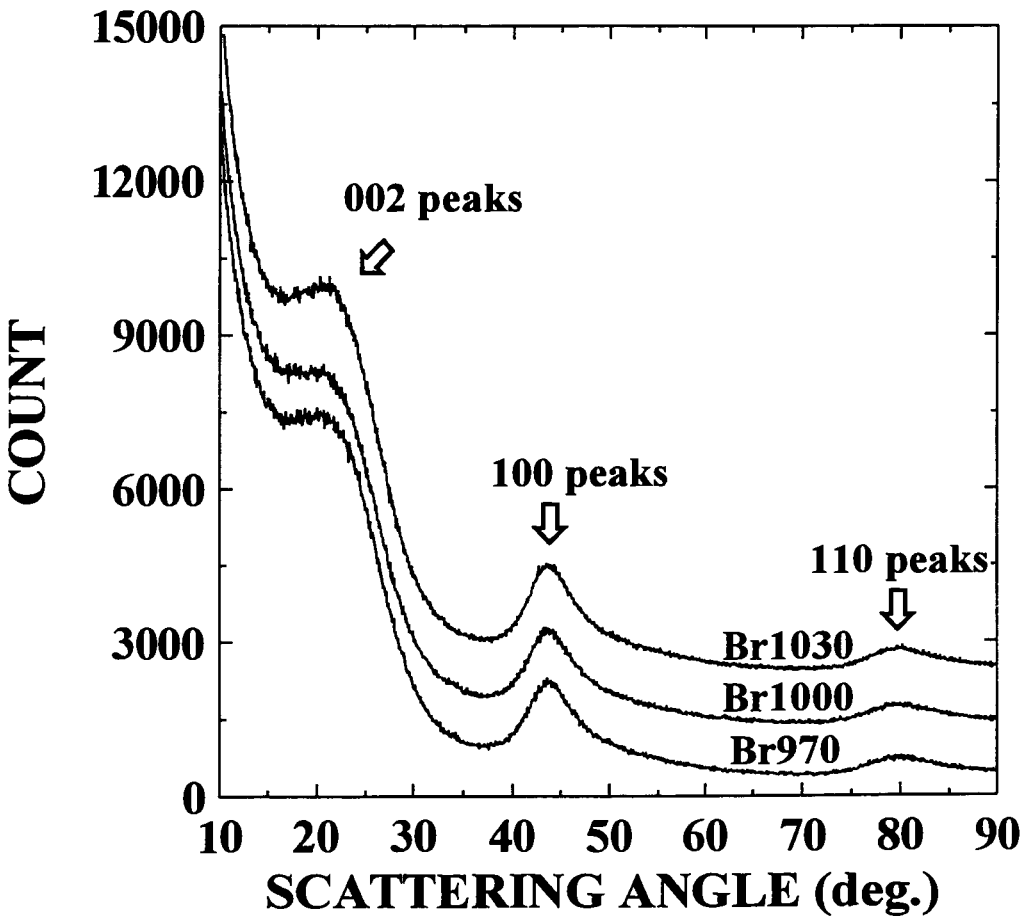

Figure 7-11. Powder X-ray diffraction profiles of three samples from the high-capacity Br samples as indicated. The profiles are offset sequentially by 1000 counts for clarity.

Since these materials have significant nanoporosity, we expect their bulk densities to be low. For example, the tap density (100 taps) of Br1000 was measured to be 0.81 g/cc, compared to 1.34 g/cc for the synthetic graphitic carbon powder, MCMB2700, measured by the same method. Thus, even though the gravimetric capacity of carbons prepared from phenolic resins far exceeds that of graphite, the volumetric capacity is similar. However, since phenolic resins are cheap, and since processing temperatures are

near 1000°C, instead of near 3000°C for graphite, materials like Br1000 may be very useful as anodes for lithium-ion cells.

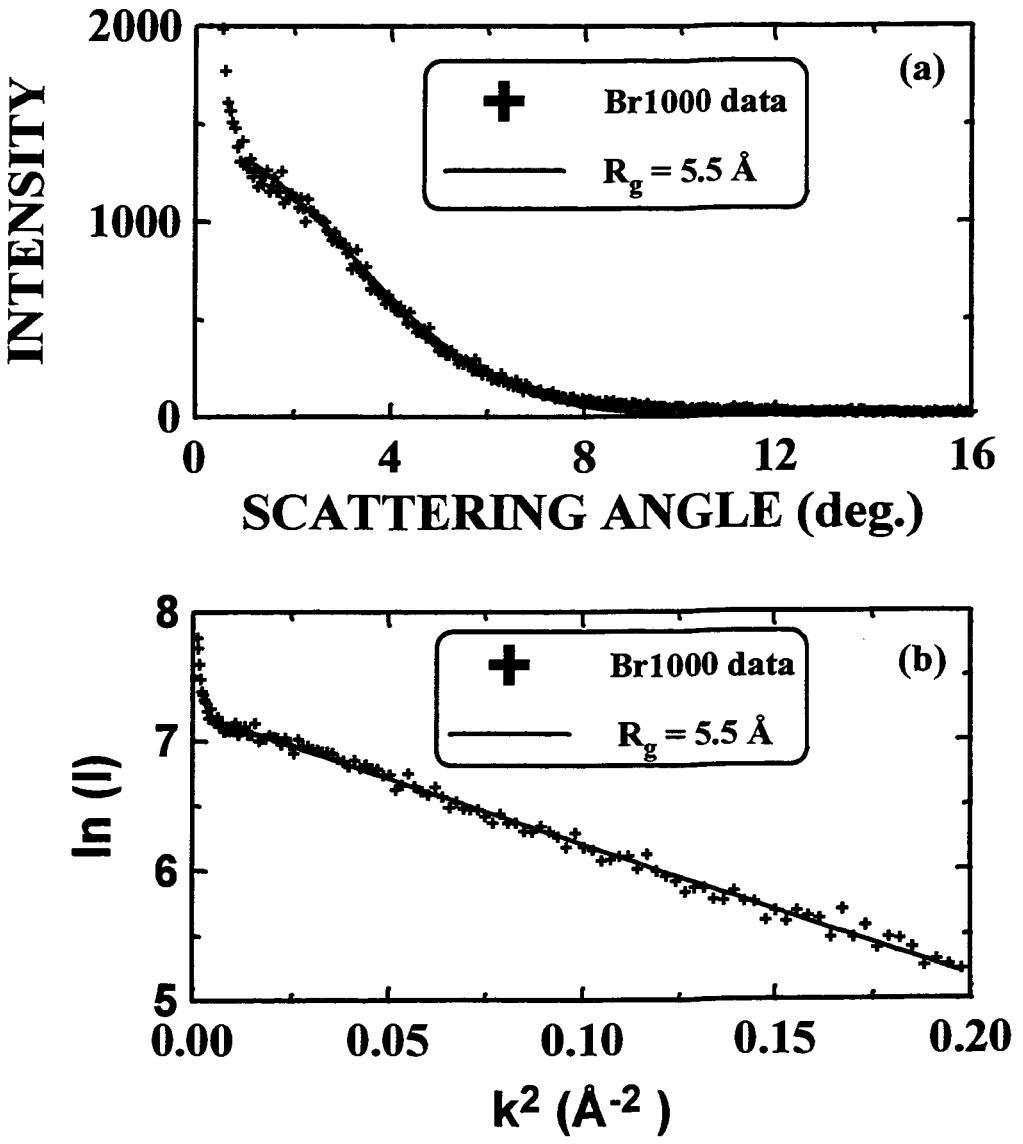

Figure 7-12. a) Small angle scattering intensity versus scattering angle for Br1000. The solid line is a fit using equation (7-1) with R_g = 5.5 Å. b) Natural log of the scattered intensity versus k^2. The straight-line fit allows R_g to be extracted from equation (7-1). The large intensity at very small k is caused by the scattering from macropores (see equation (3-13)) in the sample.

7.2 The Importance of "R"

Powder X-ray diffraction of the samples Arv1000, Brv1000, and Crv1000 are compared in figure 7-13. The samples are measured under the same condition with 2 hours of scan time which is different from that of figure 7-11. This figure shows the similarity of the well formed (100) peak, which indicates the in-plane structure of the graphene layers is more or less the same for each of the samples. The (002) peak is broad for each sample which indicates the poor stacking of the graphene layers. We believe that the capacity of the hard carbons is intimately related to the amount of BSUs which only contain single graphene layers.

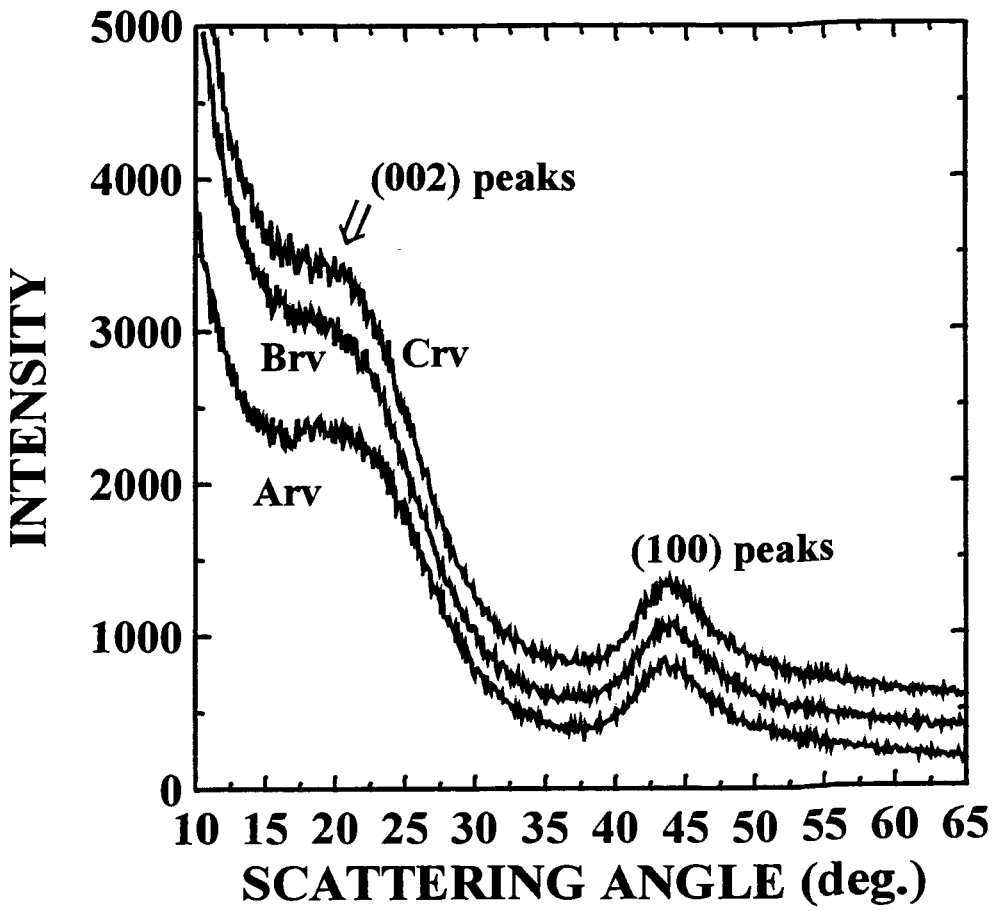

Figure 7-13. Powder X-ray diffraction profiles of samples Arv1000, Brv1000, and Crv1000. The data have been offset sequentially by 200 counts for Brv1000, and 400 counts for Crv1000 for clarity.

In our previous work (Liu, 1996), we showed that the amount of single graphene layers in hard carbon samples can be quantified by the empirical parameter, R. Figure 7-14 shows how we measure the parameter, R, defined to be the ratio of the peak count rate at the (002) peak divided by the background level (estimated by linear extrapolation) at the same angle. In figure 7-13, R is about 1.40 for the sample Arv1000, but 1.33 and 1.32 for the samples Brv1000 and Crv1000 respectively. These samples have high capacity with long low voltage plateaus on charge as shown in figure 7-9. We now show the meaning and importance of R.

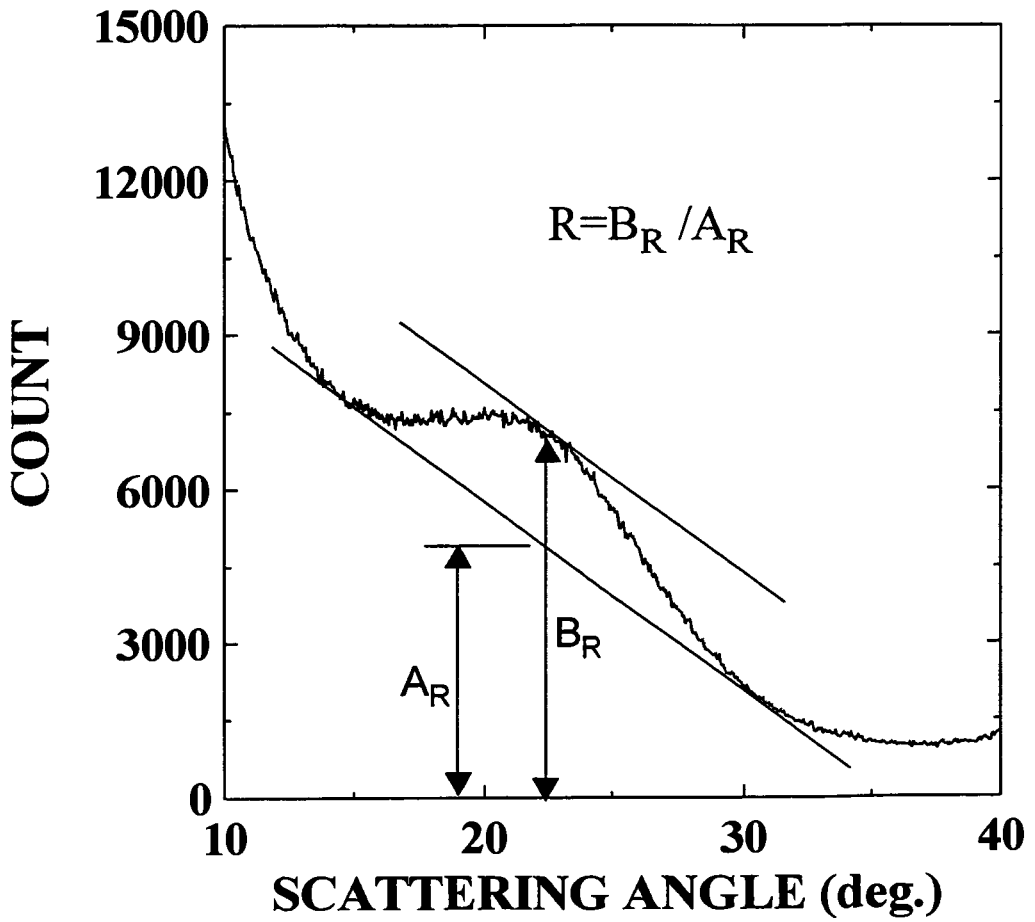

Figure 7-14. Schematic graph showing the definition of the parameter, R, used to empirically estimate the fraction of single graphene layers in hard carbon samples.

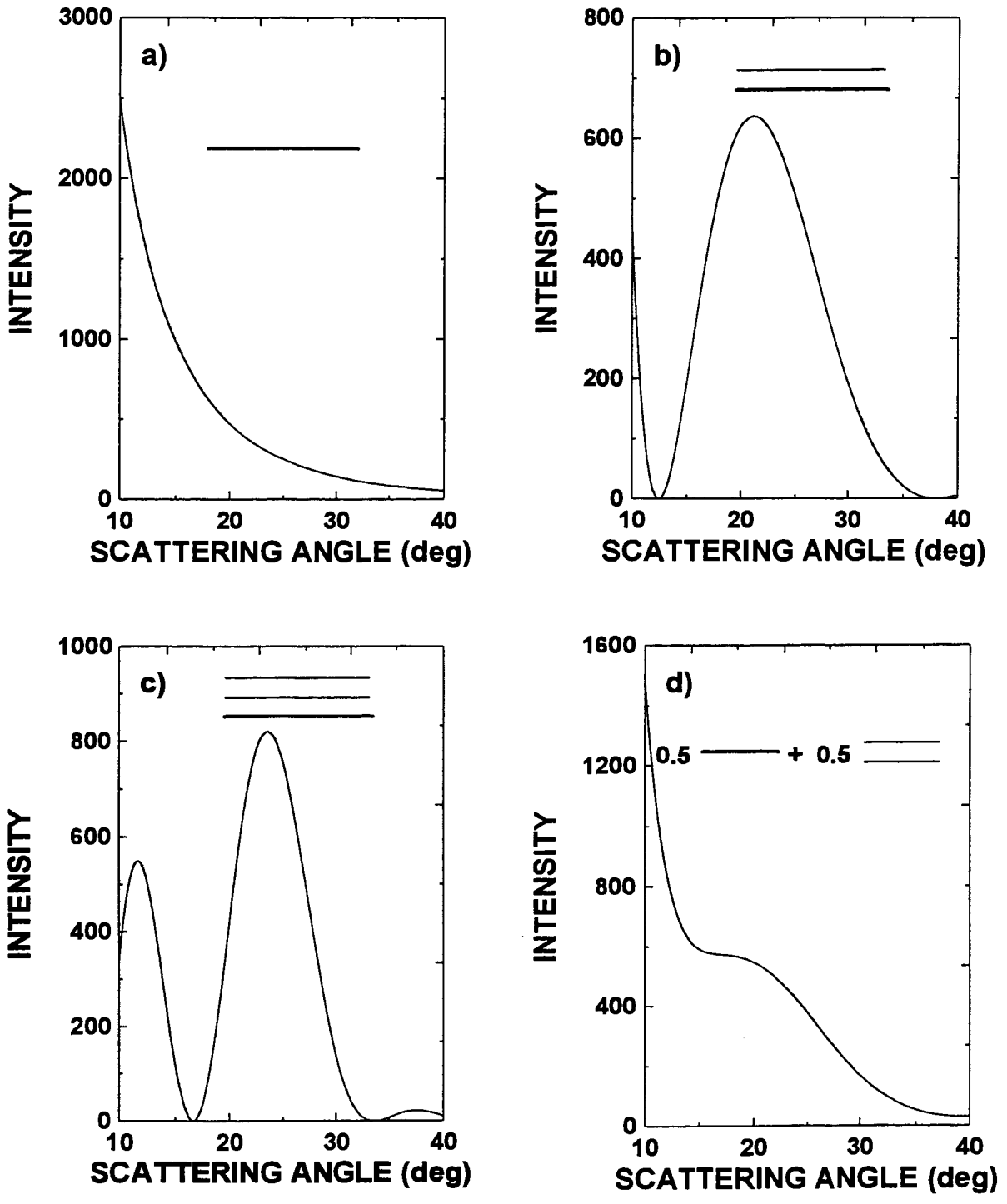

Figure 7-15. Calculated (002) Bragg peaks for carbons made up of randomly positioned: a) single graphene sheets, b) bilayers, c) trilayers and d) mixtures of single layers and bilayers, each containing 50% of the carbon in the specimen (Liu, 1996).

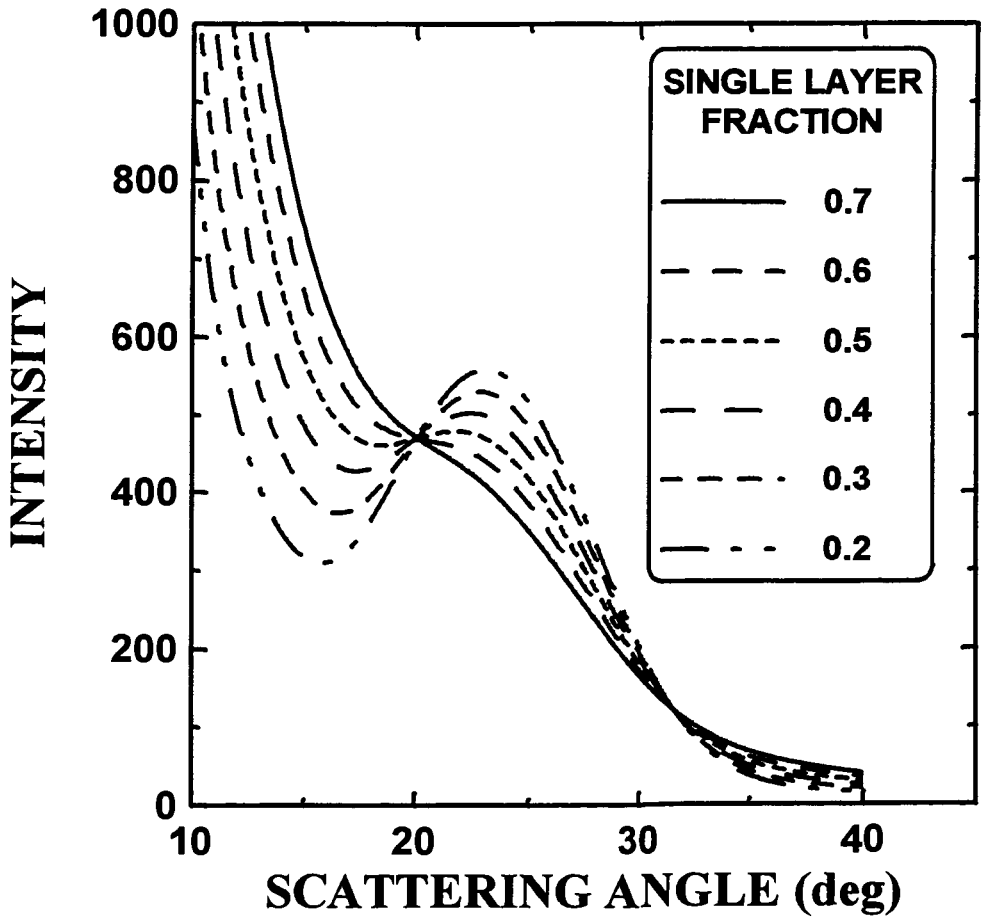

Figure 7-16. Calculated (002) Bragg peaks for various single layer fractions of the sample. The calculations assumed that a fraction, f, of the carbon was in single layers and that fractions 2/3(1-f) and 1/3(1-f) were included in bilayers and trilayers respectively (Liu, 1996).

Here we reproduce some of the arguments discussed by Liu et al. (Liu, 1996). Let us consider a powder sample of randomly positioned particles each made up of M graphene layers spaced a distance $d_{(002)}$ apart (Drits, 1991). The powder intensity of the (002) peak, $I_{(002)}(k)$, at wave vector, k, is

$$I_{(002)}(k) = |F(k)|^2 \left\{ 1 + 2\,\mathrm{Re}\left(\sum_{n=1}^{M-1} \frac{M-n}{M} e^{2\pi i \cdot k \cdot d_{(002)}} \right) \right\}, \qquad (7\text{-}2),$$

where F(k) is the amplitude contributed by a single graphene layer and n is a summation index. The intensity per carbon layer is $I_{(002)}/M$. This expression is valid for the (002) peak and therefore when the scattering angle is below about 36° where scattering from other Bragg peaks, like (100), is not observed. This expression further assumes that the graphene layers have infinite lateral extent, which they do not have actually. Layers with finite lateral extent have different low-angle scattering behavior due to their small size. For graphene layers larger than 20 Å in lateral size, equation (7-2) is accurate for scattering angles above ~10°. Therefore equation (7-2) can be used to estimate the single layer fraction of the hard carbons.

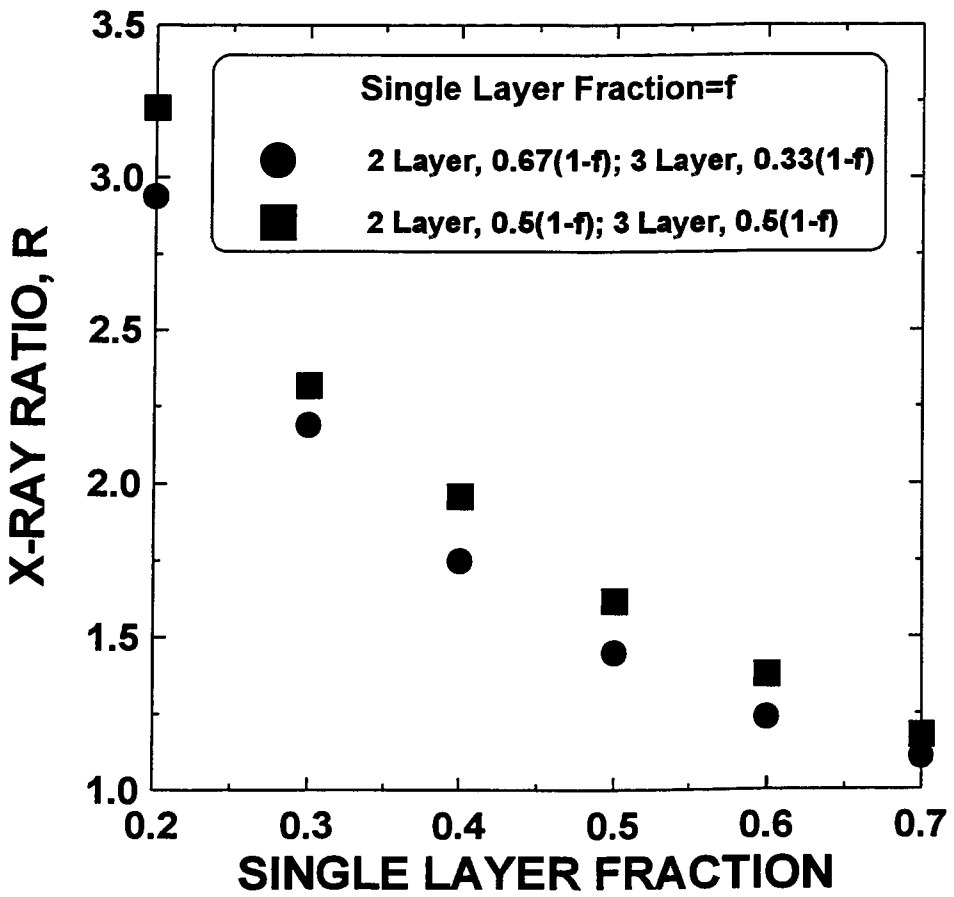

Figure 7-17. The dependence of R on single-layer fraction for the calculated patterns of figure 7-16, and for a second set of calculations where the fraction of carbon atoms in bilayers and trilayers is equal (Liu, 1996).

To examine the stacking of the layers in the hard carbon samples, we need the theoretical (002) peak for powder samples made up of randomly oriented single, bi, and trilayers. These are shown in figure 7-15a, 7-15b, and 7-15c respectively. Figure 7-15d shows a calculated pattern for a carbon sample with 50% of the carbon in randomly oriented single graphene layers and 50% of the sample in randomly oriented bilayers

Figure 7-16 shows a series of calculated patterns for carbon samples with a fraction, f, of carbon atoms in randomly oriented single layers, a fraction 2/3(1-f) in bilayers and a fraction 1/3(1-f) in trilayers. These curves can be used to estimate the dependence of the ratio, R, defined by figure 7-14, on the single layer fraction. Figure 7-17 shows the dependence of R on single layer fraction for the calculated patterns in figure 7-16, and for another set of calculated patterns (not shown) where the fraction of carbon atoms in bilayers and trilayers was taken to be 1/2(1-f). Both curves in figure 7-17 clearly show that R decreases as the single layer content of the sample increases and is fairly insensitive to how the carbon is distributed in bilayers and trilayers.

In the next section, we will prepare a number of hard carbons from different coals. We will see how the parameter, R, for the hard carbons is related to reversible capacity for lithium insertion.

7.3 Carbons Prepared from Coals for Anodes of Lithium-Ion Cells

Coal has a large carbon content and can have a highly aromatic condensed structure. Both features lead to high product yields after heat treatment. Therefore, coals might be good precursors to make inexpensive carbon electrodes for lithium-ion batteries. Here, we tried to prepare hard carbons, with high capacity for lithium, from coal. Eight different standard coal samples were pyrolyzed near 1000°C and then tested as electrodes in lithium/carbon cells. The physical properties of the heated coals were used to show that their capacity for lithium is consistent with our model of hard carbons. That is, coals with the fewest parallel-stacked graphene sheets and the largest number of nanoscopic pores gave the largest reversible capacity for lithium. Since the coals are initially of varied

chemistry this gives further confidence that our model for the reversible capacity in such carbons is correct.

7.3.1 Coal Samples

Eight pulverized coal samples were obtained from Argonne National Laboratory (Illinois, USA). These samples make up the Argonne Premium Coal sample bank (Vorres, 1990). The coal samples are stored and shipped in amber borosilicate glass ampoules under nitrogen gas. We opened the ampoules just prior to pyrolysis. Table 7-4 shows rank and elemental analysis data which is supplied with the samples (Vorres, 1990). The moisture and ash-free values are given in %, except for sulfur and ash which are in dry %. The eight raw coals are designated here as Ac, Bc, Cc,..., to Hc.

Table 7-4. Sources, ranks and elemental analysis data of coal samples.

Coal	Sample Designator	Source	Rank	C	H	O	S	Ash	Yield
Upper Freeport	Ac	Pennsylvania	MVB*	85.5	4.70	7.5	2.32	13.2	71%
Wyodak-Anderson	Bc	Wyoming	SB#	75.0	5.35	18.0	0.63	8.8	38%
Illinois #6	Cc	Illinois	HVB+	77.7	5.00	13.5	4.83	15.5	57%
Pittsburgh #8	Dc	Pennsylvania	HVB	83.2	5.32	8.8	2.19	9.2	64%
Pocahontas #3	Ec	Virginia	LVB**	91.1	4.44	2.5	0.66	4.8	80%
Blind Canyon	Fc	Utah	HVB	80.7	5.76	11.6	0.62	4.7	53%
Lewiston-Stockton	Gc	W. Virginia	HVB	82.6	5.25	9.8	0.71	19.8	68%
Beulah-Zap	Hc	N. Dakota	Lignite	72.9	4.83	20.3	0.8	9.7	38%

* MVB—Medium volatile bituminous;
\# SB—Subbituminous;
\+ HVB—High volatile bituminous;
** LVB—Low volatile bituminous.

Table 7-5. Summary of all carbon samples heated from coals.

Carbon	Yield (± 1%)	Irreversible Capacity (mAh/g) (±20 mAh/g)	Reversible Capacity (mAh/g) (±20 mAh/g)	Low Voltage Plateau (mAh/g)	X-ray Ratio, R	Relative Nanopore Amount, B	Inactive mass (± 1%)	Corrected Rev. Cap. (mAh/g)	Corrected Low V Plateau Cap. (mAh/g)
Ac1000	71%	220	330	10	5.7	16.2	19%	407	12
Bc1000	38%	90	350	72	2.5	42.0	23%	455	75
Cc1000	57%	130	430	68	2.5	21.4	27%	589	93
Dc1000	64%	90	400	34	4.4	25.0	14%	465	39
Ec1000	80%	80	370	18	6.7	18.4	6%	394	19
Fc1000	53%	130	450	76	2.8	33.0	9%	494	83
Gc1000	68%	80	350	54	3.4	21.5	29%	493	76
Hc1000	38%	160	320	58	3.5	26.5	25%	427	77
Fc950	54%	160	450		2.8		9%		
Fc1050	52%	130	440		2.8		9%		
Sugar	20%	170	610	210	1.6	35.5	0%	610	210
CRO1000	45%	100	340	0	8.55	12.4	0%	340	0
PVC1000	8%	80	340	0	10.2	9.6	0%	340	0
Arv1000	58%	270	520	240	1.40	50.8	0%	520	240
Brv1000	55%	250	550	255	1.33	46.5	0%	550	255
Crv1000	57%	250	550	260	1.32	48.6	0%	550	260

The eight coal samples were heat treated at 1000°C. At this temperature, most heteroatoms have been removed from the samples. The product yield is the ratio of final mass of the pyrolyzed sample to the sample mass before pyrolysis. Blind Canyon coal was also heat treated at 950°C and 1050°C as we will describe later. All pyrolyzed samples were ground and coded according the starting material and pyrolysis temperature. For example, Ac1000 designates Upper Freeport coal pyrolyzed at 1000°C, and Fc1050 designates Blind Canyon coal pyrolyzed at 1050°C. Table 7-5 lists all the samples which were heat treated.

Samples for comparison were made by pyrolyzing sugar, PVC and petroleum pitch. The sugar sample was prepared by first heating table sugar at 185°C in air for several hours to "caramelize" or "dewater" it. After this procedure, the hard brown lumps were ground into powder and then pyrolyzed under vacuum at 1050°C. We call this sample SUGAR. Polyvinyl Chloride (PVC) and Crowley Pitch (Crowley Tar, Co., New York, U.S.A.) were pyrolyzed under flowing argon gas at 1000°C. They are called PVC1000 and CRO1000 which are the same samples as described in table 6-1. The properties of these samples are also included in table 7-5 for comparison.

7.3.2 Powder Diffraction and Small-Angle X-Ray Scattering Measurements

The values of R measured for the (002) peaks of the pyrolyzed coals, pitch, PVC and sugar are given in tables 7-5 and 7-6. These tables also include three hard carbons made from phenolic resins, Arv1000, Brv1000, and Crv1000, which were discussed in section 7.1. The pyrolyzed sugar and pyrolyzed resins have the smallest value of R, and the pitch and PVC have the largest values of R. We expect the coals to show intermediate electrochemical behavior, based on their intermediate values of R. We believe that the samples with the smallest "R", will have the highest capacities (Liu, 1996). We will see later that this is true.

The SAXS measurement was described in section 3.3. The sample masses and attenuation factors are listed in table 7-6.

The small angle x-ray scattering results were quantitatively fitted using the form (3-13) as we described in section 3.3. The intensity, I(k), as a function of the scattered wave vector, k, is taken here to be

$$I(k) = \frac{A_k}{k^n} + \frac{B_k R_1^4}{(1+k^2R_1^2)^2} + \frac{C_k R_2^4}{(1+k^2R_2^2)^2} + D_k \qquad (7\text{-}3),$$

where R_1 and R_2 are two characteristic correlation lengths for electron density variations in the carbon. (We assume that there are only two different pores in the samples, which allows good fitting to all the data). The radius of gyration of the corresponding pores is $\sqrt{6}$ times either R_1 or R_2 as we described in section 3.3. A_k, B_k, and C_k are constants that here are proportional to the total surface areas of macropores, small nanopores, and larger nanopores respectively. D_k is a constant used to model a constant background. As we described in section 3.3, Porod's law gives n=4, but in cases where slit-type (not pinhole) measuring systems are used, the smearing of the data by the slits can give lower apparent values for n at low scattering angles (Guinier, 1957).

Table 7-6. Powder Diffraction and SAXS parameters for the samples. R, A_k, B_k, C_k and D_k are described in the text.

sample	X-ray ratio, R	SAXS mass, mg	SAXS $e^{+\mu d}$	$e^{\mu d}$/m norm.†	A_k ($Å^{-3.5}$)	B_k ($Å^{-4.0}$)	C_k ($Å^{-4.0}$)	D_k
Ac1000	5.7	217	28	9.3	0.21	16.2	0.102	16
Bc1000	2.5	158	7.7	3.5	0.54	42.0	0.76	7.7
Cc1000	2.5	199	79	29	0.087	21.4	0.145	29
Dc1000	4.4	225	16.6	5.3	0.070	25.0	0.164	5.9
Ec1000	6.7	193	6.0	2.2	0.10	18.4	0.037	14
Fc1000	2.8	206	5.0	1.8	0.046	33.0	0.11	10
Gc1000	3.4	233	28	8.7	0.15	21.5	0.30	6.4
Hc1000	3.5	163	9.0	4.0	0.29	26.5	0.152	14
SUGAR	1.6	163	2.25	1.00	0.037	35.5	0.0	22
CRO1000	8.55	166	2.5	1.09	0.027	12.4	0.035	1.8
PVC1000	10.2	183	3.3	1.13	0.34	9.6	0.152	11
Arv1000	1.40	167	2.33	1.01	0.016	50.8	0.0	50
Brv1000	1.33	160	1.91	0.87	0.008	46.5	0.0	56
Crv1000	1.32	157	1.88	0.87	0.004	48.6	0.0	56

† The absorption and mass factors are normalized to that of sugar.

The strategy employed in the fits made here is motivated by comparison of the SAXS data for coals to that of the pyrolyzed pitches, phenolic resins, and sugar. We also used the non-porous graphite powder sample, JMI (chapter 5), to help estimate a good choice for n. Figure 7-18 shows SAXS data for the graphite powder, the pyrolyzed sugar and the pyrolyzed pitches. The fit to the data is shown by the dashed curve and each of the four terms of the fit is individually plotted for the latter three samples. For the graphite data, B_k and C_k were set to zero for the fitting. The best fit to the graphite data gave n=3.5. Then, n was set to 3.5 for the rest of the fits to be described in this paper. The small peak near k =0.4Å^{-1} is from the kapton window. For the sugar data, A_k, B_k, C_k, D_k, R_1 and R_2 were allowed to vary and the best fit (shown) describes the data well. R_1 refined to 2.47Å and R_2 to 16.6Å. (C_k is much smaller than B_k, and in fact good fits are obtained when C_k=0.) Other workers in the lab have shown that sugar reacts reversibly with about 600 mAh/g of lithium (Xing, 1996). Thus we decided to attempt to fit the SAXS data for all the other carbon samples using the same values of R_1, R_2 and n, and only let A_k, B_k, C_k, and D_k vary. The fits to the pitch and heated PVC in figure 7-18c and 7-18d were made in this way.

Figure 7-19 shows SAXS data and fits for three of the coal samples and the graphite sample for comparison. The fits were made with fixed values of R_1=2.47Å and R_2=16.6Å. Our goal is to be able to compare the absolute amounts of the nanoscopic pores (the B_k, R_1 term) in each of the three samples. To do this, we must measure the scattered intensity per unit mass, in the absence of absorption of the incident and scattered x-rays in the beam. Since the coals have different impurities, their absorptions are quite different and we must correct for these differences. Let the measured intensity be I. The intensity one would measure per unit mass for an infinitely thin sample, I_o is then proportional to

$$I_0 = I \cdot e^{\mu d} / m \qquad (7\text{-}4),$$

where μ is the linear absorption coefficient, d is the sample thickness and m is the sample mass. We measured $e^{\mu d}$ (by the attenuation of the direct beam) and m for each of the samples (see table 7-6), so the correction given by equation (7-4) could be made. In practice, the fits of equation (7-3) (with n=3.5, R_1 = 2.47Å and R_2 = 16.6Å) were made to

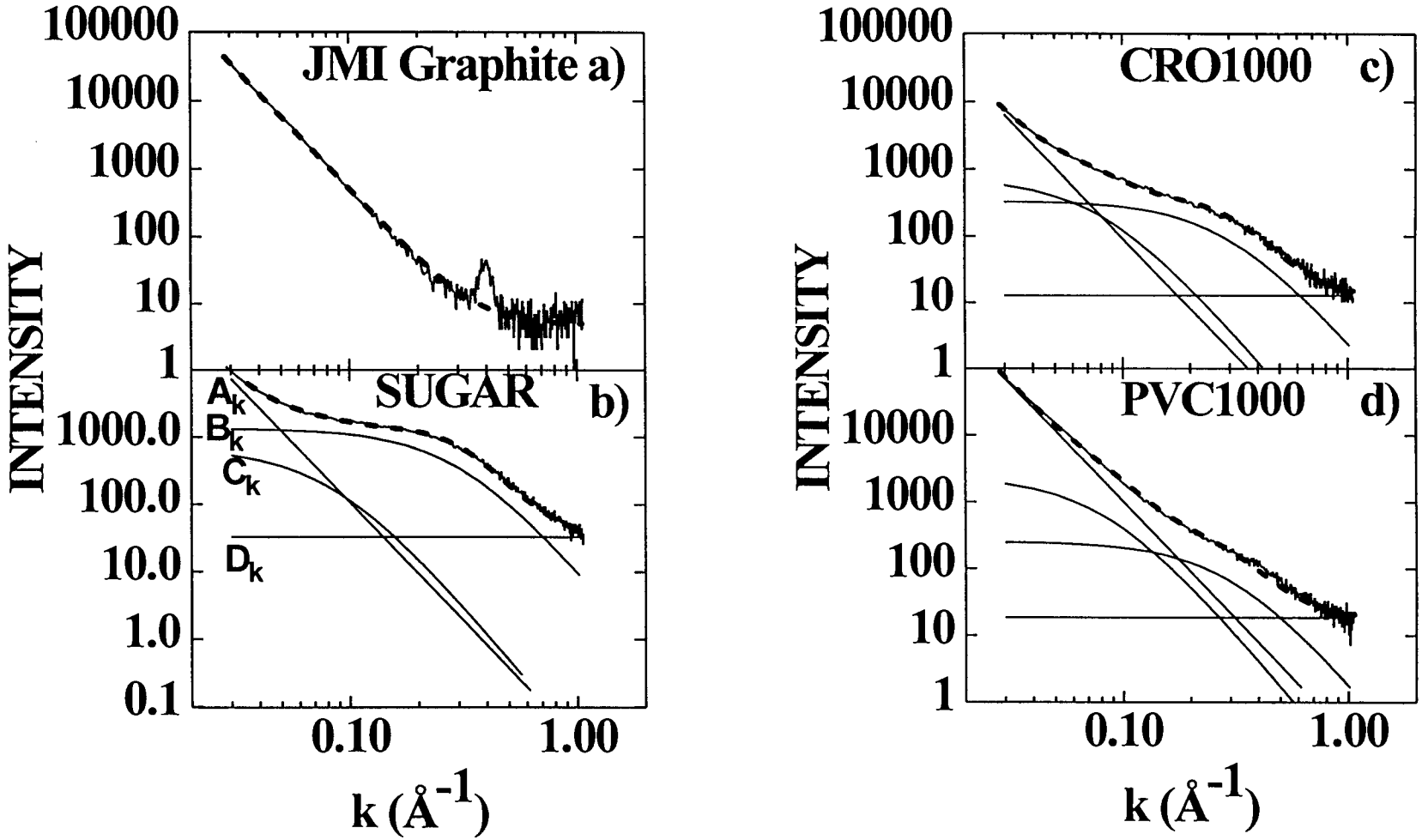

Figure 7-18. Small angle X-ray Scattering data (solid curve with noise) for a) graphite, b) sugar heated at 1000°C, c) CRO1000, and d) PVC1000. Also shown in b), c) and d) are each of the 4 terms in equation (7-3) which comprise the best fit. The dashed lines are the best fit.

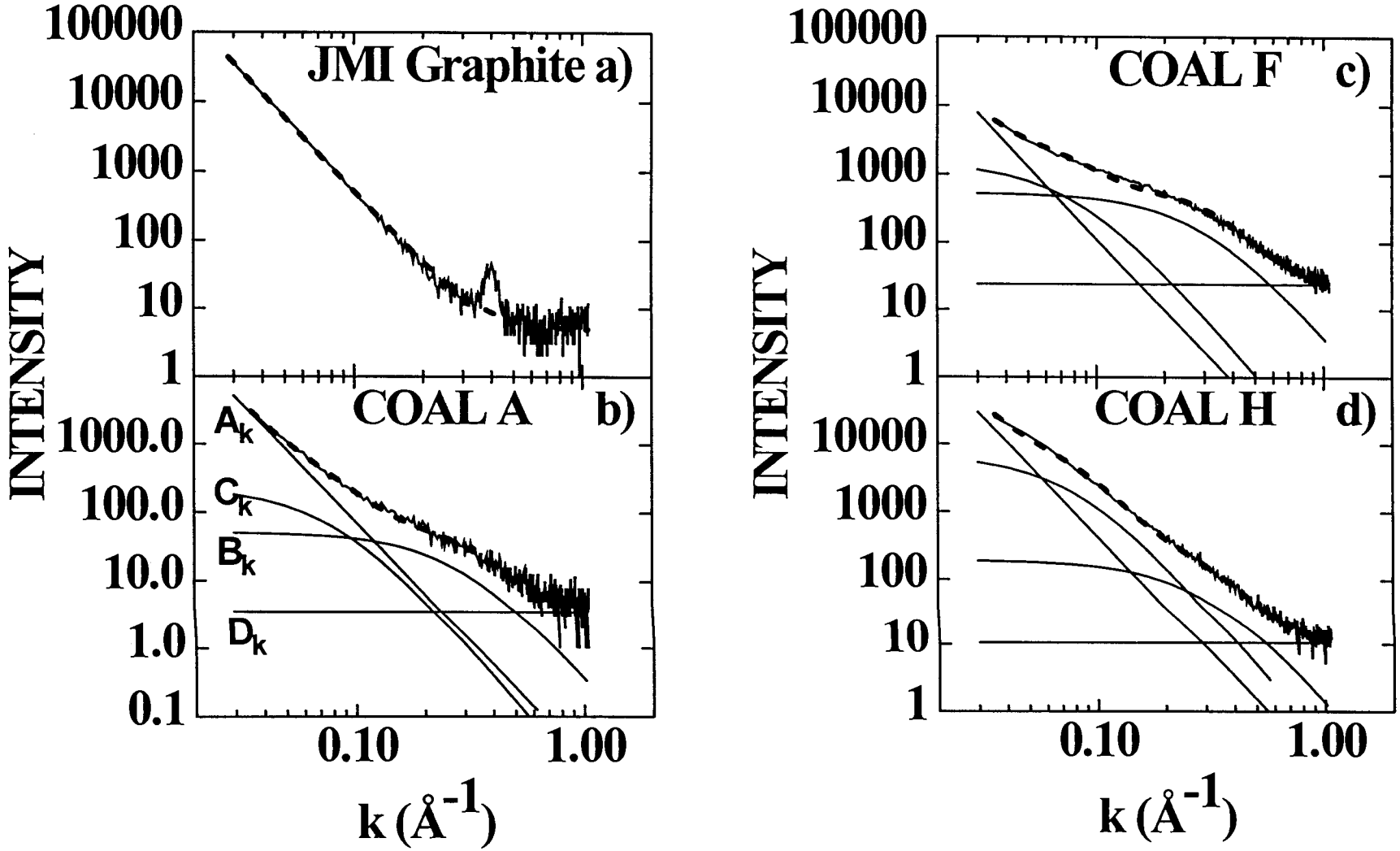

Figure 7-19. Small angle X-ray Scattering data (solid curve with noise) for a) graphite, b) Coal A, c) Coal F, and d) Coal H. Also shown in b), c) and d) are each of the 4 terms in equation (7-3) which comprise the best fit. The dashed lines are the best fit.

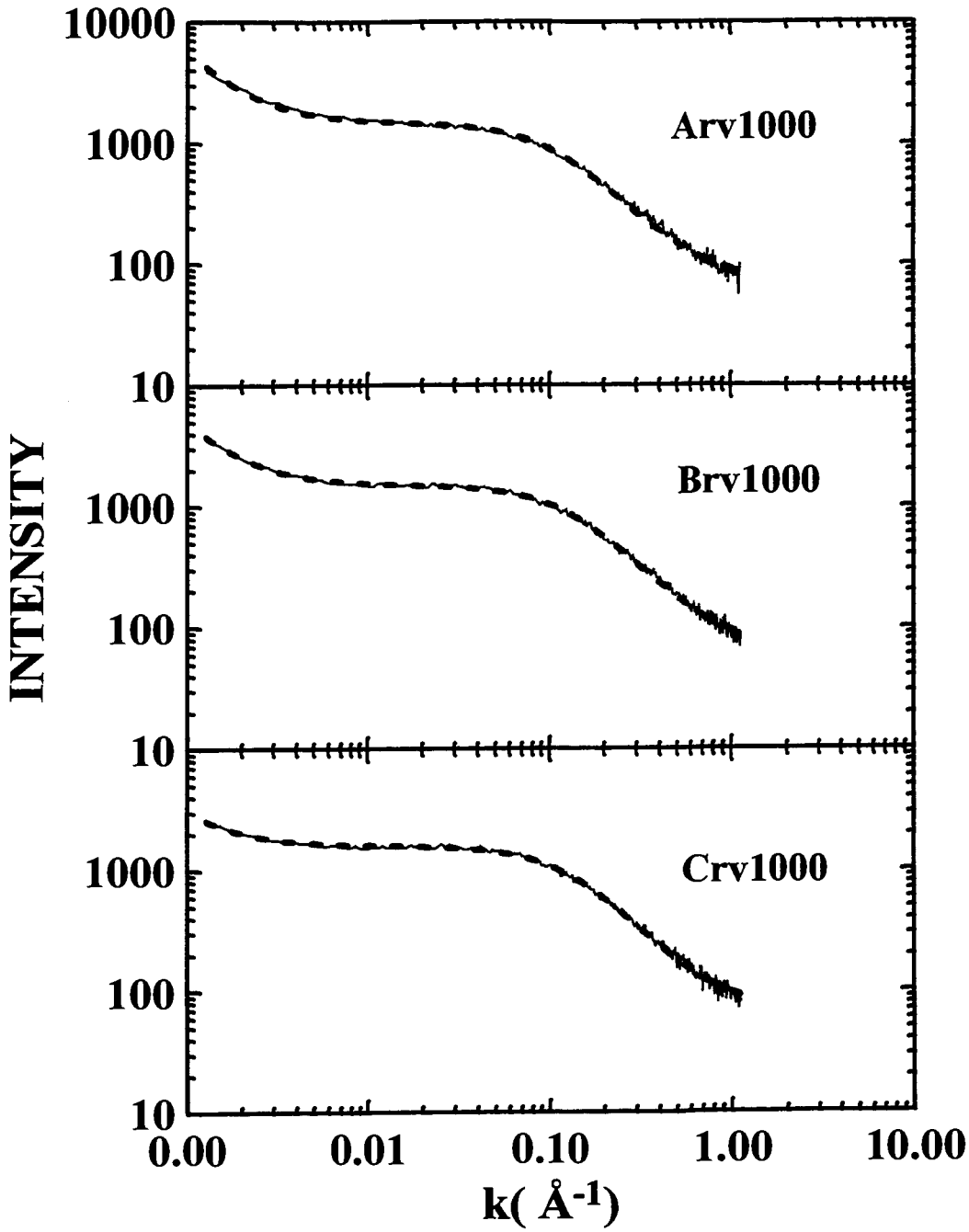

Figure 7-20. Small angle X-ray Scattering data (solid curve with noise) for a) Arv1000, b)Brv1000, c) Crv1000. The dashed lines are the best fit. R_1 for each sample is 2.47Å.

the measured data, and then the values of A_k, B_k, C_k and D_k were multiplied by the normalization factor $e^{\mu d}/m$. Table 7-6 lists the normalized values of A_k, B_k, C_k and D_k obtained for all the samples. It is worth noting that the trends in table 7-6 are preserved even if R_1 and R_2 are changed by up to 20% or so.

Figure 7-20 shows SAXS data and fits for the samples Arv1000, Brv1000, and Crv1000 pyrolyzed from resins. We assume that only one type of nanopore is present in each sample. The dashed lines in figure 7-20 are the best fits for the three samples based on equation (7-3). The SAXS parameters for these three samples are summarized in table 7-6.

7.3.3 Electrochemical Results and Discussion

We next made electrochemical lithium/carbon cells for the heated coal samples.

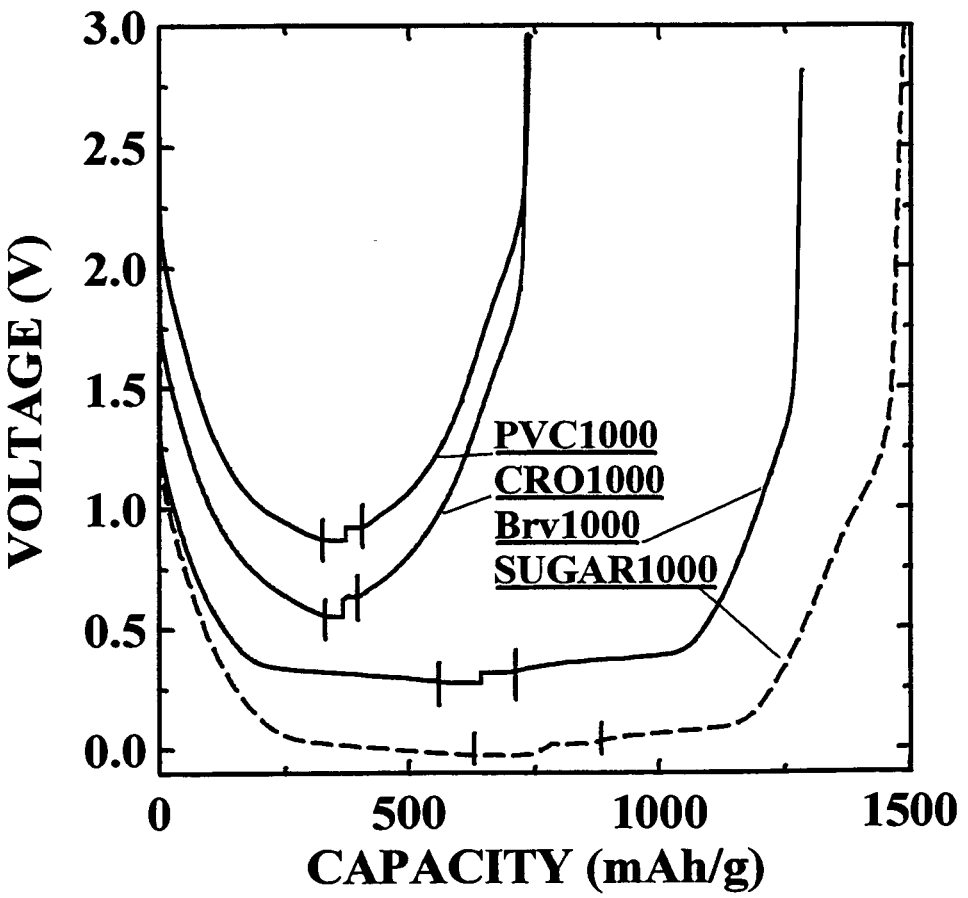

Figure 7-21. Voltage-capacity profiles for the second cycle of lithium carbon cells made from pyrolyzed sugar, Brv1000, CRO1000 and PVC1000. The data for Br1000, CRO1000 and PVC1000 have been shifted sequentially by 0.3V for clarity. The vertical lines indicate the onset of lithium plating during discharge and the termination of lithium stripping during charge.

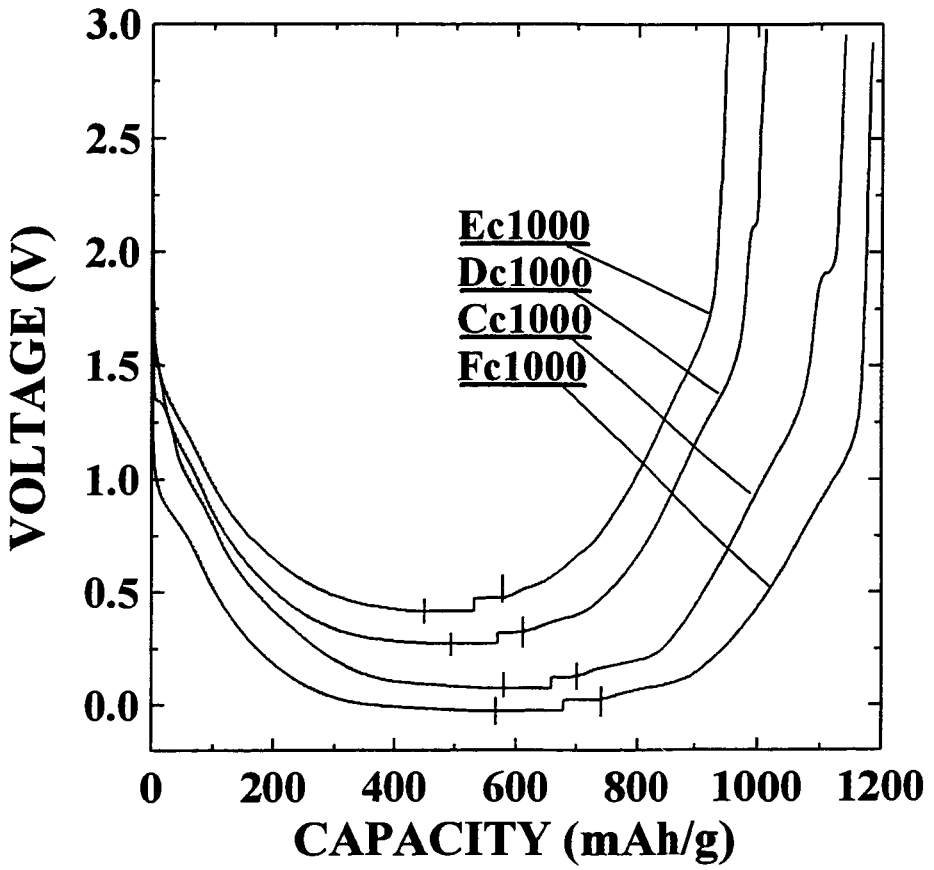

Figure 7-22. Voltage curves for the first cycle of lithium/carbon cells made from coals Ec, Dc, Cc and Fc as indicated. The data has been offset by 0.0V for coal Fc, by 0.1V for coal Cc, by 0.3V for coal Dc and by 0.45V for coal Ec. The vertical lines indicate the onset of lithium plating during discharge and the termination of lithium stripping during charge.

Two cells were made from each sample and tested. Figure 7-21 shows the voltage profile for the second cycle of the sample Brv1000 and the standard samples (pyrolyzed sugar, PVC1000, and CRO1000). The small vertical lines mark the onset of lithium plating during discharge and the termination of lithium stripping during charge. The sugar sample and Brv1000 differ most markedly from the others in that they both show an extended low voltage plateau. We believe that the plateau is due to the adsorption of lithium atoms on the walls of the nanoscopic pores in the material. The sugar sample and Brv1000 have smaller R and the largest values of B_k, consistent with small graphene sheets stacked at arbitrary angles and the small pores between them. On the other hand, the PVC1000 and

CRO1000 samples have large R (R=8.55, 10.2, respectively), consistent with 5 to 10 (roughly estimated using the Scherrer equation) parallel-stacked graphene sheets and small values of B_k, consistent with the presence of few nanoscopic pores. The PVC sample has an order of magnitude more macropores (compare A_k in table 7-6) than the CRO sample, which leads to a large BET surface area for the PVC1000 sample (see table 6-1), but this does not apparently affect the voltage profile or capacity of the material. Therefore, we believe that the presence of the nanoscopic pores (B_k term) gives rise to the low voltage plateau. If this hypothesis is correct, the coals with the largest low voltage plateaus will be those with the largest B_k and the smallest R.

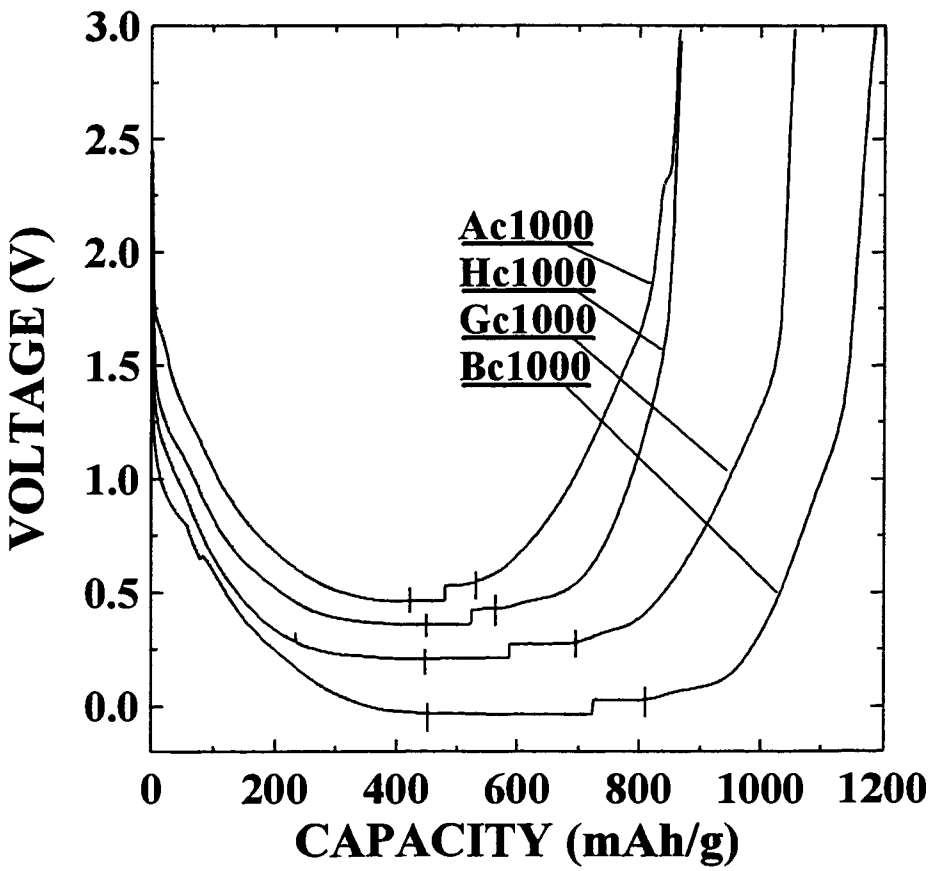

Figure 7-23. Voltage curves for the first cycle of lithium/carbon cells made from coals Ac, Hc, Gc and Bc as indicated. The data has been offset by 0.0V for coal Bc, by 0.25V for coal Gc, by 0.4V for coal Hc and by 0.5V for coal Ac.

Figures 7-22 and 7-23 show the voltage versus capacity for the first cycle of the eight coal samples. Figures 7-24 and 7-25 show the voltage versus capacity for the second cycle. The capacity data plotted here has not been corrected for the impurity content of the coals, therefore it is the raw data. Coals Ac and Ec show little evidence for low voltage plateaus and they have the smallest values of B_k and the largest values of R for all the coals as shown in table 7-6.

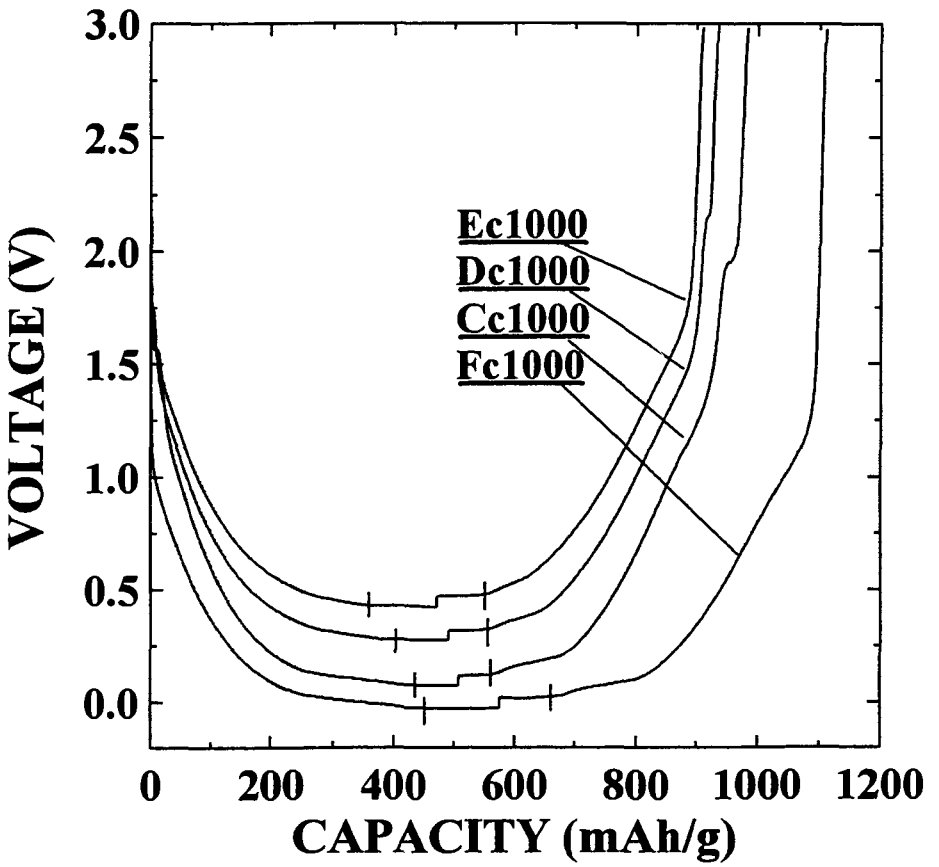

Figure 7-24. Voltage curves for the second cycle of lithium/carbon cells made from coals Ec, Dc, Cc and Fc as indicated. The data has been offset by 0.0V for coal Fc, by 0.1V for coal Cc, by 0.3V for coal Dc and by 0.45V for coal Ec. The vertical lines indicate the onset of lithium plating during discharge and the termination of lithium stripping during charge.

To measure the size of the low voltage plateau, we first plotted the differential capacity, $-dx/dV$, versus voltage for each sample. Figure 7-26 shows the results for

sugar, CRO1000 and coal Fc. The size of the low voltage plateau during charge was then obtained by the area of the peak (above the "background" from the CRO1000 sample) in $-dx/dV$ indicated near 0.07V. The results are given in table 7-5.

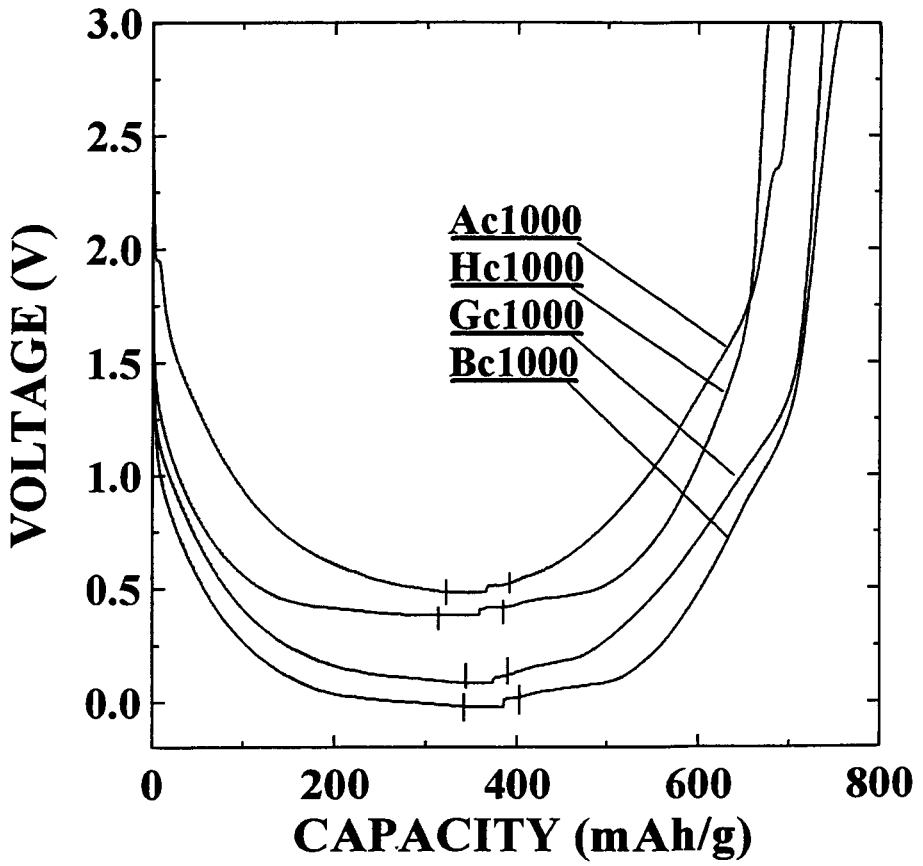

Figure 7-25. Voltage curves for the second cycle of lithium/carbon cells made from coals Ac, Hc, Gc and Bc as indicated. The data has been offset by 0.0V for coal Bc, by 0.1V for coal Gc, by 0.4V for coal Hc and by 0.5V for coal Ac.

We corrected the measured reversible capacities for the ash content in the coals which we assume to be electrochemically inactive. The correction was made by assuming that the inactive mass fraction in the pyrolyzed coal was the ash content of the original coal divided by the pyrolysis yield. That is, we assume that the ash mass does not change during pyrolysis. Table 7-5 lists the estimated inactive mass fractions for the pyrolyzed coals. Then, the full capacity and the low voltage plateau capacity were corrected for the

ash content of the samples and these were then correlated to the changes in R and B_k of the samples.

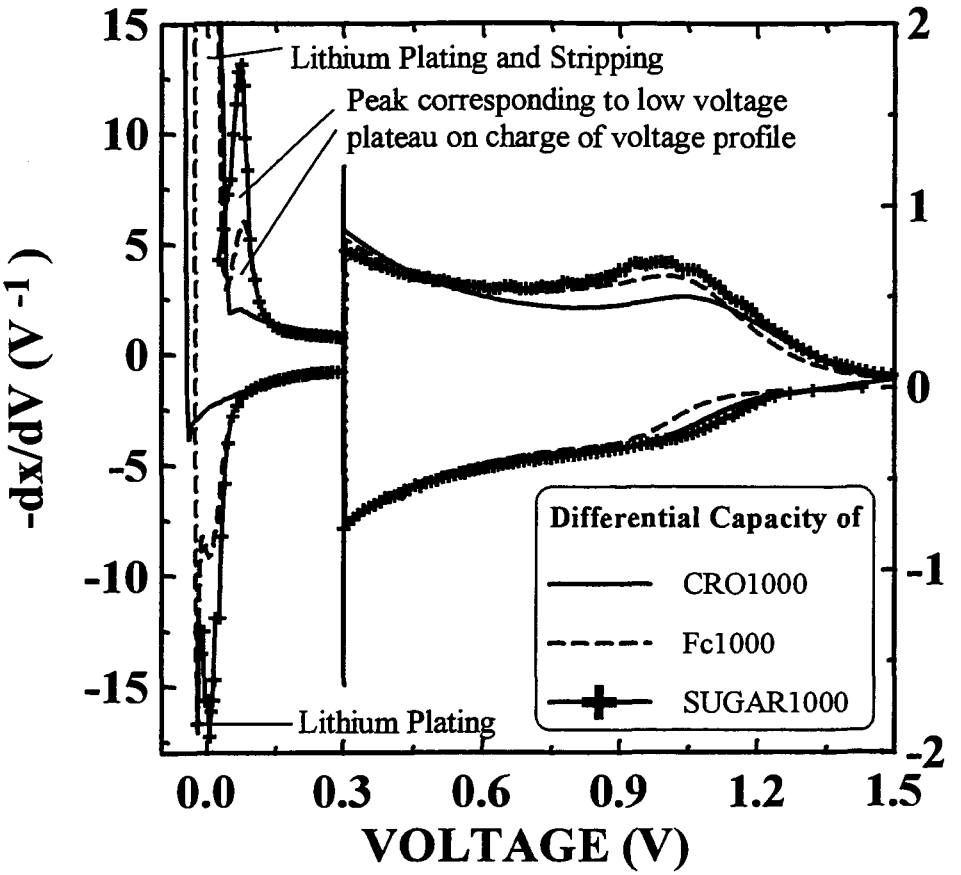

Figure 7-26. $-dx/dV$ *versus V for CRO1000, sugar and coal Fc. The peak corresponding to the low voltage plateau is indicated. Notice that the vertical scale changes for data to the left and right of 0.3V.*

Figure 7-27 shows the low voltage plateau capacity, the reversible capacity and B_k, all plotted versus the X-ray ratio, R. There is an excellent correlation shown. That is, coals with the fewest parallel-stacked layers (smallest R) and the largest number of nanopores (largest B_k) have the biggest low voltage plateaus and reversible capacities.

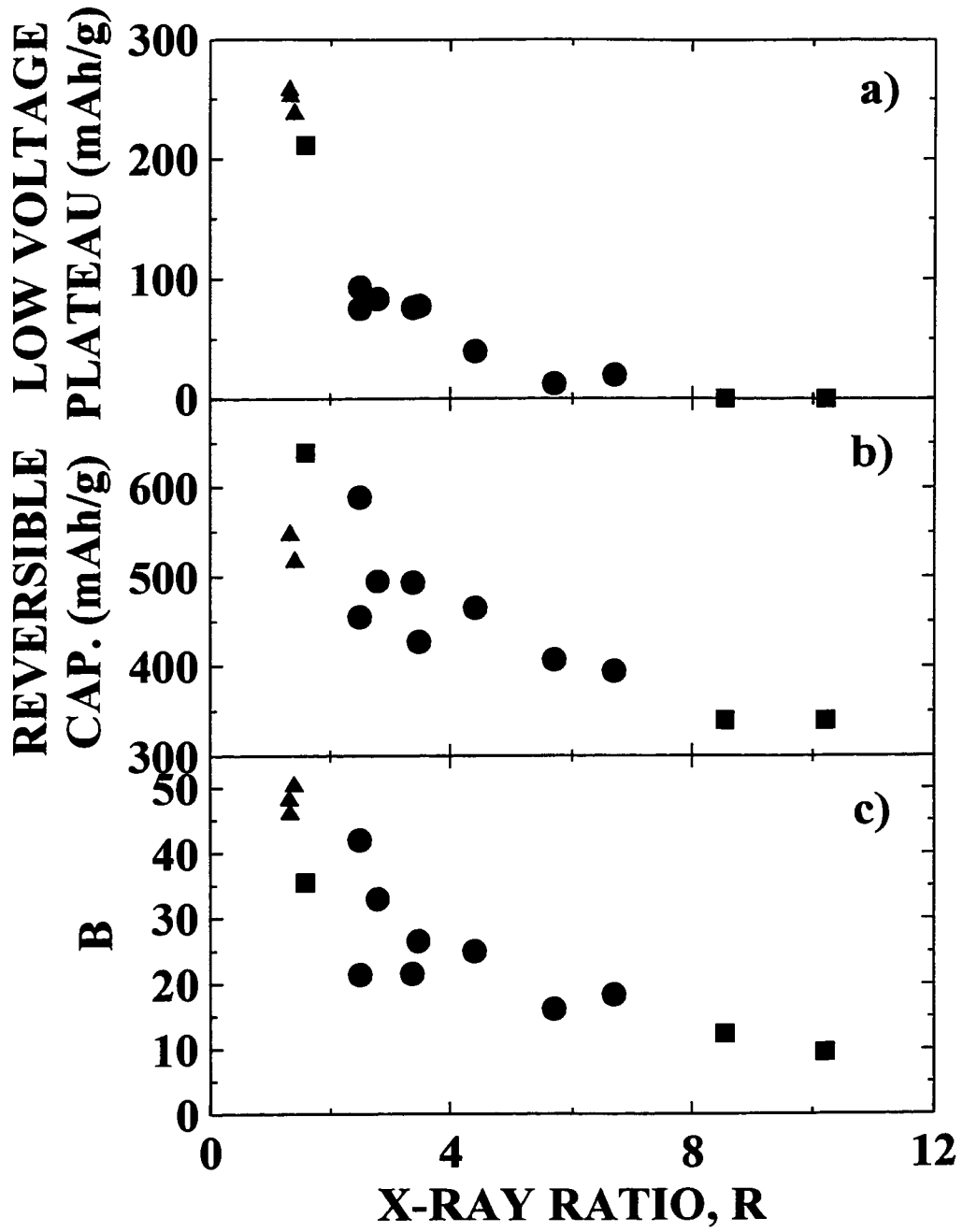

Figure 7-27. a) low voltage plateau capacity, b) total reversible capacity and c) nanopore amount, B, plotted versus the X-ray ratio, R, for the coal samples (round data points), the standard samples (square points), and the vacuum pyrolyzed phenolic resins (triangles).

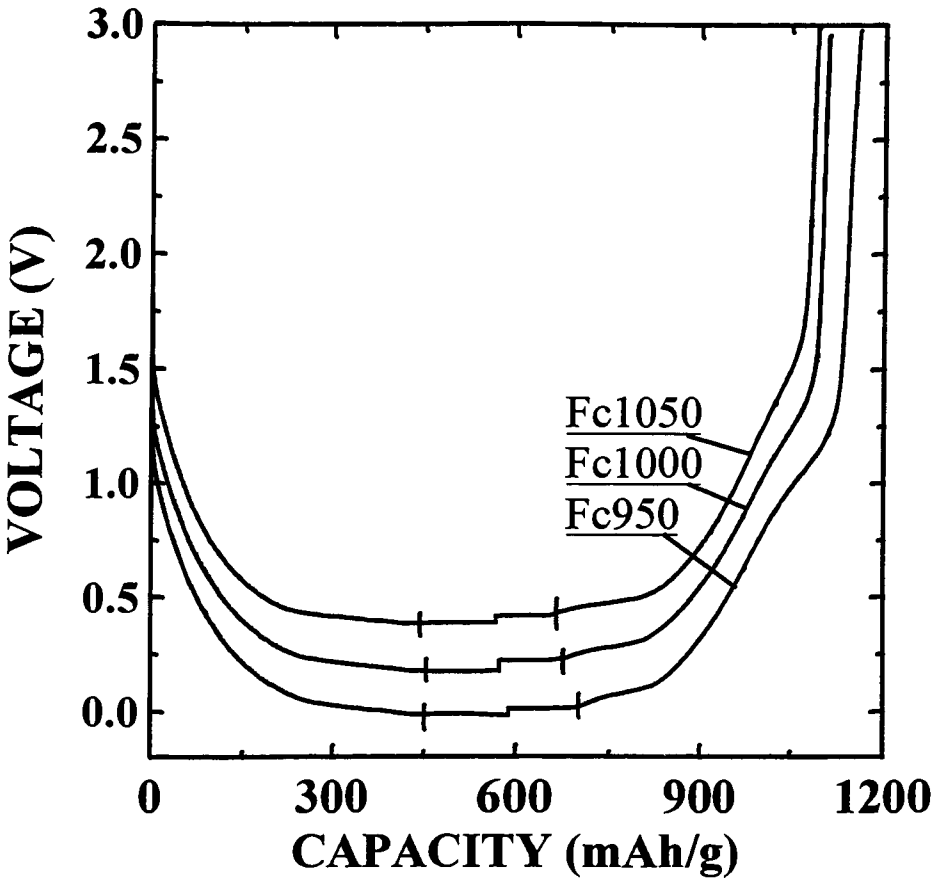

Figure 7-28. Voltage-capacity profiles for the second cycle of lithium/carbon cells made from coals Fc950, Fc1000 and Fc1050 respectively.

The coal samples described here span the range between the sugar sample and the pyrolyzed pitch and PVC samples. Their low voltage plateau capacities vary in a way which is expected based on the number of nanopores present and on the way their graphene layers are stacked.

Coals Ac, Cc, and Dc show a small reversible plateau near 1.5V in figures 7-22, 7-23, 7-24 and 7-25. This is due to an impurity, FeS or troilite, in the pyrolyzed coals as discussed in Appendix 2.

Since the Fc1000 sample was shown to be the material with the highest uncorrected reversible capacity, we decided to pyrolyze the Blind Canyon coal to temperatures of 950°C and 1050°C to see how variations to the pyrolysis temperature affect the capacity.

The irreversible and reversible capacities for samples Fc950 and Fc1050 are listed in table 7-5. The voltage profiles for the second cycle of cells with electrodes of Fc950, Fc1000 and Fc1050 are shown in figure 7-28. The capacity of the low-voltage plateau increases slowly and the small plateau near one volt on charge tends to disappear as the heat treatment temperature increases. The one volt plateau on charge is believed to be due to hydrogen in these carbon materials as we described in chapter 5. Since the hydrogen content decreases with heat treatment temperature, so does the capacity of the one volt plateau.

The tap density is a simple way to measure the bulk density of a carbon powder. We measured the 30-tap density of Fc1000 to be 0.93 g/cm^3 compared to 1.34 g/cm^3 for a synthetic graphitic carbon powder, MCMB2700, measured in the same way. Although the gravimetric capacity of sample Fc1000 is higher than that of graphite, lower bulk density for the coal derived sample gives materials of a similar volumetric capacity.

7.3.4 Conclusions

This study of pyrolyzed coal samples has demonstrated that heated coals which have the highest capacity for lithium also have the smallest fraction of parallel-stacked graphene sheets (small R) and the largest number of nanoscopic pores (large B_k). Heated sugar (or resins) and heated pitch, which are hard and soft carbon precursors, respectively, bracket the behavior shown by the coal samples. The high volatile bituminous coals, samples C_k, D_k, F_k and G_k, give the best performance, suggesting that this class of coals is most useful. If suitable coals, which give hard carbon upon pyrolysis, can be obtained with low ash contents, then it is apparent that acceptable materials for lithium-ion cells can be prepared cheaply from coal.

CONCLUSIONS

8.1 Conclusions of this Thesis

In order to prepare high capacity carbon for lithium-ion batteries, it is important to understand the physics and chemistry of the insertion of lithium in carbonaceous materials. In this thesis, we report that the mechanism of lithium insertion depends on the carbon type. The carbonaceous materials of commercial relevance as lithium-ion anodes are divided into three regions: (1) graphitic carbons, (2) hydrogen containing carbons heated to between 500°C and 800°C, and (3) some hard carbons heated to about 1000°C.

Graphitic carbons have been carefully studied in this thesis. Firstly, we showed that the probability P of turbostratic disorder (random shifts or rotations between adjacent carbon layers) in graphitic carbons determines the capacity Q for lithium intercalation, that is, $Q = 372(1-P)$ mAh/g. This finding suggests that no lithium can be inserted between adjacent parallel layers which are turbostratically misaligned. The effect of turbostratic disorder on staging phase transitions which occur during the intercalation of lithium in graphitic carbons was carefully studied by in-situ X-ray diffraction and electrochemical methods. A staging phase diagram was then developed for the P-x plane, where x is the lithium concentration in intercalated graphitic carbons.

We next studied many samples prepared from organic precursors heated between 500 and 800°C which contain substantial amounts of hydrogen. They all have similar voltage profiles, with very large capacity, approaching 900 mAh/g, but also have large hysteresis between charge and discharge. We demonstrated for the first time that this high capacity exhibiting large hysteresis is proportional to the hydrogen content of the carbons. We have carefully studied the electrochemical insertion of lithium in these hydrogen-containing carbons using a variety of charge-discharge rates and cycling temperatures. These measurements allow the hysteresis to be quantified. Tthe lithium atoms may bind

on hydrogen-terminated edges of hexagonal carbon fragments causing a change in the bond from sp^2 to sp^3. A simple model has been developed to understand the hysteresis. Achieving high capacity carbons needs a coupling of fundamental research (understanding) and applied research (to apply concepts in synthesis). Good understanding will lead to high quality samples.

We have pyrolyzed a number of disordered hard carbons from phenolic resins. These materials have reversible capacities of 500 to 600 mAh/g, a low voltage plateau near zero volts, and little hysteresis in their voltage profiles. These hard carbons with high capacity were found to be made up with a large fraction of single layers, stacked like a "house of cards". The lithium can be adsorbed onto both sides of the carbon sheets, leading to a large capacity. Using small-angle scattering techniques, we showed that the micropore sizes in these carbons are on the order of 10 to 15 Å in diameter. The understanding of the high capacity of hard carbons makes it possible to prepare high capacity carbon with low cost and good performance.

More recently, we have been studying ways to make such hard carbons with high capacity from coal. Coal has a large carbon content and can have a highly aromatic condensed structure, leading to high product yields after heat treatment. We thought this might be a cheap way to make carbon electrode material for lithium-ion batteries. The physical properties of the pyrolyzed coals varies from sample to sample because of the varied chemistries of the initial coals. Nevertheless, the amount of lithium that the pyrolyzed coals can accommodate is largest for coals with small R and many nanoscopic pores. This gives us further confidence that our model for the reversible capacity of coals is correct.

8.2 Future Work

Hydrogen-containing carbons are currently good candidates for anodes of lithium-ion cells (Yata, 1995). We have made these carbons with capacity up to 900 mAh/g. However, the capacity of these samples decreases rapidly after a few cycles, and there is large hysteresis in their voltage profiles. We have proposed a simple model to understand

the hysteresis in the samples. Perhaps the hysteresis can be reduced by using precursors which yield to products with smaller activation energy for the bonding change from sp^2 to sp^3. We do not understand the loss of capacity upon cycling yet. More fundamental research is needed to understand this. We need to do open circuit voltage measurements on more of these samples. The results should give more of the information needed to understand these samples.

We qualitatively understand the importance of single carbon layers and nanoscopic pores in hard carbons. These single layers are stacked like a "house of cards" so significant amounts of nanopores are formed. Nanopores with large openings will allow the electrolyte penetration into the internal surface of pores and a passivating film formed, leading to large irreversible capacity (Xue, 1995). Pores with small openings are believed to be the origin of large reversible capacity. Therefore the nanoporosity in hard carbon is playing a critical role. Since different pyrolysis conditions (such as, heating temperature, flushing speed, and temperature ramp) will affect the size and openings of nanopores in samples, it will take a substantial amount of work to pyrolyze hard carbon from different organic precursors to learn how the pyrolysis conditions affect the micropore size distribution and openings.

Table sugar has been found to be a cheap source to make hard carbon. Carbon samples made from de-watered table sugar have shown very high capacity, up to 600 mAh/g (Xing, 1996). It will be a good project to make hard carbon from table sugar with suitable pore size distribution to achieve higher reversible capacity materials with little irreversible capacity, based on the above fundamental research.

APPENDIX 1

Development of the Model---We develop simple models to describe the stage 2 and stage 1 behavior of lithium intercalation in graphitic carbons. Three reasonable assumptions are made:

1) $x_{max}=1-P$ and no lithium in blocked galleries;

2) Full galleries cannot be adjacent;

3) The amount of lithium in the compound should be maximized subject to condition 2.

Thus, there are only three kinds of galleries in our samples: filled, empty and blocked galleries. They are labeled F, E and B, respectively.

To simulate the stacking in our models, we use a matrix method to represent the three kinds of galleries.

$$F = \begin{pmatrix} 1 & 0 & 0 \end{pmatrix} \tag{A1-1}$$

$$E = \begin{pmatrix} 0 & 1 & 0 \end{pmatrix} \tag{A1-2}$$

$$B = \begin{pmatrix} 0 & 0 & 1 \end{pmatrix} \tag{A1-3}$$

To introduce the correlation between galleries, two neighboring galleries are considered now. Assume that the probability that F is followed by F is $A_1^{(11)}$; by E is $A_1^{(12)}$; and by B is $A_1^{(13)}$. The probability that E is followed by F is $A_1^{(21)}$; by E is $A_1^{(22)}$; and by B is $A_1^{(23)}$. The probability that B is followed by F is $A_1^{(31)}$; by E is $A_1^{(32)}$; and by B is $A_1^{(33)}$. Hence, the following is always true:

$$A_1^{(m1)} + A_1^{(m2)} + A_1^{(m3)} = 1,$$

with m=1,2,3.

The correlation between second neighbors can be calculated by multiplying near neighbor correlations. For example, the probability of finding the third gallery filled if the first gallery is filled is

$$A_2^{(11)} = A_1^{(11)} \cdot A_1^{(11)} + A_1^{(12)} \cdot A_1^{(21)} + A_1^{(13)} \cdot A_1^{(31)}.$$

If a 3×3 generation matrix,

$$M = \begin{pmatrix} A_1^{(11)} & A_1^{(12)} & A_1^{(13)} \\ A_1^{(21)} & A_1^{(22)} & A_1^{(23)} \\ A_1^{(31)} & A_1^{(32)} & A_1^{(33)} \end{pmatrix},$$

is introduced, the probabilities of finding the 1st, 2nd or nth neighbor in a specified state is easily calculated. For example, if the first gallery is filled, multiplying the array (A1-1) by M will give the probabilities for the type of the second gallery, multiplying by M^2 will give the third gallery,..., and by M^n will give the (n+1)th gallery. The probabilities for the nth gallery to be filled, empty or blocked if the first gallery is filled are represented by the elements of the first row in the matrix M^{n-1}, $A_{n-1}^{(11)}$, $A_{n-1}^{(12)}$ and $A_{n-1}^{(13)}$, respectively. So, the probability of finding filled galleries in an n-layer sample is

$$\left(\frac{1}{n}\right) \cdot \sum_n A_{n-1}^{(11)} \tag{A1-4}$$

the probability of finding empty galleries is

$$\left(\frac{1}{n}\right) \cdot \sum_n A_{n-1}^{(12)} \tag{A1-5}$$

and the probability of finding blocked galleries is

$$\left(\frac{1}{n}\right) \cdot \sum_n A_{n-1}^{(13)}, \tag{A1-6}$$

for large n (approaching ∞). In fact, the results of (A1-4), (A1-5), and (A1-6) are the measurables x_{2max}, x_{21} and P, respectively!

Two models are developed next to simulate the compositions of stage 2 and stage 1.

Model 1---A random distribution of blocked galleries is assumed (refer to figure 5-16). Consider two consecutive galleries labeled A and B. We assume, if A is filled, there will be probability P'' for B to be blocked and a probability $(1-P'')$ for B to be empty. If A is empty, there will be probability P'' for B to be blocked and a probability $(1-P'')$ for B to be filled. If A is blocked, there will be probability P'' for B to be blocked and a probability $(1-P'')$ for B to be filled. Then the generation matrix M is

$$\begin{pmatrix} 0 & 1-P'' & P'' \\ 1-P'' & 0 & P'' \\ 1-P'' & 0 & P'' \end{pmatrix}.$$

If we take an infinite layer model, the probability of finding a blocked gallery is

$$P = P''.$$

The capacities, x_{2max} and x_{21} can be calculated from (A1-4) and (A1-5), giving

$$x_{2\max} = \frac{1-P}{2-P},$$

$$x_{21} = \frac{(1-P)^2}{2-P}.$$

The results of model 1 for x_{2max} and x_{21} are presented in figure 5-15 and compared to experimental data. This model does not work well.

Model 2---Blocked galleries can not be adjacent (refer to figure 5-16). Consider two consecutive galleries labeled A and B. If A is filled, there will be probability P'' for B to be blocked and a probability $(1- P'')$ for B to be empty. If A is empty, there is a probability P'' for B to be blocked and a probability $(1- P'')$ for B to be filled. If A is blocked, the layer B is always filled. Hence, the generation matrix is

$$M = \begin{pmatrix} 0 & 1-P'' & P'' \\ 1-P'' & 0 & P'' \\ 1 & 0 & 0 \end{pmatrix}.$$

The probability P to find a blocked gallery is

$$\frac{P''}{1+P''} = P.$$

Using equation (A1-4) and (A1-5) we find,

$$x_{2\max} = \frac{1}{(1+P'')\cdot(2-P'')} = \frac{(1-P)^2}{2-3P},$$

$$x_{21} = \frac{1-P''}{(1+P'')\cdot(2-P'')} = \frac{(1-P)\cdot(1-2P)}{2-3P}.$$

In Figure 5-15, the results of model 2 for x_{2max} and x_{21} are compared to the experimental data. The results fit the data well.

APPENDIX 2

We noticed that only coals Ac1000, Cc1000, and Dc1000 show a small reversible plateau near 1.5 volts as shown in figures 7-22, 7-23, 7-24, and 7-25. This small plateau is due to an impurity in these coals as shown below.

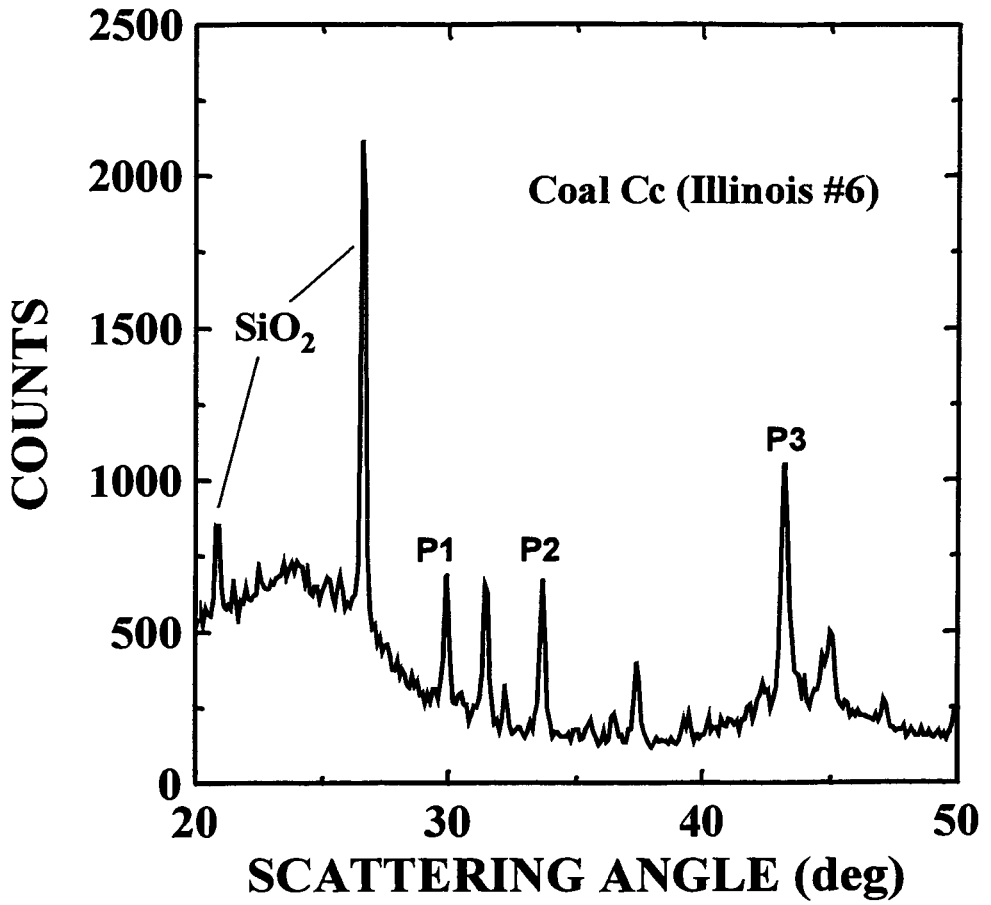

Figure A-1. Powder X-ray diffraction pattern of sample Cc1000. Peaks from SiO_2 impurities are labeled, as are those of the extra peaks (P1, P2, and P3) only found in Coals Ac1000, Cc1000 and Dc1000.

We carefully compared the X-ray diffraction pattern of all eight coals heated to 1000°C. Three extra peaks in the diffraction patterns of samples Ac1000, Cc1000 and Dc1000 were found. These peaks were not found in the patterns of the other samples.

The X-ray pattern of the sample Cc is shown in figure A-1 where the three extra peaks are labeled as P1, P2 and P3.

Table A-1. Major mineral matter analysis data for the coal samples.

Coal	Sample Designator	Quartz (SiO_2) (%)*	Pyrite (FeS_2) (%)*	Calcite ($CaCO_2$) (%)*	Total Clay (%)*	Total mineral matter in coal (%)*
Upper Freeport	Ac	1.5	3.4	1.0	9.4	15.3
Wyodak-Anderson	Bc	2.0	0.1	0.4	6.2	8.7
Illinois #6	Cc	3.4	5.5	1.9	7.3	18.1
Pittsburgh #8	Dc	1.7	2.4	0.5	6.3	10.9
Pocahontas #3	Ec	0.3	0.1	1.7	3.4	5.5
Blind Canyon	Fc	0.8	0.5	1.3	2.7	5.3
Lewiston-Stockton	Gc	2.6	0.3	0.3	18.4	21.6
Beulah-Zap	Hc	0.6	0.3	1.7	6.1	8.7

* Weight percentage.

Table A-2. Positions and Intensities of FeS peaks from JCPDS card #37-0477.

Miller Indices (hkl)	Peak Position ($2\theta_B$)	Relevant Peak Intensity	Measured Peak	Measured Angle ($2\theta_B$)	Measured Intensity
(103)	28.558°	2			
(110)	29.919°	50	P1	29.90°	681
(004)	30.378°	14			
(112)	33.666°	50	P2	33.70°	661
(200)	34.687°	2			
(201)	35.524°	6			
(203)	41.845°	6			
(105)	42.173°	5			
(114)	43.145°	100	P3	43.19°	1052
(006)	46.283°	1			
(210)	46.458°	3			
(204)	46.762°	4			
(211)	47.123°	8			
(212)	49.098°	1			
(106)	49.698°	1			

Based on a search of the JCPDS powder diffraction database, the three extra impurity peaks in figure A-1 might be caused by FeS or troilite. Later on, we confirmed this by table A-1 and by in-situ X-ray measurement. Table A-2 compares positions and intensities of three FeS peaks, (110), (112) and (114), from the JCPDS files to peaks P1, P2 and P3. We did not correct the background from the measured intensity for the these peaks. Other peaks between 20 to 50° of scattering angle from the JCPDS files are also listed in the table A-2.

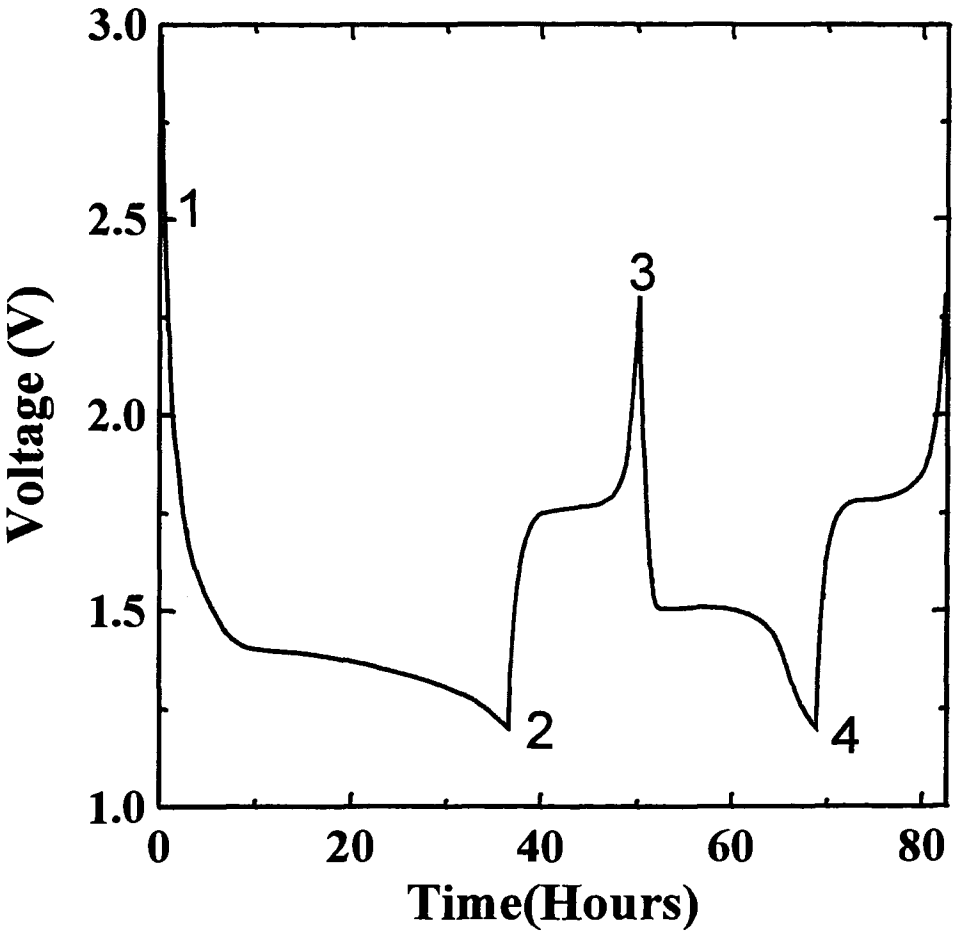

Figure A-2. The first and the second cycles for a lithium/carbon cell made from Cc1000. The cell was cycled between 1.2 and 2.5 volts. Position 1 corresponds to the fresh cell, then the cell was discharged to 1.2 volts, position 2. After this, the cell was recharged to 2.5 Volts, position 3, and discharged to 1.2 volts again, position 4.

Table A-1 gives mineral analysis data which is supplied with the eight raw coals (Vorres, 1990). These results are for the unheated coals. It is obvious that the three coals Ac, Cc, and Dc have the largest amount of Pyrite (FeS_2). FeS_2 is unstable and converts to FeS upon heating to 700°C (Parkes, 1961).

The in-situ X-ray diffraction measurement was described carefully in chapter 4. This technique was employed in chapter 5 to explore the changes in structure during lithium intercalation in the graphitic carbons. Here, we made an in-situ X-ray cell from the coal sample Cc1000, because it showed the largest plateau at about 1.5 volts as shown in figures 7-19, 7-21 and figure A-2.

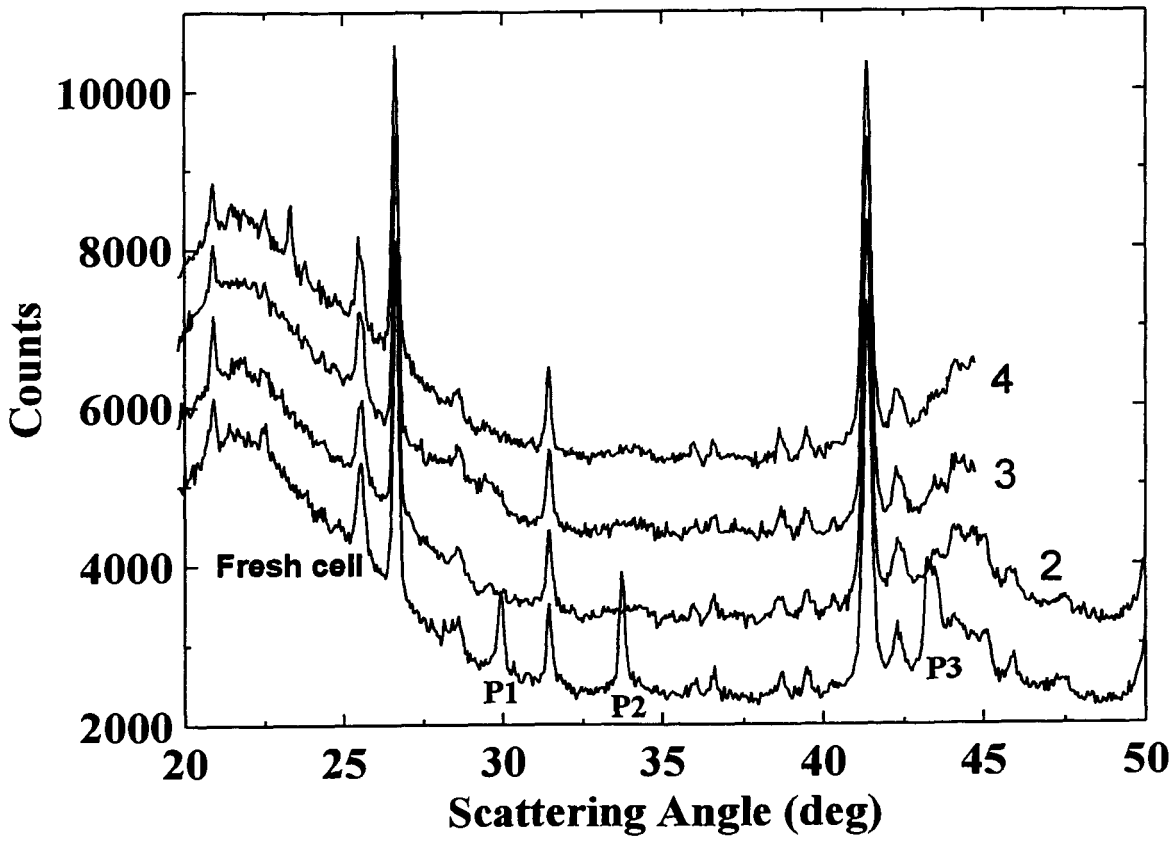

Figure A-3. In-situ X-ray diffraction data for the peaks P1, P2, and P3 at different voltage points in the first two cycles. The data presented at bottom is for the fresh cell, then for the positions 2,3, and 4 respectively, corresponding to figure A-2. The data have been offset sequentially by 1000 counts for clarity. The three peaks P1, P2, P3 have been marked.

Figure A-2 shows voltage profile between 1.2 and 2.5 volts for one of the lithium/carbon electrochemical cells made from Cc1000 (referring to chapter 7). The charge-discharge current used for this cell was 1.34 mA/g. In figure A-2, plateaus are observed at about 1.5 volts for discharge, and at about 1.8 volts for charge. The total capacity contained in these plateaus is about 20 mAh/g of carbon. Therefore we decided to compare the diffraction pattern for in-situ cells fixed at 1.2 volts and 2.5 volts respectively, to see what happens to the three peaks, P1, P2, and P3.

Figure A-3 shows the diffraction data for the in-situ cell at the different voltage points corresponding to positions 1, 2, 3, and 4 respectively in figure A-2. The peaks P1, P2, and P3 only appear in the diffraction pattern for the fresh cell. They are hard to see in the sequential diffraction profiles which means that the structure of troilite was more or less destroyed during reaction with lithium.

We believe the reversible plateau is caused by the reaction,

$$2Li + FeS \leftrightarrow Li_2S + Fe\,.$$

Initially the FeS is crystalline, but after conversion to Li_2S and Fe, it does not recrystallize into FeS grains with appreciable size when the lithium is removed. Disproportionation reactions, such as this have been observed in numerous other sulfides (Selwyn, 1987; Fong, 1989).

REFERENCES

Berlinsky A.J., Unruh W.G., McKinnon W.R., and Haering R.R., Solid State Commun. 31, 135(1979).

Boehm R.C., and Bannerjee A., J. Chem. Phys. **96**, 1150 (1992).

Chermin H.A.G., and van Krevelen D.W., Fuel **36**, 85 (1957).

Cullity B.D., *Elements of X-Ray Diffraction*, second edition (Addison-Wesley, USA, 1978).

Dahn J.R., Py M.A., and Haering R.R., Can. J. Phys. **60**, 307 (1982).

Dahn J.R., and McKinnon W.R., J. Phys. C **17**, 4231 (1984).

Dahn J.R., Phys. Rev. B **44**, 9170 (1991a).

Dahn J.R., von Sacken U., Juzkow M.W., and Al-Janaby H., J. Electrochem. Soc. **138**, 2207 (1991b).

Dahn J.R., Sleigh A.K., Shi Hang, Way B.W., Weydanz W.J., Reimers J.N., Zhong Q., and von Sacken U., " Carbons and Graphites as Substitutes for the Lithium Anode", in *Lithium Batteries*, edited by Pistoia G. (Elsevier, North Holland, 1993).

Dahn J.R., Zheng Tao, Liu Y., Xue J.S., Science 270, 590 (1995).

Daumas N., and Herold A., C. R. Acad. Sci. (Paris), Ser. C **268**, 373 (1969).

Debye P., Anderson H.R., and Brumberger H., J. Appl. Phys. **28**, 679 (1957).

Diamond R., in *Proceedings of the Third Conference on Carbon*, page 367, Buffalo, New York (1957), published by Pergamon Press, New York (1959).

Drits V.A., and Tchoubar C., *X-Ray Diffraction by Disordered Lamellar Structures* (Springer-Verlag, 1991)

Enoki T., Miyajima S., Sano M., and Inokuchi H., J. Mater. Res. **5**, 435 (1990).

Fischer J.E., in *Chemical Physics of Intercalation*, edited by Legrand A.P. and Flandrois S. (Plenum, New York, 1987).

Fitzer E., Schaefer W. and Yamada S., Carbon 7, 643 (1969).

Fitzgerald D., and van Krevelen D.W., Fuel **38**, 17 (1959).

Fong R., Dahn J.R., and Jones C.H.W., J. Electrochem. Soc. **136**, 3206-3210 (1989).

Fong R., von Sacken U., and Dahn J.R., J. Electrochem. Soc. **137**, 2009 (1990).

Franklin R.E., J. Chim. Phys. **47**, 573 (1950).

Franklin R.E., Acta Cryst. **4**, 253 (1951a).

Franklin R.E., Proc. Roy. Soc. (London), Ser. **A** 209, 196 (1951b).

Gerischer H., Kolb D.M., and Sass J.K., Advances in Phys. **27**, 437 (1978).

Guinier A., Fournet G., *Small-Angle Scattering of X-Ray* (John Wiley & Sons, New York, 1955).

Harrison W.A., *Electronic Structure and the Properties of Solids* (Dover, New York, 1989).

Herold A., Bull. Soc. Chim. (Fr.) **187**, 999 (1955).

Hossain S., "Rechargeable Lithium Batteries (Ambient Temperature)", in *Handbook of Batteries*, edited by Linden D., 2nd edition (McGraw-Hill Inc., 1995).

Kakinoki J., Katada K., and Hanawa T., Acta Cryst. **13**, 448 (1960).

Kalliat M., Kwak C.Y., and Schmidt P.W., *New Approaches in Coal Chemistry*, edited by Blaustein B.D., Bockrath B.C., and Friedman S., American Chemical Society, Washington D.C., page 3(1981).

Kambe N., Dresselhaus M.S., Dresselhaus G., Basu S., McGhie A.R., and Fischer J.E., Mater. Sci. Eng. **40**, 1 (1979).

Linden D., *Handbook of Batteries*, page xvii, 2nd edition (McGraw-Hill Inc., 1995).

Liu Y., Xue J.S., Zheng Tao, and Dahn J.R., Carbon **34**, 193 (1996).

McKinnon W.R., Thesis, University of British Columbia (1980).

McKinnon W.R., J. Less-Commom Met. **91**, 293 (1983a).

McKinnon W.R., and Haering R.R., Modern Aspects of Electrochemistry, Number 15, edited by White R.E., Bockris J. O'm, and Conway B.E., (Plenum, New York, 1983b).

Mabuchi A., Tokumitsu K., Fujimoto H., and Kasuh T., 7th International Meeting on Lithium Batteries, May 15-20 (1994), Boston, USA, paper I-A-10, page 207 of extended abstracts; also see Fujimoto H., Mabuchi A., Tokumitsu K., and Kasuh T., ibid, paper II-B-12, page 540.

Marsh H., Murdie N., and Edwards, I.A.S., "Intercalation of Carbons, Cokes, and Graphites with Potassium and Sodium", in *Chemistry and Physics of Carbon*, edited Thrower P.A., Vol. 20, 213-272 (Marcel Dekker Inc., N.Y., 1987).

Nagaura T., and Tozawa K., Prog. Batt. Solar Cells **9**, 209 (1990).

Nalimova V.A., Guerard D., Lelaurain M., and Fateev O.V., Carbon **33**, 177 (1995).

Oberlin A., "High-Resolution TEM Studies of Carbonization and Graphitization", in *Chemistry and Physics of Carbon*, edited Thrower P.A., Vol. 22, 1-144 (Marcel Dekker Inc., N.Y., 1989).

Omaru A., Azuma H., Aoki M., Kita A. and Nishi Y., paper #25, 182nd Meeting of the Electrochemical Society, Toronto, Canada (1992), Extended Abstracts of Battery Division, page 34.

Papanek P., Radosavljievic M., and Fischer J.E., submitted to Chem. Matter., Feb (1996).

Parkes G.D., *Mellor's Modern Inorganic Chemistry*, p.923 (Longmans, Green and Co Ltd., 1961)

Peled E., J. Electrochem. Soc. **126**, 2047 (1979).

Porod G., Kolloid-Z **124**, 83 (1951).

Porod G., "Method-General Theory", in *Small Angle X-Ray Scattering*, edited by Glatter O. and Kratky O. (Academic Press Inc. (London) Ltd., 1982).

Puri B.R., "Surface Complexes on Carbons", in *Chemistry and Physics of Carbons*, edited by Walker P.L., Jr., Vol. 6, 191 (Marcel Dekker Inc., N.Y., 1970).

Rayleigh L., Proc. Roy. Soc. (London), A-**84**, 25 (1911).

Sato K., Noguchi M., Demachi A., Oki N., and Endo M., Science 264, **556** (1994).

Scherrer P. Nachr Göttinger Gesell., 98 (1918).

Schick M., Walkwe J.S., and Wortis M., Phys. Rev. B **16**, 2205 (1977).

Safran S.A., Phys. Rev. Lett. **44**, 937 (1980).

Selwyn L.S., McKinnon W.R., von Sacken U., and Jones C.A., Solid State Ionics **22**, 337 (1987).

Shi Hang, Ph.D. Thesis, Simon Fraser University (1993a).

Shi Hang, Reimers J.N., and Dahn J.R., J. Appl. Cryst. **26**, 827 (1993b).

Sonobe N., Ishikawa M. and Iwasaki T., 35th Battery Symposium in Japan, Nov. 14-16 (1994), Nagoya, Japan, paper 2B09, extended abstracts, page 47.

Takahashi Y., Oishi J., Miki Y., Yoshimura M., Shibahara K. and Sakamoto H., 35th Battery Symposium in Japan, Nov. 14-16 (1994), Nagoya, Japan, paper 2B05, extended abstracts, page 39.

Tarascon J.M., and Guyomard D., Electrochem. Acta **38**, 1221 (1993).

Thomas J.M., Millword G.R., Schlögl R.F., Boehm H.P., Mat. Res. Bull. **15**, 671 (1980).

Thompson A.H., Phys. Rev. Lett. **40**, 1511 (1978).

Vorres K.S., Energy & Fuels **4**, 420 (1990).

Walker P.L., Jr., see paper in volumes 1 and 2 in *Chemistry and Physics of Carbon*, (Marcel Dekker Inc., N.Y., 1965, 1966).

Warren B.E., Phys. Rev. **9**, 693 (1941).

Warren B.E., *X-Ray Diffraction*, page 254 (Dover, N.Y., 1990).

Xue J.S., and Dahn J.R., J. Electrochem. Soc **142**, 3668 (1995a).

Xue J.S., Wilson A.M., and Dahn J.R., Canadian Patent application, filed May 20 (1995b).

Xing W., Xue J.S., and Dahn J.R., submitted to Carbon, Feb. (1996).

Yata S., Kinoshita H., Komori M., Ando N., Kashiwamura T., Harada T., Tanaka K., and Yamabe T., Synth. Met. **62**, 153 (1994).

Yata S., Hato Y., Kinoshita H., Ando N., Anekawa A., Hashimoto T., Yamaguchi M., Tanaka K., Yamabe T., Synth. Met. **73**, 273-277 (1995).

Zheng Tao, Reimers J.N., and Dahn J.R., Phys. Rev. B, **51**, 734-741 (1995a).

Zheng Tao, and Dahn J.R., Synth. Met., **73**, 1-7 (1995b).

Zheng Tao, Liu Yinghu, Fuller E.W., Tseng Sheilla, von Sacken U., and Dahn J.R., J. Electrochem. Soc. **142**, 2581-2590 (1995c).

Zheng Tao, Zhong Q., and Dahn J.R., J. Electrochem. Soc., **142**, L211-L214 (1995d).

Zheng Tao, Xue J.S., and Dahn J.R., Chemistry of Materials, **8**, 389-393 (1996a).

Zheng Tao, and Dahn J.R., Phys. Rev. B, **53**, 3061-3071 (1996b).

Zheng Tao, McKinnon W.R., and Dahn J.R., *Hysteresis During Lithium Insertion in Hydrogen-Containing Carbon*, accepted by J. Electrochem. Soc., February (1996c).

Zheng Tao, Xing W., and Dahn J.R., *Carbons Prepared from Coals for Anodes of Lithium-Ion Cells*, submitted to Carbon, February (1996d).

Zumdahl S.S., Chemistry, 3rd edition, page 573 (D.C. Heath Co., Toronto, 1993).